TU Delft

Delft University of Technology

Direction of arrival estimation and self-calibration techniques using an array of acoustic vector sensors

Theory, algorithms and applications

Nambur Ramamohan, K.

DOI
10.4233/uuid:f5ab45a2-376b-48e7-b83d-55f755c12e3b

Publication date
2022

Document Version
Final published version

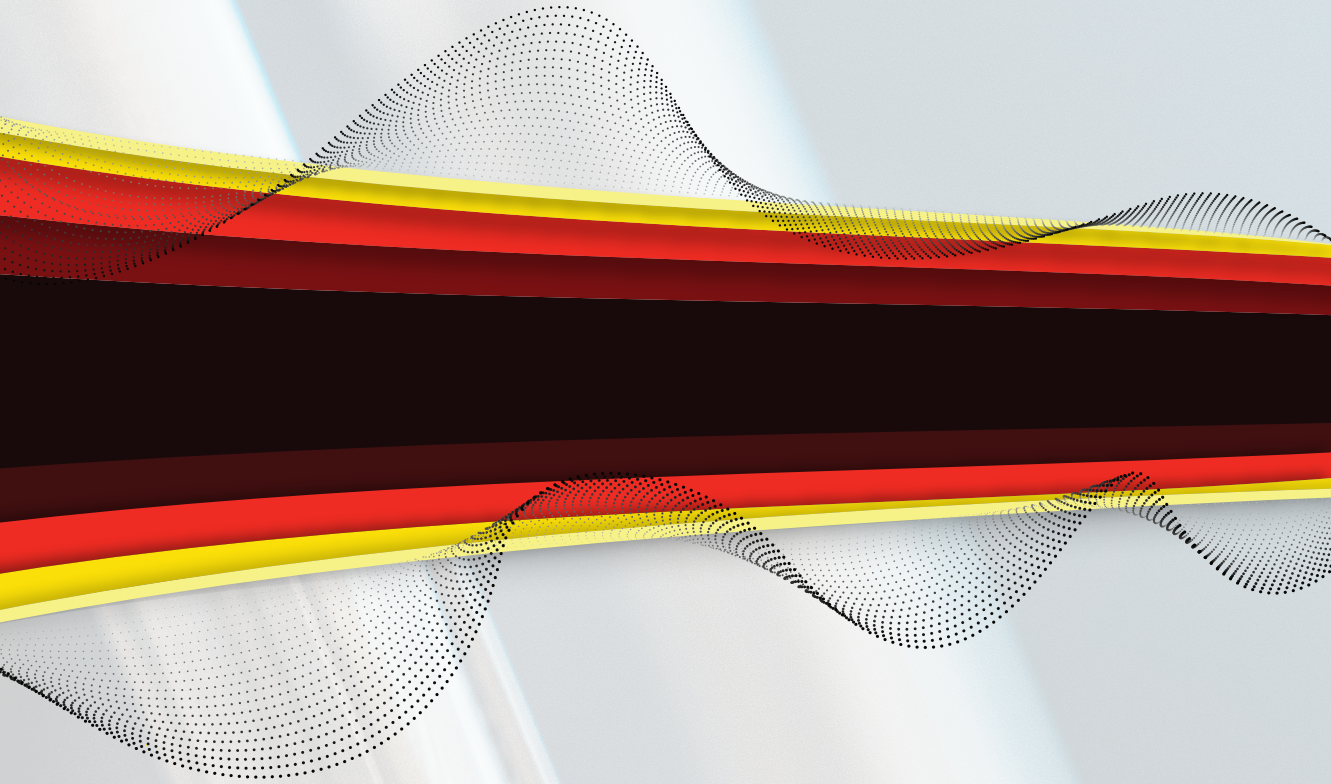
Citation (APA)
Nambur Ramamohan, K. (2022). *Direction of arrival estimation and self-calibration techniques using an array of acoustic vector sensors: Theory, algorithms and applications*.
https://doi.org/10.4233/uuid:f5ab45a2-376b-48e7-b83d-55f755c12e3b

Important note
To cite this publication, please use the final published version (if applicable).
Please check the document version above.

Copyright
Other than for strictly personal use, it is not permitted to download, forward or distribute the text or part of it, without the consent of the author(s) and/or copyright holder(s), unless the work is under an open content license such as Creative Commons.

Takedown policy
Please contact us and provide details if you believe this document breaches copyrights.
We will remove access to the work immediately and investigate your claim.

This work is downloaded from Delft University of Technology.
For technical reasons the number of authors shown on this cover page is limited to a maximum of 10.



Direction of Arrival Estimation and Self-Calibration Techniques Using an Array of Acoustic Vector Sensors

Krishnaprasad Nambur Ramamohan

TU Delft

Direction of Arrival Estimation and Self-Calibration Techniques Using an Array of Acoustic Vector Sensors

Theory, Algorithms and Applications

Dissertation

for the purpose of obtaining the degree of doctor
at Delft University of Technology
by the authority of the Rector Magnificus prof. dr. ir. T.H.J.J. van der Hagen
chair of the Board for Doctorates
to be defended publicly on
Wednesday 8 June 2022 at 10:00 o'clock

by

Krishnaprasad Nambur Ramamohan

Master of Science in Electrical Engineering,
Delft University of Technology, The Netherlands,
born in Kolar, Karnataka, India.

This dissertation has been approved by the

promotor: Prof. dr. ir. G.J.T Leus

Composition of the doctoral committee:

Rector Magnificus,	chairperson
Prof. dr. ir. G.J.T. Leus,	Delft University of Technology
Independent members:	
Prof. dr. ir. M. Snellen	Delft University of Technology
Prof. dr. V. Koivunen	Aalto University, Finland
Prof. dr. ir. M. Moonen	University of Leuven, Belgium
Prof. dr. A. Bhandari	Imperial College, London
Prof. dr. ir. A.J. van der Veen	Delft University of Technology, reserve member
Other members:	
Prof. dr. ir. SP. Chepuri	Indian Institute of Science, Bangalore, India
Dr. D. F. Comesaña	Microflown Technologies, The Netherlands

The work described in this thesis is a part of the ASPIRE project 14926, within the STW OTP program of Netherlands Organization for Scientific Research (NWO), and financially supported by Microflown AVISA.



Keywords: acoustic vector sensor, direction-of-arrival, self-calibration, array signal processing, spatial under-sampling, Cramér-Rao lower bound

Front & Back: *An artistic representation of the AVS ULA beampattern.*

Art concept & design: Fabio Markus D'Apice, Microflown Technologies.

Printed by: www.ridderprint.nl

Copyright © 2022 by K. Nambur Ramamohan

ISBN 978-94-6366-556-8

An electronic version of this dissertation is available at
http://repository.tudelft.nl/.

To my parents

CONTENTS

Summary xi

Samenvatting xiii

1 Introduction 1
- 1.1 Acoustic Vector Sensor . . . 2
  - 1.1.1 Applications . . . 4
- 1.2 Context and research objectives of this thesis . . . 6
- 1.3 Novelties of this work . . . 8
- 1.4 Outline of this thesis . . . 9
- 1.5 List of Publications . . . 12
- References . . . 13

2 Background on DOA estimation using AVS arrays and Contributions 17
- 2.1 Fundamentals of DOA estimation using an AVS array . . . 18
  - 2.1.1 Measurement Model . . . 18
  - 2.1.2 Beampattern of AVS array . . . 23
  - 2.1.3 Cramér-Rao lower bound on DOA estimation . . . 24
- 2.2 Overview of the Contributions . . . 26
  - 2.2.1 Chapter 3 - DOA Estimation and Beamforming using Spatially Under-Sampled AVS Array . . . 26
  - 2.2.2 Chapter 4 - Self-Calibration of Scalar and Vector Sensor Arrays . . . 28
  - 2.2.3 Chapter 5 - Blind Sensor Array Calibration and DOA estimation of Broad-band sources . . . 30
  - 2.2.4 Chapter 6 - Blind Calibration for Acoustic Vector Sensor Arrays . . . 32
  - 2.2.5 Chapter 7 - Uniaxial Acoustic Vector Sensors for Direction-of-Arrival Estimation . . . 33
- 2.3 Chapter Summary and Remarks . . . 35
- References . . . 35

I Acoustic Vector Sensor Array for DOA Estimation 39

3 DOA Estimation and Beamforming using Spatially Under-Sampled AVS arrays 41
- 3.1 Introduction . . . 42
- 3.2 Preliminaries . . . 42
  - 3.2.1 AVS array measurement model . . . 42
  - 3.2.2 Matched filter beam pattern of an AVS array . . . 43
- 3.3 Cramér-Rao lower bound for DOA estimation . . . 43
- 3.4 Classical and MVDR beamformer . . . 46
- 3.5 Interference cancellation . . . 48
- References . . . 50

II Self-Calibration and DOA Estimation **53**

4 Self Calibration of Scalar and Vector Sensor Arrays **55**
4.1 Introduction . . . 56
4.1.1 Self-calibration methods . . . 56
4.1.2 Our contributions . . . 58
4.1.3 Notation and outline . . . 58
4.2 Problem statement . . . 58
4.3 Ambiguity and identifiability . . . 60
4.4 Self calibration with the element-space model . . . 65
4.5 Self calibration with the co-array data model . . . 66
4.6 Numerical experiments . . . 68
4.6.1 Element-space model . . . 68
4.6.2 Co-array data model . . . 70
4.6.3 Monte-Carlo experiments . . . 74
4.7 Experimental Results . . . 77
4.8 Concluding Remarks . . . 80
References . . . 81

5 Blind Sensor Array Calibration and DOA estimation of Broadband Sources **85**
5.1 Introduction . . . 86
5.2 Problem Formulation . . . 87
5.3 Proposed calibration technique . . . 88
5.4 Simulation Results . . . 89
5.5 Experimental Results . . . 91
5.6 conclusions . . . 93
References . . . 93

6 Blind Calibration for Acoustic Vector Sensor Arrays **95**
6.1 Introduction . . . 96
6.2 System model . . . 96
6.3 Estimation of sensor gains . . . 98
6.4 Estimation of sensor phases . . . 99
6.5 Simulations . . . 101
6.6 Concluding remarks . . . 103
References . . . 104

III Reduced Channel Alternate Configuration AVS Array for DOA Estimation **105**

7 Uniaxial Acoustic Vector Sensors for Direction-of-Arrival Estimation **107**
7.1 Introduction . . . 108
7.2 Review of beampattern analysis of AVS array . . . 110
7.2.1 Measurement model of an AVS Array . . . 110
7.2.2 Beampattern of an AVS array . . . 111
7.3 Beampattern analysis of U-AVS array . . . 112
7.3.1 Measurement model of a U-AVS array . . . 112
7.3.2 Beampattern of a U-AVS array . . . 112

7.4 Bias analysis of a U-AVS array 114
7.5 Review of Cramér-Rao bounds for AVS, U-AVS and APS array 116
7.5.1 CRB for multi-sensor and multi-source configuration 116
7.5.2 Evaluation of CRB for a single source 118
7.6 Experimental results 123
7.6.1 Beampattern variation due to changes in the source signal frequency . . 124
7.6.2 Bias variation due to an increase in the aperture of the U-AVS ULA . . . 125
7.7 Conclusions 125
7.8 Acknowledgements 126
7.A Appendix Bias expression for U-AVS array 126
7.B Appendix CRB expression for a U-AVS array and a single source 127
References 128

8 Conclusion & Research Trends **133**
8.1 Concluding Overview and Remarks 133
8.2 Future Research Opportunities 135
8.2.1 DOA estimation using spatially under-sampled AVS array 135
8.2.2 Self-Calibration and DOA Estimation using Sensor Arrays 136
8.2.3 DOA Estimation using U-AVS Array 137
References 137

Acknowledgements **141**

Curriculum Vitæ **143**

SUMMARY

The localization and characterization of sound have played a vital role in various applications, ranging from noise control of machinery to battlefield awareness. Microphone arrays are commonly used to find sound sources, which implicitly inherits a series of limitations. Alternatively, acoustic vector sensors (AVSs) have shown promising results in overcoming most of those limitations, specifically having a larger operation frequency while requiring a smaller number of sensor nodes. However, literature about this topic is still evolving and mainly focused on the theoretical aspects, disregarding most real-world limitations. This thesis extends the AVS arrays' theoretical framework for direction-of-arrival (DOA) estimation of far-field sources while considering practical constraints. Specifically, the study considers the DOA estimation problem using AVS arrays in three main scenarios: spatially under-sampled configurations, the presence of calibration errors, and sensors with a reduced number of channels.

The idea of spatial sampling by AVS arrays has a different interpretation compared to the equivalent acoustic pressure sensor (APS) arrays. Notably, it is possible to carry out unambiguous DOA estimation using a spatially under-sampled AVS array, which is the main topic of interest in the first part of this work. Here we study the effects of the grating lobes or spatial aliasing on the performance of DOA estimation. We will observe that this idea can also be extended to beamforming applications.

Subsequently, in the second part of this work, we consider the DOA estimation problem using AVS arrays in the presence of calibration errors. First, identifiability conditions are derived for the solution to exist. Then two main classes of self-calibration approaches are proposed. The first calibration approach is array geometry independent and is based on sparse recovery techniques that lead to a one-step solver to estimate both the source DOAs and the calibration parameters jointly. Further, the extension of the proposed self-calibration approach in the presence of wide-band sources is also presented. The second calibration approach applies only to a uniform linear array (ULA) of AVSs, where the Toeplitz block structure of its covariance matrix is exploited to estimate the calibration errors followed by the estimation of the source DOAs.

In the last part of the thesis, an alternate configuration of an AVS is considered for DOA estimation with a reduced channel count. We refer to such an AVS as a uniaxial AVS (U-AVS). The DOA estimation performance using a U-AVS array is analyzed, and specifically, the impact of the extra degree-of-freedom originating from the fact that each U-AVS in the array can have arbitrary orientation is studied comprehensively. Furthermore, all the analyses and proposed algorithms in this thesis are supported by real experimental results performed with AVS arrays in an anechoic chamber.

To conclude, this research on AVS arrays paves the way to achieve an increased situational awareness across our society; this could be either by detecting and localizing problems or threats occurring in an urban environment or assisting soldiers on the battlefield to make a timely decision to achieve peace.

SAMENVATTING

De lokalisering en karakterisering van geluid speelt een belangrijke rol in vele toepassingen, van ruiscontrole in machines tot geluidsdetectie in oorlogsvoering. Doorgaans worden microfoonroosters gebruikt om geluid te lokaliseren, maar dat brengt een aantal beperkingen met zich mee. Akoestische vectorsensoren daarentegen laten hoopgevende resultaten zien om deze beperkingen te omzeilen. Zo kunnen ze bijvoorbeeld werken bij hogere frequenties en met minder sensoren. De literatuur over dit onderwerp is echter beperkt en richt zich vooral op theoretische aspecten zonder oog voor de praktijk. Deze thesis breidt de theorie van roosters van akoestische vectorsensoren uit voor richtingsschatting van bronnen in het verre veld, daarbij rekening houdend met de praktische beperkingen. Meer specifiek worden drie scenario's bestudeerd: spatiale onderbemonstering, de aanwezigheid van kalibratiefouten, en sensoren met een beperkt aantal kanalen.

Het spatiaal bemonsteren door roosters van akoestische vectorsensoren verschilt in interpretatie van het bemonsteren door roosters van akoestische druksensoren. Zo is het mogelijk om ondubbelzinnige richtingsschatting uit te voeren met een onderbemonsterd rooster van akoestische vectorsensoren, wat het hoofdonderwerp is van het eerste deel van deze thesis. Meer specifiek zullen we de effecten van hoge zijlobben en spatiale aliasering op de prestatie van richtingsschatting bestuderen. Hierbij zullen we opmerken dat dit idee ook kan uitgebreid worden naar bundelvorming toepassingen.

Vervolgens zullen we in het tweede deel van deze thesis het effect van kalibratiefouten op roosters van akoestische vectorsensoren bestuderen. Eerst leiden we de voorwaarden af waaronder een oplossing bestaat. Daarna stellen we twee zelfkalibratietechnieken voor. De eerste techniek is onafhankelijk van de roostergeometrie en is gebaseerd op de reconstructie van schaarse signalen met veel nullen. Deze techniek leidt tot een oplossing in één stap voor zowel de bronrichtingen als de kalibratiefouten. Verder wordt ook een uitbreiding van deze techniek naar breedband bronnen voorgesteld. De tweede techniek is alleen toepasbaar voor uniforme lineaire roosters van akoestische vectorsensoren en maakt gebruik van de Toeplitz blokstructuur van de covariantiematrix om de kalibratiefouten te schatten. Op basis van deze schatting worden dan in een tweede stap de bronrichtingen geschat.

In het laatste deel van deze thesis bestuderen we een alternatieve configuratie van een akoestische vectorsensor met een gereduceerd aantal kanalen, genaamd een uniaxiale akoestische vectorsensor. De prestatie van richtingsschatting met behulp van een rooster van zulke uniaxiale akoestische vectorsensoren wordt geanalyseerd, waarbij vooral de impact van de extra vrijheidsgraad bekomen door de willekeurige oriëntatie van elke uniaxiale sensor uitvoerig wordt bestudeerd. Al de analyses en voorgestelde algoritmen in deze thesis worden ondersteund door daadwerkelijke experimentele resultaten uitgevoerd met akoestische vectorsensoren in een echovrije kamer.

Tot slot baant dit onderzoek over akoestische vectorsensoren de weg naar een verbeterd omgevingsbewustzijn binnen onze samenleving; zij het door het detecteren en lokaliseren van problemen of bedreigingen in een stedelijke omgeving of door het assisteren van soldaten op het slagveld om snel tot vrede te komen.

1

INTRODUCTION

We, humans, are gifted with ears that sense air particle oscillations, which along with our built-in processing system, allows us to hear the sounds around us. Further, we can process the acoustic signals to extract information about our environment and communicate with others. Our two-ear acoustic array also provides us spatial information of the acoustic field around us, which allows us to sense the sound direction of arrival. Starting from developing primitive tools to passively amplify sound, we have evolved to develop complex acoustic systems that can autonomously detect and estimate the parameters of interest. Among them arrays of spatially distributed sensors that can sense, process, and estimate the direction-of-arrival (DOA) of multiple acoustic waves, including the sound produced by moving ships in the water across thousands of miles of ocean or a blast from a weapon across several kilometers.

Nowadays, the DOA estimation problem is dealt with in the field of array signal processing where an array of sensor elements is used to generate or pick up waves. Apart from acoustics, the array signal processing framework plays an integral part in numerous diverse applications, including radar, wireless communications, seismology, and radio astronomy. The differences lie in the nature and medium of propagation. The array processing framework and its tools are employed to extract useful information from the measurements captured by a spatially spread array of sensors. Usually, it is achieved by the fusion of spatial and temporal measurements with the prior information such as array geometry, sensor characteristics, etc. The information of interest mainly involves detection of an event and/or subsequently either estimating spatio-temporal parameters such as time-of-arrival (TOA), time-difference-of-arrival (TDOA), direction-of-arrival (DOA), source spectrum, etc., or the content of the source signals itself based on beamforming.

In the field of acoustics, traditionally, microphones that measure acoustic pressure are employed in the array, and those are commonly referred to as acoustic pressure sensor (APS) arrays. Since acoustic pressure is a scalar quantity, those traditional measuring systems are also referred to as scalar sensor arrays. The spatial diversity of the sensors provides information related to spatio-temporal parameters of interest. Equivalent systems can be found for electromagnetic applications, where they employ antennas that measure the scalar quantity of the electric field (electric potential), and they are commonly referred to as antenna

or phased arrays. On the other hand, the propagating wavefields are associated with vector information which include,

- For acoustic waves, we have acoustic particle velocity, which is the spatial gradient of the acoustic pressure.
- For electromagnetic waves, we have an electric field, which is the spatial gradient of the electric potential, and the magnetic field.

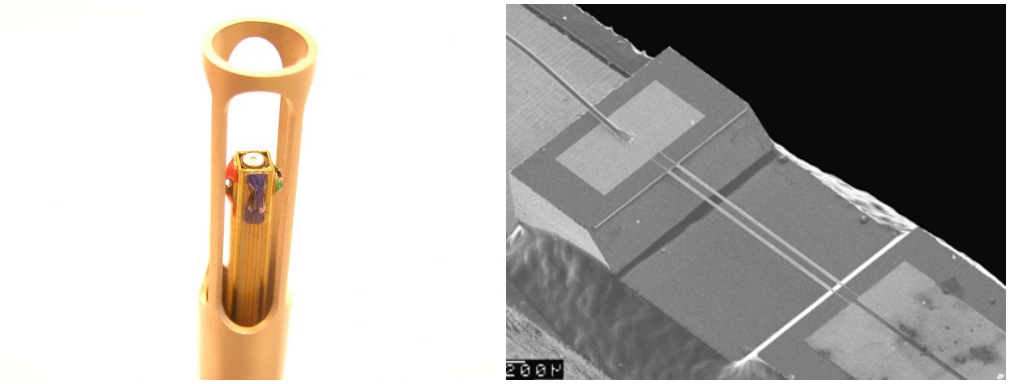
With the recent advancements in micro-electro-mechanical systems (MEMS) technology, the transducers that are capable of measuring vector information are nowadays available. One such device is an acoustic vector sensor (AVS), which measures both acoustic pressure and particle velocity [1]. The application of such sensors that measure the vector information in an array configuration has distinct advantages in comparison to the conventional scalar sensor array [2, 3]. Unlike a traditional microphone, a single sensor can be used for estimating the direction-of arrival (DOA) of sources [4].

1.1. ACOUSTIC VECTOR SENSOR

Transducers that are capable of measuring acoustic variations are essential to observe acoustic events; specifically, it is important to characterize the two fundamental building blocks of acoustics: sound pressure and particle velocity. The transducers to measure those quantities include:

- Microphones are the most common devices used to measure sound. They have an internal membrane that responds to air pressure fluctuations in the same way as our eardrums, moving backward and forward as the pressure force acts over the membrane surface. The motion of the membrane is converted into an electrical signal by a transducing element.
- Acoustic particle velocity sensors, or Microflowns [5], are transducers that are able to capture the particle velocity in air. The transducers were inspired by hot-wire anemometers: a wire is heated up by an electrical current and is cooled down when exposed to an acoustic flow. Due to temperature changes in the wire, its resistance changes accordingly, producing a variable electrical signal proportional to the incident flow. Using two closely-spaced heated wires and measuring the difference in temperature between them provides a measure of the acoustic particle velocity. The small size of this device allows three orthogonal sensors to be placed close to each other to characterize the acoustic particle velocity vector of the sound field.

An acoustic vector sensor (AVS) measures both acoustic pressure and particle velocity. It is constructed by placing multiple transducers nearly at the same point, including a combination of a microphone and three (two) particle velocity transducers that are orthogonal to each other placed in $\mathbb{R}^3$ ($\mathbb{R}^2$). One such AVS manufactured by Microflown Technologies is illustrated in Figure 1.1 (a), where all the transducers are placed on a pillar, with a microphone on the top and three orthogonally placed particle velocity transducers on the sides of it. A close-up picture of the hot wire anemometers principle-based particle velocity transducer is presented in Figure 1.1 (b).



(a) Acoustic vector sensor (b) Acoustic particle velocity sensor

Figure 1.1: Acoustic vector sensor manufactured by Microflown Technologies [5, 6].

Multiple AVSs can be arranged in an array configuration as seen in the Figure 1.2. Such arrays are used for multiple indoor applications, which can either be operated as a stand-alone unit as seen in Figure 1.2 (a) or as a handheld unit as seen in Figure 1.2 (b). An out-



(a) Stand-alone array of AVSs. (b) Handheld array of AVSs.

Figure 1.2: An array of acoustic vector sensors manufactured by Microflown Technologies.

door version of the AVS array can be seen in Figure 1.3 [1], where each sensor is equipped with a wind and rain protection layer that is acoustically characterized during the calibration process of each AVS. These arrays can either contain AVSs with three channels (referred as 2D-AVS) including acoustic pressure, x and y channels of the particle velocity as seen in Figure 1.3 (a) or with four channels (referred as 3D-AVS) including an additional z-channel particle velocity transducer as seen in Figure 1.3 (b). Additionally it is possible that the AVS array can be placed on a moving platform with space constraints imposed by the vehicle dimensions. A typical scenario where the AVSs are placed on a vehicle is depicted in Figure 1.4.

Depending on the application, these AVS arrays can be used as a standalone passive system that can report the direction-of-arrival (DOA) and the time-difference-of-arrival (TDOA)

[1] Further details on these sensors can be found on www.microflown-avisa.com.



(a) Two dimensional AVS array with three channels each.

(b) Three dimensional AVS array with four channels each.

Figure 1.3: The outdoor versions of the AVS array.

of the acoustic events. However, it is also possible that the AVS array (viewed as a single node) is part of a network with many other nodes, and they can communicate to the main station through radios. A typical scenario of such a network is depicted in Figure 1.5, which is deployed for acquiring situational awareness based on acoustics, such that we can detect, localize and track multiple sound sources. Further, each of these arrays additionally can contain a weather station to report local wind and temperature information to fine tune the sound position estimates, and a global positioning service (GPS) device to provide location and synchronized time information.

1.1.1. APPLICATIONS

In practice, the AVS and its arrays have applications in a wide range of problems. The use cases of AVS arrays can either be indoor or outdoor with near-field or far-field propagation of the acoustic waves in air or in an underwater medium. Depending on the nature of the environment, propagation, and medium, AVS arrays have found their applicability in a wide variety of fields, ranging from automotive, battlefield acoustics, and underwater applications, among many others. They are used for tasks such as sound visualization and imaging [7, 8], acoustic intensity and impedance measurement [9–11] and sound source detection, localization and tracking [12–15]. In the following, we look at different case studies where an AVS and its arrays are useful,

Case 1: Imaging of near-field acoustic events

The acoustic vector sensor, along with near-field sound imaging techniques such as Scan&Paint [16] or near field holography (NAH) [17, 18] can be used for visualization of sound fields in the form of sound maps. Usually, the sound maps are obtained for a given frequency range of interest, and they can be visualized in both two and three dimensional space. Further, the obtained sound maps can be superimposed on a photograph or 3D model of the measured object, allowing to localize the sound origin for either low, mid, or high frequencies in a clear and intuitive manner. A example of such a scenario is presented in Figure 1.6, where the sound leakage of a car door is visualized. There are numerous automotive applications where such near-field sound visu-



Figure 1.4: The outdoor version of the AVS array deployed on a vehicle [5].

alization techniques are beneficial for noise source identification, component testing, noise ranking, soundproofing, and benchmarking.

Case 2: Far-field sound source localization

Multiple AVS arrays can be used in a cooperative network configuration to provide real-time localization of sound sources. Those sound sources can either be impulsive (such as mortars, artillery, and rocket projectiles) or tonal (like drones, boats, helicopters, or unmanned aerial vehicles) in nature. Such a scenario of impulsive sound source localization by a network of multiple spatially spread AVS arrays is presented in Figure 1.7. The estimated localization (white circle) of the impulsive sound source (the blue square) is achieved by combining the DOA estimated by each AVS array. This localization approach can be used in combination with a source tracking algorithm extending the capability to track moving sources such as boats, helicopters, or drones. There are numerous applications where such techniques that enable situational awareness are helpful. Some of them include localization of accidents, illegal fireworks [19], gunshots, sniper localization, helicopter localization, and tracking [12, 14, 20].

Case 3: Sound visualization of low-frequency noise

An AVS array can be deployed for sound visualization of a far-field and low-frequency sound source such as wind turbine. The usage of AVS arrays allows for understanding how different mechanical defects have an impact on the perceived sound. The sound field studied through an array of AVSs enables locating low-frequency sound sources with a relatively small aperture. The far-field sound field produced by a wind turbine can be investigated using multiple beamforming techniques [21], and the sound maps are obtained for a frequency range of interest. An example of such a sound map that is super imposed on the image of a wind turbine is presented in Figure 1.8,

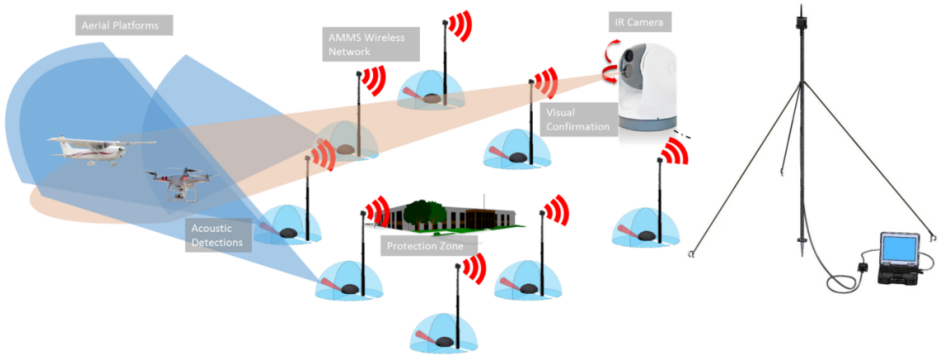


Figure 1.5: A typical scenario of an acoustic network for situational awareness inference.



Figure 1.6: Applications of Acoustic Vector Sensor arrays - Sound visualization using two dimensional scan and paint approach.

and we can observe that the sound is produced by the downstroke movement of the wind turbine blades. Such approaches can also be used for monitoring and visualizing any annoying low frequency sound generated by machines or other pollution noise sources [15].

1.2. CONTEXT AND RESEARCH OBJECTIVES OF THIS THESIS

The idea of exploring array processing concepts for direction-of-arrival (DOA) estimation of far-field sources using an AVS array was carried out by the author as an MSc thesis project in 2015. This task was a collaboration between TU Delft and Microflown AVISA (who kindly funded the project). The promising results achieved triggered the creation of a Ph.D. proposal with the same collaborators to further explore AVS array-based research topics for DOA estimation.

In this thesis, we focus on exploring the capabilities of an AVS array in the presence of far-field sound sources and for estimating their DOA. This scenario is suitable for applica-

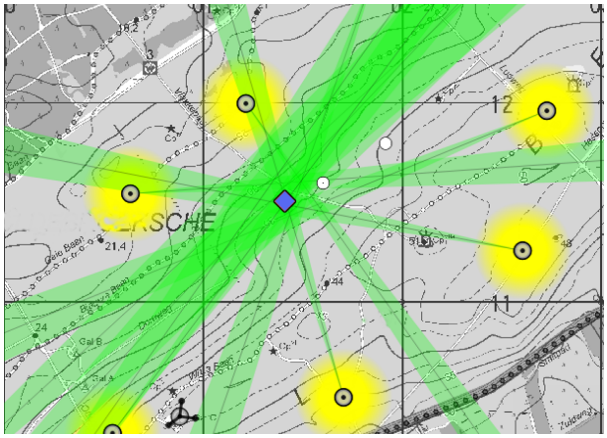


Figure 1.7: Applications of AVS arrays - Source localization using network of AVS arrays.



Figure 1.8: Applications of AVS arrays - Sound imaging to localize far-field and low frequency wind turbine noise.

tions such as the ones described above in Figure 1.7 (while focusing on local processing at an individual AVS array node within the entire network) and Figure 1.8. These arrays will be deployed permanently at a location either on the ground or on a moving platform with an overall objective of achieving accurate DOA estimation performance. Further, these arrays are battery-operated, where each operational cycle lasts for a couple of days. Such demanding conditions give rise to many unique challenges, such as the restriction on the array aperture, the fewer elements and the drifts in the receiver electronics with time, impacting the performance of DOA estimation. In this work, we address these issues through

the following five main research objectives:

- From a theoretical point of view to explore the idea of spatially under-sampling the AVS array for the purpose of beamforming and DOA estimation of far-field sources.
- Explore array processing and sparse sensing concepts for the purpose of DOA estimation of far-field acoustic events using AVS arrays.
- Investigate and develop algorithms to address practical issues such as self-calibration techniques for sensor arrays (with focus on AVS arrays) for the purpose of DOA estimation.
- Research alternate AVS array configurations such that the number of channels in the array is reduced with only a small impact on the DOA performance in comparison to the equivalent AVS and APS array.
- Contribute in the development of real-time algorithms suitable for a later integration into a commercial beamforming based DOA estimation product (specifically interesting for Microflown AVISA).

1.3. NOVELTIES OF THIS WORK

The main novelty of this thesis are listed below:

- The grating lobe's behavior with spatially under-sampled AVS arrays for DOA estimation and beamforming is analyzed [22]. For this purpose, the Cramér-Rao lower bound (CRLB) on the estimated DOAs is considered to gain insights into spatially under-sampled AVS arrays; however, the CRLB only provides local information around the DOA of the sources, and it is not possible to know what is the impact at the location of grating lobes. To overcome this issue, we consider the multi-source CRLB with one of the sources scanning the entire direction range such that the grating lobe's behavior is also known. Based on this study, it is concluded that it is indeed possible to unambiguously estimate the DOAs of the far-field sources using spatially under-sampled AVS arrays.
- Insights into classical and minimum variance distortion-less response (MVDR) beamforming based DOA estimation using spatially under-sampled AVS arrays (especially at the location of grating lobes) are presented [22]. It is worth noting that the MVDR based DOA estimators can significantly attenuate the grating lobes when the SNR is relatively high, allowing for DOA estimation without ambiguities using the spatially under-sampled AVS arrays. Further, a brief look into improvements of interference cancellation using beamforming based on spatial under-sampled AVS arrays is also presented in [22].
- Self-calibration techniques for AVS arrays with calibration errors are studied, such that a set of conditions are derived for the existence of a unique solution to estimate both the calibration errors and source DOAs [23]. Unlike the equivalent APS array [24], based on the derived conditions, it is observed that we require only one reference channel (where its gain and phase errors are known) of one of the AVSs within the array for a unique solution to exist. As a consequence, we show that AVS

arrays do not suffer from the progressive phase factor ambiguity [24–26] (that exists for equivalent APS arrays), and the resulting calibration errors can be estimated with respect to the reference channel of a considered AVS within the array.

- Two novel self-calibration algorithms that are applicable for both scalar and vector sensor arrays are proposed [23, 27]. Unlike many of the past self-calibration approaches, which rely on iterative alternating minimization methods, we exploit the algebraic structure in the measurement data and develop a convex solver for jointly estimating calibration errors and source DOAs. One of the proposed algorithms is developed based on the element-space measurement model[2], and another one is developed based on the co-array measurement model[2]. Under ideal cases, we show that the proposed convex formulation leads to the actual solution showcasing the effectiveness of our approaches.

- An extension of the proposed self-calibration algorithm based on the co-array measurement model in the presence of broadband sources is proposed [28]. The fact that the calibration errors across frequencies change slowly, such that it can be assumed constant or piece-wise linear for a specific range of frequencies, and the source DOA remains the same, is exploited to improve the performance of the proposed narrowband version of the self-calibration algorithms. Further anechoic chamber-based experimental results are performed to validate the improvement obtained from the proposed broadband version of the self-calibration algorithms.

- A new reduced channel alternate AVS array configuration is introduced such that it contains one acoustic pressure and one particle velocity transducer [29]. The particle velocity transducer has an extra degree of freedom where its orientation can be arbitrary. We refer to them as uniaxial acoustic vector sensors (U-AVSs). This framework of U-AVSs and their arrays for DOA estimation generalizes much past work on alternate/spatially spread acoustic pressure and particle velocity transducers. It was demonstrated that the performance of the U-AVS arrays for DOA estimation is comparable to the equivalent AVS arrays and superior to the equivalent APS arrays. Further, it is observed that by increasing the aperture and correctly choosing each of the U-AVS orientations in the array, the DOA estimation performance can come very close to the equivalent AVS arrays despite the use of significantly less channels.

- Experiments were carried out in an anechoic chamber to validate the proposed self-calibration algorithms and the applicability of the U-AVS array for DOA estimation [23, 28, 29]. Those experimental results are in agreement with the simulation results of the proposed algorithms demonstrating the validity of the proposed theoretical framework and algorithms.

1.4. OUTLINE OF THIS THESIS

This chapter provides a brief overview of the AVS and its application in the field of sound localization, clarifying the motivation and research objectives of this work. In the initial part of the following chapter we present the fundamentals of DOA estimation using an array of AVSs and then a detailed overview of the contributions of this work is discussed.

[2] Measurement models for the APS and AVS arrays are introduced in Chapter 2.

1

From Chapter 3 to Chapter 7, this thesis is structured into three parts. In the first part of this thesis (i.e., in Chapter 3), We discuss DOA estimation and beamforming using spatially under-sampled AVS arrays. In the second part of this thesis (i.e., in Chapter 4-6), we look into the of DOA estimation problem in the presence of calibration errors within the sensor arrays (specifically focusing on AVS arrays). Finally, in the third part of the thesis (i.e., Chapter 7), an alternative version of the AVSs with reduced channels (referred to as uniaxial AVSs) is discussed for DOA estimation and its performance is compared with conventional APS and AVS arrays. The detailed outline for this thesis is as follows:

- **Chapter 2**: This chapter is divided into two sections. In the first section we discuss the fundamentals of DOA estimation using AVS arrays. In that process, firstly, we discuss the measurement model for the AVS arrays in the presence of far-field acoustic sources. This measurement model is referred to as the element-space data model. Also, we will discuss the data model based on the second-order statistics, which is referred to as the covariance (or co-array) data model. Based on the element-space data model of the AVS arrays, we go through the beampattern of the AVS array and compare it with the equivalent APS arrays. Furthermore, we discuss the advantages of the AVS array by considering the Cramér-Rao lower bound (CRLB) on the DOA estimate in comparison to the equivalent APS array. In the second section of this chapter, we provide a detailed review of the contributions of this work discussed in Chapters 3 to 7.

- **Chapter 3**: In this chapter, based on the measurement model discussed in Chapter 2, we look into one of the less explored aspects of spatially under-sampling of the AVS arrays. Due to the measurement of vector quantities such as particle velocity, the grating lobes occur when the array is under-sampled, and they behave differently from the conventional APS array. This behavior is beneficial for DOA estimation and beamforming. We provide insights into the theoretical performance of an under-sampled AVS array for its DOA estimation performance using the Cramér-Rao lower bound (CRLB). We also show that the minimum variance distortionless response (MVDR) beamformer suppresses the grating lobes considerably compared to the classical (or Bartlett) beamformer leading to unambiguous DOA estimates. Finally, through zero-forcing (ZF) and minimization of maximum side lobe beamformers, the advantages of an under-sampled AVS array for interference cancellation are presented.

  This chapter has been published as

  - **K. Nambur Ramamohan**, M.C. Coutino, S.P. Chepuri, D.F. Comesana and G. Leus, "DOA Estimation and Beamforming using Spatially under-sampled AVS arrays", in *Proc. of the IEEE Workshop on Comp. Adv. in Multi-Sensor Adaptive Proc. (CAMSAP 2017)*, Curacao, Dec. 2017.

- **Chapter 4**: In this chapter, we focus on the DOA estimation problem using both APS and AVS arrays in the presence of calibration errors and without reference sources. The problem requires estimating both the calibration errors and the DOA of the sources. Such estimation problems in literature are referred to as self-calibration techniques. Initially, in this chapter, we derive identifiability conditions for the existence of a unique solution to estimate the source DOAs and the calibration errors for all the considered scenarios. Subsequently, we derive novel self-calibration algorithms based on both the element-space data model and the covariance (or co-array) data model that

are independent of the array geometry. The developed algorithms are obtained by transforming the underlying bilinear calibration model into a linear model and using standard convex relaxation techniques to estimate the unknown calibration and source DOA parameters jointly. To demonstrate the effectiveness of the proposed approach, numerical experiments and comparisons to the state-of-the-art methods are provided for both APS and AVS arrays. Finally, the results from an actual experiment performed in an anechoic chamber using an AVS array are presented to demonstrate the usefulness of the proposed self-calibration techniques.

This chapter has been published as

- **K. Nambur Ramamohan**, S.P. Chepuri, D.F. Comesana and G. Leus, "Self-Calibration of Scalar and Vector sensor arrays", *IEEE Transactions on Signal Processing (To appear)*, submitted in Apr 2021.

- **Chapter 5**: In this chapter, we extend the discussion on the self-calibration approaches seen in Chapter 4 to a scenario in the presence of multiple far-field broadband sources. By leveraging the fact that the calibration errors vary across frequencies smoothly and the DOAs of broadband sources are the same for the frequency range of interest, we propose a blind calibration method to estimate the calibration errors and source DOAs jointly. This joint estimation problem is a non-convex optimization problem. Hence, it is relaxed to a convex optimization problem by exploiting the underlying algebraic structure. Numerical and experimental results using real measurement data are presented to illustrate the efficiency of the proposed solver. Both results are based on an AVS linear array.

  This chapter has been published as

  - **K. Nambur Ramamohan**, S.P. Chepuri, D.F. Comesana and G. Leus, "Blind Sensor Array Calibration and DOA estimation of Broadband sources", in *Proc. of Asilomar Conf. Signals, systems, and Computers (Asilomar 2019)*, Pacific Grove, California, USA, Nov. 2019.

- **Chapter 6**: In this chapter, we present a calibration algorithm for a specific case of AVSs arranged in a uniform linear array configuration that exploits redundancies in its second-order statistics. To do so, we leverage the Toeplitz blocks present in the data covariance matrix. We develop linear estimators for estimating sensor gains and phases. Further, we discuss the differences of the presented blind calibration approach for acoustic vector sensor arrays compared to the approach for acoustic pressure sensor arrays. In order to validate the proposed blind calibration algorithm, simulation results for DOA estimation with an uncalibrated and calibrated uniform linear array based on MVDR and multiple signal classification (MUSIC) algorithms are presented. The calibration performance is analyzed using the CRLB of the DOA estimates.

  This chapter has been published as

  - **K. Nambur Ramamohan**, S.P. Chepuri, D.F. Comesana, G.C. Pousa and G. Leus, "Blind Calibration for Acoustic Vector Sensor arrays", in *Proc. of the International Conference on Acoustics, Speech, and Signal Processing (ICASSP 2018)*, Calgary, Canada, April. 2018.

- **Chapter 7**: In this chapter, we move to the third part of this thesis, where we propose a specific reduced-channel AVS comprising one omnidirectional microphone and only one particle velocity transducer, such that it can have an arbitrary orientation. Such a reduced transducer configuration is referred to as a uniaxial AVS (U-AVS). The DOA performance of an array of U-AVSs is analyzed through its beampattern and compared to conventional configurations. It is shown that the U-AVS array beampattern results in an asymptotically biased estimate of the source location, and it can be varied by choosing the orientation angles of the particle velocity transducers. Analytical expressions for the asymptotic bias are proposed and verified both numerically as well as experimentally. Furthermore, the CRLB and the mean square error (MSE) expressions are derived and numerically evaluated for a U-AVS array under a single-source scenario. Finally, a design criterion is suggested to find proper orientation angles for each of the U-AVSs in the array based on the derived MSE expressions.

  This chapter has been published as

  – **K. Nambur Ramamohan**, D.F. Comesana and G. Leus, "Uniaxial Acoustic Vector Sensors for Direction-of-Arrival Estimation", *Journal of Sound and Vibration*, vol. 437, pp. 276-291, Dec 2018.

1.5. LIST OF PUBLICATIONS

The research work done for this thesis has resulted in the following journal and conference papers. The list also contains additional conference papers that are not included in this thesis and those titles are highlighted in cyan.

JOURNAL PAPERS

J1. **K. Nambur Ramamohan**, S.P. Chepuri, D.F. Comesana and G. Leus, "Self-Calibration of Scalar and Vector sensor arrays", *IEEE Transactions on Signal Processing (To appear)*, Apr 2021.

J2. **K. Nambur Ramamohan**, D.F. Comesana and G. Leus, "Uniaxial Acoustic Vector Sensors for Direction-of-Arrival Estimation", *Journal of Sound and Vibration*, vol. 437, pp. 276-291, Dec 2018.

CONFERENCE PAPERS

C1. **K. Nambur Ramamohan**, S.P. Chepuri, D.F. Comesana and G. Leus, "Blind Sensor Array Calibration and DOA estimation of Broadband sources", in *Proc. of Asilomar Conf. Signals, systems, and Computers (Asilomar 2019)*, Pacific Grove, California, USA, Nov. 2019.

C2. **K. Nambur Ramamohan**, S.P. Chepuri, D.F. Comesana and G. Leus, "Blind Calibration of Sparse arrays for DOA estimation with analog and one-bit measurements", in *Proc. of the International Conference on Acoustics, Speech, and Signal Processing (ICASSP 2019)*, Brighton, UK, May. 2019.

C3. **K. Nambur Ramamohan**, S.P. Chepuri, D.F. Comesana, G.C. Pousa and G. Leus, "Blind Calibration for Acoustic Vector Sensor arrays", in *Proc. of the International Conference*

on Acoustics, Speech, and Signal Processing (ICASSP 2018), Calgary, Canada, April. 2018.

C4. **K. Nambur Ramamohan**, M.C. Coutino, S.P. Chepuri, D.F. Comesana and G. Leus, "DOA Estimation and Beamforming using Spatially under-sampled AVS arrays", in *Proc. of the IEEE Workshop on Comp. Adv. in Multi-Sensor Adaptive Proc. (CAMSAP 2017)*, Curacao, Dec. 2017.

C5. **K. Nambur Ramamohan**, D.F. Comesana, G.C. Pousa and G. Leus, "Analysis of a spatially under-sampled AVS array", in *Proc. of the International Congress and Exposition on Noise Control Engineering (Internoise 2019)*, Hong Kong, Aug. 2017.

C6. D.F. Comesana, **K. Nambur Ramamohan**, D.P. Cabo, and G.C. Pousa, "Modelling and Localizing low frequency noise of a wind turbine using an array of Acoustic vector sensors", in *Proc. of 7th Wind Turbine Noise Conference*, Rotterdam, The Netherlands, May. 2017.

REFERENCES

[1] H.-E. de Bree, P. Leussink, T. Korthorst, H. Jansen, T. Lammerink, and M. Elwenspoek, *The μ-flown: A novel device measuring acoustical flows, Proceedings of International Conference on Solid-State Sensors and Actuators & Eurosensors IX,* **54** (1995).

[2] J. P. Kitchens, *Acoustic vector-sensor array performance,* MSc Thesis, Massachusetts Institute of Technology (2008).

[3] M. Hawkes and A. Nehorai, *Acoustic vector-sensor beamforming and capon direction estimation,* IEEE Transactions on Signal Processing **46**, 2291 (1998).

[4] A. Nehorai and E. Paldi, *Acoustic vector-sensor array processing,* IEEE Transactions on Signal Processing **42**, 2481 (1994).

[5] H.-E. de Bree, *The microflown e-book,* Microflown Technologies, Arnhem (2007).

[6] H.-E. de Bree, *An overview of microflown technologies,* Acta acustica united with Acustica **89**, 163 (2003).

[7] D. F. Comesaña, S. Steltenpool, G. C. Pousa, H.-E. de Bree, and K. R. Holland, *Scan & paint: Theory and practice of a sound field visualization method,* ISRN Mechanical Engineering **2013** (2013).

[8] D. F. Comesaña and J. Wind, *A scanning method for source visualization and transfer path analysis using a single probe,* SAE Technical Paper (2011).

[9] E. Tijs and E. Druyvesteyn, *Spatial variation of impedance and intensity measured close to a sample in the near field of a spherical sound source,* in *Symposium on the Acoustics of Poro-Elastic Materials* (2011).

[10] E. Brandão, E. Tijs, A. Lenzi, and H.-E. de Bree, *A comparison of three methods to calculate the surface impedance and absorption coefficient from measurements under free field or in situ conditions,* Acta Acustica United with Acustica **97**, 1025 (2011).

[11] E. Tijs and E. Druyvesteyn, *An intensity method for measuring absorption properties in situ,* Acta Acustica united with Acustica **98**, 342 (2012).

[12] H.-E. de Bree, J. Wind, and P. de Theije, *Detection, localization and tracking of aircraft using acoustic vector sensors,* Inter Noise 2011 Proceedings, Osaka, Japan , 4 (2011).

[13] W.-Q. Jing, D. Fernandez Comesana, and D. Perez Cabo, *Sound source localisation using a single acoustic vector sensor and multichannel microphone phased arrays,* in *INTER-NOISE and NOISE-CON Congress and Conference Proceedings*, Vol. 249 (Institute of Noise Control Engineering, 2014) pp. 4901–4908.

[14] D. P. Cabo, H. E. de Bree, D. F. Comesaña, and M. A. S. Seoane, *Real life harmonic source localization using a network of acoustic vector sensors,* EuroNoise 2015 , 2333 (2015).

[15] J. van Muijlwijk, L. G. Escribano, D. P. Cabo, and E. Jansen, *Location of low frequency noise pollution areas.* EuroNoise 2015 (2015).

[16] D. Fernandez Comesana, *Scan-based sound visualisation methods using sound pressure and particle velocity*, Ph.D. thesis, University of Southampton (2014).

[17] E. F. Grande, *Near-field acoustic holography with sound pressure and particle velocity measurements*, Ph.D. thesis, Technical University of Denmark, Department of Electrical Engineering (2012).

[18] D. F. Comesaña, J. Wen, and E. FERNANDEZ-GRANDE, *Designing an array for performing near-field acoustic holography with a small number of pu probes,* in *45th International Congress and Exposition on Noise Control Engineering, INTER-NOISE 2016* (German Acoustical Society (DEGA), 2016) pp. 5895–5902.

[19] D. F. Comesaña, E. Jansen, Y. R. Seco, and H.-E. de Bree, *Acoustic multi-mission sensor (AMMS) system for illegal firework localisation in an ur-ban environment,* in *21-st International Congress on Sound and Vibration (ICSV 21)* (2014).

[20] H.-E. de Bree, *Acoustic vector sensors increasing UAV situational awareness,* SAE Technical Paper (2009).

[21] D. Fernandez Comesana, K. Nambur Ramamohan, D. Perez Cabo, and G. Carrillo Pousa, *Modelling and localizing low frequency noise of a wind turbine using an array of acoustic vector sensors,* 7th Wind Turbine Noise Conference (2017).

[22] K. Nambur Ramamohan, M. Contino, S. P. Chepuri, D. F. Comesaña, and G. Leus, *Doa estimation and beamforming using spatially under-sampled avs arrays,* in *2017 IEEE 7th International Workshop on Computational Advances in Multi-Sensor Adaptive Processing (CAMSAP)* (IEEE, 2017) pp. 1–5.

[23] K. Nambur Ramamohan, S. P. Chepuri, D. F. Comesana, and G. Leus, *Self calibration of scalar and vector sensor arrays,* arXiv preprint arXiv:2104.02561 (2021).

[24] A. J. Weiss and B. Friedlander, *Eigenstructure methods for direction finding with sensor gain and phase uncertainties,* Circuits, Systems and Signal Processing **9**, 271 (1990).

[25] A. Paulraj and T. Kailath, *Direction of arrival estimation by eigenstructure methods with unknown sensor gain and phase,* in *1985 IEEE International Conference on Acoustics, Speech, and Signal Processing (ICASSP)*, Vol. 10 (IEEE, 1985) pp. 640–643.

[26] D. Astély, A. L. Swindlehurst, and B. Ottersten, *Spatial signature estimation for uniform linear arrays with unknown receiver gains and phases,* IEEE Transactions on Signal Processing **47**, 2128 (1999).

[27] K. Nambur Ramamohan, S. P. Chepuri, D. F. Comesaña, and G. Leus, *Blind calibration of sparse arrays for doa estimation with analog and one-bit measurements,* in *2019 IEEE International Conference on Acoustics, Speech and Signal Processing (ICASSP)* (IEEE, 2019) pp. 4185–4189.

[28] K. Nambur Ramamohan, S. P. Chepuri, D. F. Comesaña, and G. Leus, *Blind sensor array calibration and doa estimation of broadband sources,* in *2019 53rd Asilomar Conference on Signals, Systems, and Computers* (IEEE, 2019) pp. 1304–1308.

[29] K. Nambur Ramamohan, D. F. Comesaña, and G. Leus, *Uniaxial acoustic vector sensors for direction-of-arrival estimation,* Journal of Sound and Vibration **437**, 276 (2018).

2

Background on DOA estimation using AVS arrays and Contributions

This chapter is mainly divided into two sections. In Section 2.1, we use the array processing framework to discuss fundamentals of DOA estimation by employing an array of acoustic vector sensors (AVSs). Subsequently in Section 2.2, we provide a detailed overview of the contributions of this work.

2.1. FUNDAMENTALS OF DOA ESTIMATION USING AN AVS ARRAY

In order to keep the analysis traceable, the measurement model discussed in this work is based on certain assumptions about the AVS and acoustic environment. First let us look into some assumptions about the AVS:

- Co-located sensor components - Each AVS comprises a sound pressure sensor and one (or several) particle velocity transducers, that are placed at the same location. Therefore, each AVS is represented as a single point in space.
- Acoustic particle velocity sensors have an angle dependent response. The response depends upon the cosine of the angle of arrival of the observed source with respect to the sensor orientation.

Assumptions about the acoustic environment include:

- Free-space environment - It is assumed that the acoustic environment is a homogenous isotropic medium.
- Narrow-band signals - The source signal is assumed to be narrow-band in nature, such that signal time delays across sensors in the array are smaller than the inverse bandwidth and can be represented as phase shifts of the signal.
- Plane wave propagation - We also assume that each AVS in the array measures the plane wave of the source signal and this assumption is practical only if the distance between the source and array is much larger (at least 10 times) than the array aperture (i.e., in the far field environment). Also we assume that there are no reflections present in the acoustic environment.

Based on these assumptions about the AVS and acoustic environment, we next discuss the plane wave measurement data model of an AVS array.

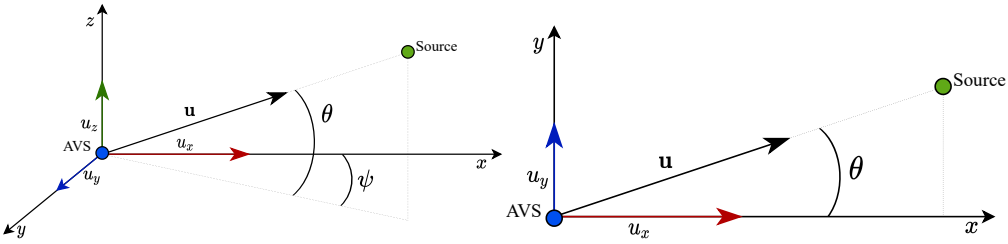
2.1.1. MEASUREMENT MODEL

In this section the measurement model of an AVS array in the presence of far-field sources for DOA estimation is discussed. Let us begin with the simple configuration consisting of a single source and an AVS. The direction of a plane wave impinging on an AVS shall be parametrized in terms of a three dimensional ($\mathbb{R}^3$) spherical coordinate basis, with azimuth $\theta \in [0, 2\pi)$ and elevation $|\psi| \in [0, \frac{\pi}{2}]$ as seen in Figure 2.1. Then we can define the unitary vector in the direction of the source as:

$$\mathbf{u} = \begin{bmatrix} u_x & u_y & u_z \end{bmatrix}^T = \begin{bmatrix} \cos(\theta)\cos(\psi) & \sin(\theta)\cos(\psi) & \sin(\psi) \end{bmatrix}^T. \tag{2.1}$$

In case of the two dimensional ($\mathbb{R}^2$) spherical coordinate basis with $\psi = 0$, (2.1) can be rewritten as:

$$\mathbf{u} = \begin{bmatrix} u_x & u_y \end{bmatrix}^T = \begin{bmatrix} \cos(\theta) & \sin(\theta) \end{bmatrix}^T. \tag{2.2}$$



(a) One 3D AVS and single source configuration in $\mathbb{R}^3$.

(b) One 2D AVS and single source configuration in $\mathbb{R}^2$.

Figure 2.1: Visualization of an AVS and single source configuration.

It can be shown that by solving the Euler equation of motion under a far-field narrowband source signal assumption, the sound pressure $p(\mathbf{p}, t)$ and the acoustic particle velocity $\mathbf{v}(\mathbf{p}, t)$ at time t are related as:

$$\mathbf{v}(\mathbf{p}, t) = -\frac{\mathbf{u}}{\rho c} p(\mathbf{p}, t), \tag{2.3}$$

where ρ corresponds to the density of the medium, c corresponds to the speed of sound in the medium and $\mathbf{p}$ is the position vector corresponding to the location of the sensor. The term (ρc) represents the characteristic acoustic impedance of the medium.

ELEMENT-SPACE MEASUREMENT MODEL

Based on the simplified linear relationship between the sound pressure and acoustic particle velocity, we can develop a data model for the AVS. Although this can be extended, in the further discussion, we will restrict ourselves to $\mathbb{R}^2$ (with $\psi = 0$). Then we can write the element-space measurement data at time instant t as:

$$\mathbf{y}(t) = e^{\mathrm{j}k(\mathbf{p}^T\mathbf{u})} \begin{bmatrix} \eta \\ \mathbf{u} \end{bmatrix} s(t) + \underbrace{\begin{bmatrix} n_\mathrm{p}(t) \\ \mathbf{n}_\mathrm{v}(t) \end{bmatrix}}_{\mathbf{n}(t)}, \tag{2.4}$$

where the exponential term corresponds to the wave phase delay with respect to the considered reference and it can be factored out because of the linear relation as seen in (2.3), $k = \frac{2\pi}{\lambda}$ is the wave number or spatial frequency of the source signal, η corresponds to the normalization term and it is proportional to the characteristic acoustic impedance of the medium (ρc), $s(t)$ is the source signal and $\mathbf{n}(t)$ is the measurement noise. For analysis purposes we consider a value of $\eta = 1$ in the rest of the discussion.

In the given scenario we assume that an AVS is placed at the origin of the coordinate system, which results in $\mathbf{p} = \mathbf{0}$. Based on this value of $\mathbf{p}$, (2.4) can be modified as:

$$\mathbf{y}(t) = \begin{bmatrix} 1 \\ \mathbf{u} \end{bmatrix} s(t) + \begin{bmatrix} n_\mathrm{p}(t) \\ \mathbf{n}_\mathrm{v}(t) \end{bmatrix}. \tag{2.5}$$

Now we extend the discussion to a scenario with N sources located in the directions pointed by the unit vectors $\mathbf{u}_1, \mathbf{u}_2, ..., \mathbf{u}_N$ and M AVSs placed at arbitrary locations indicated

by the position vectors $\mathbf{p}_1, \mathbf{p}_2, ..., \mathbf{p}_M$. For such a configuration, the element-space measurement model in (2.5) at time instant t can be modified as [1]:

$$\begin{aligned}\mathbf{y}(t) &= \begin{bmatrix}\mathbf{a}(\theta_1) & \mathbf{a}(\theta_2) & ... & \mathbf{a}(\theta_N)\end{bmatrix}\begin{bmatrix}s_1(t)\\ s_2(t)\\ .\\ .\\ .\\ s_N(t)\end{bmatrix}+\mathbf{n}(t),\\ &= \mathbf{A}(\boldsymbol{\theta})\mathbf{s}(t)+\mathbf{n}(t),\end{aligned} \tag{2.6}$$

where $\mathbf{y}(t) \in \mathbb{C}^Q$ with $Q = 3M$ in $\mathbb{R}^2$ ($Q = 4M$ in $\mathbb{R}^3$), $\boldsymbol{\theta} = \begin{bmatrix}\theta_1^T & \theta_2^T & ... & \theta_N^T\end{bmatrix}^T$, and for the n^{th} source, the terms in (2.6) are defined as,

$$\mathbf{a}(\theta_n) = \mathbf{a}_{\text{p}}(\theta_n) \otimes \mathbf{h}(\theta_n), \tag{2.7}$$

$$\mathbf{a}_{\text{p}}(\theta_n) = \begin{bmatrix}e^{\mathrm{j}k(\mathbf{p}_1^T\mathbf{u}_n)} & e^{\mathrm{j}k(\mathbf{p}_2^T\mathbf{u}_n)} & \dots & e^{\mathrm{j}k(\mathbf{p}_M^T\mathbf{u}_n)}\end{bmatrix}^T \in \mathbb{C}^{M\times 1}, \tag{2.8}$$

$$\mathbf{h}(\theta_n) = \begin{bmatrix}1 & \mathbf{u}_n^T\end{bmatrix}^T. \tag{2.9}$$

The terms $\mathbf{a}(\theta_n)$ is the AVS array response vector, $\mathbf{a}_{\text{p}}(\theta_n)$ is the equivalent APS array response vector and $\mathbf{h}(\theta_n)$ is the weighting vector containing the directional information about the far-field source with respect to the vector sensor axes, $\otimes$ represents the Kronecker product. On certain occasions it is also useful to rearrange and express the element-space measurement model in (2.4) such that the AVS array response vector is modified as,

$$\bar{\mathbf{a}}(\theta_n) = \mathbf{h}(\theta_n) \otimes \mathbf{a}_{\text{p}}(\theta_n) = \begin{bmatrix}\mathbf{a}_{\mathscr{P}}(\theta_n) & \mathbf{a}_{\mathscr{X}}(\theta_n) & \mathbf{a}_{\mathscr{Y}}(\theta_n)\end{bmatrix}^T, \tag{2.10}$$

where all the pressure channels (denoted by subscript $\mathscr{P}$) are arranged first and then followed by the two components of the particle velocity channels (denoted by subscript $\mathscr{X}$ and $\mathscr{Y}$). It should be noted that the AVS array measurement model in (2.6) reduces to an APS array measurement model when $\mathbf{h}(\theta_n) = [1]$ (i.e., $\mathbf{y}(t) \in \mathbb{C}^Q$ with $Q = M$), indicating that the APS array is a subset of an equivalent AVS array. Until now we considered the element-space measurement model at a given time instance t. If we have L samples of data then (2.6) can be modified as:

$$\begin{aligned}\mathbf{Y} &= \begin{bmatrix}\mathbf{a}(\theta_1) & \mathbf{a}(\theta_2) & ... & \mathbf{a}(\theta_N)\end{bmatrix}\begin{bmatrix}s_1(1) & s_1(2) & ... & s_1(L)\\ s_2(1) & s_2(2) & ... & s_2(L)\\ . & . & ... & .\\ . & . & ... & .\\ . & . & ... & .\\ s_N(1) & s_N(2) & ... & s_N(L)\end{bmatrix}+\mathbf{N},\\ &= \mathbf{A}(\boldsymbol{\theta})\,\mathbf{S}+\mathbf{N}.\end{aligned} \tag{2.11}$$

Also we can represent the generalized data model (2.11) in a different form, where $\mathbf{A}(\theta)$ can

be represented as the Khatri-Rao product ($\circ$) of two matrices:

$$\begin{aligned}\mathbf{Y} &= \begin{bmatrix}\mathbf{a}(\theta_1) & \mathbf{a}(\theta_2) & \dots & \mathbf{a}(\theta_N)\end{bmatrix}\mathbf{S}+\mathbf{N},\\ &= \begin{bmatrix}\mathbf{a}_\mathrm{p}(\theta_1)\otimes\mathbf{h}(\theta_1) & \mathbf{a}_\mathrm{p}(\theta_2)\otimes\mathbf{h}(\theta_2) & \dots & \mathbf{a}_\mathrm{p}(\theta_N)\otimes\mathbf{h}(\theta_N)\end{bmatrix}\mathbf{S}+\mathbf{N},\\ &= \underbrace{(\mathbf{A}_\mathrm{p}(\boldsymbol{\theta})\circ\mathbf{H}(\boldsymbol{\theta}))}_{\mathbf{A}(\boldsymbol{\theta})}\mathbf{S}+\mathbf{N},\end{aligned} \tag{2.12}$$

where

$$\begin{aligned}\mathbf{A}_\mathrm{p}(\boldsymbol{\theta}) &= \begin{bmatrix}\mathbf{a}_\mathrm{p}(\theta_1) & \mathbf{a}_\mathrm{p}(\theta_2) & \dots & \mathbf{a}_\mathrm{p}(\theta_N)\end{bmatrix}\in\mathbb{C}^{M\times N},\\ \mathbf{H}(\boldsymbol{\theta}) &= \begin{bmatrix}\mathbf{h}(\theta_1) & \mathbf{h}(\theta_2) & \dots & \mathbf{h}(\theta_N)\end{bmatrix}.\end{aligned}$$

COVARIANCE DOMAIN (CO-ARRAY) MEASUREMENT MODEL

In this section we extend the AVS array measurement model to the covariance domain [2], i.e., based on the second-order statistics of the physical process described in (2.6). This is also referred to as the co-array measurement model. For this we assume that both $\mathbf{s}(t)$ and $\mathbf{n}(t)$ are independent and identically distributed (i.i.d.), zero-mean, complex Gaussian vector processes. Further, we assume that $\mathbf{s}(t)$ and $\mathbf{n}(t)$ are independent for all t, such that they are completely characterized by their covariance matrices, $\mathbb{E}\{\mathbf{s}(t)\mathbf{s}^H(t)\}=\mathbf{R}_\mathrm{s}$ and $\mathbb{E}\{\mathbf{n}(t)\mathbf{n}^H(t)\}=\mathbf{R}_\mathrm{n}$. Based on these assumptions, the covariance matrix, $\mathbf{R}_\mathrm{y}$, of the measurement data described in (2.6) is evaluated as:

$$\mathbf{R}_\mathrm{y} = \mathbf{A}(\boldsymbol{\theta})\mathbf{R}_\mathrm{s}\mathbf{A}^H(\boldsymbol{\theta})+\mathbf{R}_\mathrm{n}. \tag{2.13}$$

If we further assume that the noise, $\mathbf{n}(t)$, is spatially white, we obtain $\mathbf{R}_\mathrm{n}=\sigma_\mathrm{n}\mathbf{I}$. If the noise variance of the pressure transducers differs from that of the particle velocity transducers due to the nature of the sensor, it can be absorbed without loss of generality into the normalization constant η as described in (2.4). Alternately, it is also possible to express the noise covariance matrix as [3],

$$\mathbf{R}_\mathrm{n}=\mathbf{I}_M\otimes\begin{bmatrix}\sigma_\mathrm{p} & 0\\ 0 & \sigma_\mathrm{v}\mathbf{I}_2\end{bmatrix},$$

where the noise variance of the pressure (σ_p) and particle velocity (σ_v) transducers is allowed to be different. If the additive noise is spatially uncorrelated but not necessarily white, then we obtain, $\mathbf{R}_\mathrm{n}=\mathrm{diag}(\boldsymbol{\sigma}_\mathrm{n})$. In practice the covariance matrix $\mathbf{R}_\mathrm{y}$ is estimated based on averaging over N samples. That is:

$$\hat{\mathbf{R}}_\mathrm{y}=\frac{1}{N}\sum_{t=1}^{N}\mathbf{y}(t)\mathbf{y}^H(t). \tag{2.14}$$

It is also useful to perform vectorization (linear transformation which converts a matrix into a column vector) on (2.13) as the resulting equation after vectorization forms the basis for covariance domain sensing. After performing vectorization on (2.13), we obtain the following co-array measurement model:

$$\begin{aligned}\mathbf{r}_\mathrm{y} &= \mathrm{vec}(\mathbf{A}\mathbf{R}_\mathrm{s}\mathbf{A}^H)+\mathrm{vec}(\mathbf{R}_\mathrm{n}),\\ &= \left(\mathbf{A}^*\otimes\mathbf{A}\right)\mathrm{vec}(\mathbf{R}_\mathrm{s})+\boldsymbol{\sigma}_\mathrm{n}.\end{aligned} \tag{2.15}$$

If the sources are uncorrelated to each other, then $\mathbf{R}_s = \text{diag}(\boldsymbol{\sigma}_s)$, and (2.15) can be modified as:

$$\begin{aligned} \mathbf{r}_y &= \left(\mathbf{A}^* \circ \mathbf{A}\right) \boldsymbol{\sigma}_s + \boldsymbol{\sigma}_n, \\ &= \mathbf{A}_{co}\, \boldsymbol{\sigma}_s + \boldsymbol{\sigma}_n. \end{aligned} \tag{2.16}$$

By comparing (2.16) and (2.6), we see that $\mathbf{r}_y$ acts as new measurement data of a virtual array whose behavior is described by the co-array manifold matrix $\mathbf{A}_{co}$. $\mathbf{A}_{co}$ is the array manifold matrix of the virtual array based on the second-order statistics which results in sensors located in the positions described by the difference set $\mathbb{S} = \{\mathbf{p}_i - \mathbf{p}_j\}$, $\forall\, i, j \in 1, 2, \ldots, M$. The difference set $\mathbb{S}$ consists of elements corresponding to the spatial correlation lag between the physical element pairs present in the array. The length of the co-array is defined as the degrees of freedom (DOF) of the co-array. The DOF of the co-array can be increased if the physical array is designed such that the number of redundant spacings in the difference set is reduced. Such non-uniform linear array configurations include the minimum redundancy array [4], nested array [5], co-prime array [6] and many more.

MEASUREMENT MODEL WITH CALIBRATION ERRORS

The measurement data model studied in (2.6) is an ideal scenario with all channels having unity gain and without phase differences between them. All practical sensors/transducers are far from ideal with different gain and phase responses, which stem from the inherent uncertainties in the transducer manufacturing process and the receiver analog electronics (e.g., conditioning units and pre-amplifier). We refer to gain and phase mismatches between different channels as calibration errors. Such calibration errors affect both the signal-of-interest and the noise part of the measurement data [7, 8], and the DOA estimates obtained from the MUSIC or MVDR spectra are highly sensitive to them [7, 9].

The calibration error for the ith channel, out of the total $3M$ channels, of an AVS array in $\mathbb{R}^2$ can be modeled as $g_i = \alpha_i e^{\jmath\phi_i}$ with α_i and ϕ_i being the magnitude and phase errors/mismatches, respectively. We collect these mismatches in the diagonal matrix $\text{diag}(\mathbf{g}) = \text{diag}(\boldsymbol{\alpha}) e^{\jmath\, \text{diag}(\boldsymbol{\phi})}$ with $\mathbf{g} = [g_1, \ldots, g_Q]^T$, $\boldsymbol{\alpha} = [\alpha_1, \ldots, \alpha_Q]^T$ and $\boldsymbol{\phi} = [\phi_1, \ldots, \phi_Q]^T$. In the presence of calibration errors the element-space measurement model (2.6) is modified as,

$$\mathbf{x}(t) = \text{diag}(\mathbf{g})\mathbf{y}(t) = \text{diag}(\mathbf{g})\left[\mathbf{A}(\boldsymbol{\theta})\,\mathbf{s}(t) + \mathbf{n}(t)\right]. \tag{2.17}$$

Usually acoustic transducers are calibrated during the manufacturing process with respect to a known reference channel in the presence of a known source at a pre-defined direction [10, 11]. However, the receiver analog electronics of the sensors deviate from its nominal performance over a period of time and is also affected by environmental conditions. As a result, they require periodic re-calibration for which self-calibration methods are useful. Self-calibration techniques do not require the presence of reference sources with known DOAs and can be performed locally at the location where the sensors are deployed without bringing them back to a controlled environment. On the other hand, it is also possible to have gain and phase errors that only affect the signal part of the measurement [7]. Such errors originate due to, the positional/orientation errors of the sensors in the array that leads to structured phase/gain errors or the perturbations in the sensors gain and phase patterns.

In Chapters 4, 5 and 6, we assume that the calibration errors are originated due to the uncertainties in the analog electronics, and mainly will consider the measurement data model where such errors affect both the signal and the noise. However in Chapter 4, the adaptation of the proposed self-calibration algorithm for the measurement model where the gain and phase errors affect only the signal is also presented.

The covariance matrix of the measurements in the presence of calibration errors as seen in (2.17) can be written as

$$\mathbf{R}_{\mathrm{x}} = \mathrm{diag}(\mathbf{g}) \left[\mathbf{A}(\boldsymbol{\theta}) \mathrm{diag}(\boldsymbol{\sigma}_{\mathrm{s}}) \mathbf{A}^{H}(\boldsymbol{\theta}) + \mathrm{diag}(\boldsymbol{\sigma}_{\mathrm{n}}) \right] \mathrm{diag}^{H}(\mathbf{g}). \tag{2.18}$$

It is also useful to express (2.18) in the vectorized form with $\mathrm{vec}(\mathbf{R}_{\mathrm{x}}) = \mathbf{r}_{\mathrm{x}}$, such that we arrive at the co-array measurement model with calibration errors,

$$\mathbf{r}_{\mathrm{x}} = \mathrm{diag}(\mathbf{g}^{*} \otimes \mathbf{g}) \mathbf{r}_{\mathrm{y}} = \mathrm{diag}(\mathbf{g}^{*} \otimes \mathbf{g}) \left[\mathbf{A}_{\mathrm{co}}(\boldsymbol{\theta}) \boldsymbol{\sigma}_{\mathrm{s}} + \boldsymbol{\sigma}_{\mathrm{n}} \right]. \tag{2.19}$$

2.1.2. BEAMPATTERN OF AVS ARRAY

Based on the measurement model described in (2.6) for a single far-field source located at θ, we analyze the beampattern or spatial response of the AVS array. The expression for the beampattern of the AVS array for a given beamformer $\mathbf{w}$ is expressed as:

$$B(\theta) \quad = \quad \mathbf{w}^{H} \mathbf{a}(\theta). \tag{2.20}$$

For a particular choice of $\mathbf{w} = \mathbf{a}(\hat{\theta})$, where $0 \leq \hat{\theta} < 2\pi$, we obtain the matched-filter based beampattern of the AVS array, i.e,

$$B(\hat{\theta}, \theta) \quad = \quad \mathbf{a}^{H}(\hat{\theta}) \mathbf{a}(\theta). \tag{2.21}$$

Substituting $\mathbf{a}(\theta)$ as in (2.6) into (2.21) results in [12, 13]:

$$B(k, \hat{\theta}, \theta) \quad = \quad \mathrm{VGM}(\hat{\theta}, \theta)\, B_{\mathrm{p}}(k, \hat{\theta}, \theta), \tag{2.22}$$

where the beampattern expression is described explicitly as a function of the wavenumber k as well as $\hat{\theta}$ and θ as those parameters change the behavior of the beampattern. It is interesting to note that the beampattern of an AVS array $B(k, \hat{\theta}, \theta)$ is expressed as a product of the equivalent APS array beampattern $B_{\mathrm{p}}(k, \hat{\theta}, \theta)$ and a velocity gain modulation (VGM) term $\mathrm{VGM}(\hat{\theta}, \theta)$. After some simplifications, this VGM term can be written as[1]

$$\mathrm{VGM}(\hat{\theta}, \theta) = 1 + \cos(\hat{\theta})\cos(\theta) + \sin(\hat{\theta})\sin(\theta). \tag{2.23}$$

We observe that the VGM term is independent of the number of sensors M in the array and wave number (or frequency) k (or f) of the source signal. This innovative observation allows us to prove distinct advantages of an AVS array in terms of array gain, ambiguity discrimination, and operation with high and low frequency source signals [12–14]. To understand these advantages, we consider a scenario in $\mathbb{R}^2$ where sensors are arranged in a

[1] The VGM term in three dimensional space ($\mathbb{R}^3$) with ψ being the elevation angle of the source and $|\hat{\psi}| \leq \frac{\pi}{2}$ being the scan angle across the range of the elevation angle can be extended as,

$$\mathrm{VGM}(\hat{\theta}, \hat{\psi}, \theta, \psi) = 1 + \left(\cos(\theta - \hat{\theta})\right) \cos(\hat{\psi})\cos(\psi) + \sin(\hat{\psi})\sin(\psi).$$

uniform linear array (ULA) configuration, which simplifies the analysis. The beampattern for an M-element APS array arranged in a uniform linear array (ULA) simplifies to:

$$B_{\mathrm{p}}(k,\hat{\theta},\theta) \quad = \quad M\left|\frac{\mathrm{sinc}\left(\frac{kd}{2}M\left(\cos(\theta)-\cos(\hat{\theta})\right)\right)}{\mathrm{sinc}\left(\frac{kd}{2}\left(\cos(\theta)-\cos(\hat{\theta})\right)\right)}\right|. \tag{2.24}$$

Based on the beampattern expressions (2.22) and (2.24), the following observations can be made,

- Conical angle (back lobe) ambiguity discrimination - If the source is located at an angle θ, it is well understood that the beampattern of an APS ULA shall always produce an ambiguity in the estimate of the source location at an angle $\theta^{'} = 2\pi - \theta$ as it suffers from a front-back lobe ambiguity [15]. But interestingly the same trend is not observed in the AVS ULA beampattern due to the presence of the VGM term in the beampattern expression which allows for unambiguous DOA estimation in the entire azimuth plane.
- Spatial aliasing discrimination - Similar to time signals producing frequency aliasing when they are under-sampled, we will have spatial aliasing in the beampattern when the APS ULA is spatially under-sampled. The resulting grating-lobes from this spatial aliasing limit the use of the APS ULA above a given design frequency (a.k.a. the Nyquist frequency) [15]. However in the case of the equialent AVS ULA, again because of the presence of the VGM term, those grating lobes including the back lobe are attenuated allowing for unambiguous DOA estimation even when the array is under-sampled. This aspect of DOA estimation and beamforming using under-sampled AVS arrays is explored in detail in Chapter 3.
- Signal-to-noise (SNR) increase - The VGM term in the beampattern of the AVS ULA results in an increase of the array gain which is seen through the amplification of the main lobe amplitude by a factor of 2. It is due to the extra channels per sensor node of the AVS ULA that measures the same phase delays made by the equivalent APS ULA.

2.1.3. CRAMÉR-RAO LOWER BOUND ON DOA ESTIMATION

As presented in [3, 16], the covariance matrix for a single source in $\mathbb{R}^3$ with θ being the azimuth angle and ψ being the elevation angle can be expressed as,

$$\mathbf{R}_{\mathrm{y}} \quad = \quad \mathbf{a}(\theta,\psi)\mathbf{a}^{H}(\theta,\psi)\sigma_{\mathrm{s}} + \mathbf{I}_M \otimes \begin{bmatrix}\sigma_{\mathrm{p}} & 0\\ 0 & \sigma_{\mathrm{v}}\mathbf{I}_3\end{bmatrix}. \tag{2.25}$$

Based on the covariance matrix in (2.25) with unknown parameters grouped as $\boldsymbol{\gamma} = [\theta,\psi,\sigma_{\mathrm{s}},\sigma_{\mathrm{p}},\sigma_{\mathrm{v}}]^{T}$, it was shown in [16] that the Fisher information matrix (FIM) has block diagonal structure and the Cramér-Rao lower bound (CRLB) on the DOA parameters is independent of the knowledge of $\sigma_{\mathrm{s}},\sigma_{\mathrm{p}},\sigma_{\mathrm{v}}$. Further in [16], the CRLB on the DOA parameters is expressed as,

$$\mathrm{CRLB}_{\mathrm{p}}(\theta,\psi) = \frac{1}{2L}\frac{1}{M\rho}\left(1+\frac{1}{M\rho}\right)\mathbf{J}^{-1}, \tag{2.26}$$

$$\mathrm{CRLB_v}(\theta,\psi) = \frac{1}{2L}\frac{1}{M\rho\rho_\mathrm{I}}\left(1+\frac{1}{M\rho\rho_\mathrm{I}}\right)[\mathbf{J}+\mathbf{K}]^{-1}, \tag{2.27}$$

where (2.26) is the CRLB of the APS linear array and (2.27) is the CRLB of the AVS linear array, $\rho = \frac{\sigma_\mathrm{s}}{\sigma_\mathrm{p}}$ is the SNR at each pressure sensor and $\rho_\mathrm{I} = 1+\frac{1}{\kappa}$ is the effective increase in SNR with $\kappa = \frac{\sigma_\mathrm{p}}{\sigma_\mathrm{v}}$ being the ratio of the pressure and particle velocity noise powers. Since ρ_I is always greater than 1 (i.e., as κ is always positive) the effective increase in SNR for an AVS array is always higher in comparison to the equivalent APS array. The terms $\mathbf{J}$ and $\mathbf{K}$ are defined as,

$$\mathbf{J} = \frac{4\pi^2}{M}\begin{bmatrix} \cos^2(\psi)\sum_{i=1}^{M}\left(\mathbf{p}_i^T\mathbf{v}_\theta\right)^2 & \cos(\psi)\sum_{i=1}^{M}\left(\mathbf{p}_i^T\mathbf{v}_\theta\right)\left(\mathbf{p}_i^T\mathbf{v}_\psi\right) \\ \cos(\psi)\sum_{i=1}^{M}\left(\mathbf{p}_i^T\mathbf{v}_\theta\right)\left(\mathbf{p}_i^T\mathbf{v}_\psi\right) & \sum_{i=1}^{M}\left(\mathbf{p}_i^T\mathbf{v}_\psi\right)^2 \end{bmatrix}, \tag{2.28}$$

$$\mathbf{K} = \frac{1}{1+\kappa}\begin{bmatrix} \cos^2(\psi) & 0 \\ 0 & 1 \end{bmatrix}, \tag{2.29}$$

where $\mathbf{v}_\theta = \frac{1}{\cos(\psi)}\frac{\partial \mathbf{u}}{\partial\theta}$ and $\mathbf{v}_\theta = \frac{\partial \mathbf{u}}{\partial\psi}$.

In case of a single source present in $\mathbb{R}^2$ (i.e., $\psi = 0$), the terms $\mathbf{J}$ in (2.28) and $\mathbf{K}$ in (2.29) in the CRLB expression with unknowns $\gamma = [\theta, \sigma_\mathrm{s}, \sigma_\mathrm{p}, \sigma_\mathrm{v}^2]^T$ are simplified as,

$$\mathbf{J} = \frac{4\pi^2}{M}\sum_{i=1}^{M}\left(\mathbf{p}_i^T\mathbf{v}_\theta\right)^2, \mathbf{K} = \frac{1}{1+\kappa}. \tag{2.30}$$

As a result, (2.26) and (2.27) can be expressed as,

$$\mathrm{CRLB_p}(\theta) = \frac{1}{2L\rho}\left(1+\frac{1}{M\rho}\right)\frac{1}{4\pi^2\sum_{i=1}^{M}\left(\mathbf{p}_i^T\mathbf{v}_\theta\right)^2}. \tag{2.31}$$

$$\mathrm{CRLB_v}(\theta) = \frac{1}{2L\rho}\left(1+\frac{1}{M\rho\rho_\mathrm{I}}\right)\left[\frac{1}{4\pi^2\rho_\mathrm{I}\left(\sum_{i=1}^{M}\left(\mathbf{p}_i^T\mathbf{v}_\theta\right)^2\right)+\frac{M}{\kappa}}\right]. \tag{2.32}$$

For a simplistic scenario where $\sigma_\mathrm{p} = \sigma_\mathrm{v}$ (i.e., $\kappa = 1, \rho_\mathrm{I} = 2$), the CRLB expression for an AVS array with a single source as seen in (2.32) becomes,

$$\mathrm{CRLB_v}(\theta) = \frac{1}{2L\rho}\left(1+\frac{1}{2M\rho}\right)\left[\frac{1}{8\pi^2\left(\sum_{i=1}^{M}\left(\mathbf{p}_i^T\mathbf{v}_\theta\right)^2\right)+M}\right]. \tag{2.33}$$

Based on (2.26) and (2.27), as discussed in [3] it can be observed that the CRLB expression of an AVS array differs from the APS array expression in two ways. Firstly it contains extra ρ_I factors and an extra additive term $\mathbf{K}$. Both these terms reduce the $\mathrm{CRLB_v}(\boldsymbol{\theta})$ relative to $\mathrm{CRLB_p}(\boldsymbol{\theta})$. The former represents an effective increase in SNR due to the greater number of measurements made by the AVS array, whereas the latter results from the direct measurement of the DOA information contained in the structure of the velocity field due to each vector sensor's inherent directional sensitivity.

- SNR increase - One of the factors that reduces the CRLB of the AVS array in comparison to the equivalent APS array is the presence of the ρ_I (or κ) factor in (2.27). The value of κ critically affects the usefulness of the AVS array; for small κ, the SNR increase ρ_I is very large but it is negligible for large κ.

- Directional sensitivity - In addition to the phase delay information that can be seen in the APS array, the AVS array contains explicit directional information ($\mathbf{h}(\boldsymbol{\theta})$ in (2.6)). This information results in the existence of the $\mathbf{K}$ matrix in the CRLB, which further reduces the AVS array CRLB relative to the APS array bound. In contrast to the $\mathbf{J}$ term in the CRLB expression, which is a representation of the phase delay information, $\mathbf{K}$ is independent of the array geometry and the DOA in $\mathbb{R}^2$ (for $\mathbb{R}^3$, the $\mathbf{K}$ term contains $\cos^2(\psi)$ which is a consequence of the singularity of the spherical coordinate system). Furthermore, the $\mathbf{K}$ matrix in $\mathbb{R}^3$ is diagonal indicating that the information of azimuth and elevation angles are independent of each other and it is non-singular. The effect of $\mathbf{K}$ in the reduction of the CRLB of AVS arrays is maximal when its contribution is comparable or larger than that of the $\mathbf{J}$ matrix. Some scenarios where $\mathbf{K}$ has a significant impact on the CRLB are presented in [3].

Based on the observations of both the SNR increase and the directional sensitivity terms, it was concluded in [3] that the advantages of an AVS array are more pronounced

- if the array is linear or planar.
- if the array has a small number of sensors.
- if the SNR is low.
- if the aperture of the array is fixed and the number of sensors in the array increases.
- if the value of κ is smaller.

2.2. OVERVIEW OF THE CONTRIBUTIONS

The purpose of this section is to provide an overview of the contributions of this Ph.D. work. As discussed in the Outline Section of Chapter 1, Chapters 3, 4, 5, 6 and 7 are published as papers, and each chapter follows its own conventions and notations that are described in the related introduction. Here we provide an overview of the proposed approaches and analyses, based on the measurement model and notations discussed in Section 2.1, to give the reader a glimpse into the content presented in each of the following chapters.

2.2.1. CHAPTER 3 - DOA ESTIMATION AND BEAMFORMING USING SPATIALLY UNDER-SAMPLED AVS ARRAY

In Section 2.1.3, the advantages of AVS arrays are highlighted in comparison to APS arrays based on the CRLB expression. It is noted that the advantages of AVS arrays are significant if the aperture of the array is small. The analysis in [3] is performed by assuming that the array is spatially sampled with the smallest inter-sensor spacing being equal to 0.5λ. However due to the presence of the frequency independent VGM term in the AVS array beampattern (as seen in Section 2.1.2) it is possible to under-sample the AVS array with smallest inter-sensor spacing being greater than 0.5λ without suffering from the effects of spatial aliasing as the grating lobes are attenuated in comparison to the main lobe. Taking this aspect into consideration, we can increase the aperture of an AVS array without increasing the number of sensor nodes whilst performing unambiguous DOA estimation. The idea of spatially under-sampling AVS arrays for the purpose of DOA estimation and beamforming

is considered in Chapter 3. The analysis of the spatially under-sampled AVS array is performed based on the CRLB expressions [1, 3]. Since the CRLB provides local information around the source DOAs, we consider a multi-source CRLB expression such that one of the sources acts as an interference at each possible scanning angle and in that way the effects of the grating lobes can be studied in an under-sampled AVS array. The suggested approach enables to analyze the DOA estimation accuracy under the potential effects induced by the interference at each possible scanning angle.

Based on the CRLB expression presented in [1] and by considering a simplistic scenario of a ULA in the presence of two uncorrelated sources, where one of the sources acts as an interference at all possible scanning angles, the influence of the VGM term at the location of grating lobes is studied. At those grating lobe locations, it is observed that the CRLB matrix is well defined indicating that under-sampled AVS arrays can be employed for unambiguous DOA estimation. It is observed that as the inter-sensor spacing increases and for low SNRs the trace of the CRLB matrix at the grating lobe locations tends to result in larger values as the attenuation of the grating lobes due to the presence of the VGM term is lower.

Further, the performance of the classical and MVDR beamformers for a unit power single source scenario with M sensors in the array is presented. For such scenario the covariance matrix in (2.13) can be written as,

$$\mathbf{R_y} = \mathbf{a}(\theta)\mathbf{a}^H(\theta) + \sigma_n \mathbf{I}. \tag{2.34}$$

Based on (2.34), the angular spectra of the classical beamformer (CBF) and MVDR beamformer for the AVS array in terms of the APS array are expressed as,

$$\begin{aligned} \mathrm{CBF_v}(\hat{\theta},\theta) &= \left(\mathrm{CBF_p}(\hat{\theta},\theta) - \frac{1}{\mathrm{SNR}}\right)\frac{\left(\mathrm{VGM}(\hat{\theta},\theta)\right)^2}{2} + \frac{1}{\mathrm{SNR}}, \\ \mathrm{MVDR_v}(\hat{\theta},\theta) &= \frac{2M(\mathrm{SNR})+1}{2M(\mathrm{SNR}) + (\mathrm{SNR})^2 \underbrace{\left(4M^2 - \left(\mathbf{a}^H(\hat{\theta})\mathbf{a}(\theta)\right)^2\right)}_{G}}, \end{aligned} \tag{2.35}$$

where $\mathrm{SNR} = \frac{1}{\sigma_n}$, $\hat{\theta}$ is the scanning angle and θ is the DOA of the source. $\mathrm{CBF_{v\,(p)}}(\hat{\theta},\theta)$ and $\mathrm{MVDR_{v\,(p)}}(\hat{\theta},\theta)$ are the angular spectra of the CBF and MVDR beamformer for an AVS (APS) array, respectively. It is shown that both the CBF and MVDR beamformer result in a maximum when $\hat{\theta} = \theta$, tending towards unity as the SNR and M increases. For a given M, the attenuation of the side lobes (including the grating lobes, i.e., $\forall\, \hat{\theta} \neq \theta$) by the CBF is independent of the SNR and is proportional to the attenuation achieved by its squared VGM term. In contrast, for the MVDR beamformer the grating lobes are attenuated considerably as the G term in the denominator is amplified by the factor $(\mathrm{SNR})^2$.

Finally, the beamformer design problem for under-sampled AVS arrays is explored where the weights for each of the channels in each AVS can be different. Such an approach allows for increased degrees of freedom. The beampattern synthesis problem can be expressed as,

$$\begin{aligned} G(\theta) &= \Big| \sum_{m=1}^{M} w_{mp} e^{\mathrm{j}2\pi(\mathbf{r}_m^T \mathbf{u}(\theta))} + \cos(\theta) \sum_{m=1}^{M} w_{mx} e^{\mathrm{j}2\pi(\mathbf{r}_m^T \mathbf{u}(\theta))} \\ &\quad + \sin(\theta) \sum_{m=1}^{M} w_{my} e^{\mathrm{j}2\pi(\mathbf{r}_m^T \mathbf{u}(\theta))} \Big| = \left|\mathbf{w}^H \mathbf{a}(\theta)\right|, \end{aligned} \tag{2.36}$$

where $\mathbf{w} = \begin{bmatrix} w_{1p} & w_{1x} & w_{1y} & \dots & w_{Mp} & w_{Mx} & w_{My} \end{bmatrix}^T \in \mathbb{C}^{3M}$ is the complex weight vector that needs to be designed such that $G(\theta)$ has a desired shape. The design problem can be written as a convex optimization program where constraints on the sensitivity, main lobe, and side lobes of the beampattern can be enforced. Based on the presented illustrations we see that the AVS array performance is superior in comparison to the equivalent aperture APS array with three times less sensor nodes.

2.2.2. CHAPTER 4 - SELF-CALIBRATION OF SCALAR AND VECTOR SENSOR ARRAYS

As seen in Section 2.1.1, each of the sensors/channels within the array has different gain and phase responses that drift over time, resulting in mismatches that significantly affect the performance of DOA estimation algorithms such as MVDR or MUSIC. Such problems for scalar arrays received lots of attention, and many self-calibration solutions without any calibrator sources have been proposed to improve the DOA estimation performance [8, 17–20]. Those approaches include:

- The techniques that rely on the structure in the array geometry to firstly estimate the calibration parameters and subsequently estimate the DOAs [8]. These array geometry-dependent approaches require an adaptation for AVS arrays as they have different array manifolds compared to conventional APS arrays [21, 22].

- The array geometry-independent techniques that result in an iterative algorithm to solve the non-convex problem for alternatively estimating the calibration parameters and DOAs. These approaches lead to a sub-optimal solution [17] and can be used as they are for AVS arrays.

Alternative to all the discussed approaches, in this work, we propose geometry-independent non-iterative approaches that are applicable for both the scalar and vector sensor arrays for jointly estimating the source DOAs and the calibration errors. Specifically, we derive two algorithms. The first is developed by considering the element-space data model, and the other is developed by considering the co-array domain data model.

Ambiguity and Identifiability: Before discussing the proposed algorithms, we derive conditions for the AVS array to obtain a unique solution for estimating the DOAs and calibration errors based on both data models. We adapt the approach discussed in [17], to derive sufficient conditions for uniquely estimating $\mathbf{g}$ and $\boldsymbol{\theta}$ from (2.17) and (2.19).

For both APS and AVS arrays to uniquely estimate both $\mathbf{g}$ and $\boldsymbol{\theta}$, one gain and phase reference channel is required to resolve the scalar ambiguity. Apart from that, APS arrays do suffer from the progressive phase factor ambiguity between $\text{diag}(\mathbf{g})$ and $\mathbf{A}(\boldsymbol{\theta})$ [8, 17, 19]. To fix this issue we can either employ an additional calibration source with a known DOA [17] or an additional phase reference channel [8] for uniquely estimating $\mathbf{g}$ and $\boldsymbol{\theta}$. On the other hand, we show that AVS arrays do not suffer from the progressive phase factor ambiguity between $\text{diag}(\mathbf{g})$ and $\mathbf{A}(\boldsymbol{\theta})$ due to which there is no requirement of a calibrator source or an additional phase reference channel for uniquely estimating $\mathbf{g}$ and $\boldsymbol{\theta}$.

Element-space data model based calibration approach: Defining the diagonal calibration matrix $\text{diag}(\mathbf{c}) = \text{diag}^{-1}(\mathbf{g})$ and assuming that the true directions are from a uniform grid of

$D \gg N$ points, i.e., $\theta_n \in \left\{0, \frac{\pi}{D} \cdots, \frac{\pi(D-1)}{D}\right\}$, for $n = 1,2,\ldots,N$, we can approximate (2.17) as

$$\mathbf{x}(t) = \text{diag}(\mathbf{c})\mathbf{y}(t) = \text{diag}(\mathbf{x}(t))\mathbf{c} = \mathbf{A}_{\mathbb{D}}\,\mathbf{z}(t) + \mathbf{n}(t), \tag{2.37}$$

where $\mathbf{A}_{\mathbb{D}}$ is a $Q \times D$ dictionary matrix that consists of column vectors of the form $\mathbf{a}(\bar{\theta}_d)$, with $\bar{\theta}_d$ being the dth point on the uniform grid of directions, i.e., $\bar{\theta}_d = \frac{\pi d}{D}$, $d = 0,1,\ldots,D-1$, and $\mathbf{z}(t)$ is a length-D vector containing the source signal related to the corresponding discretized directions. By considering multiple snapshots (L snapshots) and leveraging that the calibration parameters remain unchanged during an observation window, we can obtain more equations such that the system becomes over-determined. To see this, we further develop (2.37) for multiple snapshots as

$$\underbrace{\left[\begin{array}{c|ccc} \text{diag}(\mathbf{y}(1)) & -\mathbf{A}_{\mathbb{D}} & & \\ \vdots & & \ddots & \\ \text{diag}(\mathbf{y}(L)) & & & -\mathbf{A}_{\mathbb{D}} \end{array}\right]}_{\mathbf{G}} \underbrace{\left[\begin{array}{c} \mathbf{c} \\ \hline \mathbf{z} \end{array}\right]}_{\boldsymbol{\gamma}} = \underbrace{\left[\begin{array}{c} \mathbf{n}(1) \\ \vdots \\ \mathbf{n}(L) \end{array}\right]}_{\mathbf{n}}, \tag{2.38}$$

where $\mathbf{z} = \text{vec}(\mathbf{Z}) \in \mathbb{C}^{DL}$ with $\mathbf{Z} = [\mathbf{z}(1), \cdots, \mathbf{z}(L)] = [\mathbf{z}_1, \ldots, \mathbf{z}_D]^T$. Here the columns of $\mathbf{Z}$ share the same support, and hence we obtain $\|\mathbf{z}^{(l_2)}\|_0 = N$, where $\mathbf{z}^{(\ell_2)} = \left[z_1^{(\ell_2)}, \ldots, z_D^{(\ell_2)}\right]^T$ with $z_d^{(\ell_2)} = \|\mathbf{z}_d\|_2$. The optimization problem to jointly estimate the calibration parameters and DOAs with a sparsity constraint along the spatial domain of the matrix $\mathbf{Z}$ can then be expressed as:

$$\min_{\mathbf{c},\mathbf{z}} \quad \|\mathbf{G}\boldsymbol{\gamma}\|_2^2 + \lambda\|\mathbf{z}^{(l_2)}\|_0 \quad \text{s.t.} \quad (\mathbf{c},\mathbf{z}) \in \mathscr{C} \tag{2.39}$$

where λ is the regularization parameter. The constraint set with $N \geq 2$ for APS arrays is $\mathscr{C} := \{(\mathbf{c},\mathbf{z}) \mid c_1 = 1, \mathbf{z}_1 = \mathbf{1}\}$, while for AVS arrays it is $\mathscr{C} := \{(\mathbf{c},\mathbf{z}) \mid c_1 = 1\}$. Recall that for APS arrays, we need one reference sensor and we need to know one of the DOAs to avoid ambiguities. This is done by setting $c_1 = 1$ and $\mathbf{z}_1 = \mathbf{1}$, which is equivalent to having a calibrator source at $\bar{\theta}_1$ (without loss of generality). Since for AVS arrays, we do not need any calibrator source, we only need a reference sensor in that case.

Co-array data model based calibration approach: Similar to (2.17), the directions can be assumed to be derived from a uniform grid of $D \gg N$ points. Then (2.19) can be approximated as

$$\text{diag}(\mathbf{c}^* \otimes \mathbf{c})\mathbf{r}_y = \text{diag}(\mathbf{r}_y)(\mathbf{c}^* \otimes \mathbf{c}) = \mathbf{A}_{\text{co}\mathbb{D}}\boldsymbol{\sigma}_z + \boldsymbol{\sigma}_n, \tag{2.40}$$

where $\mathbf{A}_{\text{co}\mathbb{D}}$ is a $Q^2 \times D$ dictionary matrix that consists of column vectors of the form $\mathbf{a}^*(\bar{\theta}_d) \otimes \mathbf{a}(\bar{\theta}_d)$, with $\bar{\theta}_d$ as defined before. It can be easily observed that $(\mathbf{c}^* \otimes \mathbf{c}) = \text{vec}(\mathbf{C})$, with $\mathbf{C} = \mathbf{c}\mathbf{c}^H$, and hence (2.40) can be compactly rewritten as

$$\underbrace{\left[\text{diag}(\mathbf{r}_y) \quad -\mathbf{A}_{\text{co}\mathbb{D}}\right]}_{\mathbf{G}_{\text{co}}} \underbrace{\left[\begin{array}{c} \text{vec}(\mathbf{C}) \\ \hline \boldsymbol{\sigma}_z \end{array}\right]}_{\boldsymbol{\gamma}_{\text{co}}} = \boldsymbol{\sigma}_n. \tag{2.41}$$

The above system is under-determined with $Q^2 + D$ unknowns in Q^2 equations (note that some equations might even be redundant). However, as $\text{vec}(\mathbf{C})$ has a Kronecker structure,

the actual number of unknowns reduces to Q and $\boldsymbol{\sigma}_z$ is a sparse vector with non-zero elements at the location of the source DOAs. By considering the aforementioned constraints, the estimation problem can be cast as

$$\min_{\mathbf{C},\boldsymbol{\sigma}_z} \quad \|\mathbf{G}_{co}\gamma_{co} - \boldsymbol{\sigma}_n\|_2^2 + \lambda\|\boldsymbol{\sigma}_z\|_0 \quad \text{s.t.} \quad (\mathbf{C}, \boldsymbol{\sigma}_z) \in \mathscr{C}_{co} \tag{2.42}$$

where λ is the regularization parameter, and where similar to (2.39) with $N \geq 2$, $\mathscr{C}_{co} = \{(\mathbf{C}, \boldsymbol{\sigma}_z) \,|\, \boldsymbol{\sigma}_z \succeq \mathbf{0}, \mathbf{C} = \mathbf{c}\mathbf{c}^H, c_1 = 1, \boldsymbol{\sigma}_z(1) = 1\}$ for APS arrays and $\mathscr{C}_{co} = \{(\mathbf{C}, \boldsymbol{\sigma}_z) \,|\, \boldsymbol{\sigma}_z \succeq \mathbf{0}, \mathbf{C} = \mathbf{c}\mathbf{c}^H, c_1 = 1\}$ for AVS arrays. For APS arrays, the requirement of knowing one of the DOAs is expressed as $\boldsymbol{\sigma}_z(1) = 1$ (without loss of generality). Further for APS ULAs and some APS sparse arrays as we will see in Chapter 4, the redundancies in the co-array measurements can be used for the estimation of the source DOAs and the calibration errors with two phase reference sensors in the array. In such cases the constraint set even with $N \geq 1$ is $\mathscr{C}_{co} = \{(\mathbf{C}, \boldsymbol{\sigma}_z) \,|\, \boldsymbol{\sigma}_z \succeq \mathbf{0}, \mathbf{C} = \mathbf{c}\mathbf{c}^H, c_1 = c_2 = 1\}$.

Both (2.39) and (2.42) are non-convex problems, and the relaxed convex version of these optimization problems are presented in Chapter 4. Further, compared to (2.39), the problem (2.42) is more useful when there are more sources than sparsely placed sensors/channels. Addressing the calibration problem for sparse linear arrays with more sources than the physical sensors is unique, as we believe that apart from [23] not much attention is given to this aspect in the existing literature. Finally, numerical simulations and real experimental results (performed in the anechoic chamber) that support the proposed approaches and their comparison with existing techniques are presented in Chapter 4 as well.

2.2.3. CHAPTER 5 - BLIND SENSOR ARRAY CALIBRATION AND DOA ESTIMATION OF BROADBAND SOURCES

In acoustics, we encounter broadband sources in many practical scenarios. The DOAs of such sources remain the same for the entire bandwidth, whereas the sensor calibration errors vary. It is possible to apply the earlier presented narrow-band algorithms to each frequency bin separately, which can then be combined to obtain inference. However, if the sensor calibration errors vary smoothly across the frequencies, we can assume that the calibration errors are constant or change linearly over a specific range. Leveraging this aspect of the calibration errors and the fact that source DOAs remain the same across the frequency bins, we can extend the self-calibration approaches discussed in Chapter 4. Specifically, in Chapter 5, we focus on the co-array measurement model as its measurement vectors from all the frequency bins can be stacked into a matrix easily and (2.42) can be extended to broadband sources. On the other hand, the extension of the element-space data model-based self-calibration approach (2.39) to broadband sources is more involved and beyond the scope of this chapter.

Firstly, the measurement data in (2.17) for the source signals spread across W frequency bins for time index t and frequency bin w can be modified as:

$$\mathbf{x}(t, w) = \text{diag}(\mathbf{g}(w))\,[\mathbf{A}(w, \boldsymbol{\theta})\mathbf{s}(t, w) + \mathbf{n}(t, w)], \tag{2.43}$$

where $\mathbf{g}(w) = \boldsymbol{\psi}(w) \odot \boldsymbol{\phi}(w) \in \mathbb{C}^Q$ with $\boldsymbol{\psi}(w)$ and $\boldsymbol{\phi}(w)$ being the time-invariant gain and phase errors corresponding to the frequency bin w, respectively. The steering vector for the nth direction of an AVS array is given as

$$\mathbf{a}(w, \theta_n) = \mathbf{a}_p(w, \theta_n) \otimes \mathbf{h}(\theta_n) \in \mathbb{C}^{3M \times 1}, \tag{2.44}$$

where $\otimes$ is the Kronecker product, $\mathbf{a}_{\mathrm{p}}(w,\theta_n)$ is the steering vector of an APS array and $\mathbf{h}(\theta_n)$ contains the direction cosines:

$$\begin{aligned}\mathbf{a}_{\mathrm{p}}(w,\theta_n) &= \left[e^{-\mathrm{j}2\pi f_w \tau_1(\theta_n)} \dots e^{-\mathrm{j}2\pi f_w \tau_M(\theta_n)}\right]^T \in \mathbb{C}^{M\times 1},\\ \mathbf{h}(\theta_n) &= [1\ \mathbf{u}(\theta_n)] \in \mathbb{C}^{3\times 1}.\end{aligned} \tag{2.45}$$

Here, $\tau_m(\theta_n) = -\frac{1}{c}\mathbf{p}_m^T\mathbf{u}(\theta_n)$ (with c being the speed of the sound), and the frequency of the source signal for a given w is denoted as f_w. Similar to (2.19), for a given w, the vectorized version of the covariance matrix for the measurement data in (2.43) can be obtained as,

$$\mathbf{r}_w = \mathrm{diag}(\mathbf{g}^*(w)\otimes\mathbf{g}(w))\,[\mathbf{A}_{\mathrm{co}}(w,\boldsymbol{\theta})\mathbf{r}_{w\mathrm{s}} + \boldsymbol{\sigma}_{w\mathrm{n}}]\,. \tag{2.46}$$

where $\mathbf{A}_{\mathrm{co}}(w,\boldsymbol{\theta})$ is the co-array manifold matrix, $\mathrm{diag}(\mathbf{r}_{w\mathrm{s}})$ is the source covariance matrix, and $\mathrm{diag}(\boldsymbol{\sigma}_{w\mathrm{n}})$ is the noise covariance matrix. Again, if we assume that the source DOAs are derived from a uniform grid of D points, then (2.46) can be approximated as:

$$\mathrm{diag}(\mathbf{c}^*(w)\otimes\mathbf{c}(w))\mathbf{r}_w = \mathbf{A}_{\mathrm{D}}(w)\boldsymbol{\sigma}_w + \boldsymbol{\sigma}_{w\mathrm{n}}, \tag{2.47}$$

where $\mathrm{diag}(\mathbf{c}(w)) = \mathrm{diag}^{-1}(\mathbf{g}(w))$ and $\mathbf{A}_{\mathrm{D}}(w)$ is a $Q^2\times D$ dictionary matrix. The co-array domain data model in (2.47) for all the frequency bins can be finally rearranged as,

$$\mathbf{G}\boldsymbol{\gamma} = \boldsymbol{\sigma}_{\mathrm{n}}, \tag{2.48}$$

where $\boldsymbol{\sigma}_{\mathrm{n}} = \left[\boldsymbol{\sigma}_{1\mathrm{n}}^T \dots \boldsymbol{\sigma}_{W\mathrm{n}}^T\right]^T$, $\mathbf{G} = [\mathbf{G}_1\,|\,\mathbf{G}_2]$ with

$$\mathbf{G}_1 = \begin{bmatrix}\mathrm{diag}(\mathbf{r}_1) & & \\ & \ddots & \\ & & \mathrm{diag}(\mathbf{r}_W)\end{bmatrix}, \mathbf{G}_2 = \begin{bmatrix}-\mathbf{A}_{\mathrm{D}}(1) & & \\ & \ddots & \\ & & -\mathbf{A}_{\mathrm{D}}(W)\end{bmatrix},$$

and $\boldsymbol{\gamma} = \left[\mathrm{vec}(\mathbf{C}_1)^T \dots \mathrm{vec}(\mathbf{C}_W)^T \,\middle|\, \mathrm{vec}(\boldsymbol{\Sigma})^T\right]^T$ with $\boldsymbol{\Sigma} = [\boldsymbol{\sigma}_1\boldsymbol{\sigma}_2\dots\boldsymbol{\sigma}_W]$ and $\mathbf{C}_w = \mathbf{c}(w)\mathbf{c}^H(w)$. If we focus on a specific range of frequencies, where the calibration errors are constant, then we can approximate $\mathbf{C}_w = \mathbf{C}$ (i.e., $\mathbf{c}_w = \mathbf{c}$), $\forall\, w = 1,2,\dots,W$, such that (2.48) is modified as,

$$\hat{\mathbf{G}}\hat{\boldsymbol{\gamma}} = \boldsymbol{\sigma}_{\mathrm{n}}, \tag{2.49}$$

where $\hat{\boldsymbol{\gamma}} = \left[\mathrm{vec}(\mathbf{C})^T \,\middle|\, \mathrm{vec}(\boldsymbol{\Sigma})^T\right]^T$ and

$$\hat{\mathbf{G}} = \mathbf{G}\left[\begin{array}{c|c}\mathbf{1}_W\otimes\mathbf{I}_Q & \mathbf{0}_{WQ\times WD}\\ \hline \mathbf{0}_{WD\times Q} & \mathbf{I}_{WD}\end{array}\right].$$

The system in (2.49) is under-determined. However, by exploiting the structure in $\hat{\boldsymbol{\gamma}}$, the system of equations presented in (2.49) can be solved. The optimization problem for jointly solving the calibration parameters as well as the DOAs across frequency bins can be posed as:

$$\begin{aligned}\min_{\hat{\boldsymbol{\gamma}}} \quad & \|\hat{\mathbf{G}}\hat{\boldsymbol{\gamma}} - \boldsymbol{\sigma}_{\mathrm{n}}\|_2^2,\\ \text{subject to} \quad & ||\boldsymbol{\sigma}^{(l_2)}||_0 = N,\ \boldsymbol{\sigma}^{(l_2)} \succeq \mathbf{0},\ \boldsymbol{\sigma}_{\mathrm{n}} \succeq \mathbf{0},\\ & \mathbf{C} = \mathbf{c}\mathbf{c}^H,\ c_i = 1,\ \forall\, i = 1,\dots,R,\end{aligned} \tag{2.50}$$

where $\boldsymbol{\sigma} = \text{vec}(\boldsymbol{\Sigma})$, and R is the number of reference sensors/channels in the array. The optimization problem in (2.50) is a non-convex problem, and the relaxed convex version of it is presented in Chapter 5. Further, numerical simulations and real experimental results (performed in the anechoic chamber) that showcase the performance of the proposed approach are also presented in Chapter 5.

2.2.4. CHAPTER 6 - BLIND CALIBRATION FOR ACOUSTIC VECTOR SENSOR ARRAYS

The self-calibration algorithms presented in Chapters 4 and 5 do not make any assumptions on the array geometry. However, if the considered array has a regular structure such as ULA, they result in a structured covariance matrix that can be exploited to estimate the calibration errors. Therefore in this chapter, we present a blind calibration algorithm for the AVS ULA to estimate the DOAs of the far-field sources by exploiting the structure in its covariance matrix. The presented approach is inspired by the blind calibration algorithm presented in [8] for the APS ULA. By considering the element-space data model of the AVS ULA, whose array response vector is given by (2.10), we can observe that its covariance matrix, (2.18), has a Toeplitz block structure, i.e.,

$$\mathbf{R} \quad = \quad \text{diag}\left(\boldsymbol{\psi}\right)\text{diag}\left(\boldsymbol{\phi}\right)\mathbf{Q}\,\text{diag}(\boldsymbol{\phi}^*)\text{diag}\left(\boldsymbol{\psi}\right), \tag{2.51}$$

where $(\cdot)^*$ denotes complex conjugation and $\mathbf{Q} = \mathbf{A}(\boldsymbol{\theta})\,\text{diag}(\boldsymbol{\sigma}_\text{s})\,\mathbf{A}^H(\boldsymbol{\theta}) + \text{diag}(\boldsymbol{\sigma}_\text{n})$. The covariance matrices $\mathbf{Q}$ and $\mathbf{R}$ comprise blocks of matrices, i.e.,

$$\mathbf{R} = \begin{bmatrix} \mathbf{R}_{\mathscr{P}\mathscr{P}} & \mathbf{R}_{\mathscr{P}\mathscr{X}} & \mathbf{R}_{\mathscr{P}\mathscr{Y}} \\ \mathbf{R}_{\mathscr{X}\mathscr{P}} & \mathbf{R}_{\mathscr{X}\mathscr{X}} & \mathbf{R}_{\mathscr{X}\mathscr{Y}} \\ \mathbf{R}_{\mathscr{Y}\mathscr{P}} & \mathbf{R}_{\mathscr{Y}\mathscr{X}} & \mathbf{R}_{\mathscr{Y}\mathscr{Y}} \end{bmatrix};\ \mathbf{Q} = \begin{bmatrix} \mathbf{Q}_{\mathscr{P}\mathscr{P}} & \mathbf{Q}_{\mathscr{P}\mathscr{X}} & \mathbf{Q}_{\mathscr{P}\mathscr{Y}} \\ \mathbf{Q}_{\mathscr{X}\mathscr{P}} & \mathbf{Q}_{\mathscr{X}\mathscr{X}} & \mathbf{Q}_{\mathscr{X}\mathscr{Y}} \\ \mathbf{Q}_{\mathscr{Y}\mathscr{P}} & \mathbf{Q}_{\mathscr{Y}\mathscr{X}} & \mathbf{Q}_{\mathscr{Y}\mathscr{Y}} \end{bmatrix},$$

where,

$$\mathbf{R}_{\mathscr{M}\mathscr{N}} = \text{diag}(\boldsymbol{\psi}_{\mathscr{M}})\text{diag}(\boldsymbol{\phi}_{\mathscr{M}})\mathbf{Q}_{\mathscr{M}\mathscr{N}}\text{diag}(\boldsymbol{\phi}^*_{\mathscr{N}})\text{diag}(\boldsymbol{\psi}_{\mathscr{N}}); \tag{2.52}$$

$$\mathbf{Q}_{\mathscr{M}\mathscr{N}} = \sum_{n=1}^{N} \mathbf{a}_{\mathscr{M}}(\theta_n)\,[\boldsymbol{\sigma}_\text{s}]_n\,\mathbf{a}^H_{\mathscr{N}}(\theta_n) + \text{diag}(\boldsymbol{\sigma}_\text{n})_{\mathscr{M}\mathscr{N}}, \tag{2.53}$$

for $\mathscr{M},\mathscr{N} \in \{\mathscr{P},\mathscr{X},\mathscr{Y}\}$, are each Toeplitz resulting in a Toeplitz block structure for $\mathbf{Q}$. The subscripts $\mathscr{P}$, $\mathscr{X}$ and $\mathscr{Y}$ corresponds to the pressure, as well as x and y component of the particle velocity channels, respectively.

To estimate the unknown gain errors, $\boldsymbol{\psi}$, from (2.52) we have,

$$\left|[\mathbf{R}_{\mathscr{M}\mathscr{N}}]_{ij}\right| = \left|[\mathbf{Q}_{\mathscr{M}\mathscr{N}}]_{ij}\right|\psi_{\mathscr{M},i}\psi_{\mathscr{N},j},\ \forall i,j = 1,2,\dots M, \tag{2.54}$$

where $|\cdot|$ denotes the modulus. Since the subblock $\mathbf{Q}_{\mathscr{M}\mathscr{N}}$ is Toeplitz, we have the following relation for all $i-j = k-l$,

$$\log\left(\frac{\left|[\mathbf{R}_{\mathscr{M}\mathscr{N}}]_{ij}\right|}{\left|[\mathbf{R}_{\mathscr{M}\mathscr{N}}]_{kl}\right|}\right) = \log(\psi_{\mathscr{M},i}) + \log(\psi_{\mathscr{N},j}) - \log(\psi_{\mathscr{M},k}) - \log(\psi_{\mathscr{N},l}). \tag{2.55}$$

Taking all such non-redundant relations within the diagonal subblocks $\mathbf{R}_{\mathscr{P}\mathscr{P}}, \mathbf{R}_{\mathscr{X}\mathscr{X}}$, and $\mathbf{R}_{\mathscr{Y}\mathscr{Y}}$, and the upper-diagonal subblocks $\mathbf{R}_{\mathscr{P}\mathscr{X}}, \mathbf{R}_{\mathscr{P}\mathscr{Y}}$, and $\mathbf{R}_{\mathscr{X}\mathscr{Y}}$, we get an over-determined set of linear equations with the gain errors being the unknowns and it can be expressed as,

$$\mathbf{g} = \mathbf{H}\tilde{\boldsymbol{\psi}}, \tag{2.56}$$

where $\mathbf{H}$ collects the mapping matrices whose description is presented in Chapter 6 and $\boldsymbol{\psi}_{\mathscr{M}} = \left[\psi_{\mathscr{M},1} \dots \psi_{\mathscr{M},M}\right]^T$, with $\tilde{\boldsymbol{\psi}}_{\mathscr{M}} = \left[\log(\psi_{\mathscr{M},1}) \dots \log(\psi_{\mathscr{M},M})\right]^T$ for $\mathscr{M} \in \{\mathscr{P}, \mathscr{X}, \mathscr{Y}\}$ each of length M. The rank of $\mathbf{H}$ is $3M-3$, indicating that it does not have full column rank, due to which one reference AVS with known gain is needed to uniquely determine the unknown gains, $\boldsymbol{\psi}$.

To estimate the unknown phase errors, $\boldsymbol{\phi}$, from (2.52) we have,

$$\text{angle}([\mathbf{R}_{\mathscr{M}\mathscr{N}}]_{ij}) = \text{angle}([\mathbf{Q}_{\mathscr{M}\mathscr{N}}]_{ij}) + \phi_{\mathscr{M},i} - \phi_{\mathscr{N},j}, \tag{2.57}$$

for $i, j = 1, \dots, M$. Here, angle$(\cdot)$ denotes the phase. Using the fact that each subblock $\mathbf{Q}_{\mathscr{M}\mathscr{N}}$ is Toeplitz, we obtain the following relation for all $i - j = k - l$,

$$\text{angle}([\mathbf{R}_{\mathscr{M}\mathscr{N}}]_{ij}) - \text{angle}([\mathbf{R}_{\mathscr{M}\mathscr{N}}]_{kl}) = \phi_{\mathscr{M},i} - \phi_{\mathscr{N},j} - \phi_{\mathscr{M},k} + \phi_{\mathscr{N},l}. \tag{2.58}$$

By taking all such non-redundant relations within all the upper triangular subblocks of $\mathbf{R}$, we arrive at an over-determined set of linear equations to solve for $\boldsymbol{\phi}$, which is similar to (2.56) and details of it are elaborated in Chapter 6. Further, for uniquely estimating the phase errors, we need one phase reference AVS and an additional phase reference (it could be any transducer type) as the rank of the mapping matrix is $3M-4$. Once gain and phase errors are estimated, the data covariance matrix can be compensated with them, and well-known approaches such as MVDR or MUSIC can be used to estimate the source DOAs. Simulation results that are in agreement with the proposed calibration approach are also presented in Chapter 6.

2.2.5. CHAPTER 7 - UNIAXIAL ACOUSTIC VECTOR SENSORS FOR DIRECTION-OF-ARRIVAL ESTIMATION

This chapter looks at an alternative implementation of an AVS, which comprises only two collocated transducers per sensor. It includes an acoustic sound pressure and a particle velocity transducer with arbitrary orientation. Such a configuration is referred to as a Uniaxial AVS (U-AVS), as it captures only one component of the particle velocity field. The application of a U-AVS instead of an AVS removes one (for $\mathbb{R}^2$) data channel per sensor, hence substantially lowering hardware and power requirements. The multiple U-AVSs in an array configuration can potentially be used for DOA estimation. However, the theoretical limits of such a configuration are unknown and will be explored in this chapter.

Firstly the measurement data $\mathbf{y}(t)$ at time instant t with N sound sources located in the direction pointed by the unit vectors $\mathbf{u}_1, \mathbf{u}_2, ..., \mathbf{u}_N$ and sending plane waves impinging on M U-AVSs located at arbitrary locations indicated by the position vectors $\mathbf{r}_1, \mathbf{r}_2, ..., \mathbf{r}_M$ can be expressed as:

$$\mathbf{y}(t) = \underbrace{\begin{bmatrix}\mathbf{a}(\theta_1,\boldsymbol{\delta}) & \mathbf{a}(\theta_2,\boldsymbol{\delta}) & \dots & \mathbf{a}(\theta_N,\boldsymbol{\delta})\end{bmatrix}}_{\mathbf{A}(\boldsymbol{\theta},\boldsymbol{\delta})\in\mathbb{C}^{2M\times N}} \mathbf{s}(t) + \mathbf{n}(t) \in \mathbb{C}^{2M\times 1}, \tag{2.59}$$

where $\mathbf{y(t)} = \begin{bmatrix} y_{1p}(t) & y_{1v}(t) & \dots & y_{Mp}(t) & y_{Mv}(t) \end{bmatrix}^{\mathbf{T}}$, $y_{mp}(t)$ is the m^{th} U-AVS pressure measurement, $y_{mv}(t)$ is the m^{th} U-AVS velocity component measurement, $\mathbf{a}(\theta_n, \boldsymbol{\delta}) = \begin{bmatrix} e^{\mathrm{j}k(\mathbf{r}_1^T \mathbf{u}_n)} & e^{\mathrm{j}k(\mathbf{r}_1^T \mathbf{u}_n)} \cos(\delta_1 - \theta_n) & \dots & e^{\mathrm{j}k(\mathbf{r}_M^T \mathbf{u}_n)} & e^{\mathrm{j}k(\mathbf{r}_M^T \mathbf{u}_n)} \cos(\delta_M - \theta_n) \end{bmatrix}^T$ is the array manifold vector of the U-AVS array with each of them having an arbitrary orientation captured by the vector $\boldsymbol{\delta} = \begin{bmatrix} \delta_1 & \delta_2 & \dots & \delta_M \end{bmatrix}^T$. Based on the matched filter approach for given sensor orientation angles $\boldsymbol{\delta}$, the beampattern expression is given by:

$$\begin{aligned} B(\hat{\theta}, \theta) &= \left| \mathbf{a}^H(\hat{\theta}, \boldsymbol{\delta})\, \mathbf{a}(\theta, \boldsymbol{\delta}) \right|, \\ &= \Big| \big(1 + \cos(\delta_1 - \hat{\theta}) \cos(\delta_1 - \theta)\big)\, e^{\mathrm{j}k\left(\mathbf{r}_1^T \mathbf{u}(\theta) - \mathbf{r}_1^T \mathbf{u}(\hat{\theta})\right)} + \dots \\ &\quad + \big(1 + \cos(\delta_M - \hat{\theta}) \cos(\delta_M - \theta)\big)\, e^{\mathrm{j}k\left(\mathbf{r}_M^T \mathbf{u}(\theta) - \mathbf{r}_M^T \mathbf{u}(\hat{\theta})\right)} \Big| \end{aligned} \tag{2.60}$$

If all the U-AVSs have the same orientation angle (referred as a U-AVS array with a fixed orientation), i.e., $\boldsymbol{\delta} = \delta \begin{bmatrix} 1 & 1 & \dots & 1 \end{bmatrix}^T$, then the beampattern expression can be simplified as:

$$B(\hat{\theta}, \theta) = \mathrm{VGM}(\delta, \hat{\theta}, \theta)\; B_{\mathrm{p}}(\hat{\theta}, \theta), \tag{2.61}$$

where $\mathrm{VGM}(\delta, \hat{\theta}, \theta) = 1 + \cos(\delta - \hat{\theta}) \cos(\delta - \theta)$ is the velocity gain modulation (VGM) term, and $B_{\mathrm{p}}(\hat{\theta}, \theta)$ is given in (2.24). Similar to the AVS array, the expression in (2.61) can also be expressed as a product of an equivalent APS ULA beampattern and a VGM term. However, irrespective of the actual DOA θ, the maximum in the VGM term will always occur at $\hat{\theta} = \delta$. As the APS ULA beampattern always provides an unbiased source location estimate, a bias will be introduced by the VGM term. This bias in the estimates can be reduced by increasing the aperture of the array. If the aperture of the array is fixed then the bias can be controlled by changing the orientation angle(s) of the U-AVSs. In Chapter 7, we quantify the behavior of the bias in the DOA estimates of a U-AVS ULA.

Further, we derive the CRLB of a U-AVS ULA for a single source. Since the DOA estimates from the U-AVS array asymptotically result in a biased estimates, we also derive the mean square error (MSE) bound expression for the U-AVS ULA:

$$\mathrm{MSE}(\theta) = \mathbb{E}\left\{ \left\| \hat{\theta} - \theta \right\|^2 \right\} = (b(\theta))^2 + \mathrm{CRLB}_{\mathrm{b}}(\theta). \tag{2.62}$$

where $b(\theta)$ is the expression of the bias, and $\mathrm{CRLB}_{\mathrm{b}}(\theta) = \left(1 + \frac{\partial b(\theta)}{\partial \theta}\right)^2 \mathrm{CRLB}(\theta)$ is the CRLB expression for the biased estimates. The latter is expressed in terms of the unbiased CRLB and the bias expression. Based on the MSE bound expression, we compare the performance of the U-AVS ULA with the equivalent aperture AVS and APS ULA. From simulations, we infer that for the U-AVS ULA with a fixed orientation, the MSE bound lies in between the CRLB bound of an AVS ULA and an APS ULA. Also, we see that the MSE bound can be significantly reduced in a specific region of angular interest by focusing the orientations of the U-AVSs in the array towards it. Based on the analyses in Chapter 7, we conclude that minimizing the MSE bound on the DOA estimates can be chosen as a criterion to find the optimum orientation angle for each U-AVS in the array such that an acceptable performance is attained. In addition, we also present real experimental results performed in a semi-anechoic chamber to support the discussion and analytical expressions proposed for the U-AVS array.

2.3. CHAPTER SUMMARY AND REMARKS

In this chapter, we discussed the measurement model of AVS arrays in the presence of far-field sources. Based on the element-space measurement model, we discussed the advantages of the AVS array compared to an equivalent APS array through its beampattern and the CRLB on DOA estimates. Furthermore, based on the measurement model and notations described in Section 2.1, we reviewed in detail the contributions of this thesis presented in the following chapters. This thesis work, contributing to the existing knowledge base on signal processing techniques for AVS arrays, has also addressed fundamentals on some practical problems associated with the usage of AVS arrays.

Understanding the behavior of a spatially under-sampled AVS array and its application for DOA estimation allows for new array designs with a smaller number of sensor nodes in space-restricted moving or static platforms, such as vehicles, or drones, with an increased range of operational frequency. In addition to the proposed optimal one-step self-calibration algorithms, applicable to both scalar and vector sensor arrays, we also saw that AVS arrays do not suffer from the progressive phase factor ambiguity (existing for equivalent APS arrays). This aspect allows for performing self-calibration of the AVS array locally at the deployed location and relative to a single channel of an AVS without any constraints of knowing calibrator sources or additional phase reference channels/sensors. Furthermore, analyses on the U-AVS array with reduced channels and hardware requirements show that we achieve results closer to an equivalent AVS array. Such a U-AVS array-based sound localization solution can reduce costs and improve a battery-operated system's operational timeline. More importantly, this research on the AVS array paves the way in achieving increased situational awareness across our society; it could be either by detecting and localizing problems or threats (gunshots, explosion, illegal fireworks or low frequency annoying noise) occurring around urban environments or assisting soldiers in the battlefield for making a timely decision to achieve peace.

REFERENCES

[1] A. Nehorai and E. Paldi, *Acoustic vector-sensor array processing,* IEEE Transactions on Signal Processing **42**, 2481 (1994).

[2] S. Rao, *Sparse arrays: Vector sensors and design algorithms,* MSc Thesis, TU Delft (2016).

[3] M. Hawkes and A. Nehorai, *Acoustic vector-sensor beamforming and capon direction estimation,* IEEE Transactions on Signal Processing **46**, 2291 (1998).

[4] A. Moffet, *Minimum-redundancy linear arrays,* IEEE Transactions on Antennas and Propagation **16**, 172 (1968).

[5] P. Pal and P. Vaidyanathan, *Nested arrays: a novel approach to array processing with enhanced degrees of freedom,* IEEE Transactions on Signal Processing **58**, 4167 (2010).

[6] P. Pal and P. P. Vaidyanathan, *Coprime sampling and the music algorithm,* in *Digital Signal Processing Workshop and IEEE Signal Processing Education Workshop (DSP/SPE)* (IEEE, 2011) pp. 289–294.

[7] A. L. Swindlehurst and T. Kailath, *A performance analysis of subspace-based methods in the presence of model errors. i. the music algorithm,* IEEE Transactions on Signal Processing **40**, 1758 (1992).

[8] A. Paulraj and T. Kailath, *Direction of arrival estimation by eigenstructure methods with unknown sensor gain and phase,* in *1985 IEEE International Conference on Acoustics, Speech, and Signal Processing (ICASSP)*, Vol. 10 (IEEE, 1985) pp. 640–643.

[9] A. L. Swindlehurst and T. Kailath, *A performance analysis of subspace-based methods in the presence of model errors: Part ii-multidimensional algorithms,* IEEE Transactions on Signal Processing **41** (1993).

[10] T. Basten, J. Wind, B. Xu, H.-E. De Bree, and E. Druyvesteyn, *Amplitude, phase, location and orientation calibration of an acoustic vector sensor array, part ii: Experiments,* in *Proceedings of Meetings on Acoustics 159ASA*, Vol. 9 (ASA, 2010) p. 070004.

[11] T. G. Basten and H.-E. de Bree, *Full bandwidth calibration procedure for acoustic probes containing a pressure and particle velocity sensor,* The Journal of the Acoustical Society of America **127**, 264 (2010).

[12] K. Nambur Ramamohan, *Acoustic vector sensor based source localization,* MSc Thesis, TU Delft (2016).

[13] J. P. Kitchens, *Acoustic vector-sensor array performance,* MSc Thesis, Massachusetts Institute of Technology (2008).

[14] K. Nambur Ramamohan, D. F. Comesaña, G. C. Pousa, and G. Leus, *Analysis of a spatially under-sampled avs array,* in *INTER-NOISE and NOISE-CON Congress and Conference Proceedings* (Institute of Noise Control Engineering, 2017).

[15] H. L. Van Trees, *Detection, estimation, and modulation theory. Part IV. , Optimum array processing* (Wiley-Interscience, New York, 2002).

[16] M. Hawkes and A. Nehorai, *Effects of sensor placement on acoustic vector-sensor array performance,* IEEE Journal of Oceanic Engineering **24**, 33 (1999).

[17] A. J. Weiss and B. Friedlander, *Eigenstructure methods for direction finding with sensor gain and phase uncertainties,* Circuits, Systems and Signal Processing **9**, 271 (1990).

[18] M. P. Wylie, S. Roy, and H. Messer, *Joint doa estimation and phase calibration of linear equispaced (les) arrays,* IEEE Transactions on Signal Processing **42**, 3449 (1994).

[19] D. Astély, A. L. Swindlehurst, and B. Ottersten, *Spatial signature estimation for uniform linear arrays with unknown receiver gains and phases,* IEEE Transactions on Signal Processing **47**, 2128 (1999).

[20] P. Heidenreich and A. M. Zoubir, *Gain and phase autocalibration for uniform rectangular arrays,* in *2011 IEEE International Conference on Acoustics, Speech and Signal Processing (ICASSP)* (IEEE, 2011) pp. 2568–2571.

[21] K. N. Ramamohan, S. P. Chepuri, D. F. Comesana, G. C. Pousa, and G. Leus, *Blind calibration for acoustic vector sensor arrays,* in *2018 IEEE International Conference on Acoustics, Speech and Signal Processing (ICASSP)* (IEEE, 2018) pp. 3544–3548.

[22] A. Weiss, B. Nadler, and A. Yeredor, *Asymptotically optimal blind calibration of acoustic vector sensor uniform linear arrays,* in *2020 IEEE International Conference on Acoustics, Speech and Signal Processing (ICASSP)* (IEEE, 2020) pp. 4677–4681.

[23] K. Han, P. Yang, and A. Nehorai, *Calibrating nested sensor arrays with model errors,* IEEE Transactions on Antennas and Propagation **63**, 4739 (2015).

I

Acoustic Vector Sensor Array for DOA Estimation

3

DOA Estimation and Beamforming using Spatially Under-Sampled AVS arrays

In this paper, we show the advantages of spatially under-sampled acoustic vector sensor (AVS) arrays over conventional acoustic pressure sensor (APS) arrays for performing direction-of-arrival (DOA) estimation and interference cancellation. We provide insights into the theoretical performance of an under-sampled AVS array with respect to its DOA estimation performance using the Cramér-Rao lower bound (CRLB). We also show that the minimum variance distortionless response (MVDR) beamformer suppresses the grating lobes considerably as compared to the classical (or Bartlett) beamformer leading to unambiguous DOA estimates. Finally, through zero-forcing (ZF) and minimization of maximum side lobe beamformers, the advantages of an under-sampled AVS array for interference cancellation are presented.

3.1. INTRODUCTION

With the advent of the MEMS technology, transducers that are capable of measuring vector quantities such as acoustic particle velocity are becoming practically feasible [1–3]. An acoustic vector sensor (AVS) consists of a microphone and several particle velocity transducers aligned along each of the coordinate axes. As an AVS array can measure both acoustic pressure as well as particle velocity at a given spatial location, AVS arrays have several advantages compared to equivalent-aperture acoustic pressure sensor (APS) arrays [4, 5]. For this reason AVSs, either individually or arranged in an array configuration, have found numerous applications in passive acoustic systems, including ground surveillance [6], battlefield acoustics [3], sound source tracking [7], assessment of wind turbine noise [8] and UAV's situational awareness [9].

Typically, acoustic sensor arrays are battery-operated portable systems which are constrained by hardware and power requirements. Therefore, it is always desirable to reduce the number of sensors in the array to reduce the operational costs. By under sampling, when the number of sensors is fixed, the effective aperture of the array can be increased, thus leading to improvements in the direction-of-arrival (DOA) estimation accuracy. Equivalently, for an array with a fixed aperture, the number of elements, that provides a comparable estimation performance, can be reduced by under sampling.

Based on the narrow-band assumption, under-sampling traditional APS arrays with inter-sensor spacing greater than $\frac{\lambda}{2}$ (where λ is the wavelength of the source signal), leads to spatial aliasing effects resulting in grating lobes in its beam pattern [10]. Hence, ambiguities arise in beamforming and DOA estimation, which make them impractical. On the contrary, due to the nature of vector sensors, under-sampled AVS arrays can attenuate the grating lobes as discussed in previous works [11–13]. In [13], sufficient conditions for the linear independence of the array manifold matrix of an under- and over-sampled AVS uniform linear array (ULA) are discussed. However, the behavior of grating lobes with increasing inter-sensor spacing for unambiguous DOA estimation and the extent to which the inter-sensor spacing can be increased for performing beamforming are not yet well understood. We address this aspect in this work by analyzing the accuracy of unambiguous DOA estimation. For doing so, the multi-source Cramér-Rao lower bound (CRLB) is considered in such a way that we infer information of both the main and grating lobe locations. Furthermore, a performance analysis of the classical (or Bartlett) and minimum variance distortionless response (MVDR, or Capon) beamformer based DOA estimation under a single-source scenario is presented. In addition the behavior of the beamformers using an under-sampled AVS ULA for the problem of interference cancellation is considered.

3.2. PRELIMINARIES

3.2.1. AVS ARRAY MEASUREMENT MODEL

Consider an array with M AVS elements located at positions $\{\mathbf{p}_m \in \mathbb{R}^2\}_{m=1}^{M}$, and D far-field narrow-band sources of wavelength λ impinging from azimuth angles $\boldsymbol{\phi} = [\phi_1\ \phi_2\ \ldots\ \phi_D]^T \in [-\pi, \pi)$. We assume that $D \leq 3M-1$. The acquired data can be modeled as [4]:

$$\mathbf{y}(t) \quad = \quad \mathbf{A}(\boldsymbol{\phi})\,\mathbf{s}(t) + \mathbf{n}(t) \in \mathbb{C}^{3M\times 1}, \tag{3.1}$$

where $\mathbf{s}(t) = [s_1(t), s_2(t), \ldots, s_D(t)]^T \in \mathbb{C}^D$ is the source signal vector, $\mathbf{n}(t)$ is the noise vector, and $\mathbf{A}(\boldsymbol{\phi})$ denotes the array manifold matrix whose ith column is given by the correspond-

ing AVS array steering vector $\mathbf{a}(\phi_i) = \mathbf{a}_p(\phi_i) \otimes \mathbf{h}(\phi_i)$, with $\otimes$ the Kronecker product. Here, $\mathbf{a}_p(\phi_i)$ denotes the equivalent APS array response vector that is given by

$$\mathbf{a}_p(\phi_i) = \left[e^{\mathrm{j}2\pi\left(\mathbf{r}_1^T\mathbf{u}(\phi_i)\right)} \ \ldots \ e^{\mathrm{j}2\pi\left(\mathbf{r}_M^T\mathbf{u}(\phi_i)\right)}\right]^T \in \mathbb{C}^{M\times 1},$$

where $k = \frac{\pi f}{f_d} = \frac{2\pi d f}{c}$ is the wave number, $f_d = \frac{c}{2d}$ is the spatial sampling frequency, f is the source signal frequency, c is the speed of sound, d is the inter-sensor spacing where $\mathbf{r}_m = \frac{\mathbf{p}_m}{\lambda}$ is the position of the mth element in wavelengths and $\mathbf{u}(\phi_i) = [\cos(\phi_i)\ \sin(\phi_i)]^T \in \mathbb{R}^2$ is the unitary vector in the direction of the ith far-field source. The vector $\mathbf{h}(\phi_i) = [1\ \mathbf{u}^T(\phi_i)]^T \in \mathbb{R}^3$ is the weighting vector containing the directional information of the far-field source with respect to the vector sensor axes.

3.2.2. MATCHED FILTER BEAM PATTERN OF AN AVS ARRAY

Based on the measurement model presented above (3.1), the matched filter beam pattern of an AVS array with M sensors for a single source at DOA ϕ can be expressed as [14, 15]:

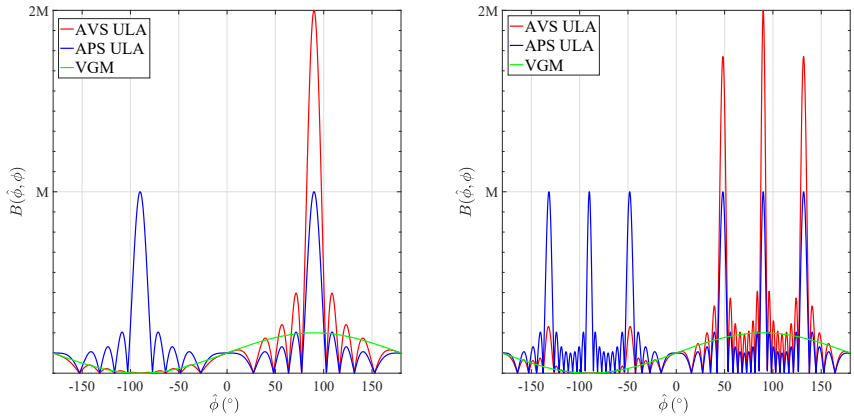
$$\begin{aligned} B(\hat{\phi},\phi) &= \left|\mathbf{a}^H(\hat{\phi})\mathbf{a}(\phi)\right| = \left|\left(\mathbf{h}^H(\hat{\phi})\mathbf{h}(\phi)\right)\left(\mathbf{a}_p^H(\hat{\phi})\mathbf{a}_p(\phi)\right)\right| \\ &= \underbrace{\left(1+\cos(\phi-\hat{\phi})\right)}_{\mathrm{VGM}(\hat{\phi},\phi)} \cdot \underbrace{\left|\sum_{m=1}^{M} e^{\mathrm{j}2\pi\left(\mathbf{r}_m^T\left(\mathbf{u}(\phi)-\mathbf{u}(\hat{\phi})\right)\right)}\right|}_{B_p(\hat{\phi},\phi)}, \end{aligned} \tag{3.2}$$

where $\hat{\phi}$ is the scanning angle, $B_p(\hat{\phi},\phi)$ is the beam pattern expression for an equivalent APS array and the term $\mathrm{VGM}(\hat{\phi},\phi)$ is the velocity gain modulation (VGM) term that is independent of the inter-sensor spacing. This VGM term plays an important role in attenuating the grating lobes when the inter-sensor spacing r (expressed in wavelengths) for a ULA is greater than the spatial Nyquist limit (i.e., $r > 0.5$). This property for the AVS ULA can be seen in the beam pattern plotted in Fig. 3.1 for $r = 0.5$ and 1.5. The beam pattern of the AVS ULA is clearly decomposed in terms of an equivalent APS ULA (red curve) and the VGM term (green curve). From (3.2) it is clear that the $\mathrm{VGM}(\hat{\phi},\phi)$ term is responsible for the possibility of under sampling AVS arrays. As the beam pattern/array response of an under-sampled AVS ULA is able to distinguish between the main lobe and the grating lobe, it is possible to employ them for performing beamforming as well as for unambiguous DOA estimation. Further, we observe that the beam pattern of an under-sampled AVS ULA is able to distinguish between the main lobe and the grating lobes. However, it does not reveal the extent to which the grating lobes can be attenuated for performing unambiguous DOA estimation. In the following section, we introduce the CRLB to provide insights on ambiguities in DOA estimation when the inter-sensor spacing is varied.

3.3. CRAMÉR-RAO LOWER BOUND FOR DOA ESTIMATION

The Cramér-Rao lower bound on the variance of an unbiased DOA estimate ϕ [cf. (3.1)], for a full rank array manifold matrix $\mathbf{A}(\phi)$, is given by [4, 16]:

$$\mathrm{CRLB}(\phi) = \frac{\sigma_{\mathbf{n}}^2}{2N}\left(\mathrm{Re}\left[\mathbf{U}\odot\left(\mathbf{D}^H\mathbf{\Pi}_c\mathbf{D}\right)^T\right]\right)^{-1}, \tag{3.3}$$



(a) $r = 0.5$ (b) $r = 1.5$

Figure 3.1: Decomposition of the beam pattern of an AVS ULA with $M = 9$ for $\phi = 90°$ in terms of an equivalent APS ULA beam pattern and the VGM term.

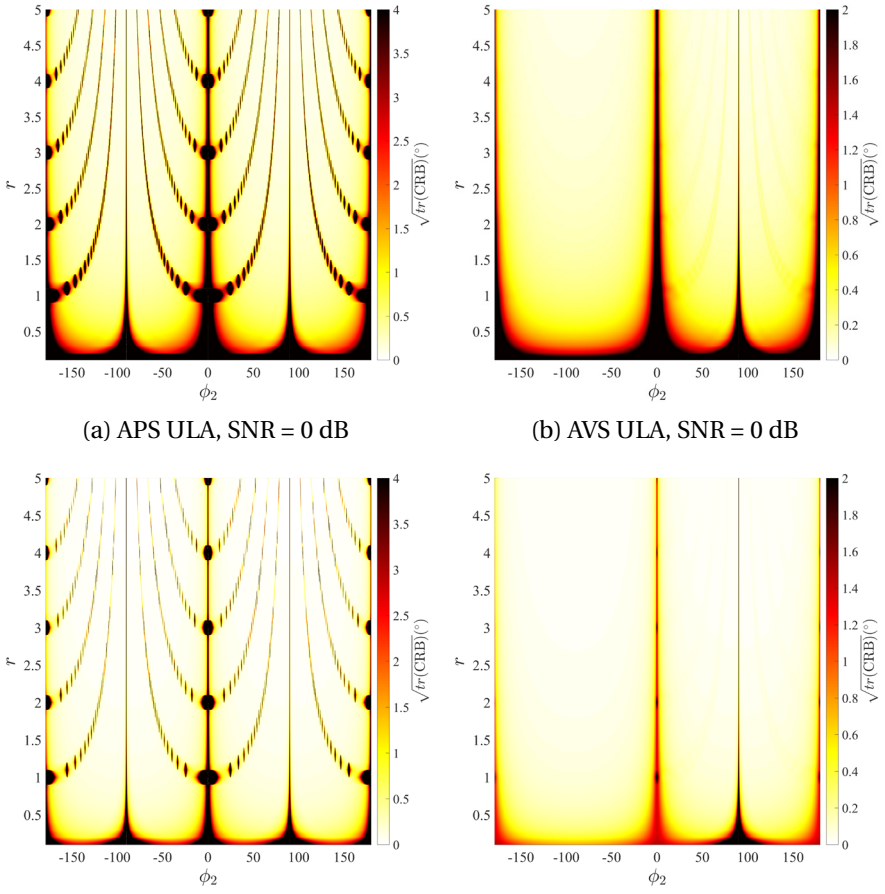
where $\odot$ is the Schur-Hadamard (element-wise) product, Re$[\cdot]$ represents the real part of the argument, N is the number of available time snapshots, and the following definitions are used

$$\mathbf{U} = \mathbf{R_s}\left(\mathbf{A}^H\mathbf{A}\mathbf{R_s} + \sigma_\mathbf{n}^2\mathbf{I}\right)^{-1}\mathbf{A}^H\mathbf{A}\,\mathbf{R_s},$$
$$\mathbf{\Pi}_c = \mathbf{I} - \mathbf{\Pi}, \quad \mathbf{\Pi} = \mathbf{A}\left(\mathbf{A}^H\mathbf{A}\right)^{-1}\mathbf{A}^H,$$
$$\mathbf{D} = \begin{bmatrix}\mathbf{d}_1 & \dots & \mathbf{d}_D\end{bmatrix}, \ \mathbf{d}_n = \frac{\partial \mathbf{a}(\phi_n)}{\partial \phi_n}, \ \forall n = 1,\dots,D.$$

Although the CRLB provides local information around the source DOAs, it can still be used to study the effect of the grating lobes in an under-sampled array. To realize that, we assume that one of the source acts as an interference at each possible scanning angle. The suggested approach enables to analyze the DOA estimation accuracy as well as any potential effects induced by the interference between multiple sources and their corresponding grating lobes.

By considering a simplistic scenario with two uncorrelated sources (ϕ_1, ϕ_2) for both the APS and AVS ULA, in Fig. 3.2 we plot the trace of the CRLB matrix with respect to an increasing inter-sensor spacing such that ϕ_1 is fixed at 90° (broadside of the array) and ϕ_2 varies over the entire azimuth range. For the APS ULA as the inter-sensor spacing is increased, the number of grating lobes increases and at those locations the Fisher information matrix becomes singular (or, in other words, the CRLB does not exist). This yields an ambiguous DOA estimation. On the other hand, for the AVS ULA, the effect of the grating lobes is attenuated considerably. In order to gain more insights for this two-source case, we simplify (3.3) by approximating $\mathbf{U} \approx \mathbf{R}_s$, by which the inner term in (3.3) can be expressed as:

$$\underbrace{\begin{bmatrix}\sigma_1^2 & 0\\ 0 & \sigma_2^2\end{bmatrix}}_{\mathbf{U}\approx\mathbf{R}_s} \odot \left(\mathbf{D}^H\mathbf{\Pi}_c\mathbf{D}\right) = \begin{bmatrix}K_1 & 0\\ 0 & K_2\end{bmatrix}, \tag{3.4}$$



(a) APS ULA, SNR = 0 dB

(b) AVS ULA, SNR = 0 dB

(c) APS ULA, SNR = 10 dB

(d) AVS ULA, SNR = 10 dB

Figure 3.2: Two-source CRLB of an APS ULA and AVS ULA for increasing inter-sensor spacing with $M = 9$, $N = 10$. The first source is located at $\phi_1 = 90°$ and the second source ϕ_2 is allowed to vary over the entire azimuth range.

where,

$$K_q = 8\pi^2\sigma_q^2\sum_{i=1}^{M}\left(\mathbf{r}_i^T\frac{\partial\mathbf{u}(\phi_q)}{\partial\phi_q}\right)^2 + M\sigma_q^2 - \underbrace{\frac{\sigma_q^2\,2M\left(B_p(\phi_1,\phi_2)\right)^2\sin^2(\phi_1-\phi_2)}{4M^2-\left(B_p(\phi_1,\phi_2)\right)^2\left(\mathrm{VGM}(\phi_1,\phi_2)\right)^2}}_{J};\ \forall q=1,2. \tag{3.5}$$

This approximation is valid under high SNR conditions and provided that ϕ_2 is not too close to ϕ_1. It is to be noted that K_q in (3.5) is expressed in terms of its equivalent APS array beam pattern and the VGM term. By restricting the discussion to a ULA, (3.5) can be further simplified when ϕ_2 is at one of the grating lobe locations of ϕ_1, given by the set [10]:

$$\mathscr{G}_{\phi_1} = \left\{\cos^{-1}\left(\cos(\phi_1)\pm\frac{n}{r}\right)\Big|\, n=1,2,3,\ldots\right\}, \tag{3.6}$$

as in that case we have $B_p(\phi_1,\phi_2)=M$. As at those grating lobe locations the VGM term is not equal to 2, the denominator of J is never zero which implies that K_q is finite, i.e., the CRLB matrix is well-defined. As a result, it can be inferred that the under-sampled AVS array can be employed for unambiguous DOA estimation even if ϕ_2 is at the grating lobe location of ϕ_1.

For the multi-source scenario in [13], it is shown that the columns of $\mathbf{A}(\phi)$ are linearly independent of each other provided that the number of sources present in a particular grating lobe set for any given angle is less than or equal to three. To illustrate the effects of an under-sampled AVS ULA under a multi-source scenario, we consider the CRLB for four sources with an increasing inter-sensor spacing in Fig. 3.3(a). The source DOAs for the first three sources are chosen such that they belong to the same grating lobe set for $r=\{2,4,\ldots\}$. The fourth source is varied over the entire range of angles. For values of r close to 2 and 4, the trace of the CRLB matrix has large values for the scanning angles belonging to the same grating lobe set indicating ambiguities in the DOA estimation. In Fig. 3.3(b), the trace of the CRLB matrix with respect to the SNR for a fixed inter-sensor spacing $r=2.5$ is shown. It is seen that at low SNRs the effect of the grating lobes is high and as the SNR increases it gets attenuated resulting in unambiguous DOA estimation.

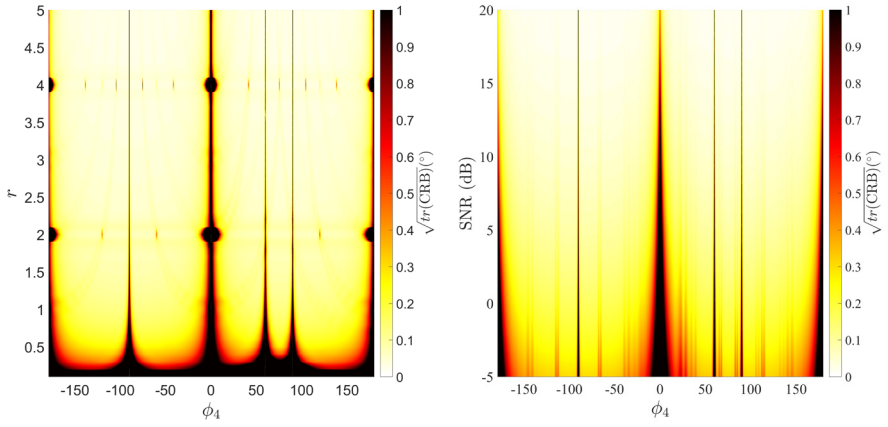
3.4. CLASSICAL AND MVDR BEAMFORMER

Based on the observations of the CRLB for an under-sampled AVS ULA we now evaluate the performance of the classical [10] and MVDR [17] beamformers for the single source (ϕ) scenario. Firstly, for a unit power source signal with zero mean, the covariance matrix of the measurement data [cf. (3.1)] is given by:

$$\mathbf{R}_\mathbf{y} = \mathbf{a}(\phi)\mathbf{a}^H(\phi)+\sigma_\mathbf{n}^2\mathbf{I}. \tag{3.7}$$

Using $\mathbf{R}_\mathbf{y}$ and defining SNR $=\frac{1}{\sigma_\mathbf{n}^2}$, the classical and MVDR beamformers angular spectrum can be written as:

$$\begin{aligned}\mathrm{CBF_v}(\hat{\phi},\phi) &= \frac{\left(\mathbf{a}^H(\hat{\phi})\mathbf{a}(\phi)\right)^2}{2M}+\frac{1}{\mathrm{SNR}}, \\ &= \left(\mathrm{CBF}_p(\hat{\phi},\phi)-\frac{1}{\mathrm{SNR}}\right)\frac{\left(\mathrm{VGM}(\hat{\phi},\phi)\right)^2}{2}+\frac{1}{\mathrm{SNR}},\end{aligned} \tag{3.8}$$



(a) SNR = 10 dB (b) $r = 2.5$

Figure 3.3: CRLB variation with four sources (three fixed at $90°, 60°, -90°$ and the fourth varying), $M = 9$, $N = 10$. In (a) the trace of the CRLB for increasing inter sensor spacing is considered. In (b), the trace of the CRLB for increasing SNR is considered.

$$\text{MVDR}_v(\hat{\phi},\phi) = \frac{2M(\text{SNR})+1}{2M(\text{SNR})+(\text{SNR})^2\underbrace{\left(4M^2-\left(\mathbf{a}^H(\hat{\phi})\mathbf{a}(\phi)\right)^2\right)}_{G}}, \tag{3.9}$$

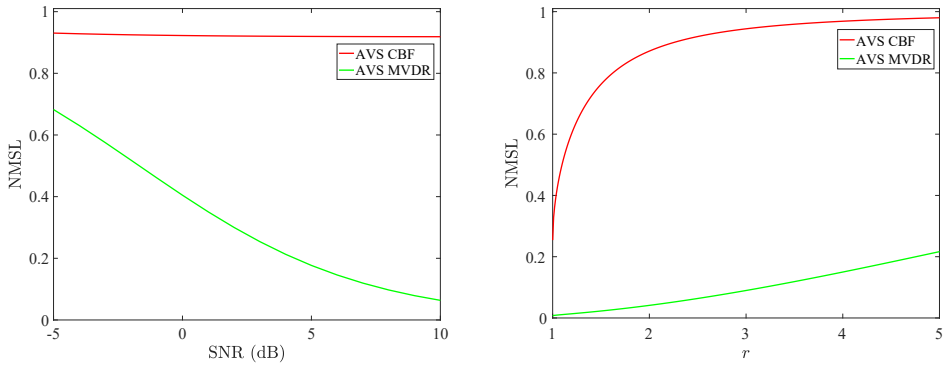
where $\text{CBF}_v(\hat{\phi},\phi)$ and $\text{MVDR}_v(\hat{\phi},\phi)$ are the CBF and MVDR beamformer spectrum of an AVS ULA, respectively, and where $\text{CBF}_p(\hat{\phi},\phi)$ is the CBF beamformer spectrum of an equivalent APS ULA. It is shown that both the CBF and MVDR beamformer result in a maximum when $\hat{\phi} = \phi$, tending towards unity as the SNR and M increases. For a given M, the attenuation of the side lobes by the classical beamformer is independent of SNR and is proportional to the attenuation achieved by its squared beam pattern. In contrast, for the MVDR beamformer the side lobes are attenuated considerably as the G term in the denominator is amplified by the factor $(\text{SNR})^2$. At the location of the grating lobes ($\hat{\phi} \in \mathcal{G}_\phi$) of an undersampled AVS ULA, (3.8) and (3.9) reduce to:

$$\text{CBF}_v(\hat{\phi},\phi) = \frac{M^2(\text{SNR})\left(\text{VGM}(\hat{\phi},\phi)\right)^2+2M}{\text{SNR}}, \tag{3.10}$$

$$\text{MVDR}_v(\hat{\phi},\phi) = \frac{2M(\text{SNR})+1}{2M(\text{SNR})+M^2(\text{SNR})^2\left(4-\left(\text{VGM}(\hat{\phi},\phi)\right)^2\right)}, \tag{3.11}$$

where we use the fact that $\mathbf{a}_p^H(\hat{\phi})\mathbf{a}_p(\phi) = M$. It should be noted that as the SNR approaches ∞, $\text{MVDR}_v(\hat{\phi},\phi)$ approaches 0.

As the maximum side lobe level (MSL) is achieved at the grating lobe location (with $n = 1$ in (3.6)), the MSL behavior based on (3.10) and (3.11) for both the CBF and MVDR



(a) $r = 2.5$ (b) SNR = 10 dB

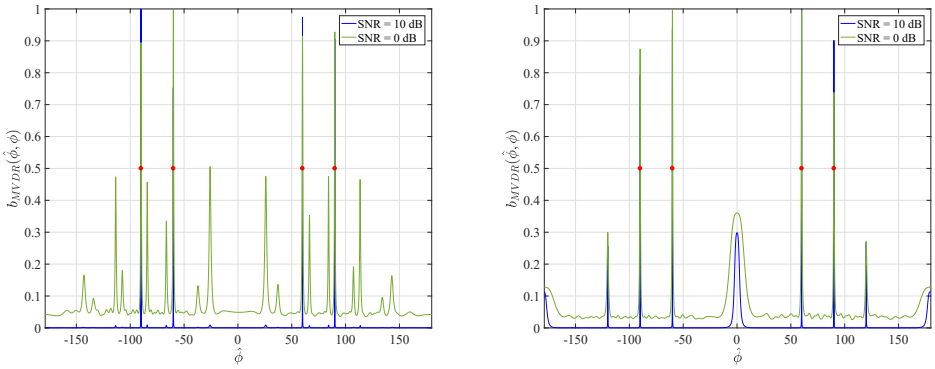
Figure 3.4: The normalized maximum side lobe level (NMSL), defined as the ratio of the MSL and main lobe level, for the Classical and MVDR beamformer using an under-sampled AVS ULA with $\phi = 90°$, $M = 9$. In (a) the inter-sensor spacing is fixed at $r = 2.5$ and the SNR is varied. In (b) the SNR is fixed at 10 dB and the inter sensor spacing is varied.

beamformer are shown in Fig. 3.4, respectively. In Fig. 3.4 (a), it is seen that the MSL for the CBF is comparable to the main lobe level. In contrast, for the MVDR beamformer its MSL decreases considerably as the SNR increases. In Fig. 3.4 (b) the MSL for both beamformers is a non-decreasing function of the inter-sensor spacing of the array. From this result it is clear that the MVDR beamformer reduces the grating lobe effects significantly allowing for unambiguous DOA estimation. Having focused on the DOA estimation using an under-sampled AVS array, in the following section we consider the problem of beamformer design for interference cancellation. The MSL levels for the MVDR beamformer are remarkably low for all r. In addition, the MVDR spectra with sources is plotted in Fig. 3.5 for two different cases of $r_{\lambda x} = 2$ and $r_{\lambda x} = 2.5$, to illustrate the observation seen in Fig. 3.3. The source DOAs are chosen as in Fig. 3.3 (c) and it is seen that for $r_{\lambda x} = 2$ that the sources are not being distinguished from grating lobes as $\mathbf{A}(\phi)$ is rank deficient. For $r_{\lambda x} = 2.5$ as the SNR increases all the sources and grating lobes are distinguished as seen in Fig. 3.3 (b).

3.5. INTERFERENCE CANCELLATION

The fact that the matched filter beam pattern weights [cf. (7.5)] have the same phase delay for all three channels in a single AVS, we can decompose the array response as the product of the interference between sensors and the directional information term. However, this simplification limits the number of available degrees of freedom in the beamformer design. Hence, if the weights for each of the channels in each AVS are not constrained in any way, significant improvements can be obtained. Formally, we can express the generic beam pattern synthesis problem for an AVS array as [5]:

$$\begin{aligned} G(\phi) \quad = \quad & \Big| \sum_{m=1}^{M} w_{mp} e^{\mathrm{j}2\pi(\mathbf{r}_m^T \mathbf{u}(\phi))} + \cos(\phi) \sum_{m=1}^{M} w_{mx} e^{\mathrm{j}2\pi(\mathbf{r}_m^T \mathbf{u}(\phi))} \\ & + \sin(\phi) \sum_{m=1}^{M} w_{my} e^{\mathrm{j}2\pi(\mathbf{r}_m^T \mathbf{u}(\phi))} \Big| = \left| \mathbf{w}^H \mathbf{a}(\phi) \right|, \end{aligned} \tag{3.12}$$



(a) $r_{\lambda x} = 2.5$ (b) $r_{\lambda x} = 2$

Figure 3.5: MVDR spectra for four sources $\phi = 90°, -60°, 60°, -90°$, belonging to the grating lobe set of $r_{\lambda x} = 2, 4, \ldots$, with $M = 10$, $N = 100$.

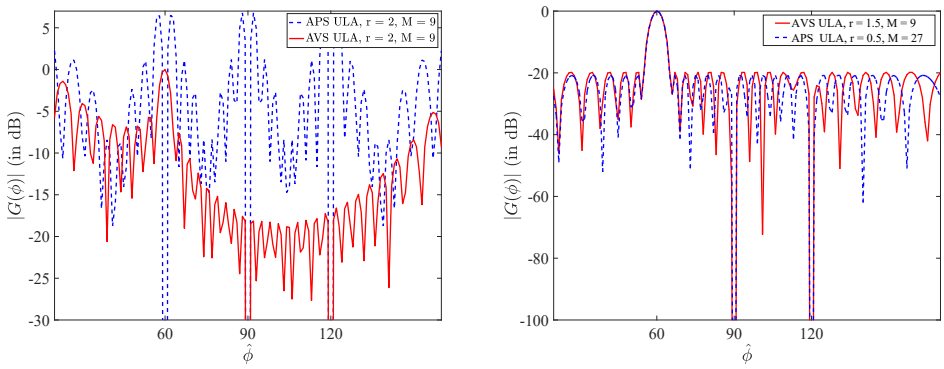
where $\mathbf{w} = \begin{bmatrix} w_{1p} & w_{1x} & w_{1y} & \ldots & w_{Mp} & w_{Mx} & w_{My} \end{bmatrix}^T \in \mathbb{C}^{3M}$ is the complex weight vector that needs to be designed such that $G(\phi)$ has a desired shape. The design problem can be written as a convex optimization program where constraints on the sensitivity, main lobe, and side lobes of the beam pattern can be enforced.

To illustrate this, we consider two beamformer design problems to suppress interferences (ϕ_n, $n = 1, 2, \ldots$) while preserving the angle of interest (ϕ_0). Firstly a simple null steering/zero forcing (ZF) beamformer [10] for both an under-sampled APS and AVS ULA with $r = 2$ is considered in Fig. 3.6 (a) with $\phi_0 = 60°$ and $\phi_1 = 90°$, $\phi_2 = 120°$. These two angles are chosen such that they belong to the same grating lobe set ($\mathscr{G}(\phi_0)$) for $r = 2$. As the steering vectors for the APS ULA are the same for all $\phi \in \mathscr{G}(\phi_0)$, the ZF beamformer suppresses not only the interferers but also the signal of interest. However, the AVS ULA is able to retain the source of interest and to suppress both interferers. Although the ZF beamformer only aims at keeping unity gain towards the signal of interest while suppressing interferers, it does not optimize the side lobe level at other directions. Therefore, we also consider an optimization problem for minimizing the maximum array response $|G(\phi)|$, $\forall \phi \in \mathscr{S}$, where $\mathscr{S}$ denotes the side lobe region, subject to having a distortion-less response for the target angle ϕ_0, a bounded sensitivity and a certain main lobe decay for angles $\phi \in \mathscr{M}$, where $\mathscr{M}$ represents the main lobe region. In addition, constraints can be included to null the interference from certain angles $\phi \in \mathscr{N}$, where $\mathscr{N}$ contains the DOAs to be nulled. This problem can be succinctly expressed as [18]

$$\begin{aligned} \min_{\mathbf{w}} \quad & \max_{\phi \in \mathscr{S}} |\mathbf{w}^H \mathbf{a}(\phi)|, \\ \text{subject to} \quad & |\mathbf{w}^H \mathbf{a}(\phi)| \leq \alpha; \ \forall \phi \in \mathscr{M} \\ & \mathbf{w}^H \mathbf{a}(\phi_0) = 1, \ \|\mathbf{w}\|_2 \leq \beta \\ & \mathbf{w}^H \mathbf{a}(\phi) = 0; \ \forall \phi \in \mathscr{N}. \end{aligned} \tag{3.13}$$

For illustration purposes, we consider an AVS ULA with $M = 9$, $r = 1.5$ and an APS ULA with $M = 27$, $r = 0.5$ such that they have the same channel count and almost a similar aper-

ture. The same angles are considered as in the previous example. The optimization problem is solved with $\alpha, \beta = 1$ and the results are shown in Fig. 3.6 (b). It is seen that the beam pattern of an AVS ULA (with $M = 9$) is comparable to that of an APS ULA (with $M = 27$) with both interferences being suppressed.



(a) ZF beamformer (b) Beamformer from (3.13)

Figure 3.6: Beam pattern synthesis of an AVS and APS ULA for $\phi_0 = 60^\circ$ and interference locations $\phi_1 = 90^\circ$, $\phi_2 = 120^\circ$. In (a) the beampattern synthesis using a ZF beamformer is considered. In (b) the beam pattern synthesis as a solution of (3.13) is considered.

REFERENCES

[1] H.-E. de Bree, *An overview of microflown technologies,* Acta acustica united with Acustica **89**, 163 (2003).

[2] H.-E. Bree, P. Leussink, T. Korthorst, H. Jansen, T. Lammerink, and M. Elwenspoek, *The μ-flown: A novel device measuring acoustical flows,* (1995).

[3] H.-E. De Bree, *The microflown e-book,* Microflown Technologies, Arnhem (2007).

[4] A. Nehorai and E. Paldi, *Acoustic vector-sensor array processing,* Signal Processing, IEEE Transactions on **42**, 2481 (1994).

[5] J. P. Kitchens, *Acoustic vector-sensor array processing,* Ph.D. thesis, Massachusetts Institute of Technology (2010).

[6] H.-E. de Bree, J. Wind, and E. Tijs, *Environmental noise monitoring with acoustic vector sensors,* in *INTER-NOISE and NOISE-CON Congress and Conference Proceedings*, Vol. 2010 (Institute of Noise Control Engineering, 2010) pp. 6225–6231.

[7] H.-E. de Bree, J. Wind, and P. de Theije, *Detection, localization and tracking of aircraft using acoustic vector sensors,* Inter Noise 2011 Proceedings, Osaka, Japan , 4 (2011).

[8] D. Fernandez Comesana, K. Nambur Ramamohan, D. Perez Cabo, and G. Carrillo Pousa, *Modelling and localizing low frequency noise of a wind turbine using an array of acoustic vector sensors,* 7th Wind Turbine Noise Conference (2017).

[9] H.-E. de Bree, *Acoustic vector sensors increasing UAV situational awareness,* SAE Technical Paper , 2009 (2009).

[10] H. L. Van Trees, *Detection, estimation, and modulation theory. Part IV. , Optimum array processing* (Wiley-Interscience, New York, 2002).

[11] M. Hawkes and A. Nehorai, *Acoustic vector-sensor beamforming and capon direction estimation,* IEEE Trans. Signal Processing **46**, 2291 (1998).

[12] K. T. Wong and M. D. Zoltowski, *Extended-aperture underwater acoustic multisource azimuth/elevation direction-finding using uniformly but sparsely spaced vector hydrophones,* IEEE Journal of Oceanic Engineering **22**, 659 (1997).

[13] Y. Wu, Z. Hu, H. Luo, and Y. Hu, *Source number detectability by an acoustic vector sensor linear array and performance analysis,* Oceanic Engineering, IEEE Journal of **39**, 769 (2014).

[14] J. P. Kitchens, *Acoustic vector-sensor array performance,* (2008).

[15] K. Nambur Ramamohan, *Acoustic vector sensor based source localization,* MSc Thesis, TU Delft (2016).

[16] A. Nehorai and E. Paldi, *Vector-sensor array processing for electromagnetic source localization,* Signal Processing, IEEE Transactions on **42**, 376 (1994).

[17] J. Capon, *High-resolution frequency-wavenumber spectrum analysis,* Proceedings of the IEEE **57**, 1408 (1969).

[18] H. Lebret and S. Boyd, *Antenna array pattern synthesis via convex optimization,* IEEE transactions on signal processing **45**, 526 (1997).

II

Self-Calibration and DOA Estimation

4

SELF CALIBRATION OF SCALAR AND VECTOR SENSOR ARRAYS

In this work, we consider the self-calibration problem of joint calibration and direction-of-arrival (DOA) estimation using sensor arrays. Unlike many previous iterative approaches, we propose array geometry independent solvers for jointly estimating the sensor gain, phase errors, and the source DOAs. We derive these algorithms for both the conventional element-space and covariance data models. We focus on sparse and regular arrays formed using scalar sensors as well as vector sensors. The developed algorithms are obtained by transforming the underlying non-linear calibration model into a linear model, and subsequently by using convex relaxation techniques to estimate the unknown parameters. We also derive identifiability conditions for the existence of a unique solution to the self-calibration problem. To demonstrate the effectiveness of the developed techniques, numerical experiments, and comparisons to the state-of-the-art methods are provided. Finally, the results from an experiment that was performed in an anechoic chamber using an acoustic vector sensor array are presented to demonstrate the usefulness of the proposed self calibration techniques.

4.1. INTRODUCTION

The problem of estimating the direction-of-arrival (DOA) of multiple far-field events impinging on an array of spatially distributed sensors has received considerable interest in various fields including communications, radio astronomy, acoustics, and seismology. Usually scalar sensor arrays, such as acoustic pressure sensor (APS) arrays, are used for DOA estimation. In recent times, transducers that measure vector quantities are becoming practically feasible [1], enabling new processing capabilities. An acoustic vector sensor (AVS) is such a device that is capable of measuring both the acoustic pressure and particle velocity. Unlike an APS, a single AVS can measure the DOA of a far-field event [2] and arrays of such AVSs have proven to have distinct advantages compared to conventional microphone arrays [3]. In practice, all sensors and their arrays are highly sensitive to model errors [4]. Among those model errors, the gain and phase mismatches between sensors, known as calibration errors are the dominant ones that degrade the DOA estimation results. Those are the focus of this work.

Many advanced subspace based algorithms, e.g., MUSIC [5], MVDR [6], and ESPRIT [7], have been developed for DOA estimation. Further sparse recovery techniques have also been widely used, whenever only a few sources are present [8]. These traditional algorithms require more physical sensors than the number of sources and use the data acquired in the *element-space* domain (i.e., at the output of the sensor elements) or in the covariance (or *co-array*) domain. Also nowadays, to reduce sensing and data processing costs, sparse sensing methods are gaining attention [9]. One can resolve and estimate DOAs of as many as $\mathcal{O}(M^2)$ sources using only M physical elements by smartly and irregularly placing the sensor elements. Such sensor placements are generally referred to as sparse arrays [10–12]. Most of the discussed algorithms developed for APS arrays can be used directly or adapted for equivalent AVS arrays as well [2, 3].

DOA estimates obtained from these aforementioned standard algorithms in the presence of calibration errors are severely degraded [4]. These errors originate from the variability in the analog electronics and the manufacturing technology across sensors in the array. They affect both the signal-of-interest and the noise part of the measurement data [4, 13]. On the other hand, it is also possible to have calibration errors that only affect the signal part of the measurements [4], whenever there are position or orientation errors of the sensors (channels) in the array for instance or perturbations in the sensors' gain and phase patterns. Usually labor intensive and expensive calibration procedures are applied to correct for these mismatches [14–16], which are impractical for large number of sensors. Furthermore, such calibration errors vary with time and changes in the environment, and as a result, the deployed sensors require periodic re-calibration. In such scenarios, self-calibration methods are inevitable. The term *self-calibration* refers to using the information collected by the array to simultaneously estimate the calibration errors and source DOAs without any reference sources with known direction and/or pre-defined waveform.

4.1.1. SELF-CALIBRATION METHODS

Self-calibration techniques for scalar sensor arrays in the presence of gain and phase uncertainties between sensors have been widely studied [13, 17–21]. It is a non-linear estimation problem with unknown calibration and array manifold matrix. Specific conditions should be satisfied such that they are independently identifiable [17, 19]. In some cases it is impossible to independently resolve both of them [17, 22].

Maximum likelihood (ML) and maximum a posteriori (MAP) based gain and phase estimation algorithms have been proposed in [23, 24] to solve the self-calibration problem. Although both ML and MAP based estimators are asymptotically efficient, they are computationally expensive and not suitable for practical applications. In contrast, there are also computationally friendly self-calibration techniques which can be broadly classified into two categories: geometry-dependent and geometry-independent approaches.

The first kind of self-calibration techniques are developed for specific/regular array geometries, where spatial redundancies are used to eliminate the array manifold information in order to estimate the calibration errors. Specifically, in [13], a self-calibration procedure for scalar sensor arrays arranged in a uniform linear array (ULA) configuration was presented, where the Toeplitz structure of the data covariance matrix was utilized. Extensions and adaptations of this self-calibration approach are presented in [18, 25–27]. A self-calibration technique based on ESPRIT for an APS ULA is derived in [17].

The second kind of self-calibration approaches are applicable to arbitrary array geometries where the array manifold and calibration matrices are estimated mostly with iterative techniques [19, 20, 28]. However, these approaches suffer from the choice of the initial estimate of the calibration errors and the algorithm might only converge to a local minimum leading to a sub-optimal solution.

Aforementioned two categories of self-calibration approaches are developed specifically for scenarios with more sensors than sources. Nonetheless, with the increased attention on sparse sensing, a self-calibration algorithm for sparse arrays was proposed in [29], where a sub-optimal method was used to estimate the phase errors.

On the other hand, apart from the DOA estimation techniques proposed in [30–34], not much attention is given to the self-calibration problem for AVS arrays. It may seem possible to adapt the second category of aforementioned self-calibration techniques for vector sensor arrays. However, due to the dissimilarities in the array manifold, the conditions for independently identifying the calibration errors and source DOAs are different and are not yet available.

In summary, we can observe that existing self-calibration approaches either require specific sensor placement to obtain an optimal solution or converge to a sub-optimal solution without geometry constrains. So in this work we try to address the issues associated with existing techniques by proposing two non-iterative *one-step* self-calibration algorithms that are array geometry independent, and applicable to both APS and AVS arrays. Furthermore, the proposed self-calibration technique using the co-array measurement model is also applicable to sparse arrays, whose preliminary results are presented in [35]. In our work, we leverage tools from sparse recovery techniques and draw inspiration from [21], which deals with the self-calibration problem for linear models, to decouple the calibration parameters from the other unknowns. However, the model we deal with is not linear anymore as the source directions are not known. In essence, the main problem of interest in this work is self-calibration with a non-linear measurement model, where we assume that the calibration errors are mainly originating from uncertainties in the analog electronics and sensor elements. Additionally, we also derive the identifiablity conditions for a unique solution to exist while using AVS and sparse APS arrays.

4.1.2. OUR CONTRIBUTIONS

This work introduces novel self-calibration methodologies combining traditional array processing theory with sparse recovery techniques. The validity of the proposed self-calibration algorithms is studied by considering the measurement model where the calibration errors affect both the signal-of-interest and noise. Further the adaptation of the proposed approaches to the measurement model where the calibration errors affect only the signal component of the data is also discussed. The main contributions can be summarized as follows:

- We develop array-independent non-iterative novel self-calibration algorithms for both the element-space and co-array data models, where the latter data model is even useful when there are more sources than sparsely placed sensors.
- We derive conditions to ensure a unique solution for estimating the DOAs and calibration errors for both AVS and sparse APS arrays. This important aspect is still not considered in the existing literature.
- We demonstrate the validity of the proposed approaches via numerical simulations as well as an experimental study. The latter shows the effectiveness of the introduced self-calibration techniques for an array of 4 AVSs measured in an anechoic chamber.

4.1.3. NOTATION AND OUTLINE

Upper (lower) bold face letters are used for matrices (column vectors); $(\cdot)^*$ denotes conjugate, $(\cdot)^T$ denotes transpose and $(\cdot)^H$ denotes conjugate transpose; $\otimes$ denotes the Kronecker product, $\circ$ denotes the Khatri-Rao product and $\odot$ denotes the Schur-Hadamard (element-wise) product; $\mathbb{E}\{\cdot\}$ denotes the expectation operator; tr$(\cdot)$ denotes the trace operator and $\mathbf{I}_n$ is the identity matrix of dimension n.

The detailed outline for this paper is as follows. In Section 4.2, we present the measurement model with calibration errors, and the problem statement of estimating both the calibration errors and the DOAs. In Section 4.3, we present the identifiability conditions for uniquely estimating the calibration errors and the source DOAs. In Section 4.4 and Section 4.5, the proposed calibration algorithms based on the element-space and the co-array domain measurement data model are presented, respectively. The simulation and experimental results of the proposed calibration algorithms are discussed in Section 4.6 and Section 4.7, respectively.

4.2. PROBLEM STATEMENT

Consider a linear array of M sensors with Q channels, where $Q = M$ for APS arrays and $Q = 3M$ for AVS arrays. We are interested in estimating the azimuth directions of N narrow-band sources, denoted by $\boldsymbol{\theta} = [\theta_1, \theta_2, \ldots, \theta_N]^T$ with $\theta_n \in [0, \pi]$ for $n = 1, \ldots, N$, where the azimuth directions are measured with respect to the phase reference of the array. Each of the considered Q channels has a different receiver gain and phase response, which are not known. We refer to the unknown receiver gains and phases as calibration errors, and for the ith channel it is denoted as $g_i = \alpha_i e^{j\phi_i}$ with α_i and ϕ_i being the gain and phase mismatch, respectively. We collect the calibration errors in the diagonal matrix diag(g) with $\mathbf{g} = [g_1, g_2, \ldots, g_Q]^T$. Let us also define the vectors $\boldsymbol{\alpha} = [\alpha_1, \alpha_2, \ldots, \alpha_Q]^T$ and $\boldsymbol{\phi} = [\phi_1, \phi_2, \ldots, \phi_Q]^T$.

Under the narrow-band assumption [5], the element-space signal, $\mathbf{x}(t)$, can be modeled as [13]

$$\mathbf{x}(t) = \text{diag}(\mathbf{g})\,[\mathbf{A}(\boldsymbol{\theta})\,\mathbf{s}(t) + \mathbf{n}(t)] \in \mathbb{C}^{Q\times 1}, \tag{4.1}$$

where

$$\mathbf{A}(\boldsymbol{\theta}) = [\mathbf{a}(\theta_1)\cdots\mathbf{a}(\theta_N)] \in \mathbb{C}^{Q\times N}$$

is the array manifold matrix, the source signals of wavelength λ are stacked in the vector $\mathbf{s}(t) \in \mathbb{C}^{N\times 1}$ and the receiver noise vector is given by $\mathbf{n}(t) \in \mathbb{C}^{Q\times 1}$. Here, we assume that both $\mathbf{s}(t)$ and $\mathbf{n}(t)$ are derived from an independent and identically distributed (i.i.d.) Gaussian distribution. The location of the mth element of the array is denoted by δ_m with $p_m = \delta_m/\lambda$. Let us also define $\mathbf{p} = [p_1, p_2, \ldots, p_M]^T$. Without loss of generality (w.l.o.g.), we consider the first sensor with $p_1 = 0$ as the phase reference of the array. The spatial signature (or the array steering vector) for the nth source in the direction described by the vector $\mathbf{u}(\theta_n) = [\cos(\theta_n)\ \sin(\theta_n)]^T$ with respect to the first sensor of the APS array with M sensors is given by

$$\mathbf{a}_{\text{APS}}(\theta_n) = \left[e^{\text{j}2\pi p_1\cos(\theta_n)}, \ldots, e^{\text{j}2\pi p_M\cos(\theta_n)}\right]^T \in \mathbb{C}^{M\times 1}, \tag{4.2}$$

whereas the related array steering vector of the AVS array is given by

$$\begin{aligned}\mathbf{a}_{\text{AVS}}(\theta_n) &= \left[\begin{array}{cc} 1 & \mathbf{u}^T(\theta_n)\end{array}\right]^T \otimes \mathbf{a}_{\text{APS}}(\theta_n),\\ &= \mathbf{h}(\theta_n)\otimes\mathbf{a}_{\text{APS}}(\theta_n) \in \mathbb{C}^{3M\times 1}.\end{aligned} \tag{4.3}$$

For the APS array, we have $Q = M$ with $\mathbf{a}(\theta_n) = \mathbf{a}_{\text{APS}}(\theta_n)$ and for the AVS array we have $Q = 3M$ channels with $\mathbf{a}(\theta_n) = \mathbf{a}_{\text{AVS}}(\theta_n)$.

Usually the signal $\mathbf{x}(t)$ is uniformly sampled and L snapshots are collected in the data matrix $\mathbf{X} = [\mathbf{x}(1), \mathbf{x}(2), \ldots, \mathbf{x}(L)] \in \mathbb{C}^{Q\times L}$ to obtain

$$\mathbf{X} = \text{diag}(\mathbf{g})\,[\mathbf{A}(\boldsymbol{\theta})\mathbf{S} + \mathbf{N}]\,. \tag{4.4}$$

Here, $\mathbf{S} = [\mathbf{s}(1), \mathbf{s}(2), \ldots, \mathbf{s}(L)] \in \mathbb{C}^{N\times L}$ and $\mathbf{N} = [\mathbf{n}(1), \mathbf{n}(2), \ldots, \mathbf{n}(L)] \in \mathbb{C}^{Q\times L}$. The covariance matrix of the signal $\mathbf{x}(t)$ is $\mathbf{R}_{\text{x}} = \mathbb{E}\{\mathbf{x}(t)\mathbf{x}^H(t)\} \in \mathbb{C}^{Q\times Q}$. We assume that the source signals $\mathbf{s}(t)$ are uncorrelated and have a diagonal covariance matrix $\mathbb{E}\{\mathbf{s}(t)\mathbf{s}^H(t)\} = \text{diag}(\boldsymbol{\sigma}_{\text{s}})$, which is not known. Similarly, the noise vector has a diagonal covariance matrix $\mathbb{E}\{\mathbf{n}(t)\mathbf{n}^H(t)\} = \text{diag}(\boldsymbol{\sigma}_{\text{n}})$, which is assumed to be known or can be estimated. Then, the covariance domain model can be written as

$$\mathbf{R}_{\text{x}} = \text{diag}(\mathbf{g})\left[\mathbf{A}(\boldsymbol{\theta})\text{diag}(\boldsymbol{\sigma}_{\text{s}})\mathbf{A}^H(\boldsymbol{\theta}) + \text{diag}(\boldsymbol{\sigma}_{\text{n}})\right]\text{diag}^H(\mathbf{g}). \tag{4.5}$$

Here, it is assumed that $\mathbf{s}(t)$ and $\mathbf{n}(t)$ are mutually uncorrelated. It is also useful to express (6.2) in vectorized form as:

$$\mathbf{r}_{\text{x}} = \text{diag}(\mathbf{g}^*\otimes\mathbf{g})\,[\mathbf{A}_{\text{co}}(\boldsymbol{\theta})\boldsymbol{\sigma}_{\text{s}} + \boldsymbol{\sigma}_{\text{n}}]\,, \tag{4.6}$$

where $\text{vec}(\mathbf{R}_{\text{x}}) = \mathbf{r}_{\text{x}}$ and $\mathbf{A}_{\text{co}}(\boldsymbol{\theta}) = \mathbf{A}^*(\boldsymbol{\theta}) \circ \mathbf{A}(\boldsymbol{\theta})$ with the subscript "co" indicating the co-array manifold. In practice, the data matrix $\mathbf{X}$ is used to compute the sample data covariance matrix $\widehat{\mathbf{R}}_{\text{x}} = L^{-1}\mathbf{X}\mathbf{X}^H$. For the sake of convenience, henceforth, we use $\mathbf{R}_{\text{x}}$ instead of $\widehat{\mathbf{R}}_{\text{x}}$ with the knowledge that only an estimate of the covariance matrix is available.

Based on the co-array model in (4.6), the sensor elements can be smartly placed irregularly along the linear axis, such that $\mathbf{A}_{\text{co}}$ has full column rank. Usually such configuration of linear arrays leads to sparse array design [12] allowing one to resolve as many as $\mathcal{O}(M^2)$ sources using M sensors. As seen in (4.1) and (4.6), both $\mathbf{g}$ and $\boldsymbol{\theta}$ are unknowns, and additionally it is a non-linear estimation problem as $\boldsymbol{\theta}$ exists in the exponential terms of the array manifold matrix.

The main goal of this paper is to jointly estimate the Q complex (i.e., $2Q$ real) receiver gains $\mathbf{g}$ and N directions $\boldsymbol{\theta}$ given $\mathbf{X}$ or $\mathbf{r}_{\text{x}}$. To do so uniquely, as will be discussed in Section 4.3, we will require a few reference sensors with known complex receiver gains in the array.

4.3. AMBIGUITY AND IDENTIFIABILITY

4

Before presenting the calibration algorithms, in this section, we discuss identifiability conditions under which a unique solution for both the calibration parameters and the source DOAs exists. The identifiability conditions for the APS arrays by considering the element-space model (4.4) is presented in [19]. We take inspiration from [19] and derive identifiability conditions for all the remaining measurement models relevant for both APS and AVS arrays. It should be immediately clear that, as both $\text{diag}(\mathbf{g})\mathbf{A}(\boldsymbol{\theta})$ and $\mathbf{S}$ (or $\boldsymbol{\sigma}_{\text{s}}$) are not known a priori, they cannot be computed uniquely as there will be a complex (or real) scaling ambiguity. Therefore, to fix the scaling ambiguity we perform calibration with respect to *sensor 1* at location $p_1 = 0$, i.e., we use $g_1 = 1$ for the element-space data model and $|g_1| = \alpha_1 = 1$ for the co-array data model.

After establishing the fact that the elements of $\mathbf{g}$ can only be estimated relative to the reference sensor, the next important question that needs to be addressed is to establish the well posedness of the self-calibration problem given the measurement data. From the element-space data model (4.4), we have $2QL$ nonlinear equations in N unknown DOAs, $2(Q-1)$ unknown calibration parameters, and $2NL$ unknown source signals. Hence, for well posedness of the calibration problem, we require

$$2QL \geq N + 2Q - 2 + 2NL \quad \Rightarrow \quad \frac{N + 2(Q-1)}{2(Q-N)} \leq L,$$

which is meaningful only for $Q > N$. Furthermore, from the co-array data model (4.6), we have $2QN - N^2 + 1$ nonlinear equations[1] in N unknown DOAs, $2(Q-1)$ unknown calibration parameters, and N unknown source powers. Hence, for well posedness, we require

$$2QN - N^2 + 1 \geq 2N + 2Q - 2 \quad \Rightarrow \quad Q \geq \frac{N^2 + 2N - 3}{2(N-1)}.$$

Finally, we study under which conditions we can uniquely estimate $\mathbf{g}$ and $\boldsymbol{\theta}$ given the measurement data. However due to the non-linear nature of the estimation problem, it is not straightforward to derive the identifiability conditions based on the element-space data model (4.4) or co-array data model (4.6). Therefore, we derive sufficient conditions for uniquely estimating $\mathbf{g}$ and $\boldsymbol{\theta}$ based on the assumption that $\text{diag}(\mathbf{g})\mathbf{A}(\boldsymbol{\theta})$ ($\text{diag}(\mathbf{g}^* \otimes \mathbf{g})\mathbf{A}_{\text{co}}(\boldsymbol{\theta})$) is given, with the knowledge that in practice only the column span of it is available from the measurement data.

[1] The covariance matrix $\mathbf{R}_{\text{x}}$ is completely characterized by $N+1$ real eigenvalues and $2QN - N^2 - N$ real parameters related to the orthonormal eigenvectors associated to the signal subspace.

THE ELEMENT-SPACE DATA MODEL

For deriving the sufficient conditions, let us define the phase of $\text{diag(g)}\mathbf{A}(\boldsymbol{\theta})$ as

$$\rho_q(n) = \frac{1}{2\pi}\text{angle}\left(g_q\left[\mathbf{A}(\boldsymbol{\theta})\right]_{qn}\right) = p_q\cos(\theta_n) + \phi_q, \tag{4.7}$$

for $q = 1,\ldots,Q$ and $n = 1,\ldots,N$. Introducing $\boldsymbol{\rho}_n = \left[\rho_1(n),\ldots,\rho_Q(n)\right]^T$ and defining $\mathbf{p}_{\text{ext}} := \mathbf{p}$ for the APS array and $\mathbf{p}_{\text{ext}} := \mathbf{1}_3 \otimes \mathbf{p}$ for the AVS array, we can write the above equation compactly as

$$\boldsymbol{\rho}_n = \mathbf{p}_{\text{ext}}\cos(\theta_n) + \boldsymbol{\phi} = \begin{bmatrix}\mathbf{p}_{\text{ext}} & \mathbf{I}_Q\end{bmatrix}\begin{bmatrix}\cos(\theta_n)\\ \boldsymbol{\phi}\end{bmatrix} \tag{4.8}$$

for $n = 1,2,\ldots,N$. This is an under-determined system of Q equations, which has rank $Q-1$ (with $\phi_1 = 0$), and Q unknowns. When $N = 1$, it is possible to solve (4.8), if another sensor/channel's phase error is known in the array (say w.l.o.g. $\phi_2 = 0$ in addition to $\phi_1 = 0$). However, when $N \geq 2$, we can eliminate $\boldsymbol{\phi}$ by considering

$$\boldsymbol{\rho}_n - \boldsymbol{\rho}_1 = \mathbf{p}_{\text{ext}}\left[\cos(\theta_n) - \cos(\theta_1)\right],$$

to obtain $N-1$ linearly independent equations in N unknown DOAs of the form

$$\mathbf{p}_{\text{ext}}^{\dagger}\left(\boldsymbol{\rho}_n - \boldsymbol{\rho}_1\right) = \cos(\theta_n) - \cos(\theta_1); \quad n = 2,\cdots,N. \tag{4.9}$$

The system in (4.9) is still underdetermined. Nonetheless, if one of the DOAs is known (say w.l.o.g. θ_1 is known) then we can identify the remaining DOAs. This result for a scalar sensor array ($Q = M$) was presented in [19].

However, for an AVS array ($Q = 3M$), the need of knowing the direction of one calibrator source θ_1 can be relaxed as the direction information is available in the magnitude of the element-space data model. This is a novel observation that is not presented in the existing literature. It can be seen by explicitly considering only the magnitude of $\text{diag(g)}\mathbf{A}(\boldsymbol{\theta})$, resulting in

$$v_q(n) = \left|g_q\left[\mathbf{A}(\boldsymbol{\theta})\right]_{qn}\right| = \alpha_q\left|h_q(\theta_n)\right| \tag{4.10}$$

for $q = 1,\ldots,3M$. Here,

$$h_q(\theta_n) = \begin{cases}1, & 1 \leq q \leq M.\\ \cos(\theta_n), & M+1 \leq q \leq 2M.\\ \sin(\theta_n), & 2M+1 \leq q \leq 3M.\end{cases} \tag{4.11}$$

Let us consider the equations related to $q = M+1$, which are given by

$$v_{M+1}(n) = \alpha_{q+1}\cos(\theta_n).$$

If we assume $N \geq 2$, we can eliminate the unknown α_{q+1} to obtain

$$\cos(\theta_1) = \frac{v_{M+1}(1)}{v_{M+1}(n)}\cos(\theta_n).$$

Thus we can compute θ_1 as

$$\theta_1 = \arccos\left(\frac{v_{M+1}(n)}{v_{M+1}(n)}\cos(\theta_n)\right).$$

This value of θ_1 can be used in (4.9), which eliminates the need of knowing one of the DOAs for uniquely identifying all the N DOAs for the AVS linear array. The array manifold matrix $\mathbf{A}(\boldsymbol{\theta})$ is known once all the N DOAs are computed. Then using (4.7) and (4.10), respectively, the phase and gain errors can be computed.

Now to check if the derived sufficient condition for the APS linear array is also necessary, we need to show that the solution of $\mathbf{g}$ and $\boldsymbol{\theta}$ is not unique if we do not consider the calibrator source. To do so, assume an M-element APS array, and N far-field sources. For such configuration, due to the structure of $\mathbf{A}(\boldsymbol{\theta})$ and the nature of $\mathbf{g}$, we can have $\text{diag}(\mathbf{g})\mathbf{A}(\boldsymbol{\theta}) = \text{diag}(\mathbf{g}\odot\mathbf{a}(\theta_0))(\mathbf{A}(\boldsymbol{\theta})\odot\mathbf{a}^*(\theta_0)) = \text{diag}(\tilde{\mathbf{g}})\mathbf{A}(\tilde{\boldsymbol{\theta}})$, where generally $\mathbf{g}\neq\tilde{\mathbf{g}}$ and $\boldsymbol{\theta}\neq\tilde{\boldsymbol{\theta}}$ indicating the non-uniqueness of the solution.

In summary, with the element-space model for a linear APS array, irrespective of the array geometry, given $N\geq 2$ and $\text{diag}(\mathbf{g})\mathbf{A}(\boldsymbol{\theta})$, the requirement of a calibrator source is a sufficient and necessary condition for a unique solution of $\mathbf{g}$ and $\boldsymbol{\theta}$ to exist. In contrast, a calibrator source is not needed for a linear AVS array.

4

THE CO-ARRAY DATA MODEL

In contrast to the element-space formulation, there are many self-calibration approaches that are developed using the co-array model [13, 19, 20]. However, the conditions for the solution to exist are still not explored. So in this section, we derive the conditions using the co-array data model in (4.6) without any constraints on the array geometry. Next, we discuss sufficient conditions to estimate $\mathbf{g}$ and $\boldsymbol{\theta}$, given $\text{diag}(\mathbf{g}^*\otimes\mathbf{g})\mathbf{A}_{\text{co}}(\boldsymbol{\theta})$. To do so, consider the phase of $\text{diag}(\mathbf{g}^*\otimes\mathbf{g})\mathbf{A}_{\text{co}}(\boldsymbol{\theta})$ that is given by

$$\begin{aligned}\rho_{pq}(n) &= \frac{1}{2\pi}\text{angle}\left(g_p^* g_q\left([\mathbf{A}^*(\boldsymbol{\theta})]_{pn}\circ[\mathbf{A}(\boldsymbol{\theta})]_{qn}\right)\right)\\ &= (p_p-p_q)\cos(\theta_n)-(\phi_p-\phi_q),\end{aligned}\tag{4.12}$$

for $p,q=1,\cdots,Q$ with $p\neq q$ and $n=1,\cdots,N$.

If $N=1$, we require two sensors/channels with known phase errors. Suppose w.l.o.g. that $\phi_1=\phi_2=0$, then we can compute the DOA as

$$\theta_1=\arccos\left(\frac{\rho_{12}(1)}{p_1-p_2}\right),\tag{4.13}$$

with no specific requirements for $p_1\neq 0$ or $p_2\neq 0$. Defining $\boldsymbol{\rho}_n=[\rho_{11}(n),\rho_{12}(n),\ldots,\rho_{QQ}(n)]^T$, we can compactly write (4.12) as

$$\boldsymbol{\rho}_n=\mathbf{D}\mathbf{p}_{\text{ext}}\cos(\theta_n)-\mathbf{D}\boldsymbol{\phi}=\begin{bmatrix}\mathbf{D}\mathbf{p}_{\text{ext}} & -\mathbf{D}\end{bmatrix}\begin{bmatrix}\cos(\theta_n)\\ \boldsymbol{\phi}\end{bmatrix},\tag{4.14}$$

where $\mathbf{D}\in\mathbb{R}^{Q^2-Q}$ is the difference matrix that we use to compute the pairwise differences in (4.12). If $N\geq 2$, irrespective of the array geometry, the phase errors $\boldsymbol{\phi}$ can be eliminated by considering

$$\boldsymbol{\rho}_n-\boldsymbol{\rho}_1=\mathbf{D}\mathbf{p}_{\text{ext}}\left[\cos(\theta_n)-\cos(\theta_1)\right];\quad\forall n=2,\ldots,N,$$

which can be equivalently expressed as

$$\theta_n=\arccos\left(\left(\mathbf{D}\mathbf{p}_{\text{ext}}\right)^{\dagger}\left[\boldsymbol{\rho}_n-\boldsymbol{\rho}_1\right]+\cos(\theta_1)\right).\tag{4.15}$$

This is similar to the element-space version as seen in (4.9) and it is underdetermined. Nonetheless for APS linear arrays, similar to the element-space model, if one of the source DOAs is known (say w.l.o.g. θ_1 is known) then we can identify the remaining DOAs.

For an AVS array, similar to the element-space model, the magnitude of $\text{diag}(\mathbf{g}^* \otimes \mathbf{g})\mathbf{A}_{\text{co}}(\boldsymbol{\theta})$ also contains the direction information. Specifically,

$$\begin{aligned} \nu_{pq}(n) &= \left| g_p g_q \left([\mathbf{A}^*(\boldsymbol{\theta})]_{pn} \circ [\mathbf{A}(\boldsymbol{\theta})]_{qn} \right) \right|, \\ &= \psi_p \psi_q h_p(\theta_n) h_q(\theta_n) \end{aligned} \tag{4.16}$$

for $p, q = 1, \cdots, 3M$ and $n = 1, \ldots, N$, where we recall that $h_p(\theta_n)$ is as in (4.11). Consider w.l.o.g. the equation related to $p = M+1$ and $q = M+2$, i.e.,

$$\nu_{M+1\,M+2}(n) = \psi_{M+1}\psi_{M+2}\cos^2(\theta_n).$$

When $N \geq 2$, we can eliminate the unknown gain errors ψ_{M+1} and ψ_{M+2} in the above equation by computing

$$\cos(\theta_1) = \left[\frac{\nu_{M+1\,M+2}(1)}{\nu_{M+1\,M+2}(n)} \cos^2(\theta_n) \right]^{1/2},$$

which can now be used in (4.15) to compute the DOAs. Once the DOAs are computed, the phase errors can be computed from (4.14), with respect to one of the reference sensors/channels in the array as the rank of $\mathbf{D}$ is always $Q-1$. The gain errors can be computed from the amplitude relations in (4.16).

Thus it can be concluded that irrespective of the array geometry of the linear array with the co-array data model, it is sufficient to have one phase reference sensor and one (no) calibrator source for a linear APS (respectively, AVS) array, for uniquely estimating $\mathbf{g}$ *and* $\boldsymbol{\theta}$ *when* $N \geq 2$ *and* $\text{diag}(\mathbf{g}^* \otimes \mathbf{g})\mathbf{A}_{\text{co}}(\boldsymbol{\theta})$ *is given.*

Unlike for the element-space approach, the derived sufficient condition for the APS linear array using the co-array model is not necessary. This aspect is showcased in the subsequent discussion, with certain assumptions on the array geometry, where we will see that using the co-array model the solution of $\mathbf{g}$ and $\boldsymbol{\theta}$ can be unique even if we do not consider the calibrator source.

SPARSE APS ARRAY BASED ON CO-ARRAY DATA MODEL

In comparison to (4.8), which is an under-determined system, it can be observed that (4.14) is a tall system with (Q^2-Q) equations and $(Q+1)$ unknowns. APS linear arrays with a particular structure in the array geometry, such as specific sparse arrays or uniform linear arrays (ULAs) result in redundant relations that are part of (4.14). Those redundancies in the structured APS linear array allow for estimating $\mathbf{g}$ and subsequently $\boldsymbol{\theta}$ without the knowledge of a known calibrator source leading to another set of sufficient conditions. This is discussed in the following part.

From the co-array perspective of scalar sensor arrays, the distinct elements of $\mathbf{D}\mathbf{p}_{\text{ext}}$, as seen in (4.14), behave like virtual sensor locations given by the difference set $\{p_i - p_j, 1 \leq i, j \leq M\}$. Those virtual sensor locations increase the degrees-of-freedom (DOF) of the array allowing for estimating more sources than physical sensors, if they are placed strategically. In order to look at the self-calibration problem for such array configurations, let us reuse some definitions from [11].

Definition 1. ***(Difference co-array)*** *For an M-element sensor array, with p_i denoting the position of the ith sensor, define the set*

$$\mathscr{D} = \{p_i - p_j\},\ \forall i, j = 1, 2, \ldots, M,$$

which allows for a repetition of its elements. We also define the set $\mathscr{D}_{\mathscr{U}}$, which consists of the distinct elements of the set $\mathscr{D}$. Then, the difference co-array of the given array is defined as the array which has sensors located at positions given by the set $\mathscr{D}_{\mathscr{U}}$.

Definition 2. ***(Weight function)*** *An integer valued weight function $w : \mathscr{D}_{\mathscr{U}} \rightarrow \mathbb{N}^+$ is defined as*

$$w(p) = \textit{no. of occurances of } p \textit{ in} \mathscr{D},\ p \in \mathscr{D}_{\mathscr{U}},$$

where $\mathbb{N}^+$ is the set of positive integers. The weight function $w(p)$ denotes the number of times p occurs in $\mathscr{D}$.

The cardinality of the set $\mathscr{D}_{\mathscr{U}}$ for a given array gives the degrees of freedom (DOF) that can be obtained from the difference co-array associated with that array. The motivation of sparse array design, such as the minimum redundancy array (MRA), sparse ruler array or nested array, is to maximize the number of DOF of the co-array for a fixed M, which in other words means the value of the weight function $w(p), \forall p \in \mathscr{D}_{\mathscr{U}} \setminus \{0\}$ has to be minimized. However, from the self-calibration perspective, a value of the weight function $w(p), \forall p \in \mathscr{D}_{\mathscr{U}} \setminus \{0\}$ greater than 1 is beneficial as this results in redundancies in (4.14). By exploiting redundancies in those relations for the nth source and each p, the directional terms can be eliminated resulting in an equation with only phase terms, i.e.,

$$\rho_{pq}(n) - \rho_{kl}(n) = \rho_{pqkl}(n) = \phi_p - \phi_q - \phi_k + \phi_l, \tag{4.17}$$

where $p_p - p_q = p_k - p_l$ for $p, q, k, l = 1, \ldots, M$ and $n = 1, \ldots, N$. Such relations for all p, q, k, l can be expressed as a system of equations, i.e.,

$$\begin{bmatrix} \ldots & \rho_{pqkl}(n) & \ldots \end{bmatrix}^T = \mathbf{T} \begin{bmatrix} \phi_1 & \ldots & \phi_M \end{bmatrix}^T, \tag{4.18}$$

where $\mathbf{T}$ is a deterministic matrix, which depends on the chosen array geometry and the phase errors can be estimated by inverting it. The maximum amount of redundancies can be found in a uniform linear array (ULA), where for M elements, $w(\pm d) = M - d$, for $d = 0, 1, \ldots, M-1$. The rank of $\mathbf{T}$ is then always $M-2$, indicating that the phase errors can be estimated with respect to an arbitrary reference and within an arbitrary progressive phase factor [13, 17]. We now look into the rank of the $\mathbf{T}$ matrix for different structured sparse linear arrays and summarize how the phase errors can be estimated for each of those scenarios,

- To design an M-element sparse array, taking self calibration into consideration, there is a trade-off between DOF and redundancies. The maximum rank of $\mathbf{T}$ for an M-element APS array is upper bounded by $M-2$. The rank of $\mathbf{T}$ for structured sparse arrays including the nested array [11] and super nested array [36] is always $M-3$, whereas for the co-prime arrays [12], which enjoy more redundancies, it is $M-2$.

- If there is a provision to introduce additional sensors within a sparse array to allow for sufficient redundancies, then the rank of $\mathbf{T}$ can be increased to $M-2$. For example,

for an MRA [10], with $M = 5$ and $\mathbf{p} = [0,1,4,7,9]^T$, the rank of $\mathbf{T}$ is 1. However, if we introduce two phase reference sensors with $\mathbf{p} = [0,1,\mathbf{2},\mathbf{3},4,7,9]^T$, then the rank of $\mathbf{T}$ is 5.

On the other hand, the gain errors can be estimated by considering the redundancies in the amplitude relations of $\text{diag}(\mathbf{g}^* \otimes \mathbf{g})\mathbf{A}_{\text{co}}(\boldsymbol{\theta})$. Irrespective of the array geometry, the rank of the equivalent $\mathbf{T}$ matrix obtained by considering $|\text{diag}(\mathbf{g}^* \otimes \mathbf{g})\mathbf{A}_{\text{co}}(\boldsymbol{\theta})|$ is always $M-1$, indicating that the gain errors can be estimated with respect to the chosen reference sensor.

Using redundancies present in the co-array data model of an APS array with $N \geq 1$ and $\text{diag}(\mathbf{g}^* \otimes \mathbf{g})\mathbf{A}_{\text{co}}(\boldsymbol{\theta})$ is given, we can conclude that for a ULA, with two phase reference sensors in the array, while for sparse arrays, with at least two or more phase reference sensors in the array, it is also possible for uniquely estimating the calibration errors and source DOAs.

4

4.4. SELF CALIBRATION WITH THE ELEMENT-SPACE MODEL

In this section, we focus on estimating the complex-valued receiver gains and the source DOAs, when only a few snapshots are available. In such cases, the sample data covariance matrix will be a very poor estimate of $\mathbf{R}_x$ and hence we focus on the element-space data model. The algorithms provided in this section, do not make any assumptions on the array geometry or on the structure of the covariance matrix $\mathbf{R}_x$.

Assuming that the true directions are from a uniform grid of $D \gg N$ points, i.e., assuming that $\theta_n \in \left\{0, \frac{\pi}{D} \cdots, \frac{\pi(D-1)}{D}\right\}$, for $n = 1,2,\ldots,N$, we can approximate (4.1) as

$$\mathbf{x}(t) = \text{diag}(\mathbf{g})[\mathbf{A}_{\mathbb{D}}\,\mathbf{z}(t) + \mathbf{n}(t)], \tag{4.19}$$

where $\mathbf{A}_{\mathbb{D}}$ is a $Q \times D$ dictionary matrix with column vectors of the form $\mathbf{a}(\bar{\theta}_d)$, where $\bar{\theta}_d$ is the dth point of the uniform grid of directions, i.e., $\bar{\theta}_d = \frac{\pi d}{D}$, $d = 0,1,\ldots,D-1$, and $\mathbf{z}(t)$ is a length-Q vector containing the source signal related to the corresponding discretized directions. We emphasize here that finding the columns of $\mathbf{A}_{\mathbb{D}}$ that correspond to non-zero elements of $\mathbf{z}(t)$ amounts to finding the DOAs. As seen in (4.19), by assuming that the source DOAs lie on a pre-defined uniform grid, we transform a non-linear estimation problem into a bilinear estimation problem with $\mathbf{c}$ and $\mathbf{z}(t)$ being the unknowns (from which we can derive $\mathbf{g}$ and $\boldsymbol{\theta}$, respectively).

Defining the calibration matrix $\text{diag}(\mathbf{c}) = \text{diag}^{-1}(\mathbf{g})$, we can express the "calibrated" signal $\mathbf{y}(t)$ as

$$\mathbf{y}(t) = \text{diag}(\mathbf{c})\mathbf{x}(t) = \text{diag}(\mathbf{x}(t))\mathbf{c} = \mathbf{A}_{\mathbb{D}}\mathbf{z}(t) + \mathbf{n}(t). \tag{4.20}$$

Exploiting the nature of the calibration errors, which combined with simple algebraic manipulation, the bilinear estimation problem in (4.19) is further transformed into a linear estimation problem in (4.20). Leveraging the fact that the calibration parameters remain unchanged during an observation window where we collect L snapshots, we can obtain more equations, i.e.,

$$\underbrace{\left[\begin{array}{c|ccc} \text{diag}(\mathbf{x}(1)) & -\mathbf{A}_{\mathbb{D}} & & \\ \vdots & & \ddots & \\ \text{diag}(\mathbf{x}(L)) & & & -\mathbf{A}_{\mathbb{D}} \end{array}\right]}_{\mathbf{G}} \underbrace{\left[\begin{array}{c} \mathbf{c} \\ \hline \mathbf{z} \end{array}\right]}_{\boldsymbol{\gamma}} = \underbrace{\left[\begin{array}{c} \mathbf{n}(1) \\ \vdots \\ \mathbf{n}(L) \end{array}\right]}_{\mathbf{n}}, \tag{4.21}$$

where $\mathbf{z} = \text{vec}(\mathbf{Z}) \in \mathbb{C}^{DL}$ with $\mathbf{Z} = [\mathbf{z}(1), \mathbf{z}(2), \cdots, \mathbf{z}(L)] = [\mathbf{z}_1, \mathbf{z}_2, \ldots, \mathbf{z}_D]^T$. Here, $\mathbf{z}(l) \in \mathbb{C}^D$ and $\mathbf{z}_d \in \mathbb{C}^L$.

Although at the outset, it seems as if there are $Q + DL$ unknowns in (4.21), the vector $\mathbf{z}$ is structured. Specifically, the vectors $\mathbf{z}(l)$, $l = 1, \ldots, L$ are sparse, and more importantly, they have the *same* sparsity pattern with the indices of the nonzero pattern indicating the source directions. The prior knowledge of having sparsity along the spatial domain can be incorporated by initially considering the l_2 norm of all the time samples corresponding to a particular spatial index of $\mathbf{Z}$, i.e., by defining $z_d^{(\ell_2)} = \|\mathbf{z}_d\|_2$ for $d = 1, 2, \ldots, D$, and then by using the sparsity promoting l_1 norm penalty on the vector $\mathbf{z}^{(\ell_2)} = \left[z_1^{(\ell_2)}, z_2^{(\ell_2)}, \ldots, z_D^{(\ell_2)}\right]^T$ as $f(\mathbf{z}) = \|\mathbf{z}^{(l_2)}\|_{\ell_1} = \sum_{d=1}^{D} z_d^{(\ell_2)}$.

The optimization problem to jointly estimate the calibration parameters and DOAs with a sparsity constraint along the spatial domain of the matrix $\mathbf{Z}$ can then be expressed as:

$$\min_{\mathbf{c},\mathbf{z}} \quad \|\mathbf{G}\boldsymbol{\gamma}\|_2^2 + \eta f(\mathbf{z}) \quad \text{s.t.} \quad (\mathbf{c}, \mathbf{z}) \in \mathscr{C} \tag{4.22}$$

where $\boldsymbol{\gamma} = [\mathbf{c}^T \, \mathbf{z}^T]^T$ and η is the regularization parameter that allows for a trade off between the goodness of fit of the solution to the given data and the sparsity prior on $\mathbf{z}$. The constraint set for APS arrays is $\mathscr{C} := \{(\mathbf{c}, \mathbf{z}) \mid c_1 = 1, \mathbf{z}_1 = 1\}$ while for AVS arrays it is $\mathscr{C} := \{(\mathbf{c}, \mathbf{z}) \mid c_1 = 1\}$. Recall that for APS arrays, we need one reference sensor and we need to know one of the DOAs to avoid ambiguities. This is done by setting $c_1 = 1$ and $\mathbf{z}_1 = 1$, which is equivalent to having a calibrator source at $\bar{\theta}_1$ (w.l.o.g.). Since for AVS arrays, we do not need any calibrator source, we only need a reference sensor in that case. The optimization problem (4.22) is a convex optimization problem, which can be solved using any off-the-shelf solver. For large L, if the number of sources can be estimated, the complexity of the formulation in (4.22) can be reduced by using the ℓ_1-SVD technique [8] on the measurement data matrix $\mathbf{X}$. Furthermore, for the choice of the regularization parameter η, we follow the discrepancy principle discussed in [8].

Remark 1. *In contrast to the considered measurement model, the calibration errors affect only the signal component of the data, when the errors originate due to the perturbation of the sensors, gain and phase patterns or due to the position or orientation errors of the sensors in the array [34, 37]. In such case,* (4.1) *and* (4.20) *can be modified, respectively as,*

$$\mathbf{x}(t) = \text{diag}(\mathbf{g})\mathbf{A}(\boldsymbol{\theta})\mathbf{s}(t) + \mathbf{n}(t).$$

$$\mathbf{y}(t) = \text{diag}(\mathbf{c})\mathbf{x}(t) = \text{diag}(\mathbf{x}(t))\mathbf{c} = \mathbf{A}_{\mathbb{D}}\mathbf{z}(t) + \text{diag}(\mathbf{c})\mathbf{n}(t).$$

The proposed calibration approach in (4.22) *is still applicable here with the additive noise term being modified as* $\hat{\mathbf{n}}(t) = \text{diag}(\mathbf{c})\mathbf{n}(t)$.

4.5. SELF CALIBRATION WITH THE CO-ARRAY DATA MODEL

In this approach both the calibration errors and the source DOAs will be estimated jointly based on the covariance matrix of the measurement data. Similar to (4.19), the directions are assumed to be on a uniform grid of $D \gg N$ points. Then (4.6) can be approximated as

$$\mathbf{r}_{\text{x}} = \text{diag}(\mathbf{g}^* \otimes \mathbf{g})[\mathbf{A}_{\text{co}\mathbb{D}}\boldsymbol{\sigma}_{\text{z}} + \boldsymbol{\sigma}_{\text{n}}], \tag{4.23}$$

where $\mathbf{A}_{\text{co}\mathbb{D}}$ is a $Q^2 \times D$ dictionary matrix that consists of column vectors of the form $\mathbf{a}^*(\bar{\theta}_d) \otimes \mathbf{a}(\bar{\theta}_d)$, with $\bar{\theta}_d$ as defined before. Again similar to (4.20), defining the calibration matrix $\text{diag}(\mathbf{c}^* \otimes \mathbf{c}) = \text{diag}^{-1}(\mathbf{g}^* \otimes \mathbf{g})$, we can express (4.23) as

$$\text{diag}(\mathbf{c}^* \otimes \mathbf{c})\mathbf{r}_{\text{x}} = \text{diag}(\mathbf{r}_{\text{x}})(\mathbf{c}^* \otimes \mathbf{c}) = \mathbf{A}_{\text{co}}(\boldsymbol{\theta})\boldsymbol{\sigma}_{\text{s}} + \boldsymbol{\sigma}_{\text{n}}. \tag{4.24}$$

Since $(\mathbf{c}^* \otimes \mathbf{c}) = \text{vec}(\mathbf{C})$, with $\mathbf{C} = \mathbf{c}\mathbf{c}^H$, (4.23) can be compactly rewritten as

$$\underbrace{\begin{bmatrix}\text{diag}(\mathbf{r}_{\text{x}}) & -\mathbf{A}_{\text{co}\mathbb{D}}\end{bmatrix}}_{\mathbf{G}_{\text{co}}} \underbrace{\begin{bmatrix}\text{vec}(\mathbf{C}) \\ \boldsymbol{\sigma}_{\text{z}}\end{bmatrix}}_{\boldsymbol{\gamma}_{\text{co}}} = \boldsymbol{\sigma}_{\text{n}}. \tag{4.25}$$

Similar to the element-space formulation, we have transformed the non-linear estimation problem in (4.6) to a linear estimation problem in (4.25). The above system is underdetermined with $Q^2 + D$ unknowns in Q^2 equations (note that some equations might even be redundant). However, as $\text{vec}(\mathbf{C})$ has a Kronecker structure, the actual number of unknowns reduces to Q and $\boldsymbol{\sigma}_{\text{z}}$ is a sparse vector with non-zero elements at the location of the source DOAs. By considering the aforementioned constraints on the calibration errors and source DOAs, the estimation problem can be cast as

$$\min_{\mathbf{C},\boldsymbol{\sigma}_{\text{z}}} \quad \|\mathbf{G}_{\text{co}}\boldsymbol{\gamma}_{\text{co}} - \boldsymbol{\sigma}_{\text{n}}\|_2^2 + \eta\|\boldsymbol{\sigma}_{\text{z}}\|_0 \quad \text{s.t.} \quad (\mathbf{C}, \boldsymbol{\sigma}_{\text{z}}) \in \mathscr{C}_{\text{co}} \tag{4.26}$$

where $\boldsymbol{\gamma}_{\text{co}} = [\text{vec}^T(\mathbf{C}), \boldsymbol{\sigma}_{\text{z}}^T]^T$, η is the regularization parameter, for $N \geq 2$ the constraint set $\mathscr{C}_{\text{co}} = \{(\mathbf{C}, \boldsymbol{\sigma}_{\text{z}}) \,|\, \boldsymbol{\sigma}_{\text{z}} \succeq \mathbf{0}, \mathbf{C} = \mathbf{c}\mathbf{c}^H, c_1 = 1, \boldsymbol{\sigma}_{\text{z}}(1) = 1\}$ for APS arrays and $\mathscr{C}_{\text{co}} = \{(\mathbf{C}, \boldsymbol{\sigma}_{\text{z}}) \,|\, \boldsymbol{\sigma}_{\text{z}} \succeq \mathbf{0}, \mathbf{C} = \mathbf{c}\mathbf{c}^H, c_1 = 1\}$ for AVS arrays. For APS arrays, the requirement of knowing one of the DOAs is expressed as $\boldsymbol{\sigma}_{\text{z}}(1) = 1$ (w.l.o.g.). Further for APS ULAs and some APS sparse arrays, the redundancies in the co-array measurements can be used for the estimation of the source DOAs and the calibration errors with two phase reference sensors in the array. In such cases the constraint set even with $N \geq 1$ is $\mathscr{C}_{\text{co}} = \{(\mathbf{C}, \boldsymbol{\sigma}_{\text{z}}) \,|\, \boldsymbol{\sigma}_{\text{z}} \succeq \mathbf{0}, \mathbf{C} = \mathbf{c}\mathbf{c}^H, c_1 = c_2 = 1\}$. The optimization problem in (4.26) is non-convex due to the l_0 norm (cardinality) constraint and the rank-one equality constraint on $\mathbf{C}$. We can relax (4.26) by replacing the cardinality constraint with its convex approximation $\|\boldsymbol{\sigma}_{\text{z}}\|_1$ and by replacing the rank-one equality constraint (i.e., $\mathbf{C} = \mathbf{c}\mathbf{c}^H$) in the set $\mathscr{C}_{\text{co}}$ with a convex inequality constraint (i.e., $\mathbf{C} \succeq \mathbf{c}\mathbf{c}^H$). The new set which is same as $\mathscr{C}_{\text{co}}$ except for the rank-one convex inequality constraint is denoted as $\tilde{\mathscr{C}}_{\text{co}}$. The relaxed optimization problem can be expressed as,

$$\min_{\mathbf{C},\boldsymbol{\sigma}_{\text{z}}} \quad \|\mathbf{G}_{\text{co}}\boldsymbol{\gamma}_{\text{co}} - \boldsymbol{\sigma}_{\text{n}}\|_2^2 + \eta\|\boldsymbol{\sigma}_{\text{z}}\|_1 \quad \text{s.t.} \quad (\mathbf{C}, \boldsymbol{\sigma}_{\text{z}}) \in \tilde{\mathscr{C}}_{\text{co}}. \tag{4.27}$$

The convex inequality constraint, $\mathbf{C} \succeq \mathbf{c}\mathbf{c}^H$, is equivalent to $\begin{bmatrix}\mathbf{C} & \mathbf{c} \\ \mathbf{c}^H & 1\end{bmatrix} \succeq 0$ from Schur's lemma. The resulting problem is a semi-definite programming problem that can be solved with any off-the-shelf solver. For the choice of the regularization parameter η, we can use any standard method adopted in sparse signal recovery [38]. In practice, for the finite snapshot scenario, $\mathbf{C}$ obtained after solving (4.27) might not be rank one and the closest estimates of the calibration parameters can be obtained from the first dominant singular vector of $\mathbf{C}$. The formulation in (4.27) is also applicable to sparse arrays for estimating DOAs (when there are more sources than sensors) and calibration parameters jointly as presented in [35].

Remark 2. *If calibration errors affect only the signal component of the data, then* (4.6) *can be modified as*

$$\mathbf{r}_x = \text{diag}(\mathbf{g}^* \otimes \mathbf{g})\mathbf{A}_{co}(\boldsymbol{\theta})\boldsymbol{\sigma}_s + \boldsymbol{\sigma}_n.$$

The proposed calibration approach in (4.27) *is still applicable here with a slight modification. More specifically,* (4.25) *and* (4.26) *can then be modified, respectively as,*

$$\underbrace{\begin{bmatrix}\text{diag}(\mathbf{r}_x - \boldsymbol{\sigma}_n) & -\mathbf{A}_{co\mathbb{D}}\end{bmatrix}}_{\mathbf{G}_{co}} \underbrace{\begin{bmatrix}\text{vec}(\mathbf{C}) \\ \boldsymbol{\sigma}_z\end{bmatrix}}_{\gamma_{co}} = 0,$$

$$\min_{\mathbf{C},\boldsymbol{\sigma}_z} \quad \|\mathbf{G}_{co}\gamma_{co}\|_2^2 + \eta\|\boldsymbol{\sigma}_z\|_0 \quad \text{s.t.} \quad (\mathbf{C}, \boldsymbol{\sigma}_z) \in \mathscr{C}_{co}.$$

Before ending this section, we remark that the proposed algorithms in Section 4.4 and Section 4.5 are also useful for non-linear arrays using the identifiability conditions provided as a remark at the end of Section 4.3.

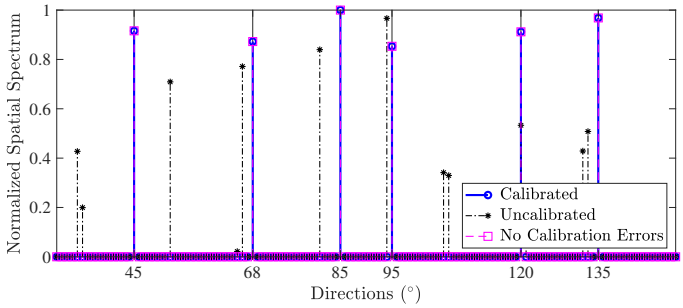
4.6. NUMERICAL EXPERIMENTS

In this section, we present numerical simulations to illustrate the performance of all the proposed solvers for the joint estimation of the source DOAs and calibration parameters. Firstly we consider the element-space model based solver in (4.22) only for AVS linear arrays. Recall that AVS arrays do not require the presence of a reference source (see Section 4.3). Then the covariance model in (4.27) is considered for both the APS and AVS linear array. Finally, we analyze the root mean square error (RMSE) of the DOA estimates obtained from the presented algorithms and compare them with existing calibration methods. The RMSE results for scenarios with more sensors than sources are also compared with the Cramér-Rao lower bound (CRLB) on the DOA estimates.

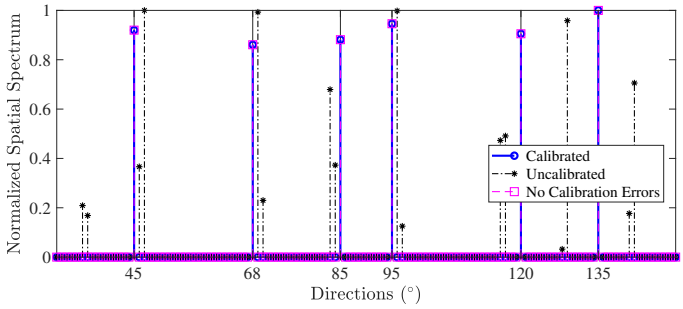
4.6.1. ELEMENT-SPACE MODEL

We consider a scenario with $M = 8$ AVSs arranged in a uniform linear array (ULA) configuration where the spacing between the consecutive sensors is half a wavelength of the considered narrowband source signals. Further, we consider a scenario with $N = 6$ narrowband far-field signals impinging on the array from distinct DOAs with an observation period consisting of $L = 50$ snapshots. The grid is chosen to be uniform between $[0^\circ\ 180^\circ]$ with 1° resolution. Without loss of generality, we assume the first channel of the first AVS in the array as the reference channel whose gain is 1 and phase is 0°. The gain and phase errors are chosen from a uniform distribution over the interval [-3; 3] dB and $[-20^\circ; 20^\circ]$, respectively.

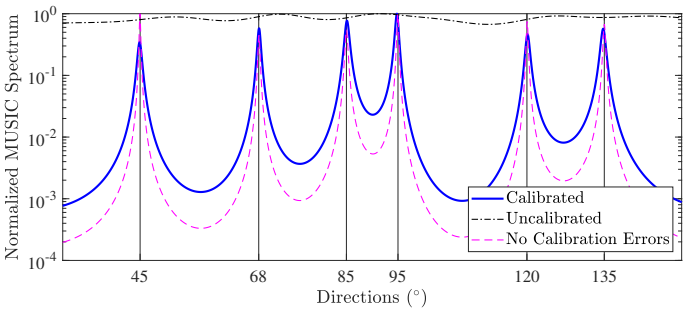
Based on the optimization problem in (4.22), the results of DOA estimation post calibration are presented in Fig. 4.1. In order to verify the correctness of the formulation in (4.22), we initially considered an ideal scenario without measurement noise. The DOA spectra based on (4.22) are presented in Fig. 4.1(a). It is seen in Fig. 4.1(a), that we recover the exact source DOAs after solving (4.22), where as for the uncalibrated data, the source DOA estimates based on the l_1-SVD algorithm [8] are very poor. Further, we considered the measurement data with a signal-to-noise ratio (SNR) of 10 dB and the corresponding DOA spectra



(a) l_1-SVD spectra without measurement noise.



(b) l_1-SVD spectra with SNR = 10 dB.



(c) MUSIC spectra with an SNR = 10 dB.

Figure 4.1: The l_1-SVD and MUSIC spectra using the element-space data model based solver in (4.22) for an AVS ULA with $M = 8$, $N = 6$ and $L = 50$. The true DOAs are indicated by the black solid lines.

obtained from solving (4.22) are presented in Fig. 4.1(b), where we draw a similar inference as in Fig. 4.1(a).

On the other hand, the issues of a pre-defined grid on the DOA estimates obtained after solving (4.22) can be minimized by applying the MUSIC algorithm on the gain and phase compensated covariance matrix. The gain and phase errors are estimated from (4.22), and the corresponding MUSIC spectra are presented in Fig. 4.1(c). It can be inferred that for the measurement data with an SNR of 10 dB, MUSIC with the uncalibrated data results in poor estimates, whereas the DOA estimates after calibration in Fig. 4.1(c) provides similar results as in Fig. 4.1(b). The two-step procedure to obtain DOA estimates from MUSIC spectrum significantly improves results when the sources do not lie on a pre-defined grid.

4.6.2. CO-ARRAY DATA MODEL

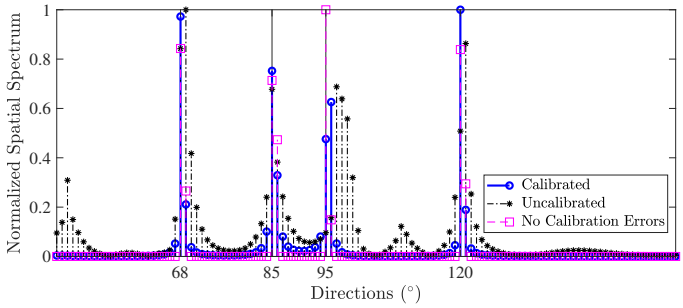
To illustrate the effectiveness of the covariance domain formulation provided in (4.27), we consider both a conventional ULA with less sources than sensors and a sparse linear array with more sources than sensors, where the smallest spacing between the consecutive sensors is half a wavelength of the considered narrowband source signals. Here, all the far-field source DOAs are chosen to be on the grid. In both the scenarios, without loss of generality, for the APS arrays we considered the first two sensors as references whereas for the AVS arrays the first channel is considered as a reference with gain of 1 and phase of 0°.

ULA WITH LESS SOURCES THAN SENSORS

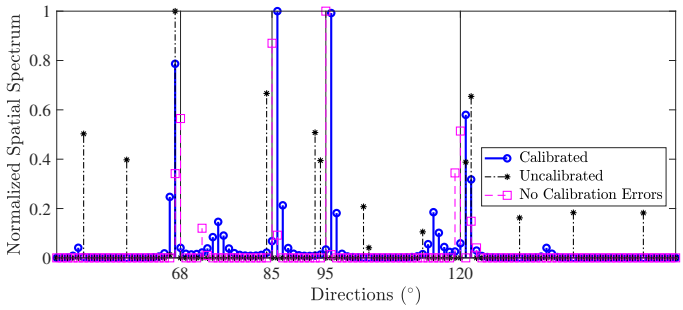
Consider a ULA with $M = 8$, $N = 4$ far-field sources and SNR = 10 dB. Firstly, we consider a finite sample scenario with the observation period consisting of $L = 1000$ snapshots whose l_1 norm based DOA spectra upon solving (4.27) are plotted in Fig. 4.2(a) for the APS ULA and in Fig. 4.2(b) for the AVS ULA. The uncalibrated data in all the plots results in low resolution DOA spectra and very poor DOA estimates. In Fig. 4.2(a), the DOA spectra upon solving (4.27) show an improvement compared to the DOA spectra computed with the uncalibrated data. However, the resulting DOA spectra still have low resolution, as the model considered in (4.27) is not exact due to the finite sample approximation of the covariance matrix estimation. On the other hand, in Fig. 4.2(b), the DOA spectra based on (4.27) are significantly superior with high resolution compared to the DOA spectra computed with the uncalibrated data. However upon closer observation, we can notice that the DOA estimates are slightly biased for a couple of sources and also there are some spurious peaks in the DOA spectra. It is observed that the model mismatches due to the finite sample approximation of the covariance matrix estimation, has higher impact on reducing the sparsity of the DOA spectra for the APS ULA in comparison to an equivalent AVS ULA.

In order to overcome the discussed issues with DOA estimates and the effects of a pre-defined grid, similar to the element-space approach, a grid-free approach such as MUSIC algorithm can be applied on the measurement data in (6.2), which is compensated for the gain and phase errors obtained from (4.27). Those MUSIC spectra based on the calibrated data are presented in Fig. 4.3. The results in Fig. 4.3(b) for the AVS ULA is compared with [19] (referred to as Weiss-Friedlander approach). The results in Fig. 4.3(a) for the APS ULA is compared with [13] (referred to as the Paulraj-Kailath approach[2]), as the Weiss-Friedlander approach is not effective for linear scalar sensor arrays.

[2] During the submission of this manuscript it came to the authors' attention that an improved version of [13] for scalar sensor arrays that considers an optimally-weighted least squares (OWLS) approach was proposed in [27].



(a) APS ULA.



(b) AVS ULA.

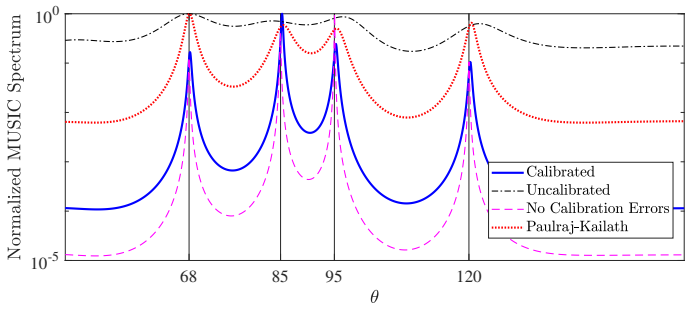
Figure 4.2: The l_1 norm based DOA spectra for both the APS and AVS ULA based on the co-array data model solver in (4.27) with $L = 1000$, SNR = 10 dB, $M = 8$ and $N = 4$ far-field sources. The true DOAs are indicated by the black solid lines.

In Figs. 4.3(a) and (b), we see that the MUSIC spectra have a higher resolution and improved estimates compared to the equivalent l_1 norm based DOA spectra. On contrary, the spectra based on the uncalibrated data is not able to resolve all the sources and the resolution of the spectra is also degraded. Further, for the APS ULA in Fig. 4.3(a), the proposed approach outperforms [13], and for the AVS ULA in Fig. 4.3(b), it can be observed that although [19] results in a sharper peaks compared to the proposed approach, the estimates are highly biased.

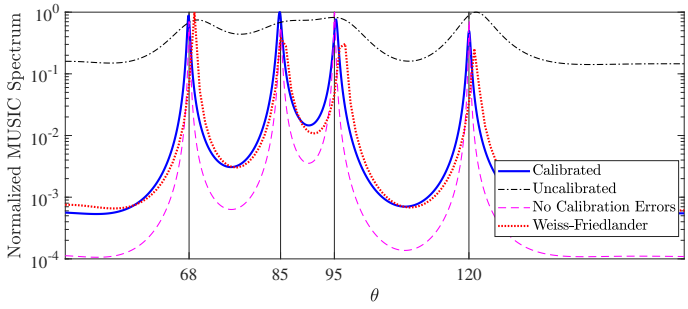
It can be summarized that based on the formulation in (4.27), it is possible to jointly estimate both the calibration errors as well as the source DOAs and the estimation results are good when the number of time snapshots are higher and the grid-mismatches are minimal. However, when the number of time snapshots are limited and we have a pre-defined grid, solving (4.27) can be used as a pre-conditioning step to estimate the calibration errors. Then a grid-free approach such as MUSIC can be applied on the gain and phase errors compensated measurement data to obtain improved and reliable DOA estimates.

SPARSE ARRAY WITH MORE SOURCES THAN SENSORS

Consider a hole-free sparse linear array with $M = 6$, $\mathbf{p} = [0\,1\,2\,3\,6\,9]^T$, $N = 8$ far-field sources and SNR = 10 dB. The rank of the $\mathbf{T}$ matrix [cf. (4.18)] for the considered sparse array is 4 (i.e., $M-2$). For this scenario, we present spatial smoothing MUSIC (SS MUSIC) spectra [11]



(a) APS ULA.



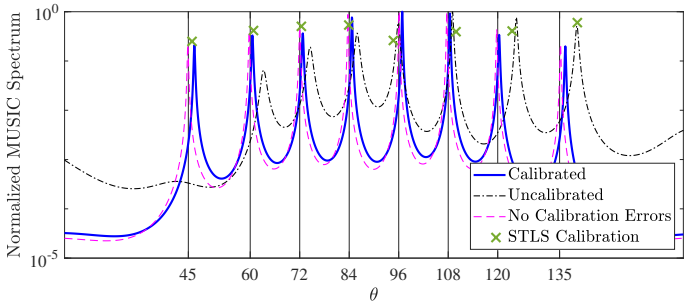
(b) AVS ULA.

Figure 4.3: The MUSIC spectra for both the APS and AVS ULA based on the co-array data model solver in (4.27) with $L = 1000$, SNR = 10 dB, $M = 8$ and $N = 4$ far-field sources. The true DOAs are indicated by the black solid lines.

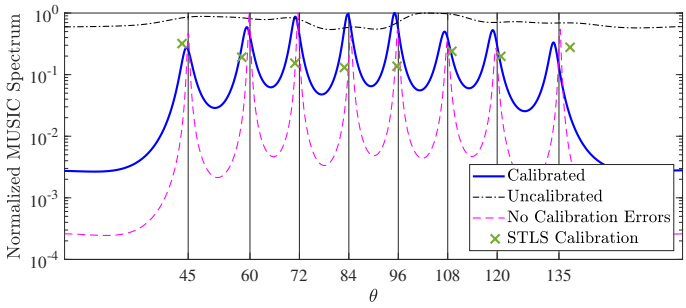
based on the gain and phase compensated measurement data, where the calibration errors are estimated by evaluating the proposed formulation in (4.27). We consider a finite sample scenario with the observation period consisting of $L = 500$ snapshots whose SS MUSIC spectra are shown in Fig. 4.4(a) for the APS array and Fig. 4.4(b) for the AVS array. The results of SS MUSIC for both the APS and AVS array are compared with the sparse total least squares (STLS) calibration approach [29].

In both Figs. 4.4(a) and (b), we see that post calibration, the SS MUSIC spectra have a higher resolution and are comparable to the scenario with no calibration errors, whereas the spectra based on the uncalibrated data are not able to resolve all the sources and the resolution of the spectra is also degraded. Furthermore, for both the APS and AVS sparse array with 500 snapshots, the performance of our proposed method is better than the STLS calibration approach [29].

The simulation setup for the AVS sparse linear array considered in Fig. 4.4(b), consists of less sources ($N = 8$) than the number of channels of the AVS array, ($3M = 18$). The proposed calibration approach in (4.27) is still applicable to an AVS sparse linear array with more sources than channels. However, because of the aperture limitation, when many sources are closely spaced it will be hard to discriminate them. To solve this issue, we can further boost the aperture by spatially undersampling the AVS array as in [39]. Such a setup is considered in Fig. 4.5, where the aperture is doubled and the smallest spacing between consecutive sensors is unit wavelength (instead of half a wavelength) of the considered narrowband source



(a) APS sparse array.



(b) AVS sparse array.

Figure 4.4: The spatial smoothing MUSIC (SS MUSIC) spectra for both the APS and AVS sparse linear array based on the co-array data model solver in (4.27) with $L = 500$, SNR = 10 dB, $M = 6$, $\mathbf{p} = [0\,1\,2\,3\,6\,9]^T$ and $N = 8$ far-field sources. The true DOAs are indicated by the black solid lines.

signals. The SS-MUSIC spectra for an ideal scenario with $M = 6$, $N = 19$ ($> 3M$), SNR = 10 dB and $L = \infty$ are shown. Similar inferences as from Fig. 4.4(b), can be made in Fig. 4.5, which

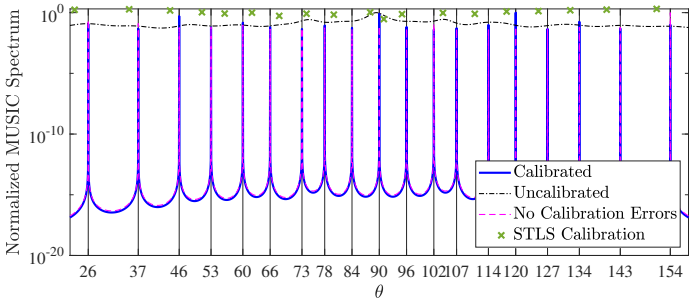


Figure 4.5: The spatial smoothing MUSIC (SS MUSIC) spectra for the AVS sparse linear array based on the co-array data model solver in (4.27) with $M = 6$, $\mathbf{p} = [0\,1\,2\,3\,6\,9]^T$ (with smallest inter-sensor spacing equals to λ of the considered narrowband source signals), SNR = 10 dB, $L = \infty$ and $N = 19$ far-field sources. The true DOAs are indicated by the black solid lines.

showcases the applicability of the proposed calibration approach in (4.27) with a spatially

undersampled AVS array with more sources than channels.

4.6.3. MONTE-CARLO EXPERIMENTS

In this section we study the statistical behavior through the root mean square error (RMSE) of the DOA estimator based on the proposed calibration procedure for different scenarios. We consider both AVSs and APSs arranged in a ULA and sparse linear array configurations.

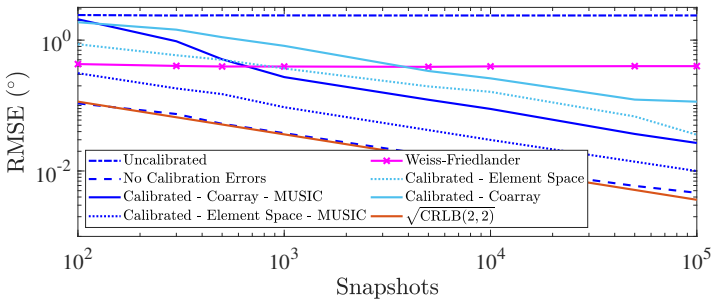
UNIFORM LINEAR ARRAY WITH LESS SOURCES THAN SENSORS

Firstly, we consider $M = 8$ sensors arranged in a ULA configuration and three far-field sources, i.e., $N = 3$ with $\boldsymbol{\theta} = [78°, 90°, 102°]$. The gain and phase perturbations follow a uniform distribution over the interval of [-2, 2] dB and $[-40°, 40°]$, respectively. For both the element-space formulation (4.22) and covariance domain formulation (4.27), we have chosen the pre-defined grid between 0° and 180° with 1° resolution. The RMSE of the DOA estimates based on the l_1 norm spectra (either by solving (4.22) or (4.27)) as well as the MUSIC spectra are presented for the considered scenarios.

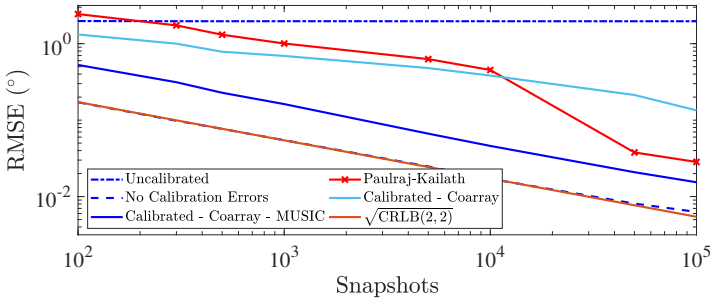
Fixed SNR and varying snapshots The RMSE of the DOA estimates for the source present at 90° based on 500 Monte-Carlo trials for both the APS and AVS ULA are presented in Fig. 4.6. Here the calibration errors and SNR of 10 dB were fixed for all the trails while the number of snapshots are varying. The RMSE of the DOA estimates in Fig. 4.6 based on the l_1 norm spectra by solving (4.22) is referred to as “Calibrated - Element Space" and by solving (4.27) is referred to as “Calibrated - Coarray". Further, the RMSE in the DOA estimates in Fig. 4.6 based on the MUSIC spectra by solving (4.22) is referred to as “Calibrated - Element Space - MUSIC" and by solving (4.27) is referred to as “Calibrated - Coarray - MUSIC".

In Fig. 4.6(a), we considered the AVS ULA with an SNR of 10 dB. It is seen that as the number of snapshots increases, the RMSE of the DOA estimates for the uncalibrated case does not decrease, whereas after calibration based on both the l_1 norm spectra and the MUSIC spectra, the results approach the ideal scenario with no calibration errors and its CRLB. For a given number of snapshots, MUSIC based DOA estimates result in lower RMSE values when compared with the equivalent l_1 norm based DOA estimates, further emphasizing the fact that the calibration estimates are robust to the model mismatches while solving either (4.22) or (4.27). On the other hand, the RMSE of the DOA estimates based on the Weiss-Friedlander approach [19] is also presented in Fig. 4.6, where the calibration parameters were initialized with a gain of 1 and a phase of 0°. It is seen that the RMSE of the DOA estimates decreases initially, however it tends to saturate as the number of snapshots increases as it leads to a sub-optimal solution depending on the initialization. Also it can be observed that the DOA estimates based on the MUSIC spectra with calibration parameters estimated from (4.27) require more snapshots to obtain better DOA estimates with low RMSE as the finite sample errors in the estimation of the covariance matrix are high for a low number of snapshots and those are not modeled in the formulation of (4.27). Furthermore, based on the MUSIC spectra in Fig. 4.6(a), it can be observed that the performance of the element-space approach is far superior than the covariance domain approach.

Similarly in Fig. 4.6(b), we considered the APS ULA with an SNR of 10 dB. For the APS ULA, only formulation in (4.27) is considered and the results of the proposed methodology are compared with the Paulraj-Kailath approach [13]. The RMSE of the DOA estimates of the proposed methodology follows same trend as seen for the AVS ULA in Fig. 4.6(a). On



(a) AVS ULA.

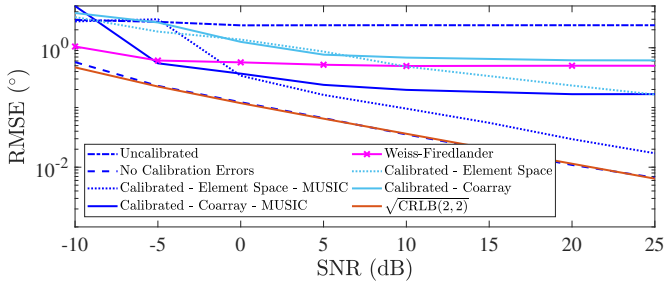


(b) APS ULA.

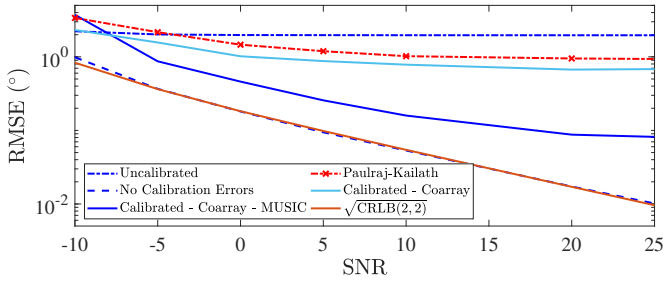
Figure 4.6: RMSE variation of the DOA estimates for the source at 90° using both the APS and AVS ULA with $M = 8$, $N = 3$ and $\boldsymbol{\theta} = [78°, 90°, 102°]$ for a fixed SNR of 10 dB as the number of snapshots are varying.

the other hand, although the calibration approach in [13] achieves the optimal solution, it requires more snapshots to achieve similar performance as the proposed methodology.

Fixed number of snapshots and varying SNR The variation of the RMSE in the DOA estimates with respect to a change in SNR for a fixed number of snapshots is considered in Fig. 4.7. The same setup as in Fig. 4.6 is considered with $N = 3$ ($\boldsymbol{\theta} = [78°, 90°, 102°]$) where the RMSE of the source at 90° is presented. In Figs. 4.7(a) and (b), we consider the AVS and the APS ULA, respectively, with 1000 snapshots and varying SNR. Similar to Fig. 4.6, it is seen that after calibration using the formulation in (4.22) as well as in (4.27) the RMSE of the DOA estimates decreases as the SNR increases for both the l_1 based spectra and the MUSIC spectra. Also as expected we can observe that the MUSIC spectra based DOA estimates outperform the l_1 based DOA estimates for a given SNR. Further, it can be inferred that the RMSE of the DOA estimates based on the proposed element-space model calibration technique asymptotically approaches the ideal scenario with no calibration errors and its CRLB. On the other hand, we can observe that the RMSE in the DOA estimates using the Weiss-Friedlander approach in Fig. 4.7(a) for the AVS ULA and the Paulraj-Kailath approach in Fig. 4.7(b) for the APS ULA, initially decreases as the SNR increases. However for an SNR greater than 5 dB the RMSE of the DOA estimates tends to saturate due to the finite sample errors in the covariance matrix estimation.



(a) AVS ULA.



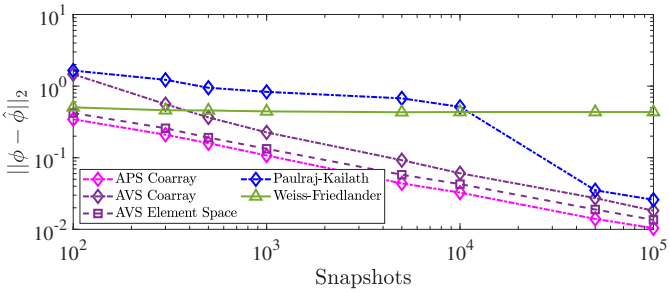
(b) APS ULA.

Figure 4.7: RMSE variation of the DOA estimates for the source at 90° using both the APS and AVS ULA with $M = 8$, $N = 3$ and $\boldsymbol{\theta} = [78°, 90°, 102°]$ as the SNR varies for a fixed number of snapshots of 1000.

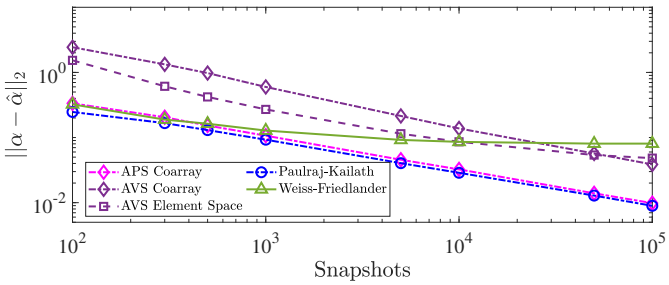
Gain and Phase RMSE estimates Finally, the RMSE in the gain and phase error estimates for the setup considered in Figs. 4.6 and 4.7 is considered. In Fig. 4.8 the norm of the difference between the estimates and the actual values of the gain and phase errors is presented. In Figs. 4.8(a) and 4.8(b), RMSE related to the phase and gain error estimates with varying snapshots is considered, with the SNR being 10 dB. It can be observed in Figs. 4.8(a) and 4.8(c) that the RMSE related to both the phase and gain errors tends to approach zero as the number of snapshots increases except for the Weiss-Friedlander approach [19] as it produces a sub-optimal solution. This trend is consistent for the proposed calibration approach based on both the element-space and co-array formulation. Further, in Figs. 4.8(a) and 4.8(b) it can be observed that the RMSE related to the phase errors based on the proposed calibration approach outperforms the Paulraj-Kailath approach.

SPARSE LINEAR ARRAY WITH MORE SOURCES THAN SENSORS

In Fig. 4.9, the RMSE of the DOA estimates for APS and AVS sparse linear array based on the SS MUSIC spectra obtained using gain and phase compensated measurement data for different SNRs and for different numbers of data snapshots is presented. Here, we use $M = 6$, $\mathbf{p} = [0\,1\,2\,3\,6\,9]^T$ and $N = 2$ with $\boldsymbol{\theta} = [70°, 90°]$. The RMSE is computed for the source at 90° using 500 independent Monte-Carlo trials, but with fixed gain and phase errors. In Figs. 4.9(a) and (b), we can observe that as the number of snapshots increases, the RMSE of the DOA estimate after calibration approaches the ideal scenario without any sensor errors. Furthermore, the RMSE for the STLS calibration saturates both when increasing the number of snapshots, as it converges to a sub-optimal solution.



(a) RMSE of phase errors.



(b) RMSE of gain errors.

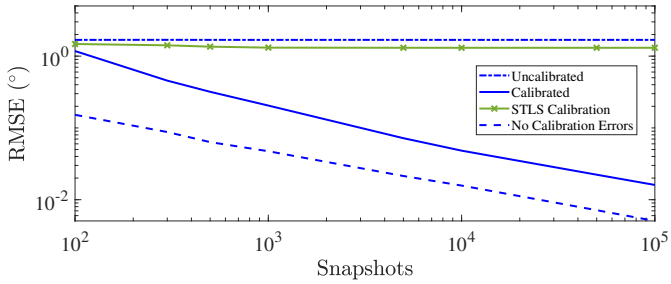
Figure 4.8: RMSE variation of the gain and phase error estimates for both the APS and AVS ULA setup considered in Figs. 4.6 and 4.7 as the snapshots varies for a fixed SNR of 10 dB.

4.7. EXPERIMENTAL RESULTS

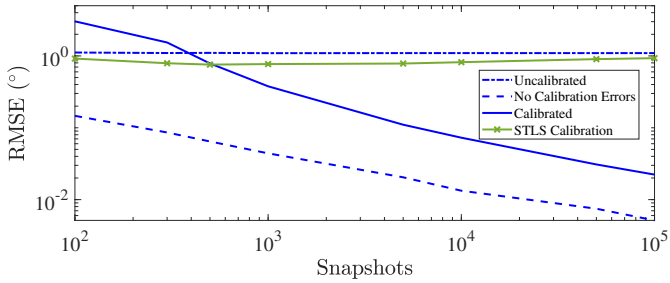
An experimental study was conducted in order to demonstrate the proposed joint DOA and calibration algorithm for AVS arrays. As discussed, each AVS consists of a pressure microphone and several orthogonal particle velocity transducers. A particle velocity transducer is commonly referred to as a Microflown [1]. A reliable calibration procedure is crucial for relating the sensor output to the physical quantity perceived. Unlike microphone calibration, there are no standardized procedures yet defined for characterizing the broadband response of particle velocity sensors.

Microflown sensors were originally calibrated using a sound pressure microphone as a reference in a standing wave tube [15], where the ratio between sound pressure and particle velocity (i.e., acoustic impedance) is well understood. Novel methods were later proposed for covering a wider frequency range, such as the “Piston-On-a-Sphere" technique (POS) [14]. This approach relies on a sound source of known impedance measured in free field conditions and it achieves good results at mid and high frequencies. Thereafter, the POS technique was extended to lower frequencies by also measuring the acoustic pressure inside the sound source [16]. As a result, a full-bandwidth calibration procedure is now available by combining two measurement steps. In this section, the DOA estimation results based on the calibrated data using the POS technique (referred to as POS calibration), the Weiss-Friedlander approach [19] and the proposed calibration techniques (both the element-space and co-array approaches) are presented.

A picture of the experimental setup is shown in Fig. 5.4, where five AVSs are seen ar-



(a) APS sparse array.



(b) AVS sparse array.

Figure 4.9: RMSE variation in the DOA estimates for the source at 90° based on the SS-MUSIC spectra using both APS and AVS sparse arrays with $M = 6$, $\mathbf{p} = [0\,1\,2\,3\,6\,9]^T$, $N = 2$, SNR = 10 dB and $\boldsymbol{\theta} = [70°, 90°]$ as the number of snapshots are varying. Here the scenario with "No Calibration Errors" is considered as the baseline reference to compare the performance of the proposed self-calibration solver.

ranged in a linear array configuration along with three speakers. The smallest inter-sensor

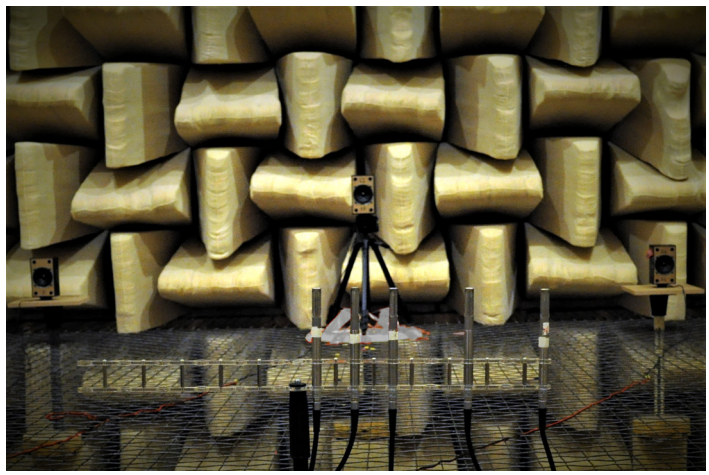
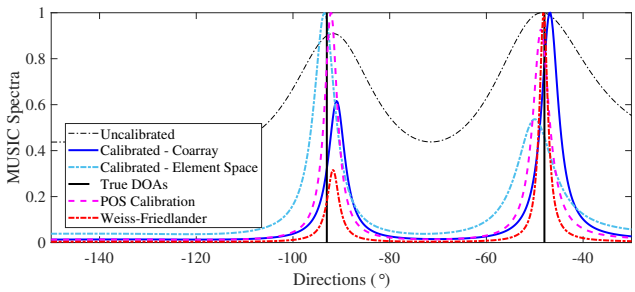


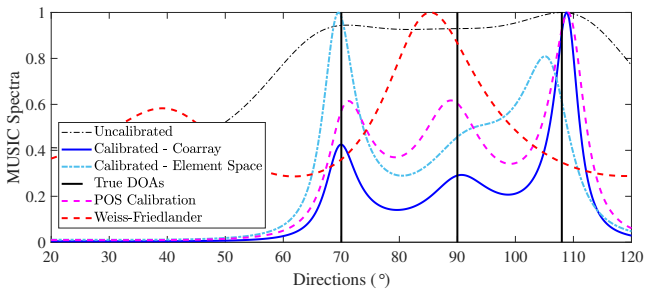
Figure 4.10: Picture of the experimental setup considering five AVSs and three speakers, located at a radius of $r = 3.6$ m.

spacing was $d = 0.05$ m with sensors located at positions $\mathbf{p} = [0,1,2,4,6]^T$ and the speakers were located along the circumference of a circle of radius $r = 3.6$ m with respect to the reference AVS in the array (the distance to the sources is more than 20 times the aperture of the array and therefore satisfying the far-field condition). The measurements were carried out in a fully anechoic chamber of the Faculty of Applied Physics of TU Delft (Netherlands) using uncorrelated white Gaussian excitations driving multiple 3 inch loudspeakers (resulting in high SNRs of approximately 30 dB). An Heim DATaRec 24 channels acquisition device with a sampling frequency of 25 kHz was used to record the data. The acoustic pressure and particle velocity information at a given frequency were obtained by computing a short time Fourier transform (STFT). Each recording was fragmented into segments of 1024 samples with 50% overlap. A Hanning window was applied to each data segment prior to the STFT.

The raw output signals from all the five AVSs at a time instant t for a particular frequency bin were collected in a vector $\mathbf{x}(t)$, similar to (4.1). Without loss of generality, we have considered the first channel of the first AVS in the array as the reference channel with known gain and phase response which is sufficient to obtain a unique solution as seen in the identifiability conditions for AVS arrays. The joint DOA and calibration algorithm based on (4.22) and (4.27) were applied on the captured measurement data $\mathbf{x}(t)$ consisting of $L = 1000$ snapshots at a frequency of $f = 2000$ Hz. The corresponding grid-free MUSIC spectra based on the post-calibration measurement data are presented in Fig. 4.11.



(a) N = 2, $\boldsymbol{\theta} = [-45°, -90°]^T$.



(b) N = 3, $\boldsymbol{\theta} = [70°, 90°, 108°]^T$.

Figure 4.11: MUSIC spectra based DOA estimates using an AVS array with $M = 5$, $N = 2$ and $f = 2000$ Hz. The true DOAs are indicated by the black solid lines.

In Fig. 4.11(a) and (b), we considered two of the three speakers with $\boldsymbol{\theta} = [-45°, -90°]^T$ and three speakers that are closely spaced with $\boldsymbol{\theta} = [70°, 90°, 108°]^T$, respectively. We can

observe that for the uncalibrated data, the resolution of MUSIC is poor. However, improved spectra with higher resolution can be seen after compensating with the estimated calibration parameters. The MUSIC spectrum obtained from (4.27), results in a high resolution comparable to the results that are obtained with the reference POS calibration approach. However, the spectrum obtained from (4.22), has a lower resolution (especially in the three source case) and shows a small bias compared to the co-array domain based solver. The, Weiss-Friedlander approach results in degraded estimates compared to the proposed approach, specifically in Fig.4.11(b) it can be observed that none of the sources are resolved.

4.8. CONCLUDING REMARKS

In this paper, we proposed a self calibration technique for both the element-space and co-array data models that is applicable to both acoustic pressure and vector sensor arrays. Also, we derived and discussed a number of identifiability conditions for all the considered cases under which a unique solution for both the calibration parameters and the source DOAs can be obtained. It is interesting to note that for the AVS array, irrespective of the considered geometry, it is possible to calibrate all the sensors with respect to only one of the channels in the array.

Based on the proposed approach, we showed that it is indeed possible to jointly estimate calibration errors and source directions using a *one-step* approach by exploiting the underlying algebraic structure and convex optimization techniques. It is shown that for infinite data records, we can in fact obtain the optimal solution suggesting the feasibility of the convex relaxations for both the element-space and co-array data models. However, when the number of time snapshots are limited and we have a pre-defined grid, we stated that the proposed methodology can be used as a pre-conditioning step to estimate the calibration errors. Then a grid-free approach such as MUSIC/SS-MUSIC can be applied on the gain and phase errors compensated measurement data to obtain improved and reliable DOA estimates. Furthermore, through simulations, we showed that even for finite data records we are able to recover all the source DOAs and we perform better than the existing calibration techniques for all the considered scenarios. Finally, experimental results based on real measurement data with an AVS linear array that are collected in an anechoic chamber are presented to showcase the effectiveness of the proposed calibration techniques using both the element-space and co-array data model.

REFERENCES

[1] H.-E. De Bree, "The microflown e-book," *Microflown Technologies, Arnhem*, 2007.

[2] J. P. Kitchens, "Acoustic vector-sensor array processing," Ph.D. dissertation, Massachusetts Institute of Technology, 2010.

[3] A. Nehorai and E. Paldi, "Acoustic vector-sensor array processing," *Signal Processing, IEEE Transactions on*, vol. 42, no. 9, pp. 2481–2491, 1994.

[4] A. L. Swindlehurst and T. Kailath, "A performance analysis of subspace-based methods in the presence of model errors. i. the music algorithm," *IEEE Transactions on signal processing*, vol. 40, no. 7, pp. 1758–1774, 1992.

[5] H. L. Van Trees, *Detection, estimation, and modulation theory. Part IV. , Optimum array processing*. New York: Wiley-Interscience, 2002.

[6] J. Capon, "High-resolution frequency-wavenumber spectrum analysis," *Proceedings of the IEEE*, vol. 57, no. 8, pp. 1408–1418, 1969.

[7] R. Roy and T. Kailath, "Esprit-estimation of signal parameters via rotational invariance techniques," *IEEE Transactions on acoustics, speech, and signal processing*, vol. 37, no. 7, pp. 984–995, 1989.

[8] D. Malioutov, M. Cetin, and A. S. Willsky, "A sparse signal reconstruction perspective for source localization with sensor arrays," *IEEE transactions on signal processing*, vol. 53, no. 8, pp. 3010–3022, 2005.

[9] S. P. Chepuri, G. Leus *et al.*, "Sparse sensing for statistical inference," *Foundations and Trends® in Signal Processing*, vol. 9, no. 3–4, pp. 233–368, 2016.

[10] A. Moffet, "Minimum-redundancy linear arrays," *IEEE Transactions on antennas and propagation*, vol. 16, no. 2, pp. 172–175, 1968.

[11] P. Pal and P. Vaidyanathan, "Nested arrays: a novel approach to array processing with enhanced degrees of freedom," *Signal Processing, IEEE Transactions on*, vol. 58, no. 8, pp. 4167–4181, 2010.

[12] P. Pal and P. P. Vaidyanathan, "Coprime sampling and the music algorithm," in *Digital Signal Processing Workshop and IEEE Signal Processing Education Workshop (DSP/SPE), 2011 IEEE*. IEEE, 2011, pp. 289–294.

[13] A. Paulraj and T. Kailath, "Direction of arrival estimation by eigenstructure methods with unknown sensor gain and phase," in *Acoustics, Speech, and Signal Processing, IEEE International Conference on ICASSP'85.*, vol. 10. IEEE, 1985, pp. 640–643.

[14] F. Jacobsen and V. Jaud, "A note on the calibration of pressure-velocity sound intensity probes," *The Journal of the Acoustical Society of America*, vol. 120, no. 2, pp. 830–837, 2006.

[15] H.-E. d. Bree, W. Druyvesteyn, and M. Elwenspoek, "Realisation and calibration of a novel half inch pu sound intensity probe," in *Audio Engineering Society Convention 106*. Audio Engineering Society, 1999.

[16] T. G. Basten and H.-E. de Bree, "Full bandwidth calibration procedure for acoustic probes containing a pressure and particle velocity sensor," *The Journal of the Acoustical Society of America*, vol. 127, no. 1, pp. 264–270, 2010.

[17] D. Astély, A. L. Swindlehurst, and B. Ottersten, "Spatial signature estimation for uniform linear arrays with unknown receiver gains and phases," *IEEE Transactions on Signal Processing*, vol. 47, no. 8, pp. 2128–2138, 1999.

[18] K. N. Ramamohan, S. P. Chepuri, D. F. Comesana, G. C. Pousa, and G. Leus, "Blind calibration for acoustic vector sensor arrays," in *2018 IEEE International Conference on Acoustics, Speech and Signal Processing (ICASSP)*. IEEE, 2018, pp. 3544–3548.

[19] A. J. Weiss and B. Friedlander, "Eigenstructure methods for direction finding with sensor gain and phase uncertainties," *Circuits, Systems and Signal Processing*, vol. 9, no. 3, pp. 271–300, 1990.

[20] S. J. Wijnholds and A.-J. Van Der Veen, "Multisource self-calibration for sensor arrays," *IEEE Transactions on Signal Processing*, vol. 57, no. 9, pp. 3512–3522, 2009.

[21] S. Ling and T. Strohmer, "Self-calibration and bilinear inverse problems via linear least squares," *arXiv preprint arXiv:1611.04196*, 2016.

[22] E. K. Hung, "A critical study of a self-calibrating direction-finding method for arrays," *IEEE Transactions on Signal Processing*, vol. 42, no. 2, pp. 471–474, 1994.

[23] Q. Cheng, Y. Hua, and P. Stoica, "Asymptotic performance of optimal gain-and-phase estimators of sensor arrays," *IEEE Transactions on Signal Processing*, vol. 48, no. 12, pp. 3587–3590, 2000.

[24] M. Viberg and A. L. Swindlehurst, "A bayesian approach to auto-calibration for parametric array signal processing," *IEEE Transactions on Signal Processing*, vol. 42, no. 12, pp. 3495–3507, 1994.

[25] M. P. Wylie, S. Roy, and H. Messer, "Joint doa estimation and phase calibration of linear equispaced (les) arrays," *IEEE Transactions on Signal Processing*, vol. 42, no. 12, pp. 3449–3459, 1994.

[26] Y. Li and M. Er, "Theoretical analyses of gain and phase error calibration with optimal implementation for linear equispaced array," *IEEE Transactions on Signal Processing*, vol. 54, no. 2, pp. 712–723, 2006.

[27] A. Weiss, B. Nadler, and A. Yeredor, "Asymptotically optimal blind calibration of acoustic vector sensor uniform linear arrays," in *ICASSP 2020-2020 IEEE International Conference on Acoustics, Speech and Signal Processing (ICASSP)*. IEEE, 2020, pp. 4677–4681.

[28] V. C. Soon, L. Tong, Y.-F. Huang, and R. Liu, "A subspace method for estimating sensor gains and phases," *IEEE Transactions on signal processing*, vol. 42, no. 4, pp. 973–976, 1994.

[29] K. Han, P. Yang, and A. Nehorai, "Calibrating nested sensor arrays with model errors," *IEEE Transactions on Antennas and Propagation*, vol. 63, no. 11, pp. 4739–4748, 2015.

[30] P. K. Tam and K. T. Wong, "Cramer-rao bounds for direction finding by an acoustic vector sensor under nonideal gain-phase responses, noncollocation, or nonorthogonal orientation," *IEEE Sensors Journal*, vol. 9, no. 8, pp. 969–982, 2009.

[31] Y. Song and K. T. Wong, "A lower bound of direction-of-arrival estimation for an acoustic vector sensor subject to sensor breakdown," *IEEE Transactions on Aerospace and Electronic Systems*, vol. 48, no. 4, pp. 3703–3708, 2012.

[32] P. K. Tam, K. T. Wong, and Y. Song, "An hybrid cramer-rao bound in closed form for direction-of-arrival estimation by an "acoustic vector sensor" with gain-phase uncertainties," *IEEE transactions on signal processing*, vol. 62, no. 10, pp. 2504–2516, 2014.

[33] X. Yuan, "Direction-finding with a misoriented acoustic vector sensor," *IEEE Transactions on Aerospace and Electronic Systems*, vol. 48, no. 2, pp. 1809–1815, 2012.

[34] Y. Song, K. T. Wong, and F. Chen, ""quasi-blind" calibration of an array of acoustic vector-sensors that are subject to gain errors/mis-location/mis-orientation," *IEEE transactions on signal processing*, vol. 62, no. 9, pp. 2330–2344, 2014.

[35] K. N. Ramamohan, S. P. Chepuri, D. F. Comesaña, and G. Leus, "Blind calibration of sparse arrays for doa estimation with analog and one-bit measurements," in *ICASS2019 IEEE International Conference on Acoustics, Speech and Signal Processing (ICASSP)*. IEEE, 2019, pp. 4185–4189.

[36] C.-L. Liu and P. Vaidyanathan, "Super nested arrays: Linear sparse arrays with reduced mutual coupling—part i: Fundamentals," *IEEE Transactions on Signal Processing*, vol. 64, no. 15, pp. 3997–4012, 2016.

[37] Z. Ma and K. Ho, "A study on the effects of sensor position error and the placement of calibration emitter for source localization," *IEEE Transactions on Wireless Communications*, vol. 13, no. 10, pp. 5440–5452, 2014.

[38] P. Pal and P. P. Vaidyanathan, "On application of lasso for sparse support recovery with imperfect correlation awareness," in *2012 Conference Record of the Forty Sixth Asilomar Conference on Signals, Systems and Computers (ASILOMAR)*. IEEE, 2012, pp. 958–962.

[39] K. Nambur Ramamohan, M. Contino, S. P. Chepuri, D. F. Comesaña, and G. Leus, "Doa estimation and beamforming using spatially under-sampled avs arrays," in *2017 IEEE 7th International Workshop on Computational Advances in Multi-Sensor Adaptive Processing (CAMSAP)*. IEEE, 2017, pp. 1–5.

5

BLIND SENSOR ARRAY CALIBRATION AND DOA ESTIMATION OF BROADBAND SOURCES

In this paper, we focus on the gain and phase calibration of a sensor array and the direction-of-arrival (DOA) estimation of multiple far-field broadband sources. By leveraging the fact that the calibration errors vary across frequencies smoothly and the DOAs of broadband sources are the same for the frequency range of interest, we propose a blind calibration method to jointly estimate the gain and phase errors. This joint estimation problem is a non-convex optimization problem. Hence, it is relaxed to a convex optimization problem by exploiting the underlying algebraic structure. Numerical and experimental results using real measurement data are presented, to illustrate the efficiency of the proposed solver. Both results are based on an acoustic vector sensor (AVS) linear array.

5.1. INTRODUCTION

Direction-of-arrival (DOA) estimation using sensor arrays is of interest in many fields including acoustics. Its applications include ground surveillance [1] and target tracking [2] for localizing outdoor acoustic events. Conventionally, microphone/acoustic pressure sensor (APS) arrays are deployed for such tasks and based on the time delays between the sensors, the DOAs of the sources are estimated. However, in recent times with the advances in sensor technology, transducers that are capable of measuring vector quantities such as particle velocity are becoming practically feasible [3–5]. An acoustic vector sensor (AVS) is one such device that can measure both acoustic pressure (scalar quantity) and particle velocity (vector quantity) at a given spatial location [6, 7]. It comprises an omni-directional microphone and two (or three) particle velocity transducers each aligned along the coordinate axes in $\mathbb{R}^2$ (or $\mathbb{R}^3$) [5]. These sensors are broadband in nature and operate in the audible range of frequencies.

For DOA estimation of broadband sources using spatially distributed AVS or APS arrays, narrowband algorithms are applied to the measurements corresponding to each frequency bin and then all these results are combined. Advanced algorithms that yield highly accurate estimates among many include the minimum variance distortionless response (MVDR) beamformer [8] and subspace-based methods like multiple signal classification (MUSIC) [9]. However, these algorithms are highly sensitive to modeling errors such as relative gain and phase variations across frequencies and sensors, which are commonly referred to as calibration errors. These sensor calibration errors are frequency dependent, but they vary smoothly across frequencies. The latter property can be used as prior information which allows us to assume that the calibration errors are constant or change linearly over a certain range of frequencies. They are similar/same or they can be linearized for certain set of frequencies. A typical microphone gain and phase variation can be seen in Fig. 5.1.

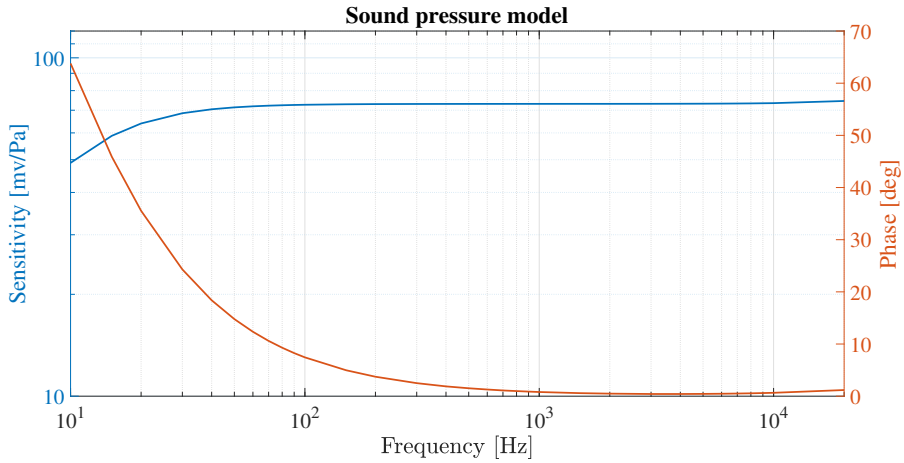


Figure 5.1: Gain and phase sensitivity of a typical microphone [5].

Based on the knowledge that the calibration parameters vary smoothly and that the DOAs of the sources remain same across frequencies, in this work we will extend the blind calibration framework for the joint estimation of calibration parameters as well as DOAs

developed in [10]. We restrict our attention to the case where the calibration errors are constant over a certain number of frequency bins, however the framework can be easily extended to the scenario where the calibration parameters vary linearly across the frequency bins as well. The proposed approach is applicable to both APS as well as AVS arrays with an arbitrary geometry (uniform or sparse).

5.2. PROBLEM FORMULATION

Consider a scenario with N far-field uncorrelated broadband sources with associated DOAs along the azimuth axis $\boldsymbol{\theta} = [\theta_1, \theta_2, \ldots, \theta_N]^T$. We assume that the source signals are spread across W frequency bins and impinge on the sensor array consisting of M sensors. The measurement data at time index k and frequency bin w can be modeled as:

$$\mathbf{x}(k,w) = \text{diag}(\mathbf{g}(w))\,[\mathbf{A}(w,\boldsymbol{\theta})\mathbf{s}(w,k) + \mathbf{n}(w,k)], \tag{5.1}$$

where $\mathbf{g}(w) = \psi(w) \odot \phi(w) \in \mathbb{C}^Q$ ($\odot$ is the element-wise product) is the vector that collects the sensor uncertainties with $\psi(w)$ and $\phi(w)$ being the time-invariant gain and phase errors corresponding to the frequency bin w, respectively.
$\mathbf{A}(w,\boldsymbol{\theta}) = [\mathbf{a}(w,\theta_1) \ \ldots \ \mathbf{a}(w,\theta_N)] \in \mathbb{C}^{Q\times N}$ is the array manifold matrix with $Q = 3M$ for AVS arrays and $Q = M$ for APS arrays. The steering vector for the nth direction of an AVS array is given as

$$\mathbf{a}(w,\theta_n) = \mathbf{a}_\text{p}(w,\theta_n) \otimes \mathbf{h}(\theta_n) \in \mathbb{C}^{3M\times 1}, \tag{5.2}$$

where $\otimes$ is the Kronecker product, $\mathbf{a}_\text{p}(w,\theta_n)$ is the steering vector of an APS array and $\mathbf{h}(\theta_n)$ contains the direction cosines:

$$\begin{aligned} \mathbf{a}_\text{p}(w,\theta_n) &= \left[e^{-\text{j}2\pi f_w \tau_1(\theta_n)} \ \ldots \ e^{-\text{j}2\pi f_w \tau_M(\theta_n)}\right]^T \in \mathbb{C}^{M\times 1}, \\ \mathbf{h}(\theta_n) &= [1 \ \mathbf{u}(\theta_n)] \in \mathbb{C}^{3\times 1}. \end{aligned} \tag{5.3}$$

Here, $\tau_m(\theta_n) = -\frac{1}{c}\mathbf{p}_m^T\mathbf{u}(\theta_n)$ with c being the speed of sound in the considered medium such that the wavelength of the source signal can be denoted as $\lambda_w = \frac{c}{f_w}$, $\mathbf{p}_m = \begin{bmatrix} x_m & y_m \end{bmatrix}^T$ being the position of the mth sensor and $\mathbf{u}(\theta_n) = [\cos(\theta_n) \ \sin(\theta_n)]^T$ being the unit vector in the direction of the nth source. The source and additive noise vector corresponding to frequency bin w are denoted as $\mathbf{s}(w,k)$ and $\mathbf{n}(w,k)$, respectively.

Assume that the source vector, $\mathbf{s}(w,k)$, and the noise vector, $\mathbf{n}(w,k)$, are uncorrelated with covariance matrices $\mathbb{E}\{\mathbf{s}(w,k)\mathbf{s}^H(w,k)\} = \text{diag}(\mathbf{r}_{w\text{s}})$ and $\mathbb{E}\{\mathbf{n}(w,k)\mathbf{n}^H(w,k)\} = \sigma_{w\text{n}}\mathbf{I}$, where we assume that the noise variance $\sigma_{w\text{n}}$ is known. The covariance matrix of the measurement data in (5.1) for a particular frequency bin w can then be expressed as

$$\begin{aligned} \mathbf{R}_w &= \text{diag}(\mathbf{g}(w))\,\mathbf{Q}_w\,\text{diag}(\bar{\mathbf{g}}(w)), \\ \mathbf{Q}_w &= \mathbf{A}(w,\boldsymbol{\theta})\text{diag}(\mathbf{r}_{w\text{s}})\mathbf{A}^H(w,\boldsymbol{\theta}) + \sigma_{w\text{n}}\mathbf{I}, \end{aligned} \tag{5.4}$$

where $(\bar{\cdot})$ denotes complex conjugation. It is also useful to express (5.4) in vectorized form as:

$$\mathbf{r}_w = \text{diag}(\bar{\mathbf{g}}(w) \otimes \mathbf{g}(w))\left[\tilde{\mathbf{A}}(w,\boldsymbol{\theta})\mathbf{r}_{w\text{s}} + \sigma_{w\text{n}}\mathbf{e}\right], \tag{5.5}$$

where $\text{vec}(\mathbf{R}_w) = \mathbf{r}_w$ and $\tilde{\mathbf{A}}(w,\boldsymbol{\theta}) = \bar{\mathbf{A}}(w,\boldsymbol{\theta}) \circ \mathbf{A}(w,\boldsymbol{\theta})$ ($\circ$ is the Khatri-Rao product) and $\mathbf{e}$ is the vectorized identity matrix. The source DOAs can be assumed to be derived from a

uniform grid of D points, with $D \gg N$, i.e., we assume that $\theta_n \in \left\{0, \frac{\pi}{D} \cdots, \frac{\pi(D-1)}{D}\right\}$, for $n = 1,2,\ldots,N$. This means (5.5) can be approximated as:

$$\text{diag}(\bar{\mathbf{c}}(w) \otimes \mathbf{c}(w))\mathbf{r}_w = \mathbf{A}_{\text{D}}(w)\boldsymbol{\sigma}_w + \sigma_{w\text{n}}\mathbf{e}, \tag{5.6}$$

where $\text{diag}(\mathbf{c}(w)) = \text{diag}^{-1}(\mathbf{g}(w))$ and $\mathbf{A}_{\text{D}}(w)$ is a $Q^2 \times D$ dictionary matrix that consists of column vectors of the form $\bar{\mathbf{a}}(w,\bar{\theta}_d) \otimes \mathbf{a}(w,\bar{\theta}_d)$, with $\bar{\theta}_d$ being the dth point of the uniform direction grid, i.e., $\bar{\theta}_d = \frac{\pi d}{D}$, $d = 0,1,\ldots,D-1$. In further discussion, for the sake of simplicity, we denote $\mathbf{A}_{\text{D}}(w)$ as $\hat{\mathbf{A}}_w$. Based on (5.6), the proposed technique is presented in the next section.

5.3. PROPOSED CALIBRATION TECHNIQUE

In this section, we will propose an approach for joint calibration and DOA estimation in the presence of broadband sources, which is an extension of the narrowband approach proposed in [10]. The covariance domain data model in (5.6) for all the frequency bins can be rearranged as,

$$\mathbf{G}\boldsymbol{\gamma} = \boldsymbol{\sigma}_{\text{n}}, \tag{5.7}$$

where $\boldsymbol{\sigma}_{\text{n}} = \left[\boldsymbol{\sigma}_{1\text{n}}^T \ldots \boldsymbol{\sigma}_{W\text{n}}^T\right]^T$, $\mathbf{G} = [\mathbf{G}_1 \,|\, \mathbf{G}_2]$, with

$$\mathbf{G}_1 = \begin{bmatrix} \text{diag}(\mathbf{r}_1) & & \\ & \ddots & \\ & & \text{diag}(\mathbf{r}_W) \end{bmatrix}, \mathbf{G}_2 = \begin{bmatrix} -\hat{\mathbf{A}}_1 & & \\ & \ddots & \\ & & -\hat{\mathbf{A}}_W \end{bmatrix},$$

and $\boldsymbol{\gamma} = \left[\text{vec}(\mathbf{C}_1)^T \ \ldots \ \text{vec}(\mathbf{C}_W)^T \,\middle|\, \text{vec}(\boldsymbol{\Sigma})^T\right]^T$, with $\boldsymbol{\Sigma} = [\boldsymbol{\sigma}_1\, \boldsymbol{\sigma}_2 \ldots \boldsymbol{\sigma}_W]$ and its vectorized version $\text{vec}(\boldsymbol{\Sigma}) = \boldsymbol{\sigma}$, and $\mathbf{C}_w = \mathbf{c}(w)\mathbf{c}^H(w)$ and its vectorized version $\text{vec}(\mathbf{C}_w) = \bar{\mathbf{c}}(w) \otimes \mathbf{c}(w)$. If we focus in the frequency range where the calibration errors are constant, we can approximate $\mathbf{C}_w = \mathbf{C}$ (i.e., $\mathbf{c}_w = \mathbf{c}$), $\forall\, w = 1,2,\ldots,W$, such that (5.7) is modified as,

$$\hat{\mathbf{G}}\hat{\boldsymbol{\gamma}} = \boldsymbol{\sigma}_{\text{n}}, \tag{5.8}$$

where $\hat{\boldsymbol{\gamma}} = \left[\text{vec}(\mathbf{C})^T \,\middle|\, \text{vec}(\boldsymbol{\Sigma})^T\right]^T$ and

$$\hat{\mathbf{G}} = \mathbf{G}\begin{bmatrix} \mathbf{1}_W \otimes \mathbf{I}_Q & \mathbf{0}_{WQ\times WD} \\ \mathbf{0}_{WD\times Q} & \mathbf{I}_{WD} \end{bmatrix}.$$

This is an under-determined system of equations with WQ^2 equations in $Q^2 + WD$ unknowns (where in general $D > Q^2$).

However, by exploiting the structure in $\boldsymbol{\Theta}$, the system of equations presented in (5.8) can be solved. Specifically, we have a rank-1 Kronecker structure $\bar{\mathbf{c}} \otimes \mathbf{c} = \text{vec}(\mathbf{C})$ with $\mathbf{C} = \mathbf{c}\mathbf{c}^H$. Also, as there are only N sources, there will be N non-zero elements in each of the columns of $\boldsymbol{\Sigma}$ which share the same support and it can be expressed as $\|\boldsymbol{\sigma}^{(l_2)}\|_0 = N$, where $\|\cdot\|_0$ is the l_0-norm that counts the number of non-zero entries of its argument. The constraint $||\boldsymbol{\sigma}^{(l_2)}||_0 = \left\| \left[\sigma_1^{(l_2)}\, \sigma_2^{(l_2)} \ldots \sigma_D^{(l_2)}\right]^T \right\|_0$ encompasses the fact that the source DOAs are frequency independent and $\sigma_d^{(l_2)} = \left\|[\sigma_{1d}\, \sigma_{2d} \ldots \sigma_{Wd}]^T\right\|_2$; $\forall d = 1,2,\ldots,D$. Further from (5.5), it can be seen that $\bar{\mathbf{g}}(w) \otimes \mathbf{g}(w)$ and $\mathbf{r}_{w\text{s}}$ share a common scalar factor and due to the Kronecker structure there is a phase ambiguity. In order to resolve these ambiguities, we require two reference sensors for APS arrays and one reference channel of one sensor for AVS arrays.

By considering all the aforementioned constraints, the optimization problem for jointly solving the calibration parameters as well as the DOAs across frequency bins can be posed as:

$$\begin{aligned} \min_{\hat{\boldsymbol{\gamma}}} \quad & \|\hat{\mathbf{G}}\hat{\boldsymbol{\gamma}} - \boldsymbol{\sigma}_{\mathrm{n}}\|_2^2, \\ \text{subject to} \quad & ||\boldsymbol{\sigma}^{(l_2)}||_0 = N, \boldsymbol{\sigma}^{(l_2)} \succeq \mathbf{0}, \boldsymbol{\sigma}_{\mathrm{n}} \succeq \mathbf{0} \\ & \mathbf{C} = \mathbf{c}\mathbf{c}^H, \, c_i = 1, \, \forall i = 1, \ldots, R, \end{aligned} \tag{5.9}$$

where R is the number of reference sensors/channels in the array. However, the optimization problem in (5.9) is non-convex due to the l_0 norm constraint on $\boldsymbol{\sigma}^{(l_2)}$ and the rank-one equality constraint on $\mathbf{C}_w$. The convex approximation of (5.9) can be obtained by relaxing the cardinality constraint with its convex approximation $\mathbf{1}^T\boldsymbol{\sigma}^{(l_2)}$ as well as by replacing the equality constraint with the rank one inequality constraint, i.e.,

$$\begin{aligned} \min_{\boldsymbol{\gamma}} \quad & \|\hat{\mathbf{G}}\hat{\boldsymbol{\gamma}} - \boldsymbol{\sigma}_{\mathrm{n}}\|_2^2, \\ \text{subject to} \quad & \mathbf{1}^T\boldsymbol{\sigma}^{(l_2)} \leq N, \boldsymbol{\sigma}^{(l_2)} \succeq \mathbf{0}, \boldsymbol{\sigma}_{\mathrm{n}} \succeq \mathbf{0} \\ & \begin{bmatrix} \mathbf{C} & \mathbf{c} \\ \mathbf{c}^H & 1 \end{bmatrix} \succeq 0, \, c_i = 1, \, \forall i = 1, \ldots, R. \end{aligned} \tag{5.10}$$

This is a semi-definite programming (SDP) problem which can be solved using any one of the off-the-shelf solvers such as CVX. It is should be noted that the resolution of the DOAs that are being estimated is restricted to the resolution of the chosen grid and if the source DOAs are not on that grid then it will suffer from grid mismatch issues. In order to reduce those effects, grid free estimators such as MUSIC can be used after compensating for the calibration errors that are estimated using (5.10).

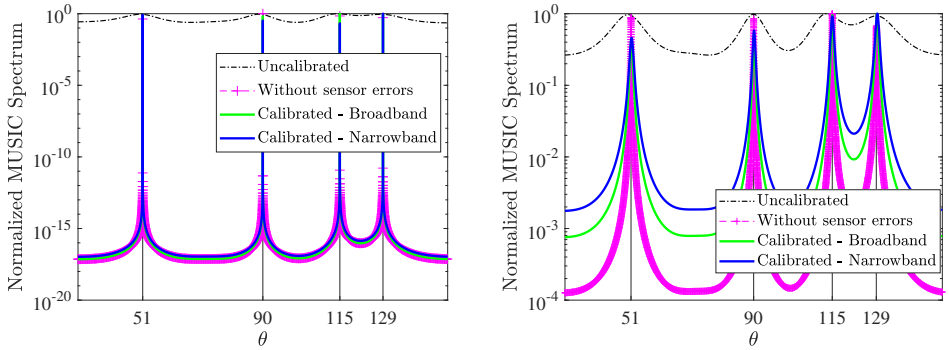
5.4. SIMULATION RESULTS

In this section, we present some simulation results to illustrate the performance of the proposed DOA estimation technique, based on the formulation in (5.10), for broadband sources and with an uncalibrated sensor array. For doing so, we consider a scenario with five AVSs, i.e., $M = 5$, arranged in a uniform linear array (ULA) configuration along the x-axis (i.e., $y_m = 0, x_m = (m-1)l$; $\forall m = 1, \ldots, M$, with l being the inter-sensor spacing). We consider four equal powered sources, i.e., $N = 4$, whose DOAs are $\boldsymbol{\theta} = [51°, 90°, 115°, 129°]$. Their signatures are spread across 11 frequency bins (i.e., $W = 11$) that are chosen around the spatial Nyquist frequency (i.e., for a particular λ_w which is equal to twice the inter-sensor spacing in the ULA). The signal-to-noise (SNR) ratio for each of the considered bins is 10 dB. The calibration is carried out by treating the pressure channel of the first AVS in the array as reference, where the nominal gain and phase corresponding to it are chosen as 1 and 0°, respectively for all the considered frequency bins. The gain and phase errors for each bin are chosen uniformly at random from the interval $[-2, 2]$ dB and $[-40°, 40°]$, respectively.

Once the calibration errors and the grid-based DOAs are estimated by solving (5.10), off-the-grid DOAs can be estimated using MUSIC based on the calibrated array covariance matrix for each of the considered frequency bins. In Fig. 5.2, the MUSIC spectra for the measurement data corresponding to one of considered frequency bins before and after the calibration procedure as well as for the measurement data without calibration errors are pre-

sented for both the narrowband approach, as in [10], and the proposed broadband method, as in (5.10). The results of the narrowband approach are based on solving the optimization problem for a particular frequency bin corresponding to the spatial Nyquist frequency.

Firstly in Fig. 5.2(a), we consider a scenario with infinite snapshots (i.e., ideal covariance matrix as seen in (5.4)). It can be seen that the DOA estimates of an uncalibrated array are not useful due to the lower resolution as well as bias in their estimates. It is also observed that the true DOAs are recovered for both the narrowband and the broadband approach, suggesting the exactness of the convex approximation. Further in Fig. 5.2(b), for finite data records with 1000 snapshots, based on the proposed broadband approach we get improved results compared to the uncalibrated as well as the narrowband version with higher resolution such that all the considered four sources are resolved and the results are closer to the scenario without any sensor errors.



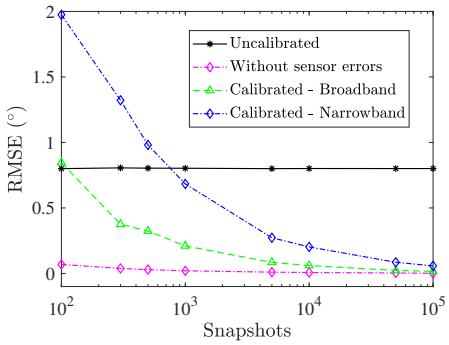
(a) With infinite snapshots.

(b) With 1000 snapshots.

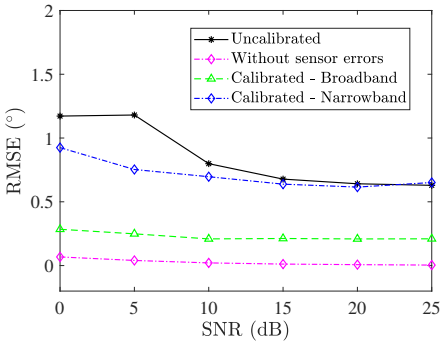
Figure 5.2: MUSIC spectra of an AVS ULA with $M = 5$, $N = 4$ and SNR = 10 dB. The black grid lines denote the true source directions.

In Fig. 5.3, the root mean squared error (RMSE) of the DOA estimates for a particular frequency bin obtained using MUSIC for varying snapshots, SNRs and number of frequency bins are presented. All the settings are same as considered in Fig. 5.2, and the RMSE plots are presented for the source at 90° based on 500 independent Monte-Carlo trails with fixed calibration errors. From Fig. 5.3(a), as the number of snapshots increases asymptotically for both the narrowband and broadband calibration approaches, the RMSE of the DOA estimates approaches the ideal scenario without any sensor errors. However even with a small number of snapshots the RMSE of the DOA estimates based on the proposed broadband approach is smaller compared to the equivalent narrowband approach suggesting its effectiveness.

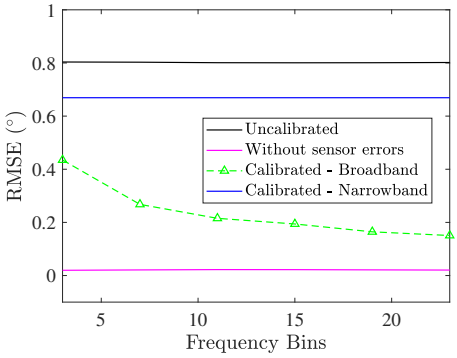
In Fig. 5.3(b), the RMSE of the DOA estimates for the source at 90° for varying SNRs is shown. It can be observed that the RMSE of the DOA estimates after the calibration procedure decreases as the SNR increases. However for a SNR above 15 dB, we see that the RMSE values saturate as expected [11]. Further in Fig. 5.3(b) we can observe that, similar to Fig. 5.3(a), for a given SNR the performance of the proposed broadband calibration procedure outperforms the equivalent narrowband approach. Finally in Fig. 5.3(c), the RMSE of the DOA estimates is considered as the number of frequency bins increases. Clearly, for the proposed broadband approach the RMSE decreases with the number of frequency bins. On



(a) SNR = 10 dB and $W = 11$.



(b) Snapshots = 1000 and $W = 11$.



(c) Snapshots = 1000 and SNR = 10 dB.

Figure 5.3: RMSE of the DOA estimates for the source at 90° obtained from MUSIC with $M = 5$, $N = 4$ and $\boldsymbol{\theta} = [51° \, 90° \, 115° \, 129°]^T$.

the other hand for the narrowband approach, since each frequency bin is treated independently, the RMSE stays constant as the number of frequency bins increases.

5.5. EXPERIMENTAL RESULTS

An experimental study in a fully anechoic chamber was conducted in order to showcase the proof of concept of the proposed joint DOA estimation and calibration algorithm. The literature on the working principle of the transducers as well as the existing reference calibration procedure can be found in [3, 12–14]. The DOA estimation results of the proposed calibration algorithm as well as the results from the narrowband approach are presented in this section.

A picture of the experimental setup is shown in Figure 5.4, where five AVSs arranged in a linear array configuration along with three speakers within its range was chosen for the experiments. The smallest inter-sensor spacing is $l = 5$ cm with sensors located at positions $[x_1 \dots x_5] = [0\,1\,2\,4\,6]$ resulting in a sparse linear array configuration. The speakers are located along the circumference of a circle of radius $r = 360$ cm with respect to the reference AVS in the array (i.e., the range of the sources is more than 20 times the aperture of the ar-

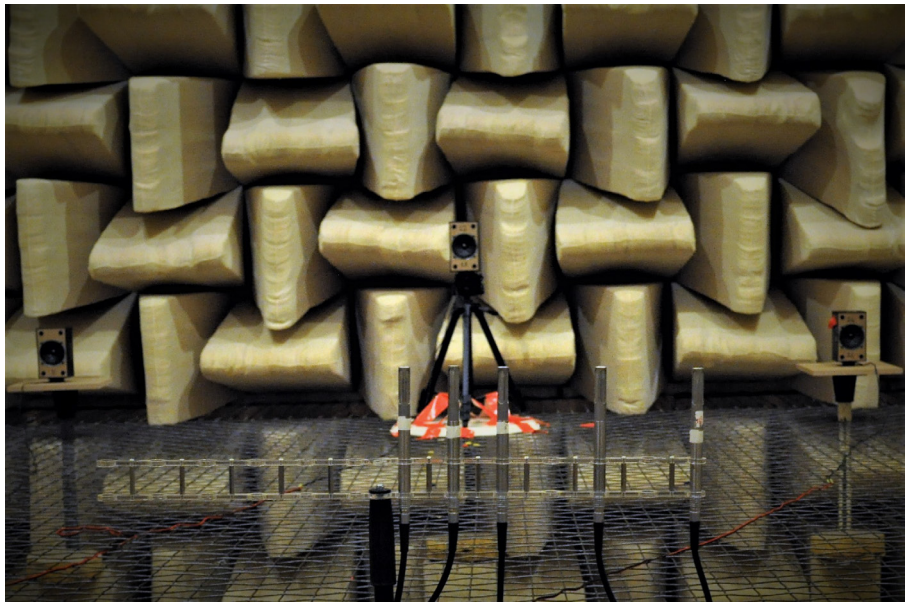
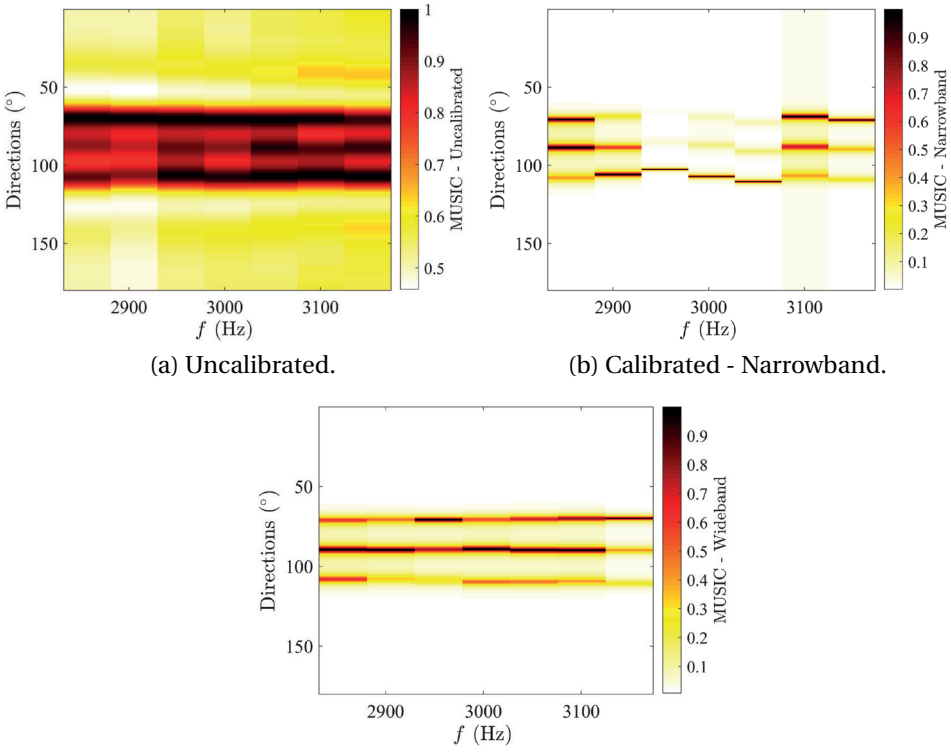


Figure 5.4: Picture of the arrangement of five AVSs and three speakers, which are located on the circumference of a circle with radius $r = 360$ cm.

ray allowing for a far-field assumption). The measurements were carried out using a white Gaussian excitation, radiated by a 3 inch loud speaker, under high SNR conditions (approximately 30 dB). For the measurements, an acquisition device with a sampling frequency of 25 kHz was used.

Based on the measurements from the setup in Fig. 5.4, the post-processing results are presented in Fig. 5.5. The proposed broadband calibration procedure was considered for $W = 7$ frequency bins between 2800 Hz and 3200 Hz. Within this frequency range, the calibration errors were assumed to be same. Firstly in Fig. 5.5(a), the MUSIC spectra based on the uncalibrated voltage signals from the AVSs in the array are presented for all the considered frequency bins. It is observed that the resolution of the spectra is poor and also the levels of the side lobes are high.

In Fig. 5.5(b), the MUSIC spectra based on the narrowband calibration approach, where each frequency bin is treated independently, is plotted. It is observed that the resolution of the spectra is improved compared to the uncalibrated version yet we can still see a bias in the estimates across frequency bins. Finally in Fig. 5.5(c), the MUSIC spectra based on the proposed broadband calibration procedure are presented. It is evident that all the three sources are completely resolved. Clearly, the resolution is better and the bias is smaller, which highlights the effectiveness of the proposed approach. Also based on the results in Fig. 5.5(c) it can be inferred that assuming the calibration errors are same across frequency bins is valid.



(a) Uncalibrated.

(b) Calibrated - Narrowband.

(c) Calibrated - Broadband.

Figure 5.5: MUSIC spectra for $M = 5$, $N = 3$ with $\boldsymbol{\theta} = [70^\circ\ 90^\circ\ 110^\circ]^T$, $W = 7$, and snapshots = 500.

5.6. CONCLUSIONS

In this work, we presented a blind calibration technique for the joint estimation of calibration errors and DOAs of far-field broadband sources. The prior information that the calibration parameters vary slowly across frequencies and the DOAs remain same for the considered range of frequencies is used to improve the estimation performance compared to the equivalent narrowband approach. Numerical simulations including RMSE plots for an AVS array are presented to showcase the effectiveness of the proposed approach. It is observed that the broadband approach outperforms the equivalent narrowband approach even when the number of snapshots are small. Further, experimental results based on real measurements carried out in an anechoic chamber were presented and it is observed that the proposed approach provides angular spectra with a higher resolution and less bias compared to the uncalibrated as well as the existing narrowband approach.

REFERENCES

[1] H.-E. de Bree, J. Wind, and E. Tijs, *Environmental noise monitoring with acoustic vector sensors,* in *INTER-NOISE Congress Proceedings*, Vol. 2010 (Institute of Noise Control Engineering, 2010) pp. 6225–6231.

[2] H.-E. de Bree, J. Wind, and P. de Theije, *Detection, localization and tracking of aircraft using acoustic vector sensors,* Inter Noise 2011 Proceedings, Osaka, Japan , 4 (2011).

[3] H.-E. de Bree, *An overview of microflown technologies,* Acta acustica united with Acustica **89**, 163 (2003).

[4] H.-E. Bree, P. Leussink, T. Korthorst, H. Jansen, T. Lammerink, and M. Elwenspoek, *The µ-flown: A novel device measuring acoustical flows,* (1995).

[5] H.-E. De Bree, *The microflown e-book,* Microflown Technologies, Arnhem (2007).

[6] A. Nehorai and E. Paldi, *Acoustic vector-sensor array processing,* IEEE Transactions on Signal Processing, **42**, 2481 (1994).

[7] J. P. Kitchens, *Acoustic vector-sensor array processing,* Ph.D. thesis, Massachusetts Institute of Technology (2010).

[8] J. Capon, *High-resolution frequency-wavenumber spectrum analysis,* Proceedings of the IEEE **57**, 1408 (1969).

[9] H. L. Van Trees, *Optimum array processing. Part IV of Detection, estimation, and modulation theory* (Wiley-Interscience, New York, 2002).

[10] K. N. Ramamohan, S. P. Chepuri, D. F. Comesana, and G. Leus, *Blind calibration of sparse arrays for doa estimation with analog and one-bit measurements,* IEEE International Conference on Acoustics, Speech and Signal Processing (ICASSP) (2019).

[11] C.-L. Liu and P. Vaidyanathan, *Cramér–Rao bounds for coprime and other sparse arrays, which find more sources than sensors,* Digital Signal Processing **61**, 43 (2017).

[12] F. Jacobsen and V. Jaud, *A note on the calibration of pressure-velocity sound intensity probes,* The Journal of the Acoustical Society of America **120**, 830 (2006).

[13] D. F. Comesaña, T. Koukoulas, B. Piper, and E.-J. Jongh, *Calibration of acoustic particle velocity sensors using a laser based method,* in *23rd International Congress on Sound and Vibration* (2016) pp. 1–8.

[14] T. G. Basten and H.-E. de Bree, *Full bandwidth calibration procedure for acoustic probes containing a pressure and particle velocity sensor,* The Journal of the Acoustical Society of America **127**, 264 (2010).

6

BLIND CALIBRATION FOR ACOUSTIC VECTOR SENSOR ARRAYS

In this paper, we present a calibration algorithm for acoustic vector sensors arranged in a uniform linear array configuration. To do so, we do not use a calibrator source, instead we leverage the Toeplitz blocks present in the data covariance matrix. We develop linear estimators for estimating sensor gains and phases. Further, we discuss the differences of the presented blind calibration approach for acoustic vector sensor arrays in comparison with the approach for acoustic pressure sensor arrays. In order to validate the proposed blind calibration algorithm, simulation results for direction-of-arrival (DOA) estimation with an uncalibrated and calibrated uniform linear array based on minimum variance distortion less response and multiple signal classification algorithms are presented. The calibration performance is analyzed using the Cramér-Rao lower bound of the DOA estimates.

6.1. INTRODUCTION

Direction-of-arrival (DOA) estimation of outdoor acoustic sources using a network of passive sensors is crucial for ground surveillance [1] and target tracking [2]. Traditionally, microphone/acoustic pressure sensor (APS) arrays are deployed for such tasks. However, with the advances in the sensor technology, transducers that are capable of measuring vector quantities such as particle velocity are becoming practically feasible [3–5]. An acoustic vector sensor (AVS) is one such device that can measure both acoustic pressure and particle velocity at a given spatial location [6, 7]. It comprises of an omni-directional microphone and two (or three) particle velocity transducers each aligned along the coordinate axes either in $\mathbb{R}^2$ (or $\mathbb{R}^3$) [5]. An array of AVSs has several advantages compared to an equivalent aperture APS array [6, 8].

For DOA estimation using spatially distributed AVS or APS arrays, many advanced algorithms that yield highly accurate estimates are developed, such as minimum variance distortionless response (MVDR) beamformer [9] and subspace-based methods like multiple signal classification (MUSIC) [10]. However, these algorithms are highly sensitive to sensor position errors, bearing errors, and other modeling parameters such as relative gain and phase variations within as well as among sensors. Although with proper care while building the array the positional and bearing errors can be minimized, modeling parameters usually vary with time and environmental conditions. Therefore, the array has to be calibrated from time to time. In this paper, we focus on gain and phase calibration of AVS arrays.

Currently, sophisticated calibration techniques are employed to correct for the gain and phase mismatch between the pressure and particle velocity channels [11, 12], e.g., using a calibrator source in a controlled environment. The data acquisition electronics (e.g., oscillator and amplifier) of the AVS drifts over period of time and it requires recalibration. Also, the lack of orthogonality between the channels of the particle velocity transducers contribute to the gain and phase mismatch. This means that a calibrator source has to be deployed in the field or the AVSs in the array have to be brought back to the calibration room. To avoid such complications, we explore calibrator-source-free or blind calibration techniques for AVS arrays arranged in a uniform linear array (ULA) configuration. The presented approach is inspired by the blind calibration method for APS ULA presented in [13], wherein the Toeplitz structure in the covariance matrix was utilized. An extension of this approach to any arbitrary array configuration was presented in [**?**]. Even though the covariance matrix of the AVS ULA is not Toeplitz, it has Toeplitz blocks. Due to which, the AVS array cannot be treated as an APS array with a larger aperture for calibration. We exploit the structure in the Covariance matrix to create a linear system of equations to estimate the unknown gain and phase uncertainties. Also, we will discuss the differences between the calibration algorithm for AVS arrays and APS arrays, which is a rather well-studied problem. Once the gain and phase uncertainties are corrected for, any standard DOA estimation technique can be employed.

6.2. SYSTEM MODEL

Consider a ULA of M AVSs. Each AVS consists of three elements (one pressure and two particle velocity transducers), which we denote with the subscripts $\mathscr{P}$, $\mathscr{X}$, and $\mathscr{Y}$ throughout this paper. With the notation, $\mathbf{A}_{\mathscr{M}}$ for $\mathscr{M} \in \{\mathscr{P}, \mathscr{X}, \mathscr{Y}\}$, we mean $\mathbf{A}_{\mathscr{P}}$, $\mathbf{A}_{\mathscr{X}}$, and $\mathbf{A}_{\mathscr{Y}}$, respectively.

Let us denote the *unknown* gain and phase parameters as $\psi \in \mathbb{R}^{3M}$ and $\phi \in \mathbb{C}^{3M}$, respectively, where these vectors have components related to the transducers in the array, i.e.,

$$\psi = \left[\psi_{\mathscr{P}}^T, \psi_{\mathscr{X}}^T, \psi_{\mathscr{Y}}^T\right]^T, \quad \text{and} \quad \phi = \left[\phi_{\mathscr{P}}^T, \phi_{\mathscr{X}}^T, \phi_{\mathscr{Y}}^T\right]^T,$$

with length-M vectors $\psi_{\mathscr{M}} = [\psi_{\mathscr{M},1} \ldots \psi_{\mathscr{M},M}]^T$ and $\phi_{\mathscr{M}} = [e^{\mathrm{j}\phi_{\mathscr{M},1}} \ldots e^{\mathrm{j}\phi_{\mathscr{M},M}}]^T$ denoting the gain and phase vectors related to the type-$\mathscr{M}$ transducer in the array.

Assume that there are D far-field narrowband uncorrelated sources with wavenumber $k = 2\pi/\lambda$ impinging on the array from azimuth angles $\boldsymbol{\theta} = [\theta_1\ \theta_2\ \ldots\ \theta_D]^T \in \mathbb{R}^{D\times 1}$. The received signal can be collected in $\mathbf{r}(t) \in \mathbb{C}^{3M\times 1}$ and is given by

$$\mathbf{r}(t) \quad = \quad \mathrm{diag}\left(\psi\right)\mathrm{diag}\left(\phi\right)\left[\mathbf{A}(\boldsymbol{\theta})\,\mathbf{s}(t) + \mathbf{n}(t)\right]. \tag{6.1}$$

where $\mathbf{s}(t) = [s_1(t)\ s_2(t)\ \cdots\ s_D(t)]^T \in \mathbb{C}^D$ is the source signal vector, $\mathbf{n}(t)$ is the noise vector, and $\mathbf{A}(\boldsymbol{\theta}) = [\mathbf{a}(\theta_1)\ \mathbf{a}(\theta_2)\ \cdots\ \mathbf{a}(\theta_D)] \in \mathbb{C}^{3M\times D}$ is the array manifold matrix. The dth column of $\mathbf{A}(\boldsymbol{\theta})$ is given by the corresponding length-$3M$ AVS array steering vector

$$\begin{aligned}\mathbf{a}(\theta_d) &= [\mathbf{a}_{\mathscr{P}}^T(\theta_d)\ \cos(\theta_d)\mathbf{a}_{\mathscr{P}}^T(\theta_d)\ \sin(\theta_d)\mathbf{a}_{\mathscr{P}}^T(\theta_d)]^T,\\ &= [\mathbf{a}_{\mathscr{P}}^T(\theta_d)\ \mathbf{a}_{\mathscr{X}}^T(\theta_d)\ \mathbf{a}_{\mathscr{Y}}^T(\theta_d)]^T,\end{aligned}$$

with

$$\mathbf{a}_{\mathscr{P}}(\theta_d) = \left[1\ e^{\mathrm{j}kl\cos(\theta_d)}\ \ldots\ e^{\mathrm{j}k(M-1)l\cos(\theta_d)}\right]^T \in \mathbb{C}^{M\times 1},$$

being the equivalent APS array steering vector. Here, l is the inter-element spacing.

In this work, we assume that $\mathbf{s}(t)$ and $\mathbf{n}(t)$ are uncorrelated, and that they are realizations of an independent and identically distributed (i.i.d.) complex Gaussian process with zero mean and unknown covariance matrix $\mathbf{R_s} = \mathbb{E}\{\mathbf{s}(t)\mathbf{s}^H(t)\}$ and $\mathbf{R_n} = \mathbb{E}\{\mathbf{n}(t)\mathbf{n}^H(t)\}$, respectively. Without loss of generality, we assume that $\mathbf{R_s}$ is a diagonal matrix with unknown entries (i.e., sources are uncorrelated) and $\mathbf{R_n} = \sigma_n^2\mathbf{I}$ (i.e., we absorb the factor that models the noise difference between the pressure and velocity channels [14] in the calibration parameters).

The data covariance matrix $\mathbf{R} = \mathbb{E}\{\mathbf{r}(t)\mathbf{r}^H(t)\} \in \mathbb{C}^{3M\times 3M}$ can be written as

$$\mathbf{R} \quad = \quad \mathrm{diag}\left(\psi\right)\mathrm{diag}\left(\phi\right)\mathbf{Q}\,\mathrm{diag}(\phi^*)\mathrm{diag}\left(\psi\right), \tag{6.2}$$

where $(\cdot)^*$ denotes complex conjugation and $\mathbf{Q} = \mathbf{A}(\boldsymbol{\theta})\mathbf{R_s}\mathbf{A}^H(\boldsymbol{\theta}) + \mathbf{R_n}$. The covariance matrices $\mathbf{Q}$ and $\mathbf{R}$ comprises blocks of matrices as

$$\mathbf{R} = \begin{bmatrix}\mathbf{R}_{\mathscr{P}\mathscr{P}} & \mathbf{R}_{\mathscr{P}\mathscr{X}} & \mathbf{R}_{\mathscr{P}\mathscr{Y}}\\ \mathbf{R}_{\mathscr{X}\mathscr{P}} & \mathbf{R}_{\mathscr{X}\mathscr{X}} & \mathbf{R}_{\mathscr{X}\mathscr{Y}}\\ \mathbf{R}_{\mathscr{Y}\mathscr{P}} & \mathbf{R}_{\mathscr{Y}\mathscr{X}} & \mathbf{R}_{\mathscr{Y}\mathscr{Y}}\end{bmatrix};\ \mathbf{Q} = \begin{bmatrix}\mathbf{Q}_{\mathscr{P}\mathscr{P}} & \mathbf{Q}_{\mathscr{P}\mathscr{X}} & \mathbf{Q}_{\mathscr{P}\mathscr{Y}}\\ \mathbf{Q}_{\mathscr{X}\mathscr{P}} & \mathbf{Q}_{\mathscr{X}\mathscr{X}} & \mathbf{Q}_{\mathscr{X}\mathscr{Y}}\\ \mathbf{Q}_{\mathscr{Y}\mathscr{P}} & \mathbf{Q}_{\mathscr{Y}\mathscr{X}} & \mathbf{Q}_{\mathscr{Y}\mathscr{Y}}\end{bmatrix},$$

where

$$\mathbf{R}_{\mathscr{M}\mathscr{N}} = \mathrm{diag}(\psi_{\mathscr{M}})\mathrm{diag}(\phi_{\mathscr{M}})\mathbf{Q}_{\mathscr{M}\mathscr{N}}\,\mathrm{diag}(\phi_{\mathscr{N}}^*)\mathrm{diag}(\psi_{\mathscr{N}}); \tag{6.3}$$

$$\mathbf{Q}_{\mathscr{M}\mathscr{N}} = \sum_{d=1}^{D}[\mathbf{R_s}]_{dd}\,\mathbf{a}_{\mathscr{M}}(\theta_d)\mathbf{a}_{\mathscr{N}}^H(\theta_d) + \sigma_n^2\mathbf{I}, \tag{6.4}$$

for $\mathcal{M},\mathcal{N} \in \{\mathscr{P},\mathscr{X},\mathscr{Y}\}$ are each Toeplitz.

In practice, the true covariance matrix is not available and we have to use a sample covariance matrix, which is evaluated from a finite number of time snapshots, N, as

$$\hat{\mathbf{R}} = \frac{1}{N}\sum_{t=1}^{N} \mathbf{r}(t)\mathbf{r}^H(t). \tag{6.5}$$

For the sake of brevity, henceforth we simply use $\mathbf{R}$ instead of $\hat{\mathbf{R}}$. In what follows, we present linear estimators for ψ and ϕ by taking into account the structure of the covariance matrix.

6.3. ESTIMATION OF SENSOR GAINS

In this section, we derive a least-squares estimator for ψ. To do so, we process each subblock of the data covariance matrix separately to build a linear system of equations in ψ. From (6.3), we have

$$\left|[\mathbf{R}_{\mathcal{M}\mathcal{N}}]_{ij}\right| = \left|[\mathbf{Q}_{\mathcal{M}\mathcal{N}}]_{ij}\right| \psi_{\mathcal{M},i}\psi_{\mathcal{N},j},\ \forall i,j = 1,2,\dots M, \tag{6.6}$$

where $|\cdot|$ denotes the modulus. Since the subblock $\mathbf{Q}_{\mathcal{M}\mathcal{N}}$ is Toeplitz, we have, for all $i-j = k-l$, the following relation

$$\log\left(\frac{\left|[\mathbf{R}_{\mathcal{M}\mathcal{N}}]_{ij}\right|}{|[\mathbf{R}_{\mathcal{M}\mathcal{N}}]_{kl}|}\right) = \log(\psi_{\mathcal{M},i}) + \log(\psi_{\mathcal{N},j}) - \log(\psi_{\mathcal{M},k}) - \log(\psi_{\mathcal{N},l}). \tag{6.7}$$

This is because, for all $i-j = k-l$, $\left|[\mathbf{R}_{\mathcal{M}\mathcal{N}}]_{ij}\right|$ and $|[\mathbf{R}_{\mathcal{M}\mathcal{N}}]_{kl}|$ lie along the same diagonal and due to the Toeplitz structure of the subblock $\mathbf{Q}_{\mathcal{M}\mathcal{N}}$, those terms are eliminated resulting in an equation corresponding to the unknown gains. However, when only a finite number of snapshots are available, (6.7) is not consistent. Now, we can collect the measurements $\{\log(|[\mathbf{R}_{\mathcal{M}\mathcal{N}}]_{ij}|) - \log(|[\mathbf{R}_{\mathcal{M}\mathcal{N}}]_{kl}|), \forall i-j = k-l\}$ in the vector $\mathbf{g}_{\mathcal{M}\mathcal{N}}$, and repeat the same procedure for all the subblocks in $\mathbf{R}$.

Taking all the non-redundant relations within the diagonal subblocks $\mathbf{R}_{\mathscr{P}\mathscr{P}}, \mathbf{R}_{\mathscr{X}\mathscr{X}}$, and $\mathbf{R}_{\mathscr{Y}\mathscr{Y}}$, we get a total of $k_{z1} = 3\sum_{i=2}^{M} 0.5\,i(i-1)$ equations, while taking the upper-diagonal subblocks along the $\mathbf{R}_{\mathscr{P}\mathscr{X}}, \mathbf{R}_{\mathscr{P}\mathscr{Y}}$, and $\mathbf{R}_{\mathscr{X}\mathscr{Y}}$, we get $k_{z2} = 3(\sum_{i=2}^{M} 0.5i(i-1) + \sum_{i=2}^{M-1} 0.5i(i-1))$ equations. In total, we have $k_z = k_{z1} + k_{z2}$ equations, which can be compactly written as

$$\begin{bmatrix} \mathbf{g}_{\mathscr{P}\mathscr{P}} \\ \mathbf{g}_{\mathscr{X}\mathscr{X}} \\ \mathbf{g}_{\mathscr{Y}\mathscr{Y}} \\ \mathbf{g}_{\mathscr{P}\mathscr{X}} \\ \mathbf{g}_{\mathscr{P}\mathscr{Y}} \\ \mathbf{g}_{\mathscr{X}\mathscr{Y}} \end{bmatrix} = \begin{bmatrix} \mathbf{H}_1 & \mathbf{0} & \mathbf{0} \\ \mathbf{0} & \mathbf{H}_1 & \mathbf{0} \\ \mathbf{0} & \mathbf{0} & \mathbf{H}_1 \\ \mathbf{H}_2 & \mathbf{H}_3 & \mathbf{0} \\ \mathbf{H}_2 & \mathbf{0} & \mathbf{H}_3 \\ \mathbf{0} & \mathbf{H}_2 & \mathbf{H}_3 \end{bmatrix} \begin{bmatrix} \tilde{\psi}_{\mathscr{P}} \\ \tilde{\psi}_{\mathscr{X}} \\ \tilde{\psi}_{\mathscr{Y}} \end{bmatrix} \Leftrightarrow \mathbf{g} = \mathbf{H}\tilde{\psi}, \tag{6.8}$$

where $\mathbf{H} \in \mathbb{R}^{k_z \times 3M}$ and $\tilde{\psi}_{\mathcal{M}} = \left[\log(\psi_{\mathcal{M},1}) \dots \log(\psi_{\mathcal{M},M})\right]^T$ for $\mathcal{M} \in \{\mathscr{P},\mathscr{X},\mathscr{Y}\}$ are each of length M.

The rows of $\mathbf{H}_1$ have one of the following forms [13]:

1. $[\dots 0\,2\,0 \dots 0\,-2\,0 \dots]$ when $i = j$ and $k = l$. All the elements in this row are zero except for a 2 and -2 at the ith and kth positions, respectively.

2. $[\ldots 0\,1\,0 \ldots 0\,-1\,0 \ldots]$ when $i \neq j$ and $j = k$. All the elements in this row are zero except for a 1 and -1 at the ith and lth positions, respectively.

3. $[\ldots 0\,1\,0 \ldots 0\,1\,0 \ldots 0\,-1\,0 \ldots 0\,-1\,0 \ldots]$ when i, j, k and l are distinct. All the elements in this row are zero except for 1, 1, -1 and -1 at the ith, jth, kth, and lth positions, respectively.

The rows of $\mathbf{H}_2$ and $\mathbf{H}_3$ have one of the following forms:

1. All the elements in the rows of $\mathbf{H}_2$ are zero except for a 1 and -1 at the ith and kth positions, respectively, and they will be of the form $[\ldots 0\,1\,0 \ldots 0\,-1\,0 \ldots]$.

2. All the elements in the rows of $\mathbf{H}_3$ are zero except for a 1 and -1 at the jth and lth positions, respectively, and they will be of the form $[\ldots 0\,1\,0 \ldots 0\,-1\,0 \ldots]$.

It is easy to see that the matrices $\mathbf{H}_1$, $\mathbf{H}_2$, and $\mathbf{H}_3$ each have the all-one vector $\mathbf{1}$ in its nullspace. This means that, $\mathbf{H}$ has $3M-3$ nonzero singular values with the vectors $\left[\mathbf{1}^T\,\mathbf{0}^T\,\mathbf{0}^T\right]^T$, $\left[\mathbf{0}^T\,\mathbf{1}^T\,\mathbf{0}^T\right]^T$, $\left[\mathbf{0}^T\,\mathbf{0}^T\,\mathbf{1}^T\right]^T$ in its nullspace. Equations corresponding to the cross correlations between $\mathscr{P}, \mathscr{X}$, and $\mathscr{Y}$ transducers, do not improve the rank of the system, but the additional equations generated from the cross blocks of $\mathbf{R}$ might be useful to improve the estimates when only a finite number of snapshots are available.

As the matrix $\mathbf{H}$ is not full column rank, one reference AVS with known gain is needed to uniquely determine the unknown gains. In other words, we can estimate the sensor gains $\tilde{\psi}_{\mathscr{M}}$, for $\mathscr{M} \in \{\mathscr{P}, \mathscr{X}, \mathscr{Y}\}$, up to an arbitrary multiplicative factor. To do so, let us include the known reference gains to obtain

$$\begin{bmatrix} \mathbf{g}_{\mathscr{P}\mathscr{P}} \\ \mathbf{g}_{\mathscr{X}\mathscr{X}} \\ \mathbf{g}_{\mathscr{Y}\mathscr{Y}} \\ \mathbf{g}_{\mathscr{P}\mathscr{X}} \\ \mathbf{g}_{\mathscr{P}\mathscr{Y}} \\ \mathbf{g}_{\mathscr{X}\mathscr{Y}} \\ \hline \mathbf{0} \end{bmatrix} = \left[\begin{array}{ccc} \mathbf{H}_1 & \mathbf{0} & \mathbf{0} \\ \mathbf{0} & \mathbf{H}_1 & \mathbf{0} \\ \mathbf{0} & \mathbf{0} & \mathbf{H}_1 \\ \mathbf{H}_2 & \mathbf{H}_3 & \mathbf{0} \\ \mathbf{H}_2 & \mathbf{0} & \mathbf{H}_3 \\ \mathbf{0} & \mathbf{H}_2 & \mathbf{H}_3 \\ \hline \mathbf{e}_1^T & \mathbf{0} & \mathbf{0} \\ \mathbf{0} & \mathbf{e}_1^T & \mathbf{0} \\ \mathbf{0} & \mathbf{0} & \mathbf{e}_1^T \end{array}\right] \begin{bmatrix} \tilde{\psi}_{\mathscr{P}} \\ \tilde{\psi}_{\mathscr{X}} \\ \tilde{\psi}_{\mathscr{Y}} \end{bmatrix} \Leftrightarrow \tilde{\mathbf{g}} = \tilde{\mathbf{H}}\tilde{\psi}, \tag{6.9}$$

where $\mathbf{e}_1$ is the first column of the identity matrix of size $M \times M$. Here, we pick, without loss of generality, the 1st AVS as the reference. Then, the sensor gains can be computed using least squares as

$$\hat{\tilde{\psi}} = (\tilde{\mathbf{H}}^T\tilde{\mathbf{H}})^{-1}\tilde{\mathbf{H}}^T\tilde{\mathbf{g}}.$$

6.4. ESTIMATION OF SENSOR PHASES

After computing the sensor gains, in order to estimate the elements of ϕ, we again process each subblock of $\mathbf{R}$ separately. From (6.3), we have

$$\text{angle}([\mathbf{R}_{\mathscr{M}\mathscr{N}}]_{ij}) = \text{angle}([\mathbf{Q}_{\mathscr{M}\mathscr{N}}]_{ij}) + \phi_{\mathscr{M},i} - \phi_{\mathscr{N},j}, \tag{6.10}$$

for $i, j = 1, \ldots, M$. Here, angle$(\cdot)$ denotes the phase. Using the fact that each subblock $\mathbf{Q}_{\mathscr{M}\mathscr{N}}$ is Toeplitz, we obtain the relation

$$\text{angle}([\mathbf{R}_{\mathscr{M}\mathscr{N}}]_{ij}) - \text{angle}([\mathbf{R}_{\mathscr{M}\mathscr{N}}]_{kl}) = \phi_{\mathscr{M},i} - \phi_{\mathscr{N},j} - \phi_{\mathscr{M},k} + \phi_{\mathscr{N},l}, \tag{6.11}$$

for all $i-j=k-l$. We can now collect the measurements $\{\text{angle}([\mathbf{R}_{\mathscr{M}\mathscr{N}}]_{ij})-\text{angle}([\mathbf{R}_{\mathscr{M}\mathscr{N}}]_{kl}), \forall\, i-j=k-l\}$ in a vector $\mathbf{p}_{\mathscr{M}\mathscr{N}}$, and repeat the same procedure for all the subblocks in $\mathbf{R}$.

Taking all the nonredundant relations within the diagonal subblocks $\mathbf{R}_{\mathscr{P}\mathscr{P}}, \mathbf{R}_{\mathscr{X}\mathscr{X}}$, and $\mathbf{R}_{\mathscr{Y}\mathscr{Y}}$, we get $k_{p1}=3\sum_{i=2}^{M-1}0.5i(i-1)$ equations while taking the upper-diagonal subblocks along the $\mathbf{R}_{\mathscr{P}\mathscr{X}}, \mathbf{R}_{\mathscr{P}\mathscr{Y}}$, and $\mathbf{R}_{\mathscr{X}\mathscr{Y}}$, we get a total of $k_{p2}=3(\sum_{i=2}^{M}0.5i(i-1)+\sum_{i=2}^{M-1}0.5i(i-1))$ equations that are of the form as in (6.11). In total, we have $k_p=k_{p1}+k_{p2}$ equations of the form

$$\begin{bmatrix}\mathbf{p}_{\mathscr{P}\mathscr{P}}\\ \mathbf{p}_{\mathscr{X}\mathscr{X}}\\ \mathbf{p}_{\mathscr{Y}\mathscr{Y}}\\ \mathbf{p}_{\mathscr{P}\mathscr{X}}\\ \mathbf{p}_{\mathscr{P}\mathscr{Y}}\\ \mathbf{p}_{\mathscr{X}\mathscr{Y}}\end{bmatrix}=\begin{bmatrix}\mathbf{G}_1 & \mathbf{0} & \mathbf{0}\\ \mathbf{0} & \mathbf{G}_1 & \mathbf{0}\\ \mathbf{0} & \mathbf{0} & \mathbf{G}_1\\ \mathbf{H}_2 & -\mathbf{H}_3 & \mathbf{0}\\ \mathbf{H}_2 & \mathbf{0} & -\mathbf{H}_3\\ \mathbf{0} & \mathbf{H}_2 & -\mathbf{H}_3\end{bmatrix}\begin{bmatrix}\tilde{\phi}_{\mathscr{P}}\\ \tilde{\phi}_{\mathscr{X}}\\ \tilde{\phi}_{\mathscr{Y}}\end{bmatrix}\Leftrightarrow \mathbf{p}=\mathbf{G}\tilde{\phi}, \tag{6.12}$$

where $\mathbf{G}\in\mathbb{R}^{k_p\times 3M}$ and $\tilde{\phi}_{\mathscr{M}}=\left[\phi_{\mathscr{M},1}\ldots\phi_{\mathscr{M},M}\right]^T$ for $\mathscr{M}\in\{\mathscr{P},\mathscr{X},\mathscr{Y}\}$ are each of length M.

The rows of $\mathbf{G}_1$ have one of the following forms:

1. $[\ldots 0\,1\,0\ldots 0\,-2\,0\ldots 0\,1\,0\ldots]$ when $i\neq j$ and $j=k$. All the elements in this row are zero except for a 1,-2 and 1 at the ith, $j(=k)$th, and the lth positions, respectively.

2. $[\ldots 0\,1\,0\ldots 0\,-1\,0\ldots 0\,-1\,0\ldots 0\,1\,0\ldots]$ when i, j, k and l are distinct. All the elements in this row are zero except for 1, -1, -1, and 1 at the ith, jth, kth and lth positions, respectively.

The matrix $\mathbf{G}_1$ has $M-2$ nonzero singular values and there are two $M\times 1$ vectors, namely, $[1\,1\ldots 1]^T$ and $[1\,2\ldots M]^T$ in its nullspace. However, $\mathbf{G}$ has $3M-4$ nonzero singular values with four $3M\times 1$ vectors in its nullspace. Those include $\left[\mathbf{1}^T\,\mathbf{0}^T\,\mathbf{0}^T\right]^T$, $\left[\mathbf{0}^T\,\mathbf{1}^T\,\mathbf{0}^T\right]^T$, $\left[\mathbf{0}^T\,\mathbf{0}^T\,\mathbf{1}^T\right]^T$, and $\left[\mathbf{t}^T\,\mathbf{t}^T\,\mathbf{t}^T\right]^T$, where $\mathbf{t}=[1\,2\,3\ldots M]^T$. By exploiting the cross correlations between $\mathscr{P},\mathscr{X}$, and $\mathscr{Y}$ channels, we gain rank, i.e, the rank is increased to $3M-4$ from $3M-6$. This is the main advantage of jointly performing the phase calibration for all the transducer types in the AVS array.

To solve (6.12), when $\mathscr{P},\mathscr{X}$, and $\mathscr{Y}$ channels are processed independently (i.e., without considering the equations related to the cross correlations between the channels), we would require two reference AVSs. In contrast, by considering entire $\mathbf{G}$, we need only one reference AVS and an additional phase reference (it could be any transducer type), as its rank is $3M-4$. Those known phase references are included as additional equations to obtain

$$\left[\begin{array}{c}\mathbf{p}_{\mathscr{P}\mathscr{P}}\\ \mathbf{p}_{\mathscr{X}\mathscr{X}}\\ \mathbf{p}_{\mathscr{Y}\mathscr{Y}}\\ \mathbf{p}_{\mathscr{P}\mathscr{X}}\\ \mathbf{p}_{\mathscr{P}\mathscr{Y}}\\ \mathbf{p}_{\mathscr{X}\mathscr{Y}}\\ \hline \mathbf{0}\end{array}\right]=\left[\begin{array}{ccc}\mathbf{G}_1 & \mathbf{0} & \mathbf{0}\\ \mathbf{0} & \mathbf{G}_1 & \mathbf{0}\\ \mathbf{0} & \mathbf{0} & \mathbf{G}_1\\ \mathbf{H}_2 & -\mathbf{H}_3 & \mathbf{0}\\ \mathbf{H}_2 & \mathbf{0} & -\mathbf{H}_3\\ \mathbf{0} & \mathbf{H}_2 & -\mathbf{H}_3\\ \hline \mathbf{e}_1^T & \mathbf{0} & \mathbf{0}\\ \mathbf{0} & \mathbf{e}_1^T & \mathbf{0}\\ \mathbf{0} & \mathbf{0} & \mathbf{e}_1^T\\ \mathbf{e}_2^T & \mathbf{0} & \mathbf{0}\end{array}\right]\begin{bmatrix}\tilde{\phi}_{\mathscr{P}}\\ \tilde{\phi}_{\mathscr{X}}\\ \tilde{\phi}_{\mathscr{Y}}\end{bmatrix}\Leftrightarrow \tilde{\mathbf{p}}=\tilde{\mathbf{G}}\tilde{\phi}, \tag{6.13}$$

where $\mathbf{e}_1$ and $\mathbf{e}_2$ are, respectively, the first and second columns of the identity matrix of size $M \times M$. Then, the sensor phases can be computed using least squares as

$$\hat{\tilde{\phi}} = (\tilde{\mathbf{G}}^T \tilde{\mathbf{G}})^{-1} \tilde{\mathbf{G}}^T \tilde{\mathbf{p}}.$$

6.5. SIMULATIONS

In this section, we present numerical simulations to illustrate the developed theory. We consider an array consisting of six AVSs arranged in an ULA configuration with an inter-element spacing of $\lambda/2$. Further, the first AVS is considered as a reference with its channels having a nominal gain of 1 and a nominal phase to be 0. For solving (6.13), it is considered that the pressure channel of the first and second AVS as phase reference. We assume five equal-powered sources at DOAs $\boldsymbol{\theta} = [-35°, 68°, 79°, -128°, 137°]^T$.

The spectral plot of the MVDR and MUSIC algorithm are presented in Figure 6.1 and 6.2. Here, we use a signal-to-noise ratio of 0 dB with respect to the source signal and the sample covariance matrix $\hat{\mathbf{R}}$ is formed using $N = 1000$ snapshots. Further, up to 4 dB and 20° (root-mean-square values) of random gain and phase uncertainties with respect to the nominal values, are chosen. For MUSIC, without gain and phase uncertainties the peaks in the spectrum are in the direction of the actual sources (as indicated by dash-dotted black color line and referred to as Ideal). For MVDR without the gain and phase uncertainties, the peaks in the spectrum are in the direction of the actual sources, however, two closely spaced sources at 68° and 79° are not resolved. When the sensors are not calibrated, it can be clearly seen that the DOA estimates are poor and the angular spectral resolution is degraded due to the sensor errors. This plot also shows that both MVDR and MUSIC are highly sensitive to the sensor errors. By following the procedure discussed in this work to estimate the sensor errors, which are then compensated during the calibration step, we can clearly see the improved spectral resolution. It is evident that the sources located at $-35°, -128°, 137°$ are well resolved and with less bias using both MUSIC and MVDR. Further, the MUSIC algorithm can even resolve the two closely spaced sources at 68° and 79°.

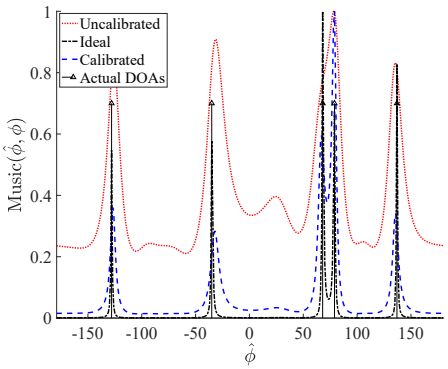


Figure 6.1: Angular spectrum with, without, and after resolving sensor errors using MUSIC algorithm (here, Ideal refers to the scenario without calibration errors).

In order to analyze the performance of the proposed blind calibration algorithm, the root mean squared error (RMSE) variation of the DOA estimates using MUSIC and MVDR

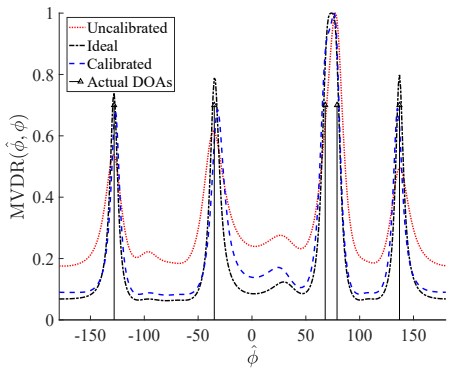


Figure 6.2: Angular spectrum with, without, and after resolving sensor errors using MVDR.

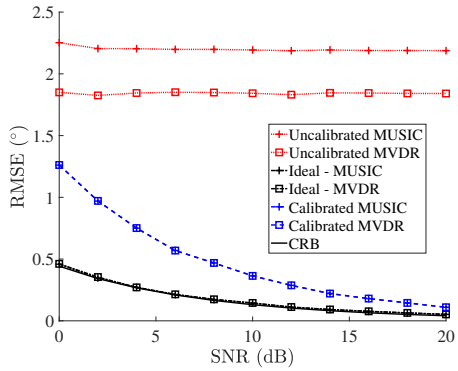


Figure 6.3: RMSE variation of the DOA estimate for increasing SNR using AVS ULA under single source scenario with $M = 3$, $\theta = 60^\circ$ and $N = 300$.

are considered for a single source scenario through Monte Carlo experiments for a fixed gain and phase parameters. Firstly, the RMSE variation of the DOA estimates corresponding to the uncalibrated and calibrated AVS ULA are plotted for different SNRs in Fig. 6.3. Also, the RMSE variation of the AVS ULA without sensor errors and the Cramér-Rao lower bound (CRB) are plotted in Fig. 6.3. For each SNR value, the RMSE value is evaluated using 1000 independent trials. It is observed that as the SNR increases, the RMSE of the DOA estimates for both MUSIC and MVDR of the calibrated ULA approaches to the ideal AVS ULA and the CRB. However, the RMSE of DOA estimates of the uncalibrated ULA does not improve with the SNR.

Finally, in Fig. 6.4, the RMSE variation of the DOA estimates using both MUSIC and MVDR for increasing number of snapshots is shown. Again for evaluating the RMSE values, 1000 Monte Carlo experiments were performed. A similar observation as in Fig. 6.3 can be made, where the calibrated array achieves the CRB as the number of snapshots increase. In a nut shell, the DOA estimates after the proposed calibration are asymptotically (with SNR and/or number of snapshots) efficient as they achieve the CRB.

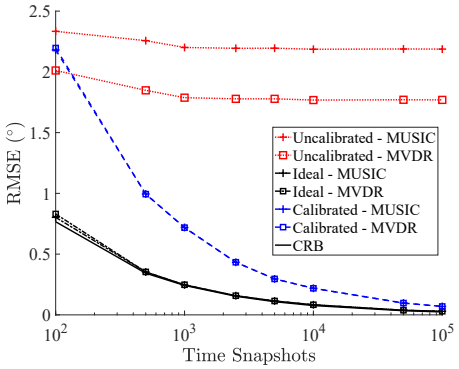


Figure 6.4: RMSE variation of the DOA estimate for increasing number of time snapshots (N) using AVS ULA under single source scenario with $M = 3$, $\theta = 60°$ and SNR = 0 dB.

6.6. CONCLUDING REMARKS

In this paper, we estimate the sensor errors present in the AVS ULA by exploiting the structure in the covariance matrix. In particular, we derived linear estimators for sensor gains and phases. The proposed calibration algorithm does not require a calibrator source, and being a blind algorithm, the unknown gains and phases are estimated relative to a reference sensor. To validate the proposed approach, simulations performed with MUSIC and MVDR for DOA estimation show a significant improvement after calibration.

REFERENCES

[1] H.-E. de Bree, J. Wind, and E. Tijs, *Environmental noise monitoring with acoustic vector sensors,* in *INTER-NOISE and NOISE-CON Congress and Conference Proceedings*, Vol. 2010 (Institute of Noise Control Engineering, 2010) pp. 6225–6231.

[2] H.-E. de Bree, J. Wind, and P. de Theije, *Detection, localization and tracking of aircraft using acoustic vector sensors,* Inter Noise 2011 Proceedings, Osaka, Japan , 4 (2011).

[3] H.-E. de Bree, *An overview of microflown technologies,* Acta acustica united with Acustica **89**, 163 (2003).

[4] H.-E. Bree, P. Leussink, T. Korthorst, H. Jansen, T. Lammerink, and M. Elwenspoek, *The µ-flown: A novel device measuring acoustical flows,* (1995).

[5] H.-E. De Bree, *The microflown e-book*, Microflown Technologies, Arnhem (2007).

[6] A. Nehorai and E. Paldi, *Acoustic vector-sensor array processing*, Signal Processing, IEEE Transactions on **42**, 2481 (1994).

[7] J. P. Kitchens, *Acoustic vector-sensor array processing*, Ph.D. thesis, Massachusetts Institute of Technology (2010).

[8] M. Hawkes and A. Nehorai, *Effects of sensor placement on acoustic vector-sensor array performance,* IEEE Journal of Oceanic Engineering **24**, 33 (1999).

[9] J. Capon, *High-resolution frequency-wavenumber spectrum analysis,* Proceedings of the IEEE **57**, 1408 (1969).

[10] H. L. Van Trees, *Detection, estimation, and modulation theory. Part IV. , Optimum array processing* (Wiley-Interscience, New York, 2002).

[11] T. G. Basten and H.-E. de Bree, *Full bandwidth calibration procedure for acoustic probes containing a pressure and particle velocity sensor,* The Journal of the Acoustical Society of America **127**, 264 (2010).

[12] T. Basten, J. Wind, B. Xu, H.-E. De Bree, and E. Druyvesteyn, *Amplitude, phase, location and orientation calibration of an acoustic vector sensor array, part ii: Experiments,* in *Proceedings of Meetings on Acoustics 159ASA*, Vol. 9 (ASA, 2010) p. 070004.

[13] A. Paulraj and T. Kailath, *Direction of arrival estimation by eigenstructure methods with unknown sensor gain and phase,* in *Acoustics, Speech, and Signal Processing, IEEE International Conference on ICASSP'85.*, Vol. 10 (IEEE, 1985) pp. 640–643.

[14] M. Hawkes and A. Nehorai, *Acoustic vector-sensor correlations in ambient noise,* IEEE Journal of Oceanic Engineering **26**, 337 (2001).

III

Reduced Channel Alternate Configuration AVS Array for DOA Estimation

7

UNIAXIAL ACOUSTIC VECTOR SENSORS FOR DIRECTION-OF-ARRIVAL ESTIMATION

In this paper, a specific reduced-channel Acoustic Vector Sensor (AVS) is proposed comprising one omni-directional microphone and only one particle velocity transducer, such that it can have an arbitrary orientation. Such a reduced transducer configuration is referred to as a Uniaxial AVS (U-AVS). The DOA performance of an array of U-AVSs is analyzed through its beampattern and compared to conventional configurations. It is shown that the U-AVS array beampattern results in an asymptotically biased estimate of the source location and it can be varied by choosing the orientation angles of the particle velocity transducers. Analytical expressions for the asymptotic bias of classical beamforming are proposed and verified both numerically as well as experimentally for Uniform Linear Arrays (ULAs). Furthermore, the Cramér-Rao Bound (CRB) and Mean Square Error (MSE) expressions are derived for a U-AVS array under a single source scenario and they are numerically evaluated for ULA. The implications of changing the orientations of the U-AVSs in the array on the MSE are discussed as well.

7.1. INTRODUCTION

Direction-of-Arrival (DOA) estimation of far-field acoustic sources is usually studied using a set of Acoustic Pressure Sensors (APSs) that are distributed spatially in an array configuration [1]. The interference pattern captured by the array of sensors provides acoustic information regarding the DOA of the far-field sources. The performance analysis of MUSIC (MUltiple SIgnal Classification) [2] and ML (Maximum Likelihood) [3] estimators, as well as the Cramér-Rao lower Bound (CRB) for an APS array have been thoroughly studied in the literature [4, 5]. A comprehensive summary of existing techniques in the field of array signal processing can be found in [6]. On the other hand, with the advent of Micro-Electronic-Mechanical Systems (MEMS) technology it is nowadays feasible to manufacture acoustic probes that are capable of measuring particle velocity along with sound pressure, typically referred to as Acoustic Vector Sensors (AVSs) [7]. Each AVS typically comprises a pressure and three (two) particle velocity transducers in $\mathbb{R}^3$ ($\mathbb{R}^2$). The parameter estimation performance of an AVS array is proven to be better than that of the equivalent APS array as they make use of the interference capture by the array of sensors as well as the intrinsic directionality of the sensors [8, 9]. However, the number of data channels of an AVS measurement system is much larger compared to the traditional APS array, resulting in higher hardware complexity and power requirements. In this work, we consider an alternative configuration of an AVS consisting of less particle velocity transducers, which preserves the benefits of conventional AVSs to a considerable extent.

A large and growing body of literature has developed the foundations of AVSs, including the sensor operation, manufacturing [7] and related array signal processing techniques. Unlike the APS, a single AVS can still be used for DOA estimation by exploiting its intrinsic directionality. In [10], the DOA estimation performance using an AVS is compared with various configurations of an APS array for a wide-band source. The maximum liklihood (ML) DOA estimator using an AVS is derived in [11]. Furthermore, the use of an AVS in source tracking applications has attracted lot of attention in the recent years [12–15]. As an extension, performance bounds on the DOA estimation error (CRB and angular mean square error) using AVS arrays were introduced in [9]. Over the following years, it was demonstrated that AVS arrays have distinct advantages over traditional pressure sensor arrays such as improved array gain and directional sensitivity [8, 16]. In addition, it was demonstrated that an AVS array with a small and limited aperture significantly outperforms an APS array of the same length, as an AVS makes use of the full acoustic information available at its spatial location [8, 9]. This aspect is key to maximize the performance achieved on space-limited platforms such as vehicles, unmanned aerial vehicles or smart glasses [17].

Conventional and MVDR (Minimum Variance Distortion-less Response) beamformers were initially extended to an AVS array in [8, 16], showing that the DOA estimation performance improvements are more significant for smaller arrays, with simple structures, and in low SNR scenarios. Furthermore, it was shown in [18, 19] that the beampattern of an AVS array can be expressed as a function of the conventional APS array, resulting in a combination of the information extracted from the spatial interference between the waveforms observed by the sensors and the intrinsic directivity of the particle velocity transducers. On the other hand, the role played by the array geometry on the performance of DOA estimation is considered in [20]. Based on the linear independence of the array manifold matrix, the maximum number of identifiable sources for under-sampled, over-sampled and critically-sampled AVS Uniform Linear Arrays (ULAs) is discussed in [21]. The extension of DOA es-

timation in the presence of coherent sources using AVS arrays was considered in [12]. Also in [22–24], the discussion of AVS arrays extends to environments with reflections and ambient noise.

A classic AVS considers that all the pressure and vector transducers coincide at the same spatial point, which is difficult to achieve in hardware. In practice, it is currently possible to integrate all the transducers required to construct an AVS within a sphere of 5 mm radius. As an alternative to the AVS, the use of non-collocated transducers comprised of a vector sensor has also been explored in the recent literature. In [25–27], the performance of DOA estimators of multiple spatially spread configurations were considered using a single pressure and up to three orthogonally oriented particle velocity transducers. It was shown that the Root Mean Square Error (RMSE) of the DOA estimates related to those configurations is better than that of one collocated AVS. Similar extensions of various configurations can be found in [28–30].

In this work, we look at a different implementation of an AVS comprising of only two transducers per sensor that are collocated, including one acoustic sound pressure and one particle velocity transducer with arbitrary orientation. Such a configuration is referred to as a Uniaxial AVS (U-AVS), as it captures only one component of the particle velocity field. The application of a U-AVS instead of an AVS removes one (for $\mathbb{R}^2$) or two (for $\mathbb{R}^3$) data channels per sensor, hence substantially lowering hardware and power requirements. The use of multiple U-AVSs can potentially be used for DOA estimation. However, the theoretical limits of such a configuration are not yet well understood. The motivation of this work is to explore how close the performance of a U-AVS array is in comparison with an equivalent aperture AVS array and conventional APS array. The main contributions of this work can be summarized as follows:

- A generalized framework is hereby introduced that accounts for any number of U-AVSs with arbitrary positions and orientations.
- We show that classical beamforming for a U-AVS array results in biased estimates of the DOA, due to which the Mean Square Error (MSE) bound, rather than the Cramér-Rao lower Bound (CRB), is considered as a theoretical criterion for assessing the performance of any DOA estimator and is compared with respect to the equivalent APS / AVS array.
- Both numerical and experimental results are provided in this work to validate the suggested expressions and show the feasibility of a practical implementation of the proposed array configuration.

For the sake of simplicity and without loss of generality, we restrict our discussion to $\mathbb{R}^2$ and focus on the estimation of the azimuth angle. However, the proposed model with a reduced number of particle velocity transducers (i.e., U-AVSs) can be extended to $\mathbb{R}^3$ for the estimation of both the azimuth and elevation angle. On the other hand, all the variants discussed in [25–30] can be considered as a specific case of the U-AVS array, with limited spatial locations. Those variants can be realized by considering either a pressure or a particle velocity transducer present at each spatial location.

The structure of the paper is as follows. In Section 7.2, we consider the measurement model of the multi-sensor multi-source AVS array. In Section 7.3, we describe the measurement model of the U-AVS array and subsequently the beampattern of the U-AVS array is

analyzed. In Section 7.4, based on the first-order Taylor series expansion of the conventional beamforming function, we derive the bias in DOA estimation of a U-AVS array. In Section 7.5, we derive the biased CRB expression for a U-AVS array with a single far-field source in its field of view and further compare it with the CRB expressions of an equivalent aperture APS and AVS array. Finally, we suggest a MSE based design criterion upon which an optimal orientation for each of the U-AVSs in the array can be chosen. In Section 7.6, an experimental study is presented, including details about the measurement process. This study is used to verify the beampattern variations of a U-AVS array and also to validate the proposed analytical expressions that predict the bias induced by the use of a U-AVS array.

The notation used in this paper can be described as follows: Upper (lower) bold face letters are used for matrices (column vectors); $(\cdot)^T$ denotes transpose and $(\cdot)^H$ denotes conjugate transpose; For any vectors $\mathbf{a}$ and $\mathbf{b}$, $(\mathbf{a}\cdot\mathbf{b})$ denotes the inner product between them. $\otimes$ denotes the Kronecker product and $\odot$ denotes the Schur-Hadamard (element-wise) product; $\mathbb{E}\{\cdot\}$ denotes the expectation operator; $\mathrm{tr}(\cdot)$ denotes the trace operator and $\mathbf{I}_n$ is an identity matrix of dimension n.

7.2. REVIEW OF BEAMPATTERN ANALYSIS OF AVS ARRAY

7.2.1. MEASUREMENT MODEL OF AN AVS ARRAY

The measurement data of M AVSs and D far-field narrow-band sources present in a homogeneous isotropic medium at a discrete time index t of the measured snapshot corresponding to frequency f (wavelength λ) can be modeled as [9]:

$$\mathbf{y}(t) = \underbrace{\begin{bmatrix}\mathbf{a}(\phi_1) & \mathbf{a}(\phi_2) & \dots & \mathbf{a}(\phi_D)\end{bmatrix}}_{\mathbf{A}(\phi)} \underbrace{\begin{bmatrix} s_1(t) \\ s_2(t) \\ \cdot \\ \cdot \\ \cdot \\ s_D(t)\end{bmatrix}}_{\mathbf{s}(t)} + \mathbf{n}(t) \in \mathbb{C}^{3M\times 1}, \tag{7.1}$$

where $\phi = \begin{bmatrix}\phi_1 & \phi_2 & \dots & \phi_D\end{bmatrix}^T \in \mathbb{R}^{D\times 1}$ collects the azimuth angles of all the D far-field sources, $\mathbf{s}(t)$ is the source signal vector, $\mathbf{n}(t)$ is the additive noise vector present in the measurement data, and $\mathbf{a}(\phi_d)$ is the AVS array manifold vector of the d^{th} source which can be expressed as $\mathbf{a}(\phi_d) = \mathbf{a}_{\text{p}}(\phi_d) \otimes \mathbf{h}(\phi_d)$. Here $\mathbf{a}_{\text{p}}(\phi_d)$ denotes the equivalent APS array manifold vector and $\mathbf{h}(\phi_d)$ denotes the directional information obtained through the vector sensors,

$$\begin{aligned}\mathbf{a}_{\text{p}}(\phi_d) &= \begin{bmatrix}e^{\mathrm{j}k(\mathbf{r}_1\cdot\mathbf{u}_d)} & e^{\mathrm{j}k(\mathbf{r}_2\cdot\mathbf{u}_d)} & \dots & e^{\mathrm{j}k(\mathbf{r}_M\cdot\mathbf{u}_d)}\end{bmatrix}^T \in \mathbb{C}^{M\times 1}, \\ \mathbf{h}(\phi_d) &= \begin{bmatrix}1 & \mathbf{u}_d^T\end{bmatrix}^T \in \mathbb{R}^{3\times 1},\end{aligned} \tag{7.2}$$

where $k = \frac{2\pi}{\lambda} = \frac{2\pi f}{c}$ is the wave number of the narrow-band source signals, $\mathbf{r}_m$ represents the position of the m^{th} AVS in the array, and $\mathbf{u}_d = \begin{bmatrix}\cos(\phi_d) & \sin(\phi_d)\end{bmatrix}^T$ is the unitary vector in the direction of the d^{th} source. In the further discussion, it is assumed that the source and noise signals are a realization of an independent and identically distributed

(i.i.d.), zero mean complex Gaussian process. The covariance matrix of $\mathbf{s}(t)$ is assumed to be $\mathbf{R}_\mathrm{s} = \mathbb{E}\{\mathbf{s}(t)\mathbf{s}^H(t)\} \in \mathbb{C}^{D\times D}$. The noise covariance matrix is modeled as $\mathbf{R}_\mathrm{n} = \mathbb{E}\{\mathbf{n}(t)\mathbf{n}^H(t)\} = \sigma_\mathrm{n}^2\mathbf{\Sigma} \in \mathbb{C}^{3M\times 3M}$, where $\mathbf{\Sigma}$ is a known positive definite Hermitian matrix. For a single AVS, $\mathbf{\Sigma}$ is given as:

$$\mathbf{\Sigma} = \begin{bmatrix} 1 & \mathbf{0}^T \\ \mathbf{0} & \beta\mathbf{I}_2 \end{bmatrix} \in \mathbb{C}^{3\times 3}, \tag{7.3}$$

where β is a gain term, that models the noise difference between the pressure and velocity channels. For the sake of simplicity, we consider $\mathbf{\Sigma} = \mathbf{I}_{3M}$ (or $\beta = 1$ for a single sensor). In practice, $\mathbf{\Sigma}$ can be estimated by assessing the noise floor of the sensors in the array. The effect of $\mathbf{\Sigma}$ (or β for a single sensor) is studied in [8, 18, 20, 23].

7.2.2. BEAMPATTERN OF AN AVS ARRAY

Based on the measurement data model of the AVS array, the beampattern for a single source at DOA ϕ can be expressed as:

$$B(\hat{\phi}) = |\mathbf{w}^H(\hat{\phi})\,\mathbf{a}(\phi)|,\ -\pi < \hat{\phi} \le \pi \tag{7.4}$$

where $\mathbf{w}(\hat{\phi})$ is the weighting function, which is explicitly shown to be dependent on the scanning angle $\hat{\phi}$. The choice of $\mathbf{w}(\hat{\phi}) = \mathbf{a}(\hat{\phi})$ results in the spatial response of the matched filter, leading to

$$\begin{aligned} B(\hat{\phi},\phi) &= |\mathbf{a}^H(\hat{\phi})\mathbf{a}(\phi)|, \\ &= \left|\left(\mathbf{h}^H(\hat{\phi})\mathbf{h}(\phi)\right)\left(\mathbf{a}_\mathrm{p}^H(\hat{\phi})\mathbf{a}_\mathrm{p}(\phi)\right)\right|, \\ &= \underbrace{\left(1+\cos(\hat{\phi})\cos(\phi)+\sin(\hat{\phi})\sin(\phi)\right)}_{\mathrm{VGM}(\hat{\phi},\phi)} \\ &\quad \underbrace{\left|\left(e^{\mathrm{j}k\left(\mathbf{r}_1\cdot\mathbf{u}(\phi)-\mathbf{r}_1\cdot\mathbf{u}(\hat{\phi})\right)}+\ldots+e^{\mathrm{j}k\left(\mathbf{r}_M\cdot\mathbf{u}(\phi)-\mathbf{r}_M\cdot\mathbf{u}(\hat{\phi})\right)}\right)\right|}_{B_\mathrm{p}(k,\hat{\phi},\phi)}. \end{aligned} \tag{7.5}$$

The expression in eq. (7.5) is similar to the expressions derived in [18] and it can be further simplified if the sensors of the array are arranged in a Uniform Linear Array (ULA) configuration along the x-axis with inter-sensor spacing d. Then the $B_\mathrm{p}(k,\hat{\phi},\phi)$ term in beampattern expression eq. (7.5) can be modified as:

$$B_\mathrm{p}(k,\hat{\phi},\phi) = \underbrace{M\left|\frac{\mathrm{sinc}\left(\frac{kd}{2}M\left(\cos(\phi)-\cos(\hat{\phi})\right)\right)}{\mathrm{sinc}\left(\frac{kd}{2}\left(\cos(\phi)-\cos(\hat{\phi})\right)\right)}\right|}_{\text{APS ULA beampattern}}. \tag{7.6}$$

Here, the beampattern expression is described explicitly as a function of k, $\hat{\phi}$ and ϕ for the sake of analyzing beampatterns with changes in those parameters. It is interesting to note that the beampattern of an AVS ULA $B(k,\hat{\phi},\phi)$ is expressed as a product of the equivalent APS ULA beampattern $B_\mathrm{p}(k,\hat{\phi},\phi)$ and a Velocity Gain Modulation (VGM) term $\mathrm{VGM}(\hat{\phi},\phi)$. It should be noted that the $\mathrm{VGM}(\hat{\phi},\phi)$ term is independent of the number of sensors M and

the wave number k of the source signal. Furthermore, eq. (7.6) can also be expressed in terms of the frequency of the source signal by substituting $k \cdot d = \frac{\pi f}{f_d}$, where $f_d = \frac{c}{2d}$ is the design frequency of the array. The presence of the VGM term significantly attenuates the side lobes, suppresses left/right ambiguity and renders its applicability for DOA estimation under changes of the source signal frequency. An extended discussion on the beampattern of an AVS array can be found in [31].

7.3. BEAMPATTERN ANALYSIS OF U-AVS ARRAY

7.3.1. MEASUREMENT MODEL OF A U-AVS ARRAY

We shall now consider a U-AVS based array with M sensors located at arbitrary positions indicated by the position vectors $\mathbf{r}_1, \mathbf{r}_2, ..., \mathbf{r}_M$ and D far-field sound sources located in the direction pointed by the unit vectors $\mathbf{u}_1, \mathbf{u}_2, ..., \mathbf{u}_D$. Each of the U-AVSs consists of a pressure sensor and a single particle velocity transducer, whose orientation is arbitrary and indicated by δ_n. The measurement data $\mathbf{y}(t)$ at a time index t of the measured snapshot corresponding to frequency f (wavelength λ) can be modeled as:

$$\mathbf{y}(t) = \underbrace{\begin{bmatrix}\mathbf{a}(\phi_1,\boldsymbol{\delta}) & \mathbf{a}(\phi_2,\boldsymbol{\delta}) & \dots & \mathbf{a}(\phi_D,\boldsymbol{\delta})\end{bmatrix}}_{\mathbf{A}(\phi,\boldsymbol{\delta})\in\mathbb{C}^{2M\times D}} \mathbf{s}(t) + \mathbf{n}(t) \in \mathbb{C}^{2M\times 1}, \tag{7.7}$$

where $\mathbf{a}(\phi_i,\boldsymbol{\delta}) = \begin{bmatrix} e^{\mathrm{j}k(\mathbf{r}_1\cdot\mathbf{u})} & e^{\mathrm{j}k(\mathbf{r}_1\cdot\mathbf{u})}\cos(\delta_1-\phi) & \dots & e^{\mathrm{j}k(\mathbf{r}_M\cdot\mathbf{u})} & e^{\mathrm{j}k(\mathbf{r}_M\cdot\mathbf{u})}\cos(\delta_M-\phi)\end{bmatrix}^T$ is the array response vector of the ith source with each U-AVS having an arbitrary orientation captured by the vector $\boldsymbol{\delta} = \begin{bmatrix}\delta_1 & \delta_2 & \dots & \delta_M\end{bmatrix}^T$, $\mathbf{s}(t)$ is the source signal vector and $\mathbf{n}(t)$ is the additive noise vector present in the measurement data. In the further discussion, we refer this setup as a U-AVS array with an arbitrary orientation or just a U-AVS array. If all the U-AVSs have the same orientation angle, i.e., $\boldsymbol{\delta} = \delta\begin{bmatrix}1 & 1 & \dots & 1\end{bmatrix}^T$, which is a specific case of a U-AVS array with an arbitrary orientation, we refer to it as a U-AVS array with fixed orientation.

7.3.2. BEAMPATTERN OF A U-AVS ARRAY

Based on the matched filter approach for given sensor orientation angles $\boldsymbol{\delta}$, the beampattern expression from eq. (7.5) for a single source at DOA ϕ is modified as:

$$\begin{aligned} B(\hat{\phi},\phi) &= \left|\mathbf{a}^H(\hat{\phi},\boldsymbol{\delta})\,\mathbf{a}(\phi,\boldsymbol{\delta})\right|, \\ &= \Big|\big(1+\cos(\delta_1-\hat{\phi})\cos(\delta_1-\phi)\big)\,e^{\mathrm{j}k\left(\mathbf{r}_1\cdot\mathbf{u}(\phi)-\mathbf{r}_1\cdot\mathbf{u}(\hat{\phi})\right)} + \dots \\ &\quad + \big(1+\cos(\delta_M-\hat{\phi})\cos(\delta_M-\phi)\big)\,e^{\mathrm{j}k\left(\mathbf{r}_M\cdot\mathbf{u}(\phi)-\mathbf{r}_M\cdot\mathbf{u}(\hat{\phi})\right)}\Big| \end{aligned} \tag{7.8}$$

and for a U-AVS array with fixed orientation (δ), the beampattern expression can be simplified as:

$$B(k,\hat{\phi},\phi) = \mathrm{VGM}(\delta,\hat{\phi},\phi)\,B_{\mathrm{p}}(k,\hat{\phi},\phi), \tag{7.9}$$

where

$$\mathrm{VGM}(\delta,\hat{\phi},\phi) = 1+\cos(\delta-\hat{\phi})\cos(\delta-\phi). \tag{7.10}$$

It can again be observed that eq. (7.9) can be expressed as the product of an equivalent APS array beampattern and the VGM term.

Restricting our study to a ULA as depicted in Figure 7.1, and expressing the beampattern explicitly as a function of $k, \hat{\phi}, \phi$ by substituting $\mathbf{a}(\hat{\phi}, \boldsymbol{\delta})$ of eq. (7.7) into eq. (7.8) results in:

$$\begin{aligned} B(k,\hat{\phi},\phi) = \Big|&\big(1+\cos(\delta_1-\hat{\phi})\cos(\delta_1-\phi)\big)+ \\ &e^{\mathrm{j}kd(\cos(\phi)-\cos(\hat{\phi}))}\big(1+\cos(\delta_2-\hat{\phi})\cos(\delta_2-\phi)\big)+\ldots+ \\ &e^{\mathrm{j}k(M-1)d(\cos(\phi)-\cos(\hat{\phi}))}\big(1+\cos(\delta_M-\hat{\phi})\cos(\delta_M-\phi)\big)\Big|. \end{aligned} \tag{7.11}$$

For a fixed orientation scenario this leads to $B(k,\hat{\phi},\phi) = \mathrm{VGM}(\delta,\hat{\phi},\phi)\, B_{\mathrm{p}}(k,\hat{\phi},\phi)$ with $\mathrm{VGM}(\delta,\hat{\phi},\phi)$ as in eq. (7.10) and $B_p(k,\hat{\phi},\phi)$ as in eq. (7.6). In Figure 7.2, the beampatterns of an AVS, APS,

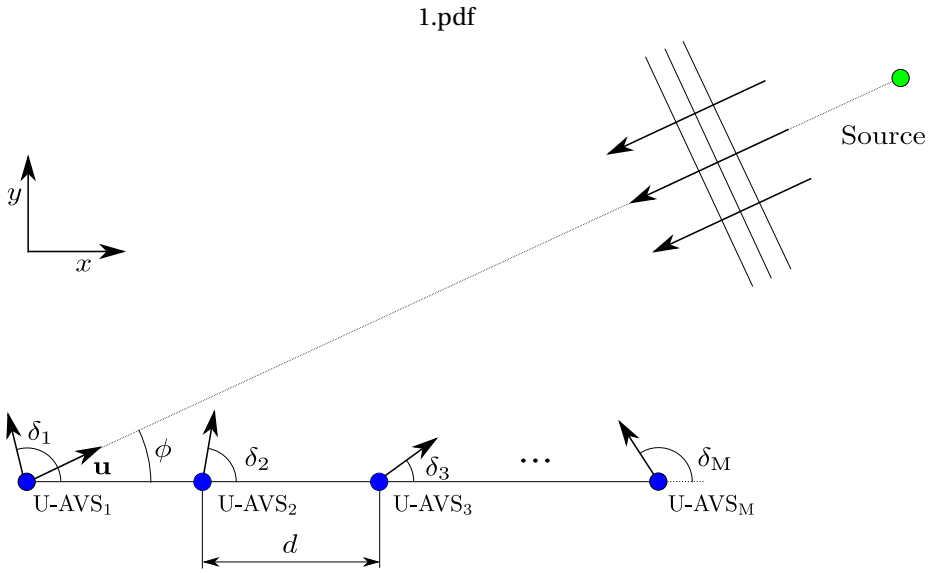
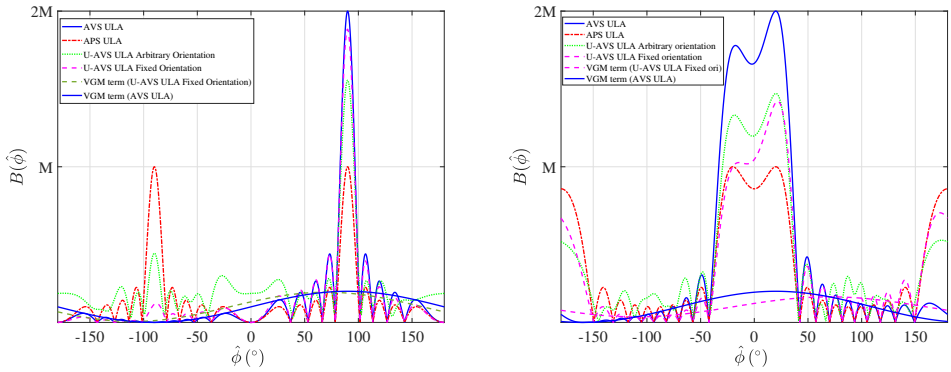


Figure 7.1: ULA of M U-AVSs and one source. Each U-AVS is represented by a combination of a dot corresponding to an APS and a black arrow corresponding to a particle velocity transducer where δ_n represents the orientation of the n^{th} U-AVS.

U-AVS ULA with a fixed and arbitrary orientation for a single source are plotted. The orientation angle, δ, for a fixed orientation configuration is chosen to be 70° and for an arbitrary orientation configuration it is chosen randomly between 0° and 180°. The VGM terms of an AVS ULA and U-AVS ULA with a fixed orientation are also plotted in Figure 7.2.

By observing closely the VGM term of the U-AVS ULA with a fixed orientation in eq. (7.10) and Figure 7.2, the maximum will always occur at $\hat{\phi} = \delta$, irrespective of the actual DOA ϕ. As the APS ULA beampattern always provides an unbiased source location estimate, a bias will be introduced by the VGM term. As the aperture of the ULA increases (i.e., as the number of sensors increases with a fixed inter-sensor spacing d), the main lobe of the APS ULA beampattern becomes narrower whereas the $\mathrm{VGM}(\delta,\hat{\phi},\phi)$ term is unaffected. Hence, the bias is expected to decrease as the aperture increases. On the other hand, for a fixed aperture, the bias can be controlled by changing the orientation angle(s) of the U-AVSs. Hence the rate of decrease of the bias depends on the aperture of the array, sensor orientation angles $\boldsymbol{\delta}$ and



(a) $\phi = 90°$ (b) $\phi = 20°$

Figure 7.2: Beampattern of an AVS, APS and U-AVS ULA with a fixed and arbitrary orientation for $M = 10$, $f = f_d$. For the U-AVS ULA with fixed orientation, $\delta = 70°$, and for a U-AVS ULA with arbitrary orientation, $\boldsymbol{\delta} = [10°, 118°, 75°, 49°, 138°, 85°, 107°, 25°, 144°, 37°]$.

the DOA. In Section 7.4 we shall quantify the behavior of the bias in the DOA estimates of a U-AVS ULA.

7.4. BIAS ANALYSIS OF A U-AVS ARRAY

The DOA estimates based on the spatial response of different beamformers (classical and Capon) or based on MUSIC, are all obtained by maximizing or minimizing the following generalized expression:

$$f(\phi) = \mathbf{a}^H(\phi)\,\mathbf{R}\,\mathbf{a}(\phi), \tag{7.12}$$

where for classical beamforming $\mathbf{R}$ is the covariance matrix ($\mathbf{R}_\mathbf{y}$) of the measurement data ($\mathbf{y}$), for Capon beamforming $\mathbf{R}$ is the inverse of the covariance matrix ($\mathbf{R}_\mathbf{y}^{-1}$), and for MUSIC $\mathbf{R}$ is the outer product of the unitary matrix which spans the null subspace of the covariance matrix ($\mathbf{R}_\mathbf{y}$). The estimates of ϕ (here denoted as ϕ_e) are the maximizers or minimizers of $f(\phi)$. They can be obtained by setting $\frac{\partial f(\phi)}{\partial \phi}\Big|_{\phi=\phi_e} = \frac{\partial f(\phi_e)}{\partial \phi}$ to zero. By using a Taylor series expansion of $\frac{\partial f(\phi_e)}{\partial \phi}$ around the true ϕ and by considering the first two terms in it, we can approximate $\frac{\partial f(\phi_e)}{\partial \phi}$ as in [8]:

$$\begin{aligned} \frac{\partial f(\phi_e)}{\partial \phi} &\approx \frac{\partial f(\phi)}{\partial \phi} + \frac{\partial^2 f(\phi)}{\partial \phi^2}(\phi_e - \phi) = 0, \\ \implies b(\phi) = \underbrace{(\phi_e - \phi)}_{\text{bias}} &\approx \hat{b}(\phi) = -\left[\frac{\partial^2 f(\phi)}{\partial \phi^2}\right]^{-1} \frac{\partial f(\phi)}{\partial \phi}. \end{aligned} \tag{7.13}$$

From eq. (7.13) it can be seen that the bias in the estimate of the source location is approximated based on the first and second derivatives of the spatial spectrum function $f(\cdot)$ evaluated at ϕ. For a U-AVS array and considering the classical beamforming approach, an analytical expression for the bias based on eq. (7.13), where $f(\phi) = \mathbf{a}^H(\phi)\mathbf{R}_\mathbf{y}\mathbf{a}(\phi)$ and

$\mathbf{R_y} = \sigma_s^2 \mathbf{a}(\boldsymbol{\delta},\phi)\mathbf{a}^H(\boldsymbol{\delta},\phi) + \sigma_n^2\mathbf{I}$, is given by (derived in 7.A):

$$\hat{b}(\phi) = -\frac{\mathrm{SNR}\,(RS)+S}{\mathrm{SNR}\left(RJ+L^2+S^2\right)+J+W}, \tag{7.14}$$

where,

$$\begin{aligned}
\mathrm{SNR} &= \frac{\text{Source power}}{\text{Noise power}} = \frac{\sigma_s^2}{\sigma_n^2},\\
R &= M + \sum_{i=1}^{M} \cos^2(\delta_i - \phi),\\
S &= \sum_{i=1}^{M} \cos(\delta_i - \phi)\sin(\delta_i - \phi),\\
J &= -k^2 \sum_{i=1}^{M} \left(\mathbf{r}_i \cdot \frac{\partial \mathbf{u}}{\partial \phi}\right)^2 \left(1+\cos^2(\delta_i-\phi)\right) - \sum_{i=1}^{M} \cos^2(\delta_i-\phi),\\
L &= k \sum_{i=1}^{M} \left(\mathbf{r}_i \cdot \frac{\partial \mathbf{u}}{\partial \phi}\right)\left(1+\cos^2(\delta_i-\phi)\right),\\
W &= k^2 \sum_{i=1}^{M} \left(\mathbf{r}_i \cdot \frac{\partial \mathbf{u}}{\partial \phi}\right)^2 \left(1+\cos^2(\delta_i-\phi)\right) + \sum_{i=1}^{M} \sin^2(\delta_i-\phi).
\end{aligned}$$

If value of SNR tends to 0, the expression for the bias in eq. (7.14) reduces to:

$$\hat{b}_0(\phi) = -\frac{S}{J+W}. \tag{7.15}$$

Asymptotically (i.e., as SNR $\to \infty$), the expression for the bias in eq. (7.14) reduces to:

$$\hat{b}_\infty(\phi) = -\frac{RS}{RJ+L^2+S^2}. \tag{7.16}$$

In practice, the bias ($\hat{b}(\phi)$) in the DOA estimate lies between $\hat{b}_0(\phi)$ and $\hat{b}_\infty(\phi)$ (i.e., $\hat{b}_0(\phi) < \hat{b}(\phi) < \hat{b}_\infty(\phi)$) for $0 < \mathrm{SNR} < \infty$. It is to be noted that the J and L terms in eq. (7.16) will have a more dominant contribution to the bias expression as the number of elements in the array/aperture of the array increases. Based on eq. (7.16) and by considering a U-AVS ULA with a fixed orientation (δ), the derived bias of the source location $\left(\hat{b}(\phi)\right)$ is compared to the bias of the actual estimate $\left(b(\phi)\right)$ obtained by the beampattern expression eq. (7.9) in Figure 7.3. As seen in Figure 7.3, the first order approximation becomes worse if the angle of arrival is closer to the end-fire direction and the sensor orientation is near the broadside region (as seen for $\phi = 10°$ and $\delta = 80°$). It can also be observed that as the number of sensors (or aperture) increases, the approximation of the bias expression improves and the rate of improvement depends on the sensor orientation angle δ and the DOA.

Furthermore, a Monte Carlo simulation for a single source scenario is performed to understand the average bias of a U-AVS ULA. The simulation considers multiple sensors oriented within a variable angular region-of-interest (ROI) centered around the broadside of the array. For a given number of sensors and ROI, 5000 iterations were performed. Within each iteration, both the DOA and the orientations of the sensors are derived from a realization of a uniform distribution within the ROI. The results are presented in Figure 7.4,

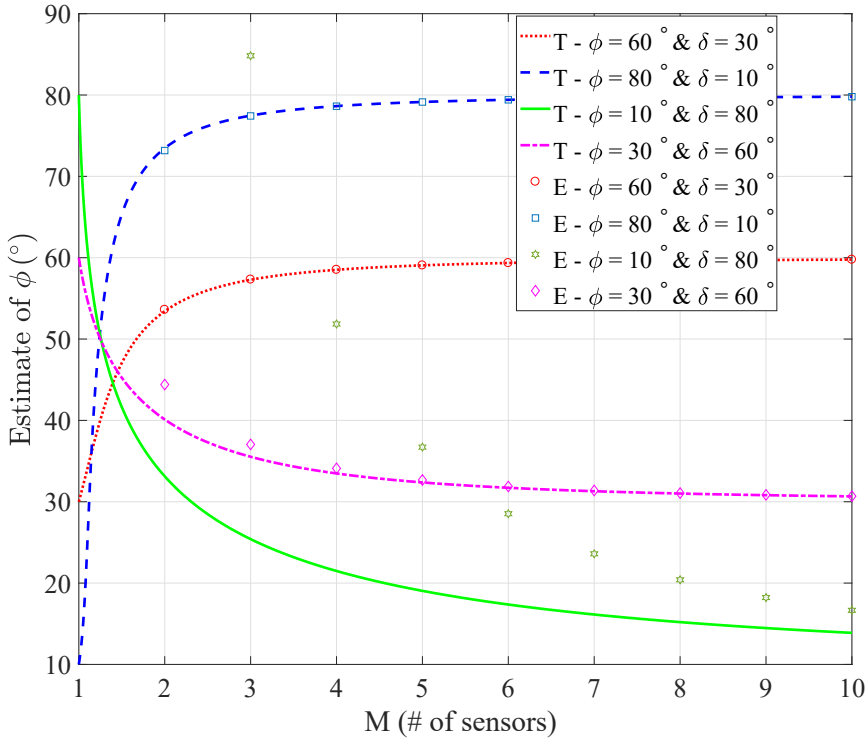


Figure 7.3: Comparison of the source DOA estimates based on a U-AVS ULA with a fixed orientation beampattern (continuous lines, labeled 'T') and based on the asymptotic bias expression eq. (7.16) (discrete markers, labeled 'E') for different DOAs and sensor orientations with an increasing aperture of the ULA.

where the bias is obtained based on the beampattern expression eq. (7.9). A large bias is only observed for configurations with a few sensors and a wide angular ROI. As the number of sensors increases, the bias becomes negligible.

7.5. REVIEW OF CRAMÉR-RAO BOUNDS FOR AVS, U-AVS AND APS ARRAY

To analyze the minimum attainable error covariance matrix of a DOA estimator, we have evaluated the Cramér-Rao lower Bound (CRB) for multiple sensor configurations with a single source in its field-of-view.

7.5.1. CRB FOR MULTI-SENSOR AND MULTI-SOURCE CONFIGURATION

The generalized sensor array data model can be written as:

$$\mathbf{y}(t) \quad = \quad \mathbf{A}(\phi)\mathbf{s}(t) + \mathbf{n}(t), \tag{7.17}$$

where $\phi = \begin{bmatrix} \phi_1 & \phi_2 & \dots & \phi_D \end{bmatrix}^T \in \mathbb{R}^{D\times 1}$.

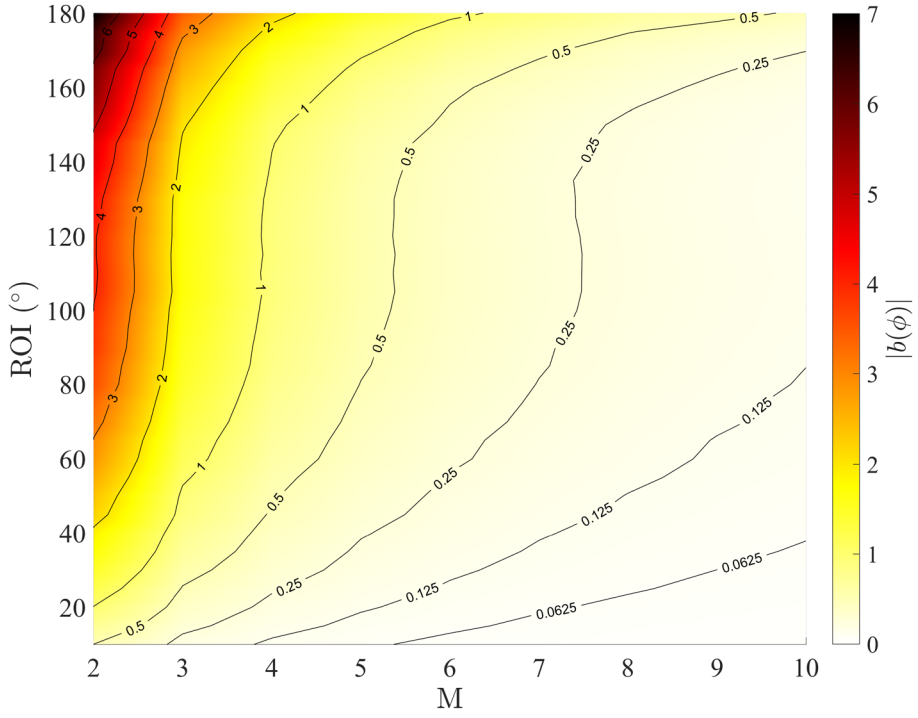


Figure 7.4: Monte Carlo simulation results to study the average bias of the U-AVS ULA with multiple sensors and considering a variable ROI.

Note that eq. (7.17) is same as:

- eq. (7.1) for an AVS array;
- eq. (7.7) for a U-AVS array, except that the dependency on the sensor orientation angles $\boldsymbol{\delta}$ is dropped;
- eq. (7.1) for an APS array, if $\mathbf{h}(\phi_n) = [1]$, $\forall n = 1, \ldots, D$.

It is assumed that the source signals $\mathbf{s}(t)$ and the noise $\mathbf{n}(t)$ are realizations of an i.i.d. complex Gaussian process with zero mean and unknown covariance $\mathbf{R_s}$ and $\mathbf{R_n} = \sigma_n^2 \mathbf{I}$. The CRB on the error covariance matrix of any (locally) unbiased estimator of the vector ϕ of the physical process described in eq. (7.17) is given by [9, 32]:

$$\mathrm{CRB}(\phi) = \mathbf{J}^{-1}(\phi) = \frac{\sigma_n^2}{2N} \left(\mathrm{Re}\left[\mathbf{U} \odot \left(\mathbf{D}^H \boldsymbol{\Pi}_c \mathbf{D} \right)^T \right] \right)^{-1}, \tag{7.18}$$

where $\mathbf{U} = \mathbf{R_s} \left(\mathbf{A}^H \mathbf{A} \mathbf{R_s} + \sigma_n^2 \mathbf{I} \right)^{-1} \mathbf{A}^H \mathbf{A} \mathbf{R_s}$, $\boldsymbol{\Pi}_c = \mathbf{I} - \boldsymbol{\Pi}$, $\boldsymbol{\Pi} = \mathbf{A} \left(\mathbf{A}^H \mathbf{A} \right)^{-1} \mathbf{A}^H$,
$\mathbf{D} = \begin{bmatrix} \mathbf{d}(\phi_1) & \ldots & \mathbf{d}(\phi_D) \end{bmatrix}$, $\mathbf{d}(\phi_n) = \frac{\partial \mathbf{a}(\phi_n)}{\partial \phi_n}$, $\forall n = 1, \ldots, D$, $\mathrm{Re}[\cdot]$ represents the real part of the

argument, $\mathbf{J}(\phi)$ is the Fisher-information matrix, and N is the number of time snapshots considered for evaluating the CRB.

As we have seen, a U-AVS array introduces a bias in the estimate when it is used in combination with the classical beamforming approach, which becomes more apparent when the aperture is small. The CRB for biased estimators can be obtained by a simple modification of eq. (7.18). Let $\hat{\phi}$ denote an arbitrary estimator of ϕ with bias $\mathbf{b}(\phi)$. Then the CRB for such a biased estimator is given by [33]:

$$\mathrm{CRB_b}(\phi) = \big(\mathbf{I} + \mathbf{D}(\phi)\big)\mathbf{J}^{-1}(\phi)\big(\mathbf{I} + \mathbf{D}(\phi)\big)^T, \tag{7.19}$$

where $\mathbf{J}^{-1}(\phi)$ is the inverse of the Fisher information matrix as seen in eq. (7.18) and $\mathbf{D}(\phi)$ is the bias gradient matrix defined by:

$$\mathbf{D}(\phi) = \frac{\partial \mathbf{b}(\phi)}{\partial \phi}. \tag{7.20}$$

It can be seen that the CRB of a biased estimator depends on the bias variations rather than the bias itself. Also in the case of a biased estimator, the Mean Square Error (MSE) is a direct measure of the estimator's performance and it can be written as:

$$\mathrm{MSE}(\phi) = \mathbb{E}\left\{\left\|\hat{\phi} - \phi\right\|^2\right\} = \|\mathbf{b}(\phi)\|^2 + \mathrm{tr}\big(\mathrm{CRB_b}(\phi)\big). \tag{7.21}$$

7.5.2. EVALUATION OF CRB FOR A SINGLE SOURCE

This section is focused on evaluating the CRB of an AVS, U-AVS and APS array with a single far-field source in its field of view. For the given scenario with $\mathbb{E}\{s(t)s^H(t)\} = \sigma_s^2$, eq. (7.18) yields:

$$\mathrm{CRB}(\phi) = \frac{\sigma_n^2}{2N}\frac{1}{\mathrm{Re}\left[U\left(\mathbf{d}^H(\phi)\mathbf{\Pi}_c\mathbf{d}(\phi)\right)\right]}, \tag{7.22}$$

where $U = \frac{\left(\mathbf{a}^H(\phi)\mathbf{a}(\phi)\right)\sigma_s^4}{\left(\mathbf{a}^H(\phi)\mathbf{a}(\phi)\right)\sigma_s^2+\sigma_n^2}$, $\mathbf{d}(\phi) = \frac{\partial \mathbf{a}(\phi)}{\partial \phi}$ and $\mathbf{\Pi} = \frac{\mathbf{a}(\phi)\mathbf{a}^H(\phi)}{\mathbf{a}^H(\phi)\mathbf{a}(\phi)}$.

Based on eq. (7.22), assuming a locally unbiased estimator, the expressions of the CRB for various scenarios are derived in 7.B. Using $\mathrm{SNR} = \frac{\sigma_s^2}{\sigma_n^2}$, the expressions of this CRB for various sensor configurations are presented in Table 7.1, where

Table 7.1: CRB for several sensor array configurations

	CRB
APS	$\frac{1}{2N\left(Mk^2\sum_{i=1}^{M}\left(\mathbf{r}_i\cdot\frac{\partial \mathbf{u}}{\partial\phi}\right)^2 - k^2\sum_{i=1}^{M}\sum_{j=1}^{M}\left(\mathbf{r}_i\cdot\frac{\partial \mathbf{u}}{\partial\phi}\right)\left(\mathbf{r}_j\cdot\frac{\partial \mathbf{u}}{\partial\phi}\right)\right)}\left(\frac{M}{\mathrm{SNR}} + \frac{1}{(\mathrm{SNR})^2}\right)$
AVS	$\frac{1}{2N\left(4Mk^2\sum_{i=1}^{M}\left(\mathbf{r}_i\cdot\frac{\partial \mathbf{u}}{\partial\phi}\right)^2 + 2M^2 - 4k^2\sum_{i=1}^{M}\sum_{j=1}^{M}\left(\mathbf{r}_i\cdot\frac{\partial \mathbf{u}}{\partial\phi}\right)\left(\mathbf{r}_j\cdot\frac{\partial \mathbf{u}}{\partial\phi}\right)\right)}\left(\frac{2M}{\mathrm{SNR}} + \frac{1}{(\mathrm{SNR})^2}\right)$
U-AVS	$\frac{1}{2NP_G}\left(\frac{\left(M + \sum_{i=1}^{M}\cos^2(\delta_i - \phi)\right)}{\mathrm{SNR}} + \frac{1}{(\mathrm{SNR})^2}\right)$

$$
\begin{aligned}
P_G = Mk^2 \sum_{i=1}^{M} \left(\mathbf{r}_i \cdot \frac{\partial \mathbf{u}}{\partial \phi}\right)^2 \left(1+\cos^2(\delta_i-\phi)\right) + M \sum_{i=1}^{M} \sin^2(\delta_i-\phi) \\
- k^2 \sum_{i=1}^{M}\sum_{j=1}^{M} \left(\mathbf{r}_i \cdot \frac{\partial \mathbf{u}}{\partial \phi}\right)\left(\mathbf{r}_j \cdot \frac{\partial \mathbf{u}}{\partial \phi}\right)\left(1+\cos^2(\delta_i-\phi)\right) \\
+ k^2 \sum_{i=1}^{M}\sum_{j=1}^{M} \left(\left(\mathbf{r}_i \cdot \frac{\partial \mathbf{u}}{\partial \phi}\right)^2 - \left(\mathbf{r}_i \cdot \frac{\partial \mathbf{u}}{\partial \phi}\right)\left(\mathbf{r}_j \cdot \frac{\partial \mathbf{u}}{\partial \phi}\right)\right) \cos^2(\delta_j-\phi) \\
\left(1+\cos^2(\delta_i-\phi)\right) \\
+ \sum_{i=1}^{M}\sum_{j=1}^{M} \left(\cos^2(\delta_j-\phi)\sin^2(\delta_i-\phi)\right. \\
\left. -\cos(\delta_i-\phi)\sin(\delta_i-\phi)\cos(\delta_j-\phi)\sin(\delta_j-\phi)\right).
\end{aligned}
\tag{7.23}
$$

For the particular case of a U-AVS ULA with a fixed orientation, $\delta_i = \delta, \forall i = 1,2,\ldots,M$, the expression of the CRB can be simplified yielding:

$$
\mathrm{CRB}(\phi) = \frac{1}{2NP_G}\left(\frac{M\left(1+\cos^2(\delta-\phi)\right)}{\mathrm{SNR}} + \frac{1}{(\mathrm{SNR})^2}\right),
\tag{7.24}
$$

where

$$
\begin{aligned}
P_G = Mk^2\left(1+\cos^2(\delta-\phi)\right) \sum_{i=1}^{M} \left(\mathbf{r}_i \cdot \frac{\partial \mathbf{u}}{\partial \phi}\right)^2 + M^2 \sin^2(\delta-\phi) \\
- k^2\left(1+\cos^2(\delta-\phi)\right) \sum_{i=1}^{M}\sum_{j=1}^{M} \left(\mathbf{r}_i \cdot \frac{\partial \mathbf{u}}{\partial \phi}\right)\left(\mathbf{r}_j \cdot \frac{\partial \mathbf{u}}{\partial \phi}\right) \\
+ k^2 \cos^2(\delta-\phi)\left(1+\cos^2(\delta-\phi)\right) \sum_{i=1}^{M}\sum_{j=1}^{M} \left(\left(\mathbf{r}_i \cdot \frac{\partial \mathbf{u}}{\partial \phi}\right)^2\right. \\
\left. - \left(\mathbf{r}_i \cdot \frac{\partial \mathbf{u}}{\partial \phi}\right)\left(\mathbf{r}_j \cdot \frac{\partial \mathbf{u}}{\partial \phi}\right)\right).
\end{aligned}
\tag{7.25}
$$

As we have seen, the conventional DOA estimate based on the beampattern for a U-AVS array results in a biased estimate. The bias in the DOA estimate for a U-AVS array is quantified in eq. (7.14). We can thus also consider the modified CRB expression of eq. (7.19) for biased estimates ($\mathrm{CRB_b}$), which incorporates the rate of change in the bias term:

$$
\begin{aligned}
\mathrm{CRB_b}(\phi) &= \left(1+\frac{\partial b(\phi)}{\partial \phi}\right)^2 \mathrm{CRB}(\phi), \\
&\approx \left(1+\frac{\partial \hat{b}(\phi)}{\partial \phi}\right)^2 \mathrm{CRB}(\phi),
\end{aligned}
\tag{7.26}
$$

where

$$
\begin{aligned}
\frac{\partial \hat{b}(\phi)}{\partial \phi} = -\frac{1}{Q^2}\left[Q\left(\mathrm{SNR}\left(R\frac{\partial S}{\partial \phi} + \frac{\partial R}{\partial \phi}S\right) + \frac{\partial S}{\partial \phi}\right)\right. \\
\left. -\mathrm{SNR}\left(\mathrm{SNR}\left(RS\right)+S\right)\left(\frac{\partial R}{\partial \phi}J + R\frac{\partial J}{\partial \phi} + 2S\frac{\partial S}{\partial \phi} + 2L\frac{\partial L}{\partial \phi}\right)\right],
\end{aligned}
\tag{7.27}
$$

$$Q = \mathrm{SNR}\left(RJ + S^2 + L^2\right) + J + W, \tag{7.28}$$

$$\frac{\partial R}{\partial \phi} = 2\sum_{i=1}^{M} \cos(\delta_i - \phi)\sin(\delta_i - \phi), \tag{7.29}$$

$$\frac{\partial S}{\partial \phi} = \sum_{i=1}^{M} \left(\sin^2(\delta_i - \phi) - \cos^2(\delta_i - \phi)\right), \tag{7.30}$$

$$\begin{aligned}\frac{\partial L}{\partial \phi} = k\sum_{i=1}^{M} \Bigg[&\left(\mathbf{r}_i \cdot \frac{\partial^2 \mathbf{u}}{\partial \phi^2}\right)\left(1 + \cos^2(\delta_i - \phi)\right) \\ &+ \left(\mathbf{r}_i \cdot \frac{\partial \mathbf{u}}{\partial \phi}\right)\left(2\cos(\delta_i - \phi)\sin(\delta_i - \phi)\right)\Bigg],\end{aligned} \tag{7.31}$$

$$\begin{aligned}\frac{\partial J}{\partial \phi} = -2k^2\sum_{i=1}^{M} \Bigg[&\left(\mathbf{r}_i \cdot \frac{\partial \mathbf{u}}{\partial \phi}\right)^2 \left(\cos(\delta_i - \phi)\sin(\delta_i - \phi)\right) \\ &+ \left(\mathbf{r}_i \cdot \frac{\partial \mathbf{u}}{\partial \phi}\right)\left(\mathbf{r}_i \cdot \frac{\partial^2 \mathbf{u}}{\partial \phi^2}\right)\left(1 + \cos^2(\delta_i - \phi)\right)\Bigg] \\ &- 2\sum_{i=1}^{M} \cos(\delta_i - \phi)\sin(\delta_i - \phi).\end{aligned} \tag{7.32}$$

7

Based on eq. (7.16) it is seen that for a given DOA with a given geometry and number of sensors, the bias in the source DOA estimate can be controlled by changing the sensor orientation angles $\boldsymbol{\delta}$. For biased estimators, minimizing the mean square error (MSE) of the estimate ($\hat{\phi}$) becomes the optimal criterion based upon which the DOA performance is evaluated and it can be written as:

$$\mathrm{MSE}(\phi) = \mathbb{E}\left\{\left\|\hat{\phi} - \phi\right\|^2\right\} \approx \left(\hat{b}(\phi)\right)^2 + \mathrm{CRB}_{\mathrm{b}}(\phi). \tag{7.33}$$

Considering the expressions in eq. (7.14), eq. (7.26) and eq. (7.33), three contrasting configurations of a U-AVS ULA are considered for the purpose of illustration. It includes one with a fixed orientation ($\delta = 90°$) and two with an arbitrary orientations $\boldsymbol{\delta}$, as listed in Table 7.2. In the first configuration, all the sensors are oriented randomly whereas in the second configuration, the sensor orientation angles are in the region between 70° to 115°.

Table 7.2: Two configurations of a U-AVS ULA with an arbitrary orientation

	U-AVS ULA with an arbitrary configuration
Configuration 1	$\boldsymbol{\delta} = [10°, 118°, 75°, 49°, 138°, 85°, 107°, 25°, 144°, 37°]$
Configuration 2	$\boldsymbol{\delta} = [70°, 75°, 80°, 85°, 90°, 95°, 100°, 105°, 110°, 115°]$

The bias in the source DOA estimate of a U-AVS array and the MSE of all the sensor configurations with respect to ϕ are respectively plotted in Figure 7.5 and Figure 7.7. Also

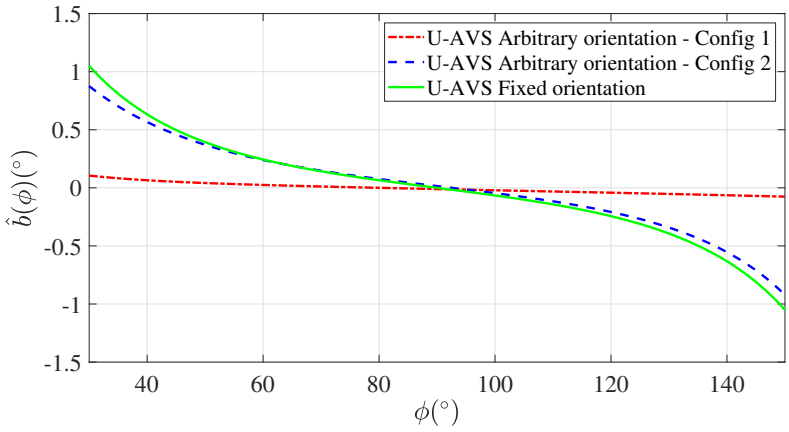


Figure 7.5: Variation of the bias in the source DOA estimates based on a U-AVS ULA for all the three configurations of a U-AVS ULA.

the derivative of bias with respect to ϕ is plotted in Figure 7.6 for all the three configurations of the U-AVS ULA. All the plots in Figures 7.5, 7.6 and 7.7 are considered for a ϕ between 30° and 150°, as the bias expression approximations in eq. (7.16) are reasonably valid for this range as seen in Figure 7.3.

It can be observed from Figure 7.5, that the bias in the DOA estimate for all ϕ is small for the first configuration of the U-AVS ULA. For the U-AVS ULA with a fixed orientation ($\delta = 90°$) and for the second configuration of a U-AVS ULA with an arbitrary orientation, the bias is small in the region where the sensors are aimed at and increases as ϕ diverges from this region .

In Figure 7.6, we observe that the rate of change of bias with respect to ϕ is negative for all three configurations, due to which the biased CRB of a U-AVS ULA is lower than that of the corresponding unbiased CRB. Especially for the fixed orientation configuration and for the second configuration of a U-AVS ULA, the change in bias $\left(\frac{\partial \hat{b}(\phi)}{\partial \phi}\right)$ rapidly grows as ϕ differs from the region the sensors point at, yielding a lower biased CRB than the corresponding unbiased version.

The MSE of all the sensor configurations is shown in Figure 7.7. For an APS and an AVS ULA, the MSE is the same as the CRB, since they result in an asymptotically unbiased estimate of the source DOA. On the other hand, for a U-AVS ULA, the MSE is comprised of the bias, the change in bias and the CRB as seen in eq. (7.33). For the fixed orientation and the second configuration of a U-AVS ULA, the MSE is similar to the results obtained for an AVS ULA for ϕ around 90° and it drifts away rapidly as ϕ differs from 90°. For the first configuration of a U-AVS ULA, the MSE lies in between the MSE of an APS and an AVS array for all ϕ. Based on the observations from Figure 7.7, for a given number of sensors/aperture, it can be inferred that the MSE of the U-AVS array can be modulated over the ϕ range by choosing the orientation angles of the U-AVSs appropriately.

In order to validate the MSE variation, Monte Carlo simulations with 1000 iterations were performed using the classical beamformer, as it is asymptotically optimal for a single source. The simulations were considered for the U-AVS ULA with a fixed and arbitrary

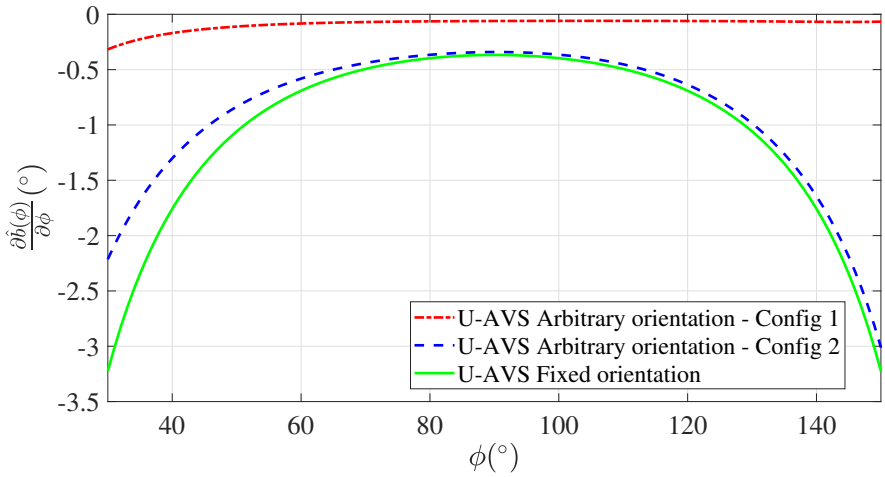


Figure 7.6: Variation of the derivative of the bias in the source DOA estimates with respect to ϕ for all the three configurations of a U-AVS ULA.

orientation (Configuration 1, as listed in Table 7.2). The results are seen in Figure 7.8. It can be observed that the simulations are in agreement with the MSE expressions derived in eq. (7.33). The CRB curves for both configurations are also plotted in dashed lines for reference. It can be seen that for the fixed orientation scenario, the MSE is far greater than the equivalent CRB, as the bias in the DOA estimates is dominant. On the other hand, the MSE for a low number of sensors is not matching the theoretical MSE plots, as the bias expression based on first order approximations is not so accurate.

Finally, we can conclude that for a given number of U-AVSs, application requirements such as a defined region-of-interest and geometry of the array, minimizing the MSE/function of the MSE of the DOA estimate can be chosen as a criterion to find the optimum orientation angle for each of the U-AVSs in the array such that an acceptable performance can be obtained. The related combinatorial optimization problem can be written as:

$$\underset{\boldsymbol{\delta}}{\arg\min} \quad f(\mathscr{R}), \tag{7.34}$$

where $f : \mathscr{M} \mapsto \mathbb{R}$ is a continuous function, defined over a manifold $\mathscr{M}$ and $\mathscr{R}$ represents a discrete angular support set, i.e., $\mathscr{R} = \{\phi_i : \phi_i \in \mathscr{M}, \forall 1 \leq i \leq J\}$. A simple sub-optimal choice of f can be the mean of the MSE for all ϕ within $\mathscr{R}$, i.e., $\sum_{i=1}^{J} \text{MSE}(\phi_i, \boldsymbol{\delta})$. However, the MSE expression eq. (7.33) is non-convex with respect to the orientation angles, $\boldsymbol{\delta}$, which makes the optimization problem tough to solve in real-time. A sub-optimal solution can be found by using non-convex algorithms like simulated annealing or genetic algorithms or by using a convex relaxation of the MSE expression eq. (7.33). Further details on this aspect are out of scope of this work as here we are mainly focusing on establishing the foundations of the U-AVS based arrays.

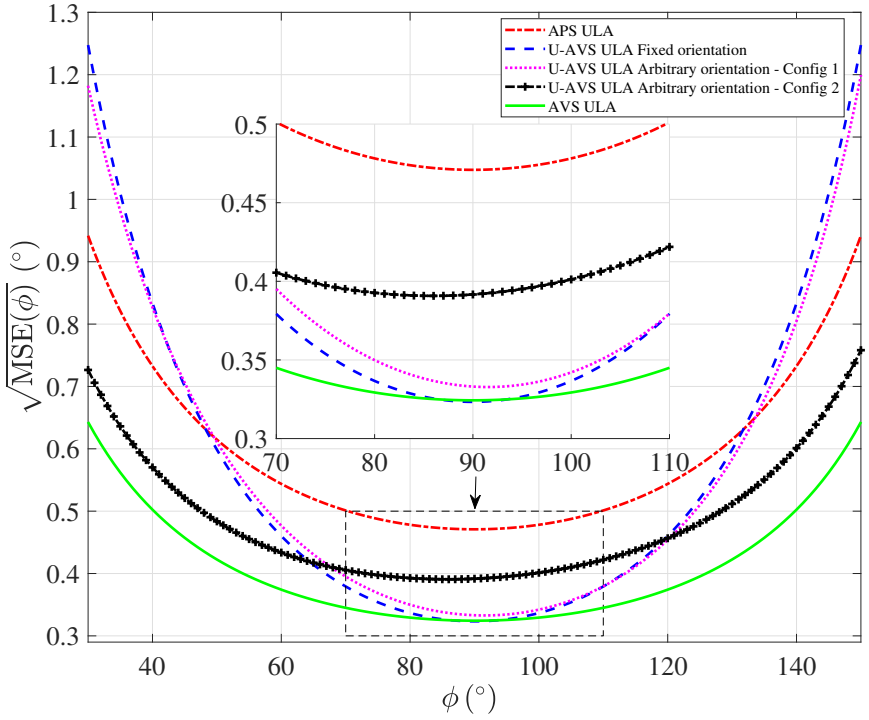


Figure 7.7: Plot of ($\sqrt{\text{MSE}}$) (in °) with $M = 10$, $N = 10$, SNR = 0 dB for an APS ULA, AVS ULA and U-AVS ULA with respect to a change in ϕ.

7

7.6. EXPERIMENTAL RESULTS

An experimental study was conducted in order to support the discussion and analytical expressions proposed for the U-AVS array. Firstly, the beampatterns of the APS, AVS and U-AVS ULA under a changing source signal frequency are assessed. Next, the bias in the source location estimate is compared to the theoretical value of the U-AVS ULA. A picture of the experimental setup is shown in Figure 7.9, where five AVSs and three loudspeakers are seen.

The measurements were performed with the first three AVSs arranged in a ULA configuration in a fully anechoic chamber using a white Gaussian excitation, radiated by a 3 inch loudspeaker, under high SNR conditions (approximately 40 dB). For the measurements, an acquisition device with a sampling frequency of 25 kHz was used. The product specifications of the AVSs used for the experiments can be found in [34]. The inter-sensor spacing d was chosen to be 5 cm and the speaker was located at a distance of 360 cm with respect to the reference of the ULA (i.e., the range of the sources is more than 20 times the aperture of the array allowing for the far-field assumption). Although the loudspeaker was driven by white Gaussian noise, the AVS ULA was designed for a frequency of $f_d = 3433$ Hz (wavelength of $\lambda_d = 10$ cm). The pressure and particle velocity information (i.e., in $\mathbf{y}(t)$) at a given frequency are obtained by a short time discrete Fourier transform (STFT). For the STFT, a

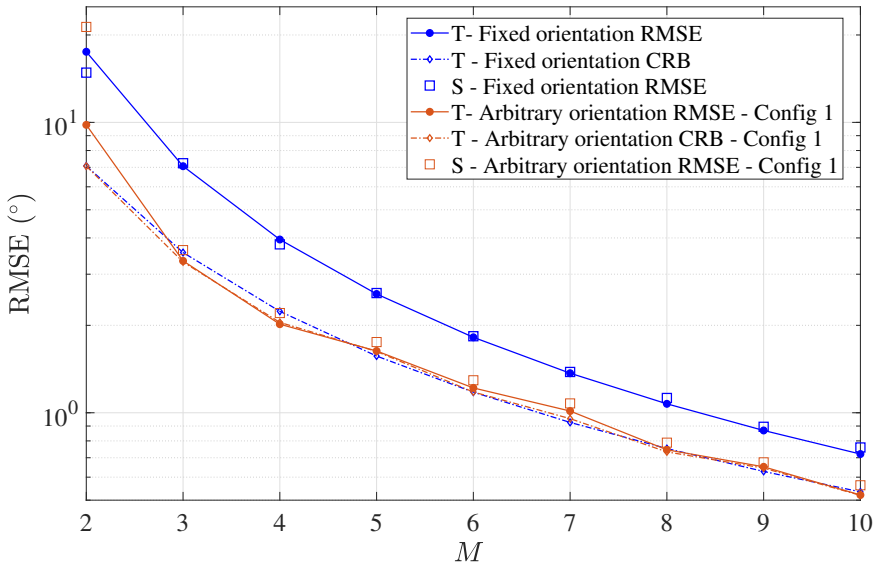


Figure 7.8: Validation of the MSE expressions of a U-AVS ULA with fixed and arbitrary orientations using 1000 Monte Carlo simulations with increasing number of sensors. For the simulations we consider $N = 10$, SNR = 0 dB, $\phi = 45°$. Also the unbiased CRB is plotted for both fixed and arbitrary orientations. The plots of the MSE and the unbiased CRB expressions are labeled as **T** and the simulation RMSEs are labeled as **S**.

segment of 1024 samples was considered with 50% overlap. A Hanning window was applied to the data segment prior to the STFT. The measurements were performed using AVSs and the U-AVS data is obtained from the corresponding AVS data, by linearly combining each vector component data along the orientation angle in an appropriate way.

7.6.1. BEAMPATTERN VARIATION DUE TO CHANGES IN THE SOURCE SIGNAL FREQUENCY

The beampattern variation of an APS, AVS and U-AVS ULA with respect to changes in the frequency is computed numerically considering the experimental sensor arrangement described above along with eq. (7.5). The results are shown in Figure 7.10 (a), (c) and (e). The orientation angles ($\boldsymbol{\delta}$) of the U-AVS ULA are chosen randomly between 50° and 130°. It can be noted from Figure 7.10 (a), (c) and (e) that the AVS and U-AVS ULA beampattern, in comparison to the equivalent aperture APS ULA, preserve the VGM modulation based directivity even at low frequencies and also the grating lobes are suppressed at high frequencies. Furthermore, the left/right ambiguity lobe is suppressed for both the AVS and U-AVS ULA beampattern.

In Figure 7.10 (b), (d) and (f), the equivalent beampattern of an APS, AVS and U-AVS ULA are plotted based on the measurement data. As it can be seen, the experimental results are comparable with the theoretical ones presented in Figure 7.10 (a), (c) and (e). The discrepancies between the experimental and the numerical results can be explained due to the unequal source radiation, as well as small positioning and calibration errors.

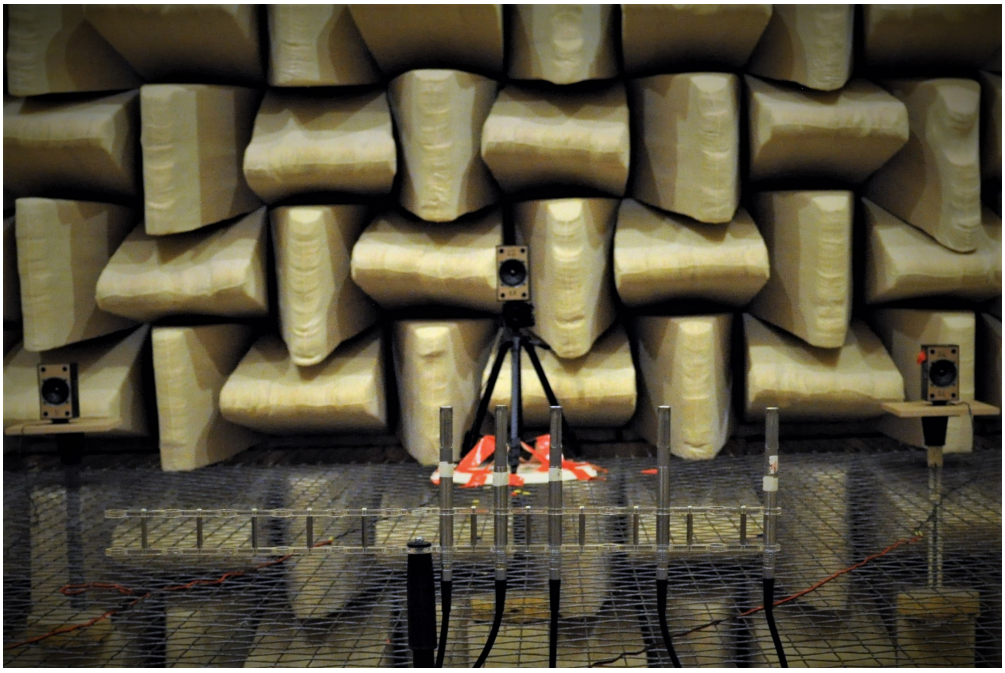


Figure 7.9: Picture of the arrangement of five AVSs and three speakers, which are located on the circumference of a circle with radius $r = 360$ cm.

7.6.2. BIAS VARIATION DUE TO AN INCREASE IN THE APERTURE OF THE U-AVS ULA

We compare the estimates based on the measurement data with the theoretical estimates in Figure 7.11 for two scenarios ($\phi = 60°$, $\delta = 45°$ and $\phi = 90°$, $\delta = 30°$). As shown, the estimates based on the measurement data are very similar to the theoretical estimates of the source location. Furthermore, we observe that the bias in the estimates based on the measurement data reduces as the aperture of the ULA increases. The DOA estimates based on the equivalent AVS and APS ULA measurement data are also indicated in Figure 7.11 for reference. The small mismatches between the theoretical and the experimental data are probably due to the positioning and orientation errors during the test.

7.7. CONCLUSIONS

In this paper, a new configuration of the AVS with two transducers (one pressure and one particle velocity transducer) is introduced, which is referred to as the U-AVS (Uniaxial Acoustic Vector Sensor). Adopting the matched filter based beampatterns, the behavior of a U-AVS array is explored. Similar to an AVS array, it is shown that the beampattern of a U-AVS array with a fixed orientation can be decomposed as the product of an equivalent APS array beampattern and a VGM term. Based on this decomposition, the advantages of an AVS array are preserved to a considerable extent in the case of a U-AVS array. In order to observe this aspect, a numerical and experimental study was performed to validate the variation of the beampattern of an APS, AVS and U-AVS ULA with respect to a change in the source

signal frequency. It is found that the DOA estimates based on the classical beamforming approach for a U-AVS array result in biased estimates. Based on the first order Taylor expansion of the beamforming function, the bias in the estimate is quantified and also validated by performing numerical simulations and experiments. Further, the bias approximation accuracy is numerically studied with a varying number of sensors and ROIs. It is seen that the bias can be altered by changing the orientation angles of the U-AVSs in an array with a fixed aperture.

The CRB for a single source scenario is evaluated for a U-AVS array and compared with the APS and AVS array. Further, the expressions for the biased CRB and the MSE of a U-AVS array were derived and their behavior was studied for three specifically chosen ULA configurations. Based on the numerical analysis of those three ULA configurations we can observe that the MSE of the estimates over different DOAs can be modulated by changing the orientations of the U-AVSs in the array. Also the MSE is numerically validated for an increasing number of sensors.

The numerical and experimental validation of the proposed theoretical framework verifies that the analytical expressions derived can be used to quantify the estimation error for a given geometry and they can ultimately be adopted to optimize the orientations of the U-AVSs for a set of requirements.

7.8. ACKNOWLEDGEMENTS

This work is part of the ASPIRE project (project 14926 within the STW OTP programme), which is financed by the Netherlands Organization for Scientific Research (NWO).

7.A. BIAS EXPRESSION FOR U-AVS ARRAY

Here, we derive the bias expression of eq. (7.16) in Section 7.4. By taking the first and second order derivatives of $f(\phi)$ with respect to ϕ, we obtain (for brevity the dependence on $\boldsymbol{\delta}$ is dropped from the steering vectors and its derivatives)

$$\hat{b}(\phi) = -\frac{\mathbf{d}^H(\phi)\mathbf{R}_\mathbf{y}\mathbf{a}(\phi)+\mathbf{a}^H(\phi)\mathbf{R}_\mathbf{y}\mathbf{d}(\phi)}{\dot{\mathbf{d}}^H(\phi)\mathbf{R}_\mathbf{y}\mathbf{a}(\phi)+2\mathbf{d}^H(\phi)\mathbf{R}_\mathbf{y}\mathbf{d}(\phi)+\mathbf{a}^H(\phi)\mathbf{R}_\mathbf{y}\dot{\mathbf{d}}(\phi)}, \tag{7.35}$$

where $\dot{\mathbf{d}}(\phi) = \frac{\partial^2\mathbf{a}(\phi)}{\partial\phi^2}$. We consider here a random source signal $s(t)$ with zero mean and variance σ_s^2, and additive noise with zero mean and variance σ_n^2. For this configuration $\mathbf{R}_\mathbf{y} = \sigma_\mathrm{s}^2\mathbf{a}(\phi)\mathbf{a}^H(\phi)+\sigma_\mathrm{n}^2\mathbf{I}$. After evaluating $\mathbf{d}(\phi)$ and $\dot{\mathbf{d}}(\phi)$, the following inner products can be derived:

$$\mathbf{a}^H(\phi)\mathbf{a}(\phi) = \underbrace{M+\sum_{i=1}^{M}\cos^2(\delta_i-\phi)}_{R}, \tag{7.36}$$

$$\mathbf{d}^H(\phi)\mathbf{a}(\phi) = -\mathrm{j}\underbrace{k\sum_{i=1}^{M}\left(\mathbf{r}_i\cdot\frac{\partial\mathbf{u}}{\partial\phi}\right)\left(1+\cos^2(\delta_i-\phi)\right)}_{L} + \underbrace{\sum_{i=1}^{M}\cos(\delta_i-\phi)\sin(\delta_i-\phi)}_{S}, \tag{7.37}$$

$$\mathbf{d}^H(\phi)\mathbf{d}(\phi) = \underbrace{k^2\sum_{i=1}^{M}\left(\mathbf{r}_i\cdot\frac{\partial\mathbf{u}}{\partial\phi}\right)^2\left(1+\cos^2(\delta_i-\phi)\right)+\sum_{i=1}^{M}\sin^2(\delta_i-\phi)}_{W}. \tag{7.38}$$

$$\begin{aligned}\dot{\mathbf{d}}^H(\phi)\mathbf{a}(\phi) = {}& \mathrm{j}k\sum_{i=1}^{M}\left(\mathbf{r}_i\cdot\frac{\partial^2\mathbf{u}}{\partial\phi^2}\right)\left(1+\cos^2(\delta_i-\phi)\right)\\ &+2\mathrm{j}k\sum_{i=1}^{M}\left(\mathbf{r}_i\cdot\frac{\partial\mathbf{u}}{\partial\phi}\right)\cos(\delta_i-\phi)\sin(\delta_i-\phi)\\ &\underbrace{-k^2\sum_{i=1}^{M}\left(\mathbf{r}_i\cdot\frac{\partial\mathbf{u}}{\partial\phi}\right)^2\left(1+\cos^2(\delta_i-\phi)\right)-\sum_{i=1}^{M}\cos^2(\delta_i-\phi)}_{J}.\end{aligned} \tag{7.39}$$

Substituting eq. (7.36), eq. (7.37), eq. (7.38) and eq. (7.39) into eq. (7.35), finally leads to eq. (7.16).

7.B. CRB EXPRESSION FOR A U-AVS ARRAY AND A SINGLE SOURCE

The CRB expression for a U-AVS array is considered in this section and the same steps can be followed to derive the expressions for an equivalent AVS and APS array. The inner products $\mathbf{a}^H(\phi)\mathbf{a}(\phi)$, $\mathbf{d}^H(\phi)\mathbf{a}(\phi)$ and $\mathbf{d}^H(\phi)\mathbf{d}(\phi)$ required for the evaluation of the CRB expression are already captured in eq. (7.36), eq. (7.37) and eq. (7.38), respectively. Based on the inner product results, we now evaluate $\mathbf{d}^H\mathbf{a}\mathbf{a}^H\mathbf{d}$, $\mathbf{d}^H\mathbf{d}\mathbf{a}^H\mathbf{a}$ and subsequently $\mathbf{d}^H\mathbf{\Pi}_c\mathbf{d}$ specified in eq. (7.18) (for brevity the dependence on ϕ is dropped):

$$\begin{aligned}\mathbf{d}^H\mathbf{a}\mathbf{a}^H\mathbf{d} = {}& k^2\sum_{i=1}^{M}\sum_{j=1}^{M}\left(\mathbf{r}_i\cdot\frac{\partial\mathbf{u}}{\partial\phi}\right)\left(\mathbf{r}_j\cdot\frac{\partial\mathbf{u}}{\partial\phi}\right)\left(1+\cos^2(\delta_i-\phi)\right)\\ &\left(1+\cos^2(\delta_j-\phi)\right)+\sum_{i=1}^{M}\sum_{j=1}^{M}\sin(\delta_i-\phi)\cos(\delta_i-\phi)\\ &\sin(\delta_j-\phi)\cos(\delta_j-\phi),\end{aligned} \tag{7.40}$$

$$\begin{aligned}\mathbf{d}^H\mathbf{d}\mathbf{a}^H\mathbf{a} = Mk^2 &\sum_{i=1}^{M}\left(\mathbf{r}_i\cdot\frac{\partial\mathbf{u}}{\partial\phi}\right)^2(1+\cos^2(\delta_i-\phi))\\ &+M\sum_{i=1}^{M}\sin^2(\delta_i-\phi)\\ &+k^2\sum_{i=1}^{M}\sum_{j=1}^{M}\left(\mathbf{r}_i\cdot\frac{\partial\mathbf{u}}{\partial\phi}\right)^2\cos^2(\delta_j-\phi)\left(1+\cos^2(\delta_i-\phi)\right)\\ &+\sum_{i=1}^{M}\sum_{j=1}^{M}\cos^2(\delta_j-\phi)\sin^2(\delta_i-\phi),\end{aligned} \tag{7.41}$$

$$\begin{aligned}\mathbf{d}^H\mathbf{\Pi}_c\mathbf{d} &= \frac{\mathbf{d}^H\mathbf{d}\mathbf{a}^H\mathbf{a}-\mathbf{d}^H\mathbf{a}\mathbf{a}^H\mathbf{d}}{\mathbf{a}^H\mathbf{a}},\\ &= \frac{P_G}{M+\sum_{i=1}^{M}\cos^2(\delta_i-\phi)},\end{aligned} \tag{7.42}$$

with P_G given in eq. (7.24). Further, the $\mathbf{U}$ term specified in eq. (7.18) results in the scalar U:

$$U=\frac{\left(M+\sum_{i=1}^{M}\cos^2(\delta_i-\phi)\right)\sigma_s^4}{\left(M+\sum_{i=1}^{M}\cos^2(\delta_i-\phi)\right)\sigma_s^2+\sigma_n^2}. \tag{7.43}$$

Finally, the CRB expression of eq. (7.18) reduces to:

$$\mathrm{CRB}(\phi) = \frac{1}{2NP_G}\left(\frac{\left(M+\sum_{i=1}^{M}\cos^2(\delta_i-\phi)\right)}{\mathrm{SNR}}+\frac{1}{(\mathrm{SNR})^2}\right). \tag{7.44}$$

REFERENCES

[1] H. L. Van Trees, *Optimum Array Processing. Part {IV} of Detection, Estimation, and Modulation theory.* (Wiley-Interscience, New York, 2002).

[2] R. Schmidt, *Multiple Emitter Location and Signal Parameter Estimation,* IEEE transactions on antennas and propagation **34**, 276 (1986).

[3] I. N. El-Behery and R. H. MacPhie, *Maximum-Likelihood Estimation of Source parameters from Time-sampled outputs of a Linear Array,* The Journal of the Acoustical Society of America **62**, 125 (1977).

[4] P. Stoica and A. Nehorai, *MUSIC, Maximum Likelihood, and Cramer-Rao bound,* IEEE Transactions on Acoustics, Speech, and Signal Processing **37**, 720 (1989).

[5] P. Stoica and A. Nehorai, *MUSIC, Maximum Likelihood, and Cramér-Rao Bound: Further Results and Comparisons,* IEEE Transactions on Acoustics, Speech, and Signal Processing **38**, 2140 (1990).

[6] H. Krim and M. Viberg, *Two decades of Array Signal Processing Research: The Parametric Approach,* IEEE Signal processing magazine **13**, 67 (1996).

[7] H.-E. De Bree, *The Microflown E-Book,* Microflown Technologies, Arnhem (2007).

[8] M. Hawkes and A. Nehorai, *Acoustic Vector Sensor Beamforming and Capon direction estimation,* IEEE Transactions on Signal Processing **46**, 2291 (1998).

[9] A. Nehorai and E. Paldi, *Acoustic Vector-Sensor Array Processing,* IEEE Transactions on Signal Processing **42**, 2481 (1994).

[10] W.-Q. Jing, D. F. Comesaña, and D. P. Cabo, *Sound Source Localisation using a Single Acoustic Vector Sensor and Multichannel Microphone phased arrays,* in *INTER-NOISE and NOISE-CON Congress and Conference Proceedings*, Vol. 249 (2014).

[11] D. Levin, E. A. P. Habets, and S. Gannot, *Maximum Likelihood Estimation of Direction of Arrival Using an Acoustic Vector-Sensor,* The Journal of the Acoustical Society of America **131**, 1240 (2012).

[12] Z. Liu, X. Ruan, and J. He, *Efficient 2-D DOA Estimation For Coherent Sources with a Sparse Acoustic Vector-Sensor Array,* Multidimensional Systems and Signal Processing **24**, 105 (2013).

[13] M. K. Awad and K. T. Wong, *Recursive Least-Squares Source Tracking Using One Acoustic Vector Sensor,* IEEE transactions on Aerospace and Electronic Systems **48**, 3073 (2012).

[14] X. Zhong and A. B. Premkumar, *Particle Filtering Approaches for Multiple Acoustic Source Detection and 2-D Direction of Arrival Estimation Using a Single Acoustic Vector Sensor,* IEEE Transactions on Signal Processing **60**, 4719 (2012).

[15] M. Shujau, C. H. Ritz, and I. S. Burnett, *Using In-Air Acoustic Vector Sensors for Tracking Moving Speakers,* in *Signal Processing and Communication Systems (ICSPCS), 2010 4th International Conference on* (IEEE, 2010) pp. 1–5.

[16] M. Hawkes and A. Nehorai, *Bearing Estimation with Acoustic Vector-Sensor Arrays,* in *AIP Conference Proceedings* (1996) pp. 345–358.

[17] D. Y. Levin, E. A. P. Habets, and S. Gannot, *Near-Field Signal Acquisition for Smart Glasses using Two Acoustic Vector-Sensors,* arXiv:1602.06582 (2016).

[18] J. P. Kitchens, *Acoustic Vector-Sensor Array Performance*, Master's thesis, Massachusetts Institute of Technology (2008).

[19] J. P. Kitchens, *Acoustic Vector-Sensor Array Processing*, Ph.D. thesis, DTIC Document (2010).

[20] M. Hawkes and A. Nehorai, *Effects of Sensor Placement on Acoustic Vector-Sensor Array Performance,* IEEE Journal of Oceanic Engineering **24**, 33 (1999).

[21] Y. Wu, Z. Hu, H. Luo, and Y. Hu, *Source number detectability by an acoustic vector sensor linear array and performance analysis,* Oceanic Engineering, IEEE Journal of **39**, 769 (2014).

[22] M. Hawkes and A. Nehorai, *Acoustic Vector-Sensor Processing in the Presence of a Reflecting Boundary,* IEEE Transactions on Signal Processing **48**, 2981 (2000).

[23] M. Hawkes and A. Nehorai, *Acoustic Vector Sensor Correlations in Ambient Noise,* IEEE Journal of Oceanic Engineering **26**, 337 (2001).

[24] D. Levin, S. Gannot, and E. A. P. Habets, *Direction-Of-Arrival Estimation Using Acoustic Vector Sensors in The Presence of Noise,* in *2011 IEEE International Conference on Acoustics, Speech and Signal Processing (ICASSP)* (IEEE, 2011) pp. 105–108.

[25] Y. Song, Y. L. Li, and K. T. Wong, *Acoustic Direction finding using a Pressure Sensor and a Uniaxial Particle Velocity Sensor,* IEEE Transactions on Aerospace and Electronic Systems **51**, 2560 (2015).

[26] Y. Song and K. T. Wong, *Azimuth-Elevation Direction finding using a Microphone and Three Orthogonal Velocity Sensors as a Non-Collocated Subarray,* The Journal of the Acoustical Society of America **133**, 1987 (2013).

[27] Y. Song and K. T. Wong, *Acoustic Direction finding using a Spatially Spread Tri-axial Velocity Sensor,* IEEE Transactions on Aerospace and Electronic Systems **51**, 834 (2015).

[28] C. H. Lee, H. R. L. Lee, K. T. Wong, and M. Razo, *The Spatial-Matched-Filter Beampattern of a Biaxial Non-Orthogonal Velocity Sensor,* Journal of Sound and Vibration **367**, 250 (2016).

[29] K. T. Wong and M. D. Zoltowski, *Root-MUSIC-based azimuth-elevation angle-of-arrival estimation with uniformly spaced but arbitrarily oriented velocity hydrophones,* IEEE Transactions on Signal Processing **47**, 3250 (1999).

[30] Y. Song, K. T. Wong, and Y. Li, *Direction finding using a Biaxial Particle-Velocity Sensor,* Journal of Sound and Vibration **340**, 354 (2015).

[31] K. N. Ramamohan, *Acoustic Vector Sensor Based Source Localization*, Master's thesis, Delft University of Technology (2016).

[32] A. Nehorai and E. Paldi, *Vector-Sensor Array Processing for Electromagnetic Source Localization,* IEEE Transactions on Signal Processing **42**, 376 (1994).

[33] S. Kay and Y. C. Eldar, *Rethinking Biased Estimation,* IEEE Signal Processing Magazine **25**, 133 (2008).

[34] Microflown, *USP Regular Product Datasheet*, Microflown Technologies (2018).

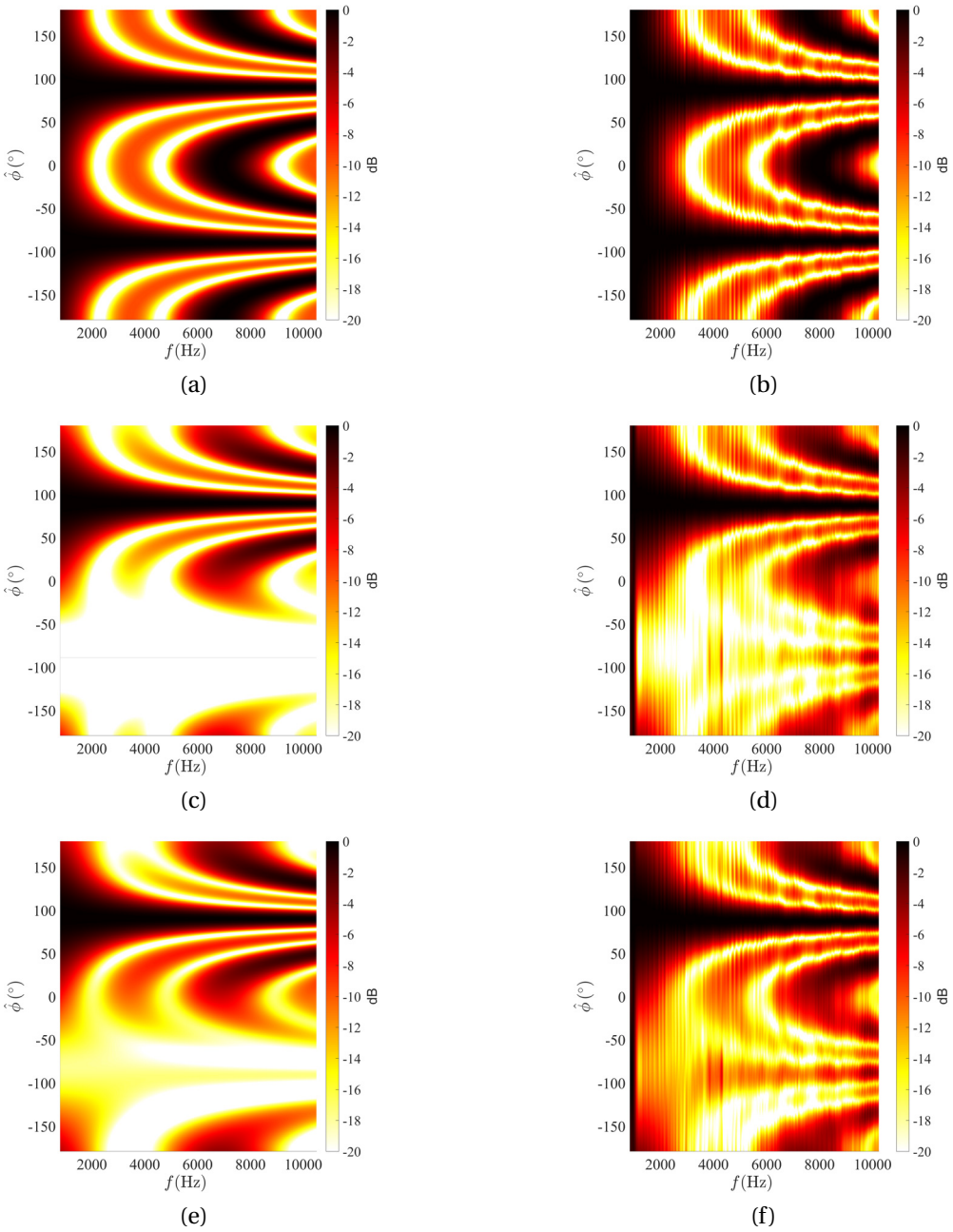


Figure 7.10: Variation in the beampattern of APS (in (a), (b)), AVS (in (c), (d)) and U-AVS (in (e), (f)) ULA as the frequency of the source signal is increased with $M = 3$, $d = 5$ cm ($f_d = 3433$ Hz) and $\phi = 90°$. The orientation angles of the U-AVS ULA are chosen as $\boldsymbol{\delta} = [57°, 124°, 109°]$. Subfigures (a), (c), (e) corresponds to simulation results and (b), (d), (f) correspond to experimental results.

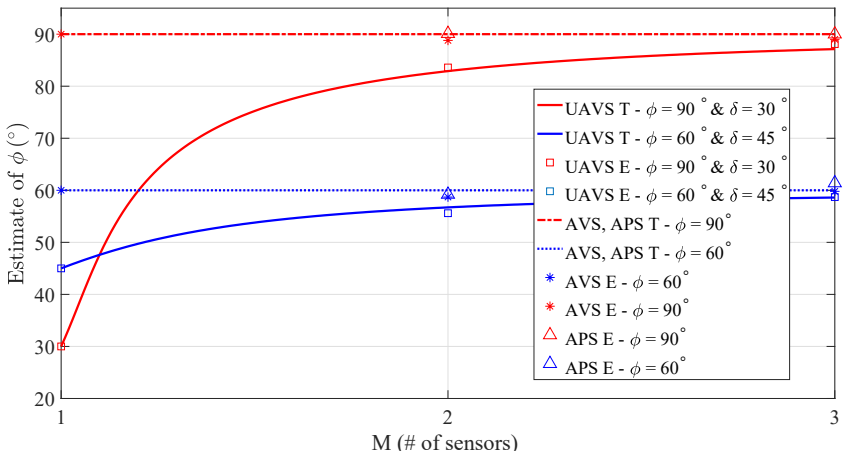


Figure 7.11: Comparison of biased estimates obtained from the measurement data (labeled **E**) with the theoretical biased estimates (labeled **T**) for two scenarios with different angle of arrival (ϕ) and U-AVS sensor orientation (δ) for $M = 2,3$. Also the DOA estimates for the equivalent AVS and APS ULA are plotted for reference.

8

CONCLUSION & RESEARCH TRENDS

In this chapter, we summarize the contributions of this thesis and show some potential further research directions. The concluding overview and remarks on this work are presented in Section 8.1. Some future research possibilities are presented in Section 8.2.

8.1. CONCLUDING OVERVIEW AND REMARKS

The theme of this work is DOA estimation of far-field sound sources using an array of spatially distributed AVSs. This study has contributed to the existing knowledge base on the DOA estimation problem using AVS arrays in three scenarios. Based on that, this thesis is broadly divided into three parts. Those include,

- The analysis of a spatially under-sampled AVS array for DOA estimation,
- The DOA estimation problem using an AVS array under the presence of sensor calibration errors, and
- Finally, the DOA estimation analysis using an array of uniaxial AVSs (U-AVSs).

In the first part of this work, we focused on analyzing a spatially under-sampled AVS array for DOA estimation. As observed in Chapter 2, the beampattern of the AVS array can be decomposed as the product of the beampattern of the equivalent APS array and the source frequency-independent velocity gain modulation (VGM) term. Due to the presence of the VGM term, the grating lobes in its beampattern, which occur when the array is under-sampled, behave differently from the conventional APS array as they are attenuated in comparison to the main lobe. In order to gain more insights into the behavior of the grating lobes, we studied the DOA estimation performance using the Cramér-Rao lower bound (CRLB) expression in Chapter 3. Since the CRLB provides local information around the source DOAs, we considered the multi-source CRLB expression with one of the sources acting as an interference at each possible scanning angle so that the effects of the grating lobes can be studied. For example, we considered a simplistic scenario of a ULA in the presence of two uncorrelated sources, where one of the sources acts as interference for all the possible scanning angles. We saw that the CRLB matrix is well defined at the grating lobe

locations indicating that spatially under-sampled AVS arrays can be employed for unambiguous DOA estimation. Furthermore, we saw that the minimum variance distortionless response (MVDR) beamformer suppresses the grating lobes considerably compared to the classical (or Bartlett) beamformer. Finally, the utility of a spatially under-sampled AVS array for beamforming applications was illustrated through the zero-forcing (ZF) and minimization of maximum side lobe beamformers.

In the second part of this work, we considered the DOA estimation problem using sensor arrays under the presence of calibration errors. As we stated and have seen in the simulation results, these calibration errors severely degrade the performance of the subspace based DOA estimation algorithms such as MUSIC or MVDR. Most of the existing literature focuses on self-calibration techniques that apply to scalar sensor arrays; however, our emphasis was on AVS arrays. Firstly, we discussed the ambiguity and identifiability issues for uniquely estimating the calibration errors and the source DOAs using AVS arrays. An important takeaway message from this analysis is that AVS arrays do not suffer from the progressive phase factor ambiguity between calibration errors and the array manifold matrix. In Chapter 4, this aspect is used to show that the AVS linear array does not require a known calibrator source or an additional phase reference channel for uniquely estimating the calibration errors and source DOAs, as is the case for the equivalent APS linear array. Furthermore, we proposed two main classes of self-calibration approaches.

In Chapters 4 and 5, the first class of array geometry-independent self-calibration algorithms that apply to both APS and AVS arrays is proposed. This approach is based on sparse recovery techniques, and it leads to non-iterative optimal convex optimization algorithms for jointly estimating the calibration errors and the source DOAs. Particularly in Chapter 4, we developed self-calibration solvers based on both the element-space and the co-array data models. Moreover, the self-calibration algorithm based on the co-array data model is also seen to be effective when more sources than the sparsely placed sensors/channels are present. Further in Chapter 5, the co-array data model-based self-calibration algorithm is extended to a scenario of multiple far-field broadband sources. Here we leveraged the fact that the calibration errors vary across frequencies smoothly or remain the same for a range of frequencies, and the DOAs of the broadband sources are the same for those frequencies. The proposed self-calibration algorithms' effectiveness was showcased through numerical and experimental results, and further comparisons to state-of-the-art methods were provided.

In Chapter 6, the second class of array geometry-dependent self-calibration algorithms that were specifically designed for a AVS ULA is proposed. We exploited the Toeplitz block structure in the AVS ULA measurement data covariance matrix to estimate the gain and phase errors. Based on the estimates of the calibration errors, the source DOAs are estimated using the gain and phase compensated covariance matrix. With M AVSs in the ULA, this approach requires one phase reference AVS and an additional phase reference (it could be any transducer type) for uniquely estimating the phase errors, and requires one gain reference AVS for uniquely estimating the gain errors.

In the last part of this work which is presented in Chapter 7, we considered an alternate configuration of an AVS with reduced channel count, referred to as uniaxial AVS (U-AVS). It consists of a pressure transducer and a single particle velocity transducer. Additionally, the particle velocity transducer has an extra degree of freedom to choose its orientation angle arbitrarily. Here we focused on understanding the DOA estimation performance of a

U-AVS array, and in this process, we analyzed its beampattern and derived an MSE bound on the DOA estimation. It was observed that the U-AVS array leads to asymptotically biased estimates, and the bias in the DOA estimates can be altered by changing the orientation angles of the U-AVSs in the array. This extra degree of freedom where each U-AVS in the array can have an arbitrary orientation is studied comprehensively for different scenarios. We see that the MSE bound on the DOA estimation can be lowered for some specific region of interest by compromising the performance at other regions. Further, we compared its performance to the conventional configurations of the equivalent APS and AVS arrays. Finally, all the analyses are supported by real experimental results performed with AVS arrays in the anechoic chamber.

The analyses and algorithms on the AVS array proposed in this work allow increased situational awareness across our society. Understanding the behavior of a spatially under-sampled AVS array and a reduced channel count U-AVS array allows for new array designs with a smaller number of sensor nodes that can even be placed on a moving platform such as vehicles or drones. Such arrays can significantly improve localizing threats such as gunshots, illegal fireworks, or explosions. Also, the knowledge gained from this research can improve the localization of defects in heavy machinery or annoying low-frequency sound sources that can cause health issues in humans. Furthermore, the proposed self-calibration algorithms, specifically for the AVS arrays with the derived identifiability conditions, simplify the re-calibration procedure and can be applied at the deployed location relative to one of the channels of an AVS within the array.

8.2. FUTURE RESEARCH OPPORTUNITIES

The work reported in this thesis opens the door to many new questions and possible further improvements of the proposed methods. Some suggestions for future research, and topics that have not been investigated in this work, are listed in the following:

8.2.1. DOA ESTIMATION USING SPATIALLY UNDER-SAMPLED AVS ARRAY

- *DOA estimation and beamforming with a spatially under-sampled AVS array in the co-array domain*

  The work presented in Chapter 3 deals with the analysis of a spatially under-sampled AVS array for DOA estimation by considering the element-space measurement model. On the other hand, it is also possible to spatially under-sample the AVS arrays for DOA estimation by considering the co-array measurement model. However, we still do not understand the extent and possible impact of the co-array measurement model for unambiguous DOA estimation. Under such settings, similar analyses as presented in Chapter 3 can be performed to understand its beampattern (including the behavior of the grating lobes) and the behavior of the DOA estimation algorithms such as spatial smoothing MUSIC (SS-MUSIC) [1, 2].

- *Design of AVS array for DOA estimation and beamforming*

  The knowledge gained by the analyses of spatially under-sampled AVS arrays using both the element-space and the co-array domain data model can be combined with sensor selection techniques [3, 4] to design an AVS array with (sub)optimal node posi-

tions such that some pre-defined performance metrics for DOA estimation and beamforming are satisfied. The pre-defined performance metrics can be constraints on the CRLB bound, beampattern parameters (such as sidelobe levels and mainlobe width), and operational frequency.

8.2.2. SELF-CALIBRATION AND DOA ESTIMATION USING SENSOR ARRAYS

- *Design of sparse scalar sensor arrays under the presence of calibration errors*

  In recent times, sparse scalar arrays evaluated in the co-array domain have gained much attention as they can estimate DOAs of more sources than the number of channels/sensors in the array. This feature is achieved by intelligently spacing the sensors such that its co-array domain contains the same information as the co-array of a uniform array [5, 6]. Such array designs among many include the minimum redundancy array (MRA)[7], sparse ruler array [8], and nested array [9]. These arrays are designed to maximize the degrees of freedom (DOF) by reducing the redundancies in the co-array domain. Furthermore, in some recent work, the design of sparse arrays accounting for sensor break-down [10–12] and mutual coupling [13–15] is also considered. However, not much attention is given in the literature to design sparse arrays in the presence of calibration errors. As discussed in Chapter 4, the redundancies in the scalar sensor array geometry are crucial from a self-calibration perspective. As the redundancies in the array geometry increase, we require fewer known references in the sparse array for uniquely estimating the calibration parameters and DOAs. Thus further research has to be carried out for optimal sparse sensor array design under the presence of calibration errors, as it involves a delicate balance between the redundancies and the DOF in the array.

- *Gridless self-calibration approaches for sensor arrays*

  In the second part of this work, we explored the problem of DOA estimation using sensor arrays under the presence of calibration errors. By leveraging the tools of sparse recovery techniques, in Chapter 4 we proposed non-iterative self-calibration algorithms based on both element-space and co-array measurement models for jointly estimating the calibration errors and source DOAs. These sparse recovery/compressive sensing techniques suffer from grid mismatch errors as the true DOAs are not always on the pre-defined grid [16], and many solutions for this issue are discussed in the literature, including [17, 18]. Recently, a family of off-grid, or grid-less approaches, which exploit sparsity in the atomic norm of the measurements, are proposed for line spectrum estimation (including DOA estimation) [19, 20]. Therefore, it will be sensible to investigate the off-grid extensions of the proposed self-calibration algorithms by considering the atomic norm of the measurements.

- *Theoretical analyses of the proposed self-calibration approaches*

  The self-calibration algorithms proposed in Chapter 4 and Chapter 5 utilize tools from sparse recovery/compressive sensing techniques, and the original problem formulations are non-convex. So we relaxed the constraints and solved the convex version of the optimization problem to estimate the calibration errors and the source DOAs. Further, the simulation results based on the proposed convex optimization problem

for the ideal case lead to the true/optimal solution, which showcases the exactness of the relaxation. However, theoretically, we did not investigate why we got the exact solution even after the convex relaxations, and it will be worthwhile to address this aspect. Furthermore, it will also be helpful to explore the sensitivity of the proposed solvers to noise (including finite-sample errors) and to the choice of the regularization parameter, conditions for the existence of a sparse solution, and many others.

- *Extension of the wide-band self-calibration approaches*

  In Chapter 5, by considering the co-array domain measurement model, we extended the self-calibration framework proposed in Chapter 4 to sensor arrays in the presence of broadband sources. Here we assumed that the calibration parameters vary smoothly and the source DOAs remain the same across frequencies. Further, we proposed a self-calibration algorithm by restricting our attention to the scenario where the calibration errors are constant over the considered number of frequency bins. However, we hinted that the proposed framework could be easily extended to a scenario where the calibration errors vary linearly across frequency bins. It will be useful to explore those extensions of the self-calibration approaches under the presence of broadband sources.

8.2.3. DOA ESTIMATION USING U-AVS ARRAY

- *Formulation of U-AVSs orientation selection problem based on pre-defined performance metrics*

  In Chapter 7, we looked into the analysis of a U-AVS array for DOA estimation. Here, we saw that U-AVS arrays lead to asymptotically biased estimates, and based on the derived MSE bound on the DOA estimation, we saw that the bias in the estimates can be controlled by altering the orientation of the U-AVSs in the array. We concluded that the minimization of the MSE bound could be used as a criterion for optimally choosing the orientation angles for each of the U-AVSs in the array. Formulating the optimization problem to minimize the MSE bound and analyze those results can be a possible research topic for designing the U-AVS array for DOA estimation and beamforming.

REFERENCES

[1] C.-L. Liu and P. Vaidyanathan, *Remarks on the spatial smoothing step in coarray music,* IEEE Signal Processing Letters **22**, 1438 (2015).

[2] T.-J. Shan, M. Wax, and T. Kailath, *On spatial smoothing for direction-of-arrival estimation of coherent signals,* IEEE Transactions on Acoustics, Speech, and Signal Processing **33**, 806 (1985).

[3] V. Roy, S. P. Chepuri, and G. Leus, *Sparsity-enforcing sensor selection for doa estimation,* in *2013 5th IEEE International Workshop on Computational Advances in Multi-Sensor Adaptive Processing (CAMSAP)* (IEEE, 2013) pp. 340–343.

[4] S. P. Chepuri, G. Leus, *et al.*, *Sparse sensing for statistical inference,* Foundations and Trends® in Signal Processing **9**, 233 (2016).

[5] R. T. Hoctor and S. A. Kassam, *The unifying role of the coarray in aperture synthesis for coherent and incoherent imaging,* Proceedings of the IEEE **78**, 735 (1990).

[6] P. P. Vaidyanathan and P. Pal, *Sparse sensing with co-prime samplers and arrays,* IEEE Transactions on Signal Processing **59**, 573 (2010).

[7] A. Moffet, *Minimum-redundancy linear arrays,* IEEE Transactions on antennas and propagation **16**, 172 (1968).

[8] D. Romero, D. D. Ariananda, Z. Tian, and G. Leus, *Compressive covariance sensing: Structure-based compressive sensing beyond sparsity,* IEEE signal processing magazine **33**, 78 (2015).

[9] P. Pal and P. Vaidyanathan, *Nested arrays: a novel approach to array processing with enhanced degrees of freedom,* IEEE Transactions on Signal Processing **58**, 4167 (2010).

[10] C.-L. Liu and P. Vaidyanathan, *Novel algorithms for analyzing the robustness of difference coarrays to sensor failures,* Signal Processing **171**, 107517 (2020).

[11] C.-L. Liu and P. P. Vaidyanathan, *Robustness of difference coarrays of sparse arrays to sensor failures—part i: A theory motivated by coarray music,* IEEE Transactions on Signal Processing **67**, 3213 (2019).

[12] C.-L. Liu and P. P. Vaidyanathan, *Robustness of difference coarrays of sparse arrays to sensor failures—part ii: Array geometries,* IEEE Transactions on Signal Processing **67**, 3227 (2019).

[13] C.-L. Liu and P. P. Vaidyanathan, *Hourglass arrays and other novel 2-d sparse arrays with reduced mutual coupling,* IEEE Transactions on Signal Processing **65**, 3369 (2017).

[14] C.-L. Liu and P. Vaidyanathan, *Super nested arrays: Linear sparse arrays with reduced mutual coupling—part i: Fundamentals,* IEEE Transactions on Signal Processing **64**, 3997 (2016).

[15] C.-L. Liu and P. Vaidyanathan, *Super nested arrays: Linear sparse arrays with reduced mutual coupling—part ii: High-order extensions,* IEEE Transactions on Signal Processing **64**, 4203 (2016).

[16] Y. Chi, L. L. Scharf, A. Pezeshki, and A. R. Calderbank, *Sensitivity to basis mismatch in compressed sensing,* IEEE Transactions on Signal Processing **59**, 2182 (2011).

[17] K. Hu, S. P. Chepuri, and G. Leus, *Near-field source localization: Sparse recovery techniques and grid matching,* in *2014 IEEE 8th Sensor Array and Multichannel Signal Processing Workshop (SAM)* (IEEE, 2014) pp. 369–372.

[18] B. N. Bhaskar, G. Tang, and B. Recht, *Atomic norm denoising with applications to line spectral estimation,* IEEE Transactions on Signal Processing **61**, 5987 (2013).

[19] S. Semper, F. Roemer, T. Hotz, and G. Del Galdo, *Grid-free direction-of-arrival estimation with compressed sensing and arbitrary antenna arrays,* in *2018 IEEE International Conference on Acoustics, Speech and Signal Processing (ICASSP)* (IEEE, 2018) pp. 3251–3255.

[20] M. Wagner, Y. Park, and P. Gerstoft, *Gridless doa estimation and root-music for non-uniform linear arrays,* IEEE Transactions on Signal Processing **69**, 2144 (2021).

ACKNOWLEDGEMENTS

Life in the Netherlands for me started back in 2014 when I decided to pursue a master's at TU Delft. Since that time it has been an incredible learning curve with lots of ups and downs. I was fortunate enough to have crossed paths with many people who have influenced and helped me in this journey. As the Ph.D. phase is coming to an end, I would like to take this opportunity to reflect and present my sincere gratitude to all of them who were part of this process with me.

Firstly, I would like to thank my promotor Geert Leus for providing me an opportunity to pursue Ph.D. under him and Microflown AVISA for financially supporting this study. Geert is an outstanding researcher and very professional in his approach. I feel fortunate to be his student and have been taught by him. Considering the fact that we work at different places, you were always there with timely responses whenever I needed your guidance. I also got some opportunities to know you personally and made some great memories during the conference trips. Your passion for cycling is admirable. Thank you Geert, for everything, it was a pleasure working with you.

Alex, thank you for giving me the opportunity to work at Microflown and funding this Ph.D. study. You have constantly supported us (signal processing group at Microflown), even during all the turbulent phases. You were generous in providing all the resources required for the work and allowing me to travel abroad for conferences.

It is a honor to have Prof. M. Snellen, Prof. V. Koivunen, Prof. M. Moonen, Prof. A. Bhandari, Prof. SP. Chepuri and Dr. D.F. Comesaña on the doctoral committee. I would like to thank all of them for taking some time to assess the initial version of this thesis and be part of the defense.

Dani, my daily supervisor at Microflown, is very instrumental in this journey. You helped me settle down in Microflown and also in Arnhem during my initial days. You always kept the work environment positive and energetic. I felt comfortable approaching you for any suggestions; you were more like a friend. Your skills in acoustics and experimental study are second to none. As I always say to you that you are a magician when it comes to visualization of the data. I cannot put it in words to describe the influence you had on me, thank you, Dani.

I would like remember all my colleagues (David, Grachi, Nico, Zahra, Michal and Bart) at signal processing group in Microflown for all your constant support and encouragement. During past several years, I traveled with you guys day in and day out, thank you for all the memories till now and many more to come in the future. David, I learned how to navigate the trade from you when it comes to processing and extracting inference from the real datasets with acoustic events from artillery, rockets and moving drones. Thank you for all the discussions and guidance. I would also like to thank other colleagues from Microflown including Ivan, Antonio, Emiel, Niels, Micheal Massen, EJ, Ashwin Nayak, Rob, Herman, Fabio, Enzo and Koen for all your support, conversations and healthy discussions. The memories created with my flatmates (Michal and Ivan), and those board game nights, once every week, were special.

In the initial three years, I often visited TU Delft to attend graduate school courses, regular meetings and catch up with my friends there. Here I would like to cherish all the memories created with Sundeep, Mario, Pim, Tarik, Jamal, Elvin and Venkat. Sundeep, thank you for taking me into your wing and guiding me to the nuances of carrying out research and writing academic papers during initial days of my Ph.D. You were like a big brother, who helped me both personally and professionally. All the trips we went together (both conference trips and the ones with Kavyakka) were close to my heart. Mario and Pim, we were the passengers traveling in the same boat. Thank you for being there and sharing all the ups and downs in this phase. All the dinners, activities, trips and conversations with you guys were memorable. You guys made this journey extra special for me. Tarik, I enjoyed all the trips and conversations with you bro. Thank you for helping me whenever I asked you for something. I also want to thank Prof. Alle-Jan van der Veen for his positive words of support whenever I visited Delft. Further, I would also like to thank Minaksie, Irma and Antoon for all your help in the administrative matters.

Pranav, Sagar and Siddarth, you guys were the family for me here. During the initial days in this foreign land you guys provided me much required solace. I will never forget all the moments that I spent with you guys. Later on Ashwini and Monika joined us and brought more happiness. You guys were there to support me even during toughest phases, thank you. Jeevan, Divya, Ashwin Nayak, Apeksha, Satish and Bhavani, thank you for being part of this journey. Also, I would like to thank Goverdhan and Nandish for your encouragement and regularly catching up with me. Furthermore, I would like to remember all the teachers and mentors who inspired me at various stages of my life.

My father-in-law, mother-in-law, brother-in-laws, aunts, uncles and cousins back in India, thank you for all your warm wishes and encouragement during all these days. My sister Roja has been a pillar of strength to me. You always stood for me and supported me in all the endeavors. My wife and better half Abhilasha, thank you from bottom of my heart for all the love and support. I am looking forward for our partnership to flourish further and create lifetime worth of memories. Finally, I would like to dedicate this thesis to my parents. Mom, you have instilled the values for leading life in a right path. Dad, you have led by example to be courageous amidst all the adversities. I will forever be indebted to you both for all your sacrifices.

K. Nambur Ramamohan,
Arnhem, May 2022.

CURRICULUM VITÆ

KRISHNAPRASAD NAMBUR RAMAMOHAN was born in Kolar, INDIA, on 18th FEB 1991. He received the Bachelor's in Electronics and Communications Engineering degree from BMS College of Engineering, Bangalore, India, in 2012. Between 2012 and 2014, he held Applications and Product Engineer positions at Cypress Semiconductors, Bangalore, India. In 2016, he received Master of Science degree from Delft University of Technology, The Netherlands. As part of the Masters degree, he carried out internship at Leiden University Medical Center (LUMC), The Netherlands in 2015 and Masters' thesis work at Microflown Technologies, Arnhem, The Netherlands in 2016. Since 2016, he is with Microflown AVISA, The Netherlands as a Research Scientist. Between 2016-2021, he was also a guest researcher while pursuing his PhD thesis work with the Circuits and Systems group at the Faculty of Electrical Engineering, Mathematics and Computer Science of the Delft University of Technology, The Netherlands. His PhD thesis work was part of NWO's "ASPIRE" project and funded by Microflown AVISA. His general research interests lie in statistical signal processing, linear algebra, convex optimization, array signal processing and acoustic signal processing.



Microphones are the most popular devices used to convert sound into electrical signals. However, with the advent of sensor technology, transducers capable of measuring vector quantities are opening up many new possibilities. One such device is an acoustic vector sensor (AVS), which measures both acoustic pressure and particle velocity, and has shown promising results with distinct advantages. In this work, we explore the characteristics of AVS arrays and their variations in comparison to the conventional microphone arrays for the purpose of direction-of-arrival estimation of far-field sound sources. Furthermore, we also look into one of the practical aspects of calibrating the AVS arrays and propose novel techniques to address this issue.

ISBN: 978-94-6366-556-8